National Library
of Canada

Acquisitions and
Bibliographic Services Branch

395 Wellington Street
Ottawa, Ontario
K1A 0N4

Bibliothèque nationale
du Canada

Direction des acquisitions et
des services bibliographiques

395, rue Wellington
Ottawa (Ontario)
K1A 0N4

Your file Votre référence

Our file Notre référence

NOTICE

The quality of this microform is heavily dependent upon the quality of the original thesis submitted for microfilming. Every effort has been made to ensure the highest quality of reproduction possible.

If pages are missing, contact the university which granted the degree.

Some pages may have indistinct print especially if the original pages were typed with a poor typewriter ribbon or if the university sent us an inferior photocopy.

Reproduction in full or in part of this microform is governed by the Canadian Copyright Act, R.S.C. 1970, c. C-30, and subsequent amendments.

AVIS

La qualité de cette microforme dépend grandement de la qualité de la thèse soumise au microfilmage. Nous avons tout fait pour assurer une qualité supérieure de reproduction.

S'il manque des pages, veuillez communiquer avec l'université qui a conféré le grade.

La qualité d'impression de certaines pages peut laisser à désirer, surtout si les pages originales ont été dactylographiées à l'aide d'un ruban usé ou si l'université nous a fait parvenir une photocopie de qualité inférieure.

La reproduction, même partielle, de cette microforme est soumise à la Loi canadienne sur le droit d'auteur, SRC 1970, c. C-30, et ses amendements subséquents.

Canada

University of Alberta

Preliminary Decay Studies at TISOL

by

Paul C. McNeely ©

A thesis submitted to the Faculty of Graduate Studies and Research in
partial fulfillment of the requirements for the degree of
Doctor of Philosophy

in

Nuclear Physics

Department of Physics

Edmonton, Alberta

Spring 1995

National Library
of Canada

Acquisitions and
Bibliographic Services Branch

395 Wellington Street
Ottawa, Ontario
K1A 0N4

Bibliothèque nationale
du Canada

Direction des acquisitions et
des services bibliographiques

395, rue Wellington
Ottawa (Ontario)
K1A 0N4

Your file Votre référence

Our file Notre référence

THE AUTHOR HAS GRANTED AN IRREVOCABLE NON-EXCLUSIVE LICENCE ALLOWING THE NATIONAL LIBRARY OF CANADA TO REPRODUCE, LOAN, DISTRIBUTE OR SELL COPIES OF HIS/HER THESIS BY ANY MEANS AND IN ANY FORM OR FORMAT, MAKING THIS THESIS AVAILABLE TO INTERESTED PERSONS.

L'AUTEUR A ACCORDE UNE LICENCE IRREVOCABLE ET NON EXCLUSIVE PERMETTANT A LA BIBLIOTHEQUE NATIONALE DU CANADA DE REPRODUIRE, PRETER, DISTRIBUER OU VENDRE DES COPIES DE SA THESE DE QUELQUE MANIERE ET SOUS QUELQUE FORME QUE CE SOIT POUR METTRE DES EXEMPLAIRES DE CETTE THESE A LA DISPOSITION DES PERSONNE INTERESSEES.

THE AUTHOR RETAINS OWNERSHIP OF THE COPYRIGHT IN HIS/HER THESIS. NEITHER THE THESIS NOR SUBSTANTIAL EXTRACTS FROM IT MAY BE PRINTED OR OTHERWISE REPRODUCED WITHOUT HIS/HER PERMISSION.

L'AUTEUR CONSERVE LA PROPRIETE DU DROIT D'AUTEUR QUI PROTEGE SA THESE. NI LA THESE NI DES EXTRAITS SUBSTANTIELS DE CELLE-CI NE DOIVENT ETRE IMPRIMES OU AUTREMENT REPRODUITS SANS SON AUTORISATION.

ISBN 0-612-01726-5

Canada

University of Alberta
Library Release Form

Name of Author: **Paul C. McNeely**

Title of Thesis: **Preliminary Decay Studies at TISOL**

Degree: **Doctor of Philosophy**

Year this Degree Granted: **1995**

Permission is hereby granted to the University of Alberta Library to reproduce single copies of this thesis and to lend or sell such copies for private, scholarly, or scientific research purposes only.

The author reserves all other publication and other rights in association with the copyright in the thesis, and except as hereinbefore provided, neither the thesis nor any substantial portion thereof may be printed or otherwise reproduced in any material form without the author's prior written permission.

Paul McNeely

Paul C. McNeely
135 Anders Close
Red Deer , AB
T4R 1C2
Canada

Date: Feb 23, 95

University of Alberta

Faculty of Graduate Studies and Research

The undersigned certify that they have read, and recommend to the Faculty of Graduate Studies and Research for acceptance, a thesis entitled **Preliminary Decay Studies at TISOL** submitted by Paul Charles McNeely in partial fulfilment of the requirements for the degree of Doctor of Philosophy in Nuclear Physics.

G. Roy
Dr. G. Roy

L.G. Greeniaus
Dr. L.G. Greeniaus

W.C. Olsen
Dr. W.C. Olsen

J C Samson
Dr. J. Samson

Robert Fedosejevs
Dr. R. Fedosejevs

LGG for
Dr. J. Lee (External Examiner)

Date: 6 March 1995

Abstract

In this thesis the development of a flexible $\beta\gamma$ spectroscopy station, which is now available for experiments at TISOL, is described. This involved the implementation of an improved ion beamline, the commissioning of a low background experimental area, a tape transport target system, a detector endstation, a CAMAC-based data acquisition system, and off-line analysis software. The new spectroscopy station was used to investigate the $\beta\gamma$ decays of ^{25,26,27}Ne. The experimental results obtained for ^{25,26}Ne — the half-life, β–endpoint energy, γ–ray energies, and relative branching ratios — are compared to previous measurements and to theoretical predictions where possible. No evidence for ^{27}Ne was found, probably due to the short half-life. A feasibility study for the parity non-conserving α–decay of ^{18}O was also conducted Recommendations are given for the development of TISOL and the existing experimental apparatus necessary for the successful completion of the full scale parity-violation experiment.

Acknowledgement

As is typical with an endeavor of this scale a great many more people than just myself contributed to the successful completion. I would first like to gratefully acknowledge the help and support given to me by my supervisor Gerry Roy over the years. This includes not only my funding over the time of the experiments and the analysis but more recently a phone call whose content was extremely important to my future. Neither experiment would have been possible without the existence of the TISOL facility and so I salute its creators John D'Auria and Marik Dombsky. Both of these people worked very hard to ensure that I had as much beam time as possible what ever the pressure from other users. As well, they diverted a great deal of their limited time to ensuring that the ion beam for the experiment was as good as possible. And lastly I would like to thank them for the many useful and interesting talks which have increased my knowledge of the mysteries of radionuclide production, among other topics discussed late at night over beer. The willing support of the overworked engineering and technical staff at TISOL was also very much appreciated.

I should also thank some other people at TRIUMF. Dave Diel, and Grant Scheffer for helping me through the teething process when I was learning about digital electronics. I very much appreciate the time Richard Helmer spent introducing me to the whacky world of nucleonics. Peter Green answered many of my NOVA questions usually very late at night, although since I was field testing the system maybe the thanks should go the other way around! In terms of getting the electronics system up and running Eli Korkmaz was absolutely crucial. He was vital to my understanding of a great many elements of detector design and integration and he allowed me to get a few hours of sleep every day during the runs which in some ways have been more useful. I shudder to think what the experimental runs would have been like without him. A great many other people at TRIUMF: Dave Hutcheon, Peter Jackson, Lothar Buchmann, and John Vincent helped in ways both great and small and believe me it was and is still appreciated.

I would like to thank the people of Red Giant for allowing me to be a part of a real full scale experiment. My only regret is not having a camcorder on that very first run. For the example they provided me and the opportunity to work with a great bunch of people I would like to thank Dick Azuma and Jim King. I should also thank James Powell for keeping my humility in line by kicking my butt all those times in Assault but then we never would do anything but physics now would we.

I would like to thank Gordon Greenius for all the help he gave me during the analysis of the data. He also spent a great deal of his own time in the pursuit of sculpting the best quality thesis that could be out of the initial stone. This may not have been appreciated at four in the morning while doing changes but I and any readers bear him a heartfelt thank you. I would also like to thank Faquir Khanna for both his excellent teaching over the courses I have taken from him but also for answering all the questions that were generated during the writing of the thesis. I would also like to thank both Norm Kolb and Allena Opper for an introduction into the american thought process and adding to my understanding of physics and physicists.

Finally, last but not least I would like to thank my fellow graduate students: Evan Hackett, Mahar Quraan, Phil Langil, Kevin Klapstein and James Powell for many interesting talks, rewarding experiences, and for being a great bunch of people. And guys I am not a crook!

Table of Contents

Chapter One: Introduction 1

1.1 Physics Possibilities of Radioactive Beams 1

1.2 Production of Radioactive Isotopes 11

1.3 The TISOL Facility at TRIUMF 15

1.4 Thesis Goals 23

Chapter 2: The Heavy Neon Search 25

2.1 Theory of Beta Decay 25

2.2 Theory of Gamma Transitions 30

2.3 The Shell Model Theory of Nuclear Structure 35

2.4 Motivation for Study of the Neon Isotopes 44

2.5 Theoretical Predictions and Previous Data 46

Chapter 3: The Experimental Apparatus 55

3.1 Experimental Endstation Hardware 55

3.2 Experimental Apparatus Used for the ^{18}N Study 62

3.3 Detector Properties 66

  3.3.1 Hyper Pure Germanium Detectors 67

    3.3.1.1 Photon Interactions 68

    3.3.1.2 Charged Particle Interactions 72

    3.3.1.3 Energy Calibration of the Germanium Detectors 74

    3.3.1.4 Efficiency Calibration of the Germanium Detectors .. 75

  3.3.2 Plastic Scintillator Detectors 84

    3.3.2.1 Calibration of the Beta Telescope 89

  3.3.3 Silicon Surface Barrier Detectors 92

  3.3.4 Neutron Detectors 95

3.4 Experimental Endstation Data Acquisition System 96
  3.4.1 The CAMAC Digital Electronics 97
  3.4.2 Master Gate Logic 99
  3.4.3 Data Acquisition System Logic 102
    3.4.3.1 Beta Trigger Electronics 103
    3.4.3.2 The ΔE–E β Telescope 104
    3.4.3.3 The Liquid Scintillator Neutron Detector 104
    3.4.3.4 The ^{3}He Neutron Detector 105
    3.4.3.5 The HPGe Detector Electronics ($\beta\gamma$) 105
    3.4.3.6 Coaxial — Planar HPGe Coincidence ($\gamma_1\gamma_2$) 106
3.5 Data Acquisition System for the ^{18}N PNC Feasibility Study 107

Chapter 4: The Decay of the Heavy Neon Isotopes 109

4.1 Experiment 597 Historic Overview 109
  4.1.1 Experimental Difficulties 113
4.2 Gamma Ray Data Analysis 114
  4.2.1 Peak Fitting Procedures 114
4.3 Summary of the Half–life Analysis Techniques 119
4.4 Summary of the Beta Spectrum Analysis Techniques 124
4.5 The ^{25}Ne(β)^{25}Na Reaction 125
  4.5.1 ^{25}Ne Gamma Ray Energies and Branching Ratios............... 125
  4.5.2 ^{25}Ne(β)^{25}Na Half–life 136
  4.5.3 ^{25}Ne Beta Energy Endpoint 141
4.6 The Results for the ^{26}Ne(β)^{26}Na Reaction 145
  4.6.1 ^{26}Ne Gamma Ray Energies and Branching Ratios 145
    4.6.1.1 High Energy γ's from ^{26}Ne(β)^{26}Na 158
  4.6.2 ^{26}Ne(β)^{26}Na Half–life 160
  4.6.3 ^{26}Ne Beta Energy Endpoint 162

4.7 The Initial Search for ^{27}Ne(β)^{27}Na 166

4.7.1 Results for ^{27}Ne 166

4.8 Production of Neon Isotopes at TISOL 169

Chapter 5: The ^{18}N($\beta\alpha$)^{14}C Decay 174

5.1 Introduction to Alpha–Decay 174

5.2 Introduction to the Parity Violating Interaction 178

5.3 Experiment Justification and Background 184

5.4 The ^{18}N($\beta\alpha$)^{14}C Parity Violation Feasibility Study 188

5.4.1 The ^{18}N($\beta\alpha$)^{14}C Decay Data 191

5.4.2 Comments on Performing the ^{18}N($\beta\alpha$)^{14}C
PNC Experiment 206

Chapter 6: Conclusions 213

6.1 TISOL Technical Developments 213

6.2 The Decay of the Heavy Neon Isotopes ^{25}Ne, ^{26}Ne, ^{27}Ne 215

6.2 The Feasibility Study for the PNC α–Decay in the
^{18}N($\beta\alpha$)^{14}C Reaction 219

References 221

Appendix 1: Abbreviations and Acronyms 229

Appendix 2: Calculation of the Mass Attenuation Coefficient 234

List of Tables

Table 1.1. The currents at the various faraday cups during the tuning process for the E597 [top half] and E589 (Red Giant) [bottom half] experimental runs. 21

Table 2.1. Selection rules for Electromagnetic (El) or Magnetic (Ml) Transitions of angular momentum l. $\Delta\pi$ is the change in parity. 34

Table 2.2. Expected transition rates for the decay of ^{26}Ne. The Statistical Factor S_l has not been included. 34

Table 2.3. The predictions of the Semi-Empirical Mass Formula (SEMF) as compared to experiment for the Neon (Z=10) isotopes from A=15 to A=33. The Q-values for neutron and proton emission are also given. 41

Table 2.4. Known decay properties of ^{26}Ne before completion of our study from [Duf87, Ten92]. 47

Table 2.5. The half-life and P_n values of ^{27}Ne. The theoretical half-life as predicted by [Wil83] is also given. 50

Table 2.6. The predicted Q values for ^{25,26,27}Ne [Wil83] compared to experimental values when possible from [Goo73]. 51

Table 2.7. The calculated yield for a 1 g/cm^2 target for production of Neon isotopes from a Uranium (Z=92, A=238) target using a 500 MeV proton beam. The Expected Production Yield at the target takes into account a 10 g/cm^2 thick target and a production current of 0.75 μA. The Expected Detectable Yield takes into account the diffusion time from the target, transit time through the TIS, ionization efficiency in the ECR, and transmission through the ion beamline. 54

Table 3.1 The known physical properties of all detectors described in Sections 3.1 and 3.4 are given below. 61

Table 3.2: The specifications on the detectors used in the experimental runs. The first half of the table is for the 1992 run while the second half is for the 1993 run. 65

Table 3.3. Some of the important physical properties of Germanium related to detection of charged particles. 68

Table 3.4. Calibration information for the sources used to calibrate the HPGe detectors. 75

Table 3.5. The table showing the data and calculations used to determine the efficiency of each detector. 82

Table 3.6. The results of the efficiency fit for each detector along with other important identifying information. 83

Table 3.7. The properties of NE102A scintillator and the RCA 8575 photomultiplier. 87

Table 3.8. This table gives the half-life and maximum beta energy of the isotopes used as input data in the calibration fits. 93

Table 3.9. This table gives the results for each isotope used in the calibration showing fitting parameters, χ^2, and the calibration values determined from them. 93

Table 4.1. The run number and purpose for each of the runs in the November 1992 beam period. 112

Table 4.2. The intensities of the known γ-rays from the decay ^{25}Ne(β)^{25}Na [Reu83]. 126

Table 4.3 The results of the fits for the energy of the observed γ-rays from ^{25}Ne. 127

Table 4.4. The intensity of the observed γ-rays along with the information used to calculate the intensities. The relative efficiency (ε_{ff}) for both detectors is adjusted for the low energy drop off by using the measured value of the far point efficiency at 81 keV. Note: the error in the number of counts is probably underestimated, but no better value is available. 129

Table 4.5. The results for the relative intensity ratio of the 980 keV peak to the 90 keV peak for both HPGe detectors and the comparison with the expected value [Goo73]. Errors are probably under-estimated. 132

Table 4.6. The results for the half-life of ^{25}Ne(β)^{25}Na from both β and γ decays. 137

Table 4.7. The results of the fits to the observed β–decay energy spectra to determine the endpoint energy. The first half of the table contains the data from the computer fit. In the second half the data from the Kurie plots is shown. HER stands for High Energy Region, T_e >3.5 MeV. The two numbers in the existing data column indicate the expected energy in the decay to the 90 keV (1070 keV) energy levels [Goo73]. 142

Table 4.8. This table shows the results for the ^{26}Ne(β)^{26}Na γ–ray energies determined for each run and each observed γ–ray. The average of all runs and the standard error of the mean (S.E.O.M) are quoted at the bottom. Note that systematic errors in the energy calibration are larger than the statistical fluctuations quoted here. 148

Table 4.9. The data on the observed counts and the adjusted counts used in calculating the branching ratios. The efficiency used for the 82 keV γ-ray is the measured value for 81 keV from the calibration. The other two efficiencies are calculated from the linear efficiency fit. 155

Table 4.10. The branching ratios determined for the ^{26}Ne(β)^{26}Na Decay. The first three columns are for the decay scheme with no cascade, and the final two columns are assuming a cascade does occur. The run average and standard error of the mean is given at the bottom of each column.... 156

Table 4.11. The average intensity [γ's observed per 100 decays of ^{26}Ne] of the observed gamma rays under the assumption of a gamma cascade for all the runs (26, 30, 31, 35, 35 RAW, 38, and 38 RAW). The sample average and standard error of the mean are given. 157

Table 4.12. The average gamma branching ratio for the 234 keV level to the ground state or the 83 keV level under the assumption of a gamma cascade for all runs (26, 30, 31, 35,35 RAW, 38 and 38 RAW). The sample average and standard error of the mean are given. 157

Table 4.13. The average difference in energy between the 234 and 83 keV energy level as compared to the average energy of the observed intermediate gamma ray for all runs (26, 30, 31, 35, 35 RAW, 38, and 38 RAW). The sample average and standard error of the mean are given. 158

Table 4.14. The results of the half-life data analysis for all runs for the β–decay of ^{26}Ne with a comparison to the existing data from the literature. The value from [Wil83] indicates the result for their pure shell model calculation. 161

Table 4.15. The data from the fit to the observed beta decay energy of ^{26}Ne summed over all runs. The first value is the result obtained by the DECAYFIT program fit of the decay curve while the bottom two results are based on Kurie plot analysis. The two values in the theoretical prediction are for transitions to the 82 keV and 234 keV levels. The *ft* values were calculated by assuming a γ–cascade. 163

Table 4.16 The values used in eq. 4.21 to calculate the theoretical event rate at the detectors. 171

Table 4.17 The values used in eq. 4.22 to calculate the observed yield of Ne isotopes based on the results of the half-life fitting. 172

Table 4.18 A comparison between the calculated, $Y_i(det)$, and observed, Y_{obs}, rates for the intensity of neon isotopes. The observed rate is determined by fitting the half-life spectrum of the ΔE–E telescope. Two different values for the diffusion time from the target were assumed. Systematic errors in the observed yields could be as large as 20%. 173

Table 5.1. Weak coupling constants from the "best value" and "reasonable range" results of Desplanques, Donoghue, and Holstein [Des80] for the Glashow–Weinberg–Salam model[a]. 183

Table 5.2: A summary of pertinent information for the $^{18}N(\beta\alpha)^{14}C$ decay. The excitation energy (E_x) in ^{18}O, β-branching ratio, and spin/parity assignments are given. As well, the expected energies of the emitted α and ^{14}C in the Laboratory frame are also given. The sub-threshold state at 6.198 MeV is included since it is relevant to the K-matrix fits. Brackets indicate uncertain values. 189

Table 5.3. The number of events seen in the experiment during each of the run periods showing the total number of α particles observed and the number of α particles observed in the 1.081 MeV peak [$N_\alpha(7.62)$]. The figure from which the data were derived is also given with (u) referring to the upper pair of spectra and (l) referring to the lower pair. 195

Table 6.1. A summary of the results obtained for $^{25}Ne(\beta)^{25}Na$ compared with previous measurements. The error in the branching ratio is not given because it is believed to be grossly under-estimated. 216

Table 6.2. The results obtained for $^{26}Ne(\beta)^{26}Na$ are compared with previous measurements and theoretical predictions. The branching ratio calculation assumes a γ–cascade and the branching ratio quoted for the 151 keV γ–ray is from the 234 keV level. 217

Table A2.1. Shown below is the calculation for μ for Al and plastic scintillator at all relevant energies for the experiment. 235

List of Figures

Figure 1.1. The tableau shows all the known elements with atomic number, $Z \leq 11$ and some of their properties. The format used is: the first line is the element symbol and its mass followed by the isospin and parity of the nuclear ground state, the second line is either the half-life if the element is unstable or elemental abundance if it is stable, the third line is the decay energy in MeV if the element is unstable or its mass if it is stable. All even-even nuclei have an 0^+ ground state. A diagonal slash following the isospin number indicates a half integral value. All stable isotopes are indicated by the use of outline font on the isotope name *i.e.* Ne. Naturally occurring radioactive elements have a black bar surrounding the element name *i.e.* ^{14}C. 4

Figure 1.2. A schematic of the production sequence for TISOL. 7

Figure 1.3. The proposed basic process that provides the energy necessary to sustain stars. 10

Figure 1.4. The complete CNO cycle, including the use of ^{20}Ne as a connection to the NeNa cycle. 10

Figure 1.5. The various burning processes occurring in a Red Giant Star and the various elements produced during a supernova (from [Rol88]). ... 12

Figure 1.6. Examples of fragmentation, spallation, and fission reactions. 14

Figure 1.7. The TRIUMF experimental beamlines. The TISOL facility is visible at the end of beamline 4A. 18

Figure 1.8. A schematic diagram of the TISOL graphite target/oven is shown. The figure is not drawn to scale. 19

Figure 1.9. Side view of the TISOL facility showing all its major components. 22

Figure 2.1. The angular distribution of gamma ray intensity for an $M1$ transition followed by an $E2$ transition. 36

Figure 2.2. A comparison between the Shell Model (S.M.) predictions of [Wil83] and the experimental results of [Goo73] for ^{25}Ne(β)^{25}Na. 47

Figure 2.3. Comparison between the known energy levels of ^{26}Na [End90] and the predicted levels obtained by [Wil83] for ^{26}Ne(β)^{26}Na. The Roman numerals indicate levels expected to be populated by β–decay from which previously unobserved γ–rays may be emitted. The numbers given in italics indicate states where theoretical predictions indicate no β–decay. The shown J^{π} values are experimental values. All of the β–decays predicted by [Wil83] are to 1^+ levels 49

Figure 2.4. A comparison between the known energy levels of ^{27}Na {End90] and those predicted by [Wil83]. Only those levels for which the predicted β–branching ratio was greater than 1% are shown. Where two levels were very close they are shown as one line with the two energies separated by a slash. The only experimentally known J^{π} value is for the ground state ($5/2^+$) all other shown values are from the predictions by [Wil83]. 50

Figure 2.5. The theoretical yield for a 1 g/cm^2 target for production of Neon isotopes from a Uranium (Z=92, A=238) target using a 500 MeV proton beam. 53

Figure 3.1. The vacuum box containing the TISOL tape transport system. The tape path used for the experiment is shown. 56

Figure 3.2. The timing pulses controlling the tape transport system. Also shown are the timing points which were used in the half-life data analysis in Chapter 4. t_o is the time required for the power supply to ramp down and t_{stop} marks the end of the ion beam collection period. t_{obs} marks the position of an event. The adjusted times t_1 and t_2 are also shown. The clock starts at the beginning of the graph and is later reset. 58

Figure 3.3. The schematic of the tape controller electronics. 59

Figure 3.4. A top view of the final detector configuration for E597. The ^{3}He detector is located below the mid-plane of the collection station. ... 60

Figure 3.5. A side view of the Red Giant target holder/detector assembly. 63

Figure 3.6. An end view of the Red Giant Target holder assembly showing the detector pairs and the foil holders. 64

Figure 3.7. Diagram defining the kinematic variables for Compton scattering. 70

Figure 3.8. The linear absorption coefficient for photon scattering in Ge and Si. Shown are the contributions of the three processes. The linear absorption coefficient is the cross-section multiplied by a constant. Thus the figure shows, as well, the variation of the process cross-section with energy.[Ort92] 71

Figure 3.9. The various processes occurring for a high energy gamma ray and what the pulse height spectrum would look like.............................. 73

Figure 3.10. The calibration curve for Ge1 using data collected during run 25. 76

Figure 3.11. The calibration curve for Ge2 using data collected during run 25. ... 76

Figure 3.12. The relative error of the fits to the calibration data from the known energies of the γ-rays included in the fit. The circles are for the Coaxial HPGe (Ge1), while the squares are for the Planar HPGe (Ge2). The data are from run 25 for each detector and correspond to Figs. 3.10 and 3.11. 77

Figure 3.13 The fit to the 1173 keV γ peak for the efficiency calibration of the coaxial HPGe (Ge1). Clearly visible in the peak shape are the two pairs of gaussian peaks symmetric about the main centroid at 2840 channels. Each peak has a σ of 3.23 ± 0.02 channels. The first pair of peaks is offset from the main centroid by 3.30 ± 0.02 channels, while the second pair of peaks is offset by 12.34 ± 0.04 channels. 79

Figure 3.14. The fit to the efficiency data for detectors Ge1 and Ge2 from data taken at the far position. 84

Figure 3.15. The most probable energy loss W_{MP} for electrons in the plastic scintillator (ΔE) of thickness 1.5 mm used in the experiment. 87

Figure 3.16. The details of the scintillators used in the β paddles, $\beta 1$ and $\beta 2$. ... 88

Figure 3.17. The details of the scintillator used in the ΔE detector. 89

Figure 3.18. The fit to the ^{6}He and ^{23}Ne beta decays showing the fit determined for each. Only every 5th data point is shown for clarity. 94

Figure 3.19. The configuration of the CAMAC crate for the experiment. 98

Figure 3.20. The electronics layout for experiment 597. 101

Figure 3.21. The schematic of the electronics used for the ^{18}N study. 107

Figure 4.1. Spectra showing the effects of the cuts in the data analysis for the coaxial HPGe, Ge1. The top spectrum is the RAW data while the bottom spectrum shows those events which passed all levels of cuts. Data are from run 29 for ^{25}Ne. 115

Figure 4.2. Spectra showing the effects of the cuts in the data analysis for the planar HPGe, Ge2. The top spectrum is the RAW data while the bottom spectrum shows those events which passed all levels of cuts. Data are from run 29 for ^{25}Ne. 116

Figure 4.3. The decay ^{8}He(β)^{8}Li. The total fit to the data is shown as a solid line. The various growth/decay components described in the text are indicated by broken lines. The growth and decay of ^{8}He is indicated by [— · —] and labeled 1. The ^{8}Li produced during the deposition is indicated by [— —] and labeled 2 and 3. The ^{8}Li produced during the decay of ^{8}He after the ion beam has been redeflected is indicated by [— - —] and labeled 4. 123

Figure 4.4. The fit to the data for the 90 and 980 keV γ-rays from run 22. The upper pair (a,b) is from the coaxial HPGe, Ge1, while the lower pair (c,d) is from the planar HPGe, Ge2. 130

Figure 4.5. The fit to the data for the 90 and 980 keV γ-rays from run 29. The upper pair (a,b) is from the coaxial HPGe, Ge1, while the lower pair (c,d) is from the planar HPGe, Ge2. 131

Figure 4.6. The efficiency for a typical 15% Canberra HPGe detector. The solid line indicates the efficiency fit to data above 200 keV. The squares are measured efficiency in the region where the detector has a non linear response. The deviation at low energy from the linear fit is clearly visible. NOTE: All data points are estimated from a graph published in the Canberra catalogue (ninth edition). 134

Figure 4.7. The fit to the ^{25}Ne(β)^{25}Na β–decay half-life determined by the event time of the ΔE–E events. The upper spectrum is for run 22 while the lower is for run 29. 138

Figure 4.8. The ^{25}Ne(β)^{25}Na half-life fits to the 90 keV γ–ray peak for the planar HPGe (Ge2) from both runs. The upper spectrum is for run 22 while the lower is for run 29. 139

Figure 4.9. The comparison between both the observed half-lives of ^{25}Ne for the different runs and detectors and with the previous work [End90]. 140

Figure 4.10. The fit to the β decay energy in the thick E scintillator. Only every fifth data point is shown to prevent confusion. The upper is for run 22 while the lower is for run 29. 143

Figure 4.11. The Kurie plot of the data from run 29 for ^{25}Ne. 144

Figure 4.12. The Kurie plot to the beta decay data in the thick E scintillator from run 29 for ^{25}Ne for the region $T_e > 3.5$ MeV. Only every fifth data point was plotted. 144

Figure 4.13. The fits to the γ–ray peaks for the combined runs 26,30, and 31. ... 149

Figure 4.14. The fits to the γ–ray peaks for run 35. 150

Figure 4.15. The fits to the γ–ray peaks for the RAW data from run 35. 151

Figure 4.16. The fits to the γ–ray peaks for run 38. 152

Figure 4.17. The fits to the γ–ray peaks for the RAW data from run 38. 153

Figure 4.18. The energy level diagrams for the two possible decay schemes. The cascade scheme, on the right, also shows the γ branching ratio for the 234 keV level. 156

Figure 4.19. The spectrum from the coaxial HPGe for ^{26}Ne from run 38 showing the high energy region. The 1808 keV peak is from the decay of the daughter ^{26}Na. 159

Figure 4.20. The level scheme for the decay ^{24}Ne(β)^{24}Na from [End90]. 160

Figure 4.21. The fit to the beta-decay time spectrum to determine the half-life of ^{26}Ne. All runs (26, 30, 31, 35, and 38) were combined. 161

Figure 4.22. The fit from the program DECAYFIT to the β–decay energy spectrum of ^{26}Ne(β)^{26}Na for all runs combined. 164

Figure 4.23. The Kurie plot for the β–decay energy spectrum of ^{26}Ne(β)^{26}Na for all runs combined. 165

Figure 4.24. The Kurie plot for the β–decay energy spectrum of ^{26}Ne(β)^{26}Na for all runs combined, for $T_e > 3.5$ MeV. 165

Figure 4.25. The spectrum collected by the planar HPGe during Run 45. 167

Figure 4.26. The thick E scintillator spectrum collected during Run 45. 168

Figure 5.1. A diagram showing the situation facing a S–wave α–particle attempting to exit the nucleus. R is the nuclear radius. The centrifugal barrier is zero in this case. 176

Figure 5.2. All possible one boson exchange contributions to a NN interaction. The weak vertex is indicated by the cross. 180

Figure 5.3. The results for the four experiments performed to determine f_π [Els84, Eva85, Lan85, Sno83]. As described in the text, the result for ^{21}Ne has the same scaling factor of 1/3 applied to it as was used for ^{18,19}F. 186

Figure 5.4. The energy level diagram for ^{18}N(β)^{18}O* from [Ajz87]. 190

Figure 5.5. TRIM calculations for the sum of the energy loss in both the carbon collector foil and the gold layer of the SSB. Curves are given for both α and ^{14}C particles. 193

Figure 5.6. The spectra of the observed ratio between the pulse height in Detector 2 to Detector 1 for all the data which survived the first level skim. The upper spectrum is from July 92 and the lower from June 93. 194

Figure 5.7. The spectra of the energy ratio versus alpha energy for both the July, 92 (upper) and June, 93 (lower) experimental periods. All of the data which survived the first level skim are shown in the graphs. ... 197

Figure 5.8. The spectra collected during the July 92 running period. The upper two spectra are the α and ^{14}C spectra with only the first level skim cuts applied. The lower two spectra are the α and ^{14}C spectra with the tighter ratio constraints applied. 198

Figure 5.9. The spectra collected during the June 93 running period. The upper two spectra are the α and ^{14}C spectra with only the first level skim cuts applied. The lower two spectra are the α and ^{14}C spectra with the tighter ratio constraints applied. 199

Figure 5.10. The spectra of the time difference between the first detector pair for both running periods. The upper spectrum is from July 92 and the lower from June 93. 200

Figure 5.11. The 2D spectra for the first detector pair. The first contour level signifies 2 events in the energy bin. The upper spectrum is from July 1992 and the lower from June 1993. 203

Figure 5.12. The area where parity violating α particles are expected to be observed. The upper spectrum has only the first level skim applied while the lower has the all the tighter constraints applied. The size of the rectangle indicates the number of events / bin. The smallest rectangle indicates 1 event. The spectra are from the July 1992 running period. The large box indicates the energy region in which the majority of the PNC events are expected. 204

Figure 5.13. The area where parity violating α particles are expected to be observed. The upper spectrum has only the first level skim applied while the lower has the all the tighter constraints applied. The size of the rectangle indicates the number of events / bin. The smallest rectangle indicates 1 event. The spectra are from the June 1993 running period. The large box indicates the energy region in which the majority of the PNC events are expected. 205

Figure 5.14. The results of a SILT based calculation for the production of heavy Nitrogen isotopes from a Zeolite target. The typical target thickness of the current TISOL target (13.6 g/cm^2) is used. 211

Figure A2.1. Comparison between the attenuation coefficient for Al listed in the Ortec catalog and the value calculated from eq. A2.1. The calculated value contains only the Compton cross-section. Also shown are the parameters of the fit to the observed data. 236

Chapter One: Introduction

The main body of this thesis is divided into two parts. Part one deals with the use of the TISOL facility to search for the beta branching ratios and gamma decay schemes of ^{26}Ne and ^{27}Ne. A theoretical introduction to the shell model, β–decay, and γ transitions are included. This investigation was carried out as TRIUMF experiment 597. Details will also be given of the detector station and associated data acquisition systems developed as part of the TRIUMF TISOL facility during the course of the thesis. The data collected in the various runs are summarized and presented.

Due to the restricted availability of beam time at TRIUMF to complete the Ne studies to our complete satisfaction, it was decided to include a feasibility study of the search for Parity Violation in the ^{18}N$(\beta\alpha)^{14}$C decay as part of the thesis. The goal of this part of the thesis work was to determine which elements of the experiment need to be improved to allow a proper measurement to be conducted at a later date [Roy93]. The data to be analysed were collected during the periods July 21–26, 1992 and June 15–20, 1993. A brief description of the collection station and its electronics is included. An introduction to the relevant parts of the theory of Nuclear Parity Violation and alpha decay are presented.

1.1 Physics Possibilities of Radioactive Beams

The field of radioactive beam physics is young, having begun in the 1960's with the construction of such facilities as GANIL, TOFI at LAMPF, and ISOLDE at CERN. These facilities allow for the production of radioisotopes as beams rather than by activation of a target followed by chemical separation and analysis.

Initially, radiochemical separation was used to study radionuclides. However, this method does not allow access to radionuclides with short half-lives (≤ minutes).

Radioactive nuclear beams (RNB), on the other hand, allow access to radionuclides of considerably shorter half-lives (≥ nanoseconds). The production of a radioactive beam is accomplished in different ways depending on the production method chosen (see Section 1.2). In early 1991 the accelerator complex at Louvain La Neuve (LLN), Belgium became the first facility in the world to produce and accelerate a radioactive beam, thus allowing the beam to be used as the projectile particle in further experiments. The world-wide nuclear physics community shows great interest in building a facility capable of producing a wider spectrum of isotopes and having higher energies per nucleon than is currently available at LLN. This interest has resulted in the formation of both a steering committee and a user group in North America that is pushing for the development of the Isospin Laboratory (ISL)[ISL91]. The steering committee has produced a brief guide which lists the main operational requirements of such a facility. At present there are several existing facilities, including TRIUMF, that are starting to do some of the initial research and development that will be required to build ISL. For example, Rutherford Laboratory in England is planning to build a 20 mA proton test facility to study target design, and the Oak Ridge Laboratory in the USA is building a limited isotope-production facility based on their tandem Van de Graaff Accelerator.

It is safe to conclude from the above information that the field of accelerated radioactive beams, although in its infancy, shows strong signs of having many exciting possibilities for growth and development. Of the many possible uses for radioactive beams, I will address two that are directly related to my thesis: nuclear structure and nuclear astrophysics. For many other exciting possibilities see ref. [ISL91].

The field of nuclear physics has always used the decay of radioactive nuclei as a window on the processes that bind together the stable nuclei which make up the world around us. Fig. 1.1 shows all the possible elements, both radioactive and stable, for $Z \leq 11$ Sodium (Na) where Z is the atomic number.

In the past 50 years most of the naturally-occurring or easy-to-produce radionuclides have been exhaustively studied. Since the sixties and early seventies,

Figure 1.1. The tableau shows all the known elements with atomic number, $Z \leq 11$ and some of their properties. The format used is: the first line is the element symbol and its mass followed by the isospin and parity of the nuclear ground state, the second line is either the half-life if the element is unstable or elemental abundance if it is stable, the third line is the decay energy in MeV if the element is unstable or its mass if it is stable. All even-even nuclei have an 0^+ ground state. A diagonal slash following the isospin number indicates a half integral value. All stable isotopes are indicated by the use of outline font on the isotope name *i.e.* **Ne**. Naturally occurring radioactive elements have a black bar surrounding the element name *i.e.* ^{14}C.

Atomic Number (Z)

11									Na 19 19.01388	Na 20 2+ 447ms E 13.89	Na 21 3/+ 22.48s E 3.548	Na 22 3+ 2.605a E 2.842	**Na**23 3/+ 100 22.9998	Na 24 20.2ms/ 14.96h	Na 25 5/+ 60.s E 3.833	Na 26 3+ 1.07s E 9.31	Na 27 5/+ 0.290s E 8.99	Na 28 1+ 30.5ms E 13.9	Na 29 3/+ 44ms E 13.3
10							Ne 16 4E-21s 16.0257	Ne 17 1/- 109ms E 14.53	Ne 18 1.67s E 4.45	Ne 19 1/+ 17.22s E 3.24	**Ne** 20 90.48 19.9924	**Ne** 21 3/+ 0.27 20.9988	**Ne** 22 9.25 21.9913	Ne 23 5/+ 37.2s E 4.376	Ne 24 3.38 m E 2.47	Ne 25 0.61s E 7.30	Ne 26 ~0.2s E 7.3	Ne 27 32 ms 27.006	Ne 28 28.0115
9							F 15 5E-22s 15.018	F 16 0- ~1E-20s 16.011	F 17 5/+ 64.5s E 2.76	F 18 1+ 1.830 h E 1.66	**F** 19 1/+ 100 18.9964	F 20 2+ 11.0 s E 7.03	F 21 5/+ 4.16s E 5.69	F 22 4+ 4.23s E 10.86	F 23 2.2s E 8.5	F 24 0.3s E 13.5			
8					O 12 ~1E-22s 12.0344	O 13 8.9 ms E 17.77	O 14 71s E 5.15	O 15 1/- 124s E 2.76	**O** 16 99.759 15.9949	**O** 17 5/+ 0.037 16.9914	**O** 18 0.204 17.9992	O 19 5/+ 26.9s E 4.82	O 20 13.5s E 3.81	O 21 3.4s E 8.111	O 22 ~3s E 6.6	15	16	17	18
7						N 12 1+ 0.011s E 17.6	N 13 1/- 9.96m E 2.2	**N** 14 1+ 99.63 14.0031	**N** 15 1/- 0.37 15.0001	N 16 2- 7.35s E 10.4	N 17 1/- 4.14s E 8.7	N 18 1- 0.62s E 13.90	N 19 0.3s E 12.54	N 20 0.10s E 18.1	N 21 21.027				
6				C 9 0.13s	C 10 19s E 3.6	C 11 3/- 20.5m E 1.98	**C** 12 98.89 12.0000	**C** 13 1/- 1.11 13.0034	C 14 5730y E 0.156	C 15 1/+ 2.25s E 9.77	C 16 0.74s E 8.0	C 17 20 ms E 13.16	C 18 0.07s E 11.80	C 19 19.035	C 20 20.040				
5				B 8 0.78s E 18	B 9 8E-19s 9.0133	**B** 10 3+ 19.78 10.0129	**B** 11 3/- 80.22 11.0093	B 12 1+ 0.020s E 13.4	B 13 3/- 0.019s E 13.4	B 14 2- 14 ms E 20.84	B 15 9 ms E 19.1		B 17 17.046		B 19 19.064				
4			Be 6 5E-6s 6.0198	Be 7 3/- 53d E 0.86	Be 8 ~3E-16s 8.0053	**Be** 9 3/- 100 9.0122	Be 10 2.7E+6y E 0.56	Be 11 13.6s E 11.5	Be 12 0.011s										
3			Li 5 3/- ~1E-21s 5.0125	**Li** 6 1+ 7.42 6.0151	**Li** 7 3/- 92.58 7.0160	Li 8 2+ 0.85s E 16.0	Li 9 0.17s E 14												
2		**He** 3 1/+ 0.00013 3.0160	**He** 4 ~100 4.0026	He 5 3/- 7.6E-22s 5.0123	He 6 0.81s E 3.51		He 8 0.03s E 10.67												
1	**H** 1 1/+ 99.985 1.0078	**H** 2 1+ 0.015 2.0141	H 3 1/+ 12.26 y E 0.0181																
0		n 1 1/+ 12 m 1.0087																	
	0	1	2	3	4	5	6	7	8	9	10	11	12	13	14				

Number of Neutrons (*N*)

Element	Atomic Mass Number	Ground State J^{π}

Isotopic Abundance
or half-life

Atomic Mass
(amu)
or Decay Energy
(MeV)

with the completion of modern isotope-production facilities, many more have been observed and studied. Isotopes which are ionizable by the surface ionization method (mainly the alkali metals) have been studied extensively, often from the proton to the neutron drip lines. The drip line is the name given to the chain of isotopes on a periodic chart beyond which the nuclei are no longer stable against emission of either a proton or a neutron. Beyond the neutron drip line no more neutrons can be added while beyond the proton drip line no more neutrons can be removed without the immediate decay (half-life $< 10^{-21}$ s) of the isotope.

A major goal of nuclear physics is the prediction of nuclear properties. Predicting the mass, decay characteristics, half-life and spin of previously unobserved nuclei is a strong motivation behind the development of most nuclear theories. Most of these theories can be used to predict nuclear properties far from the valley of stability only by fitting to observed nuclear properties on or close to stability. It is immediately obvious that the farther one goes from stability the less reliable such predictions become. To overcome this it is necessary to have detailed information on isotopes lying far from stability. Besides improving the predictive powers of the theories by putting tighter constraints on their variable parameters, this knowledge also tests our understanding of stable nuclei. Thus more knowledge allows not only better predictions to be made but also opens a window into the fundamental processes going on in stable nuclei and our understanding of them.

To investigate properties of nuclei it is useful to be able to study chains of isotopes. If it is also possible to study the corresponding isobaric chains, then an incredible wealth of information is obtained. These chains enable one to study how the structure and properties of the nucleus change as the number and composition of its constituents change. In principle, the easiest states to calculate theoretically have one nucleon outside of a closed shell because the properties of the nucleus are determined by the single valence nucleon [Pre75]. Since the simplicity of such states permits much more reliable theoretical calculations, a rigorous test of the theoretical principles is possible.

The decay processes themselves also may be studied in detail. By selecting an appropriate "designer" nucleus it is possible to study a particular decay path or even aspects of a more general decay theory. For example, to study the $E1$ cross section of the astrophysically important $^{12}C(\alpha,\gamma)^{16}O$ reaction, the $^{16}N \rightarrow \beta \rightarrow ^{16}O^{*} \rightarrow \alpha + ^{12}C$ inverse decay has been used [Buc93a, Zha93, Azu94]. The TRIUMF experiment [Buc93a, Buc93b, Azu94, Pow95], known as the Red Giant Experiment, measured the $E1$ cross section down to $E_{\alpha} = 600$ keV. The $^{12}C(\alpha,\gamma)^{16}O$ reaction is important because of its effect on the $^{12}C/^{16}O$ abundance ratio. Although the $3(^{4}He) \rightarrow ^{12}C + \gamma$ reaction rate at stellar burning temperatures (~ 2×10^{8} K) is known to ±15%, the extrapolation to the cross section for the $^{12}C(\alpha,\gamma)^{16}O$ reaction at stellar burning temperatures, even though it has been extensively studied, varies by two orders of magnitude. Using the TISOL facility it was possible to produce a sufficiently intense ^{16}N ion beam to study the decay via the inverse reaction. The results of this experiment constrain the relevant $^{12}C(\alpha,\gamma)^{16}O$ cross section with an error of ~25%. This experiment was possible because of the existence of the TISOL production facility.

Using radioactive beams it would be possible, given a sufficiently general production system, to provide nuclei *on demand* for such studies. One could choose nuclei whose beta decay energies vary from 0.5 MeV to 13 MeV or whose decay proceeds via neutron emission. It would even possible to study specific elements of a decay process, such as the 1st–forbidden beta decay matrix elements of the $0^{+} \rightarrow 0^{-}$ states by creating the required initial state nucleus in a radioactive beam facility. In Fig. 1.2 a typical production chain for TISOL is shown, illustrating all the system elements in the sequence starting from the production of the radionuclides to the detection of their decay products.

The field of nuclear astrophysics offers some of the most exciting uses of Radioactive Nuclear Beams, but these applications generally require the acceleration of the resulting ion beams. Although not all astrophysical reactions of interest require ion beam acceleration, many of them take place with isotopes whose half-lives are less than a few seconds. In such cases it is impossible to produce a low energy ion beam of these isotopes, implant the ions on a target matrix and then bombard the target with a stable beam, for example, a ^{4}He beam. The *only* way to study such a reaction is with a radioactive ion beam. Although the Red Giant Experiment does not form part of this thesis, I made a major contribution to it and its success was dependent on many of the technical developments I made for the Ne and parity violation studies. A brief description of the important physics is included.

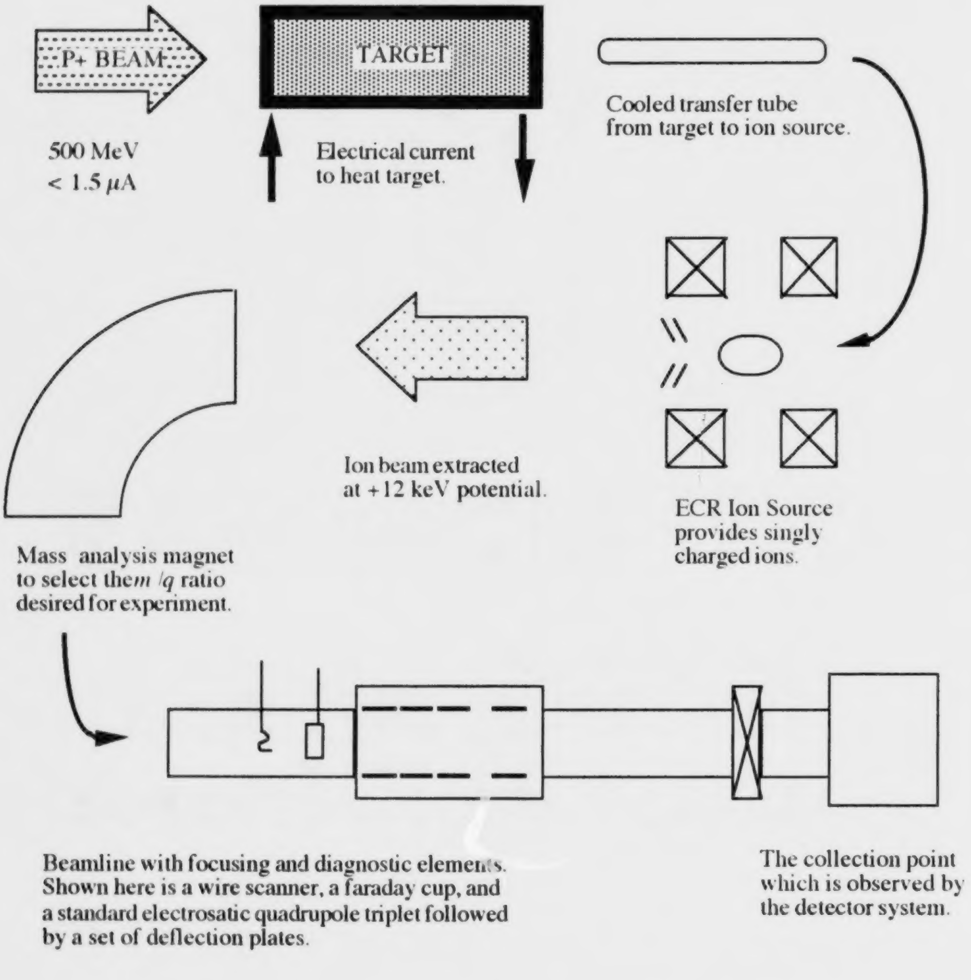
P+ BEAM
TARGET
Cooled transfer tube from target to ion source.
500 MeV
< 1.5 μA
Electrical current to heat target.
Ion beam extracted at +12 keV potential.
ECR Ion Source provides singly charged ions.
Mass analysis magnet to select the m/q ratio desired for experiment.
Beamline with focusing and diagnostic elements. Shown here is a wire scanner, a faraday cup, and a standard electrosatic quadrupole triplet followed by a set of deflection plates.
The collection point which is observed by the detector system.

Figure 1.2. A schematic of the production sequence for TISOL.

All the current theories of stellar nucleosynthesis and the isotopic abundances depend on theoretical calculations of reaction cross sections based on a very few measured cross sections. It is imperative that more of the important cross sections be measured in the laboratory. First, these measurements check the cross section calculations and constrain the fitting parameters used to estimate the unknown relevant cross sections. Also, experimental measurements can dramatically change all related predictions if the measurements disagree with earlier calculations. A very good example of how one reaction can change our understanding of astrophysical processes is the $^{12}C(\alpha,\gamma)^{16}O$ reaction, mentioned above. New measurements of the reaction rate [Dye74, Red87, Kre88, Zha93, Azu94] have resulted in changes to the theoretical description of the supernova process and what its final products are. The new rate implies a reduced ability of stars to burn carbon and neon. This means more oxygen burning takes place, resulting in an increase in the size of the iron core and more intermediate-mass elements, silicon to calcium, in the supernova debris. This larger iron core affects the result of the explosion. With the old rate, a $25M_{\oplus}$ (25 Solar masses) star would leave a large neutron star residue. Using the new rate, one predicts that an extremely heavy neutron star, or more likely, a black hole would be left [Fow85].

Many interesting astrophysical phenomena occur very quickly, *i.e.*, high energy γ–ray bursts, and the last stages of a supernova. The time scales of these processes are on the order of a second or less, thus it is impossible to study the nuclei involved by traditional production and radiochemical separation/extraction. The nuclei can be studied by the tape implantation technique as developed for this thesis work and used in the study of ^{26}Ne (see Chapters 3 and 4). However, to study reactions of the form He(A,B)C or *p*(A,B)C, both a radioactive and accelerated ion beam are necessary to interact with a hydrogen or helium target.

The origin of the elements which make up our world is still one of the most pressing questions in astrophysics. This alone justifies the use of radioactive ion beams. The early universe was composed of hydrogen (and for a brief period neutrons). The basic reaction which begins the complicated process through which all the heavier masses are then produced is: $4p \rightarrow {}^4\mathrm{He} + 2e^+ + 2\nu$ (Q=26.73 MeV). However, the actual process occurring in stars is much more complicated and consists of a series of chains (see Fig. 1.3) of fusion reactions. The light elements lithium and beryllium are also produced by similar fusion reactions between He, H, and D.

These reactions obviously cannot account for all the elements of the universe — where did the heavier elements come from? In an interesting irony, the answer is found in the most catastrophic event in the universe—a supernova. The processes that occur during the last few moments of the supernova are believed to produce most of the heavier ($A > 12$) elements in the universe, A is the total number of nucleons in the nucleus. It is not surprising, given their importance to us, that the first elements whose production was studied were C, N, and O. Carbon can be produced by either the unlikely fusion of three ^{4}He nuclei or through a series of compound reactions which produce the same net result. The most important of these compound reactions is $^8\mathrm{Be}(\alpha,\gamma)^{12}\mathrm{C}$.

Starting with carbon it is possible to describe a series of nuclear reactions whose net result is the conversion of $4p$ into an α accompanied by a release in energy. The conversion of four protons into helium is the process that is assumed to be the basic fuel of stars. In these reactions, however, other isotopes are used as catalysts. The complete CNO cycle is shown in Fig. 1.4. Using the first cycle, **I**, as an example, it is clear that the C which begins the cycle is eventually regenerated to serve as a catalyst again. Counting the protons involved in the reaction one arrives at the required conversion of four protons into one helium. This cycle also produces heavier mass elements. These heavier mass elements begin to accumulate in the star much as *ash* from a fire. As the temperature and pressure in a star begins to grow due to the increased gravitational attraction of its increasing mass, other avenues of catalysed fusion open up, namely the NeNa and the MgAl cycles. These cycles produce the medium weight ($A \approx 20$–30) elements.

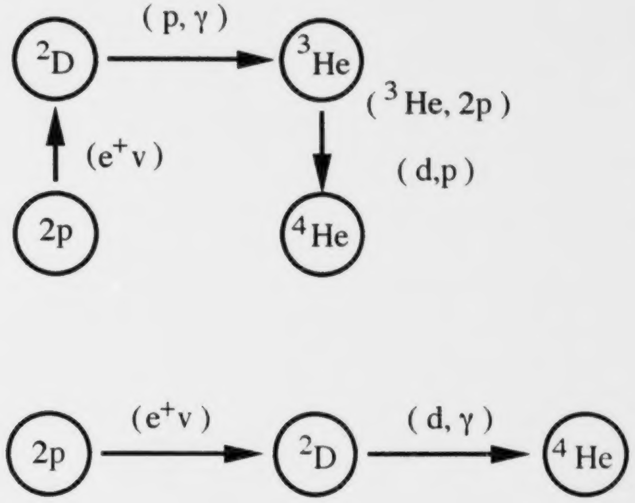
(p, γ)
²D
³He
(³He, 2p)
(e⁺v)
(d,p)
2p
⁴He
(e⁺v)
(d, γ)
2p
²D
⁴He

Figure 1.3. The basic process that provides the energy necessary to sustain stars.

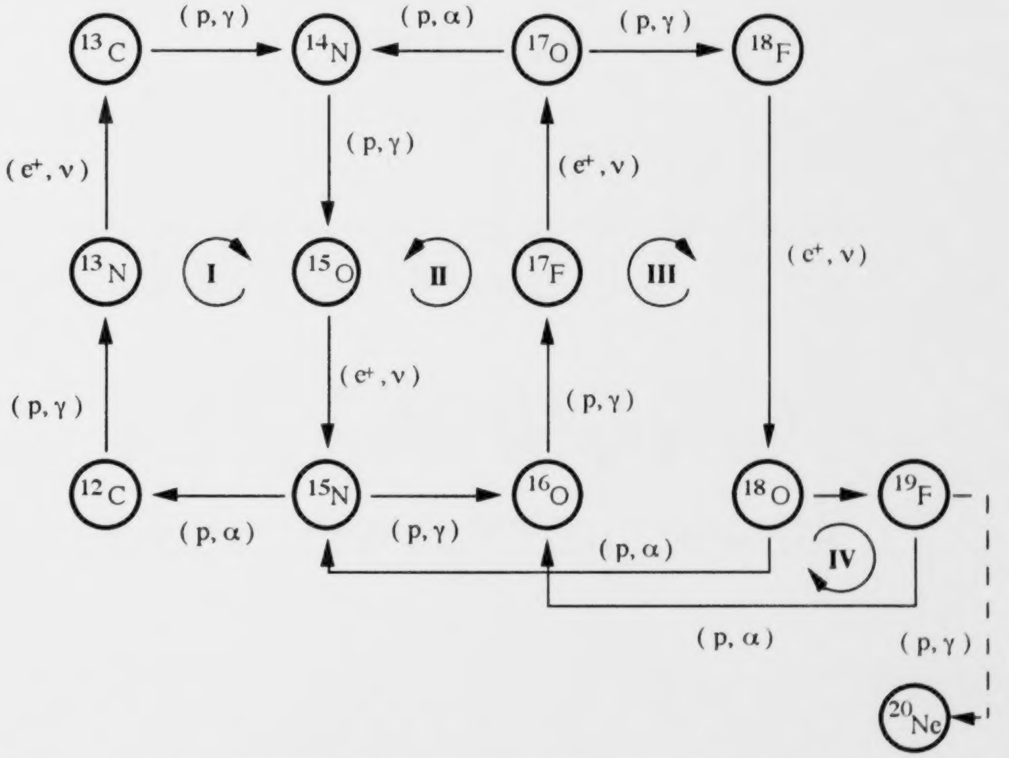
¹³C
(p, γ)
¹⁴N
(p, α)
¹⁷O
(p, γ)
¹⁸F
(e⁺, ν)
(p, γ)
(e⁺, ν)
¹³N
I
¹⁵O
II
¹⁷F
III
(e⁺, ν)
(e⁺, ν)
(p, γ)
(p, γ)
¹²C
¹⁵N
¹⁶O
¹⁸O
¹⁹F
(p, α)
(p, γ)
(p, α)
IV
(p, α)
(p, γ)
²⁰Ne

Figure 1.4. The complete CNO cycle, showing ^{20}Ne as a link to the NeNa cycle.

The last reaction shown in Fig. 1.4, $^{19}F(p,\gamma)^{20}Ne$, is proposed as the linkage from the CNO to the NeNa cycle. To maintain itself the star begins to burn fuel other than hydrogen or helium as is shown in Fig. 1.5. It begins burning the ash, the leftovers of the previous fuel cycles, moving through C, Ne, O, and Si. By the time it reaches Si burning, the core of the star is entirely Fe–Ni. Eventually the star is unable to support its own mass, it starts to collapse and the supernova event begins. The core collapses until nuclear repulsion forces it to rebound. This core bounce sends an outward travelling pressure wave through the infalling material of the star that results in tremendous pressures and energies. It is during this stage of the supernova where the so called *rp*, *s* and *r* processes occur that produce the heavier elements beyond iron. Eventually the outer atmosphere of the star, now rich in heavy stable elements, is ejected into the stellar vacuum. Some of this material, when dispersed through the galaxy, will coalesce into new solar systems. The various processes occurring in a Red Giant are shown in Fig. 1.5, including the estimated density and temperature of the various shells.

Looking at the CNO cycle in Fig. 1.4, it is obvious that its predictive powers are highly dependant on a good knowledge of nuclear physics, and more importantly, nuclear reaction rates. Most of these rates can only be found by direct measurement and this is the single most important justification for accelerated radioactive beams.

1.2 Production of Radioactive Isotopes

There are two methods for the production of radioisotopes. The first is the thin target recoil fragmentation method. This method uses a thin target bombarded by an energetic primary beam. The products of any interaction between the target and beam are also energetic and the particles which escape the far side of the target are a mixture of the scattered primary beam and the radioisotopes of interest. This mixed beam is separated by a mass analysis system into beams of different mass and charge which can then be used for further experiments. This system has the advantage that the half-life of the produced radioisotope does not affect the yield since in-flight decay is the only worry. The disadvantages are related to the relatively large energy and momentum of the radioisotopes. They must be slowed down before many experiments can be performed and, since they are highly energetic, the magnetic separation system requires the use of strong magnetic fields.

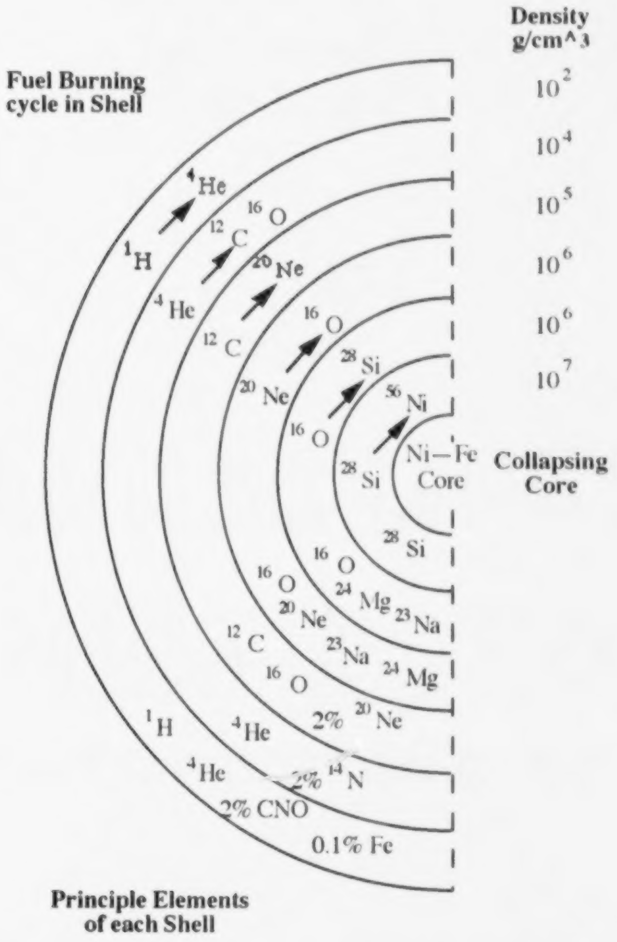
Density g/cm^3
Temp °K
Fuel Burning cycle in Shell
10^2 2×10^7
10^4 2×10^8
10^5 5×10^8
10^6 1×10^9
10^6 2×10^9
10^7 4×10^9
^{1}H → ^{4}He
^{4}He → ^{12}C ^{16}O
^{12}C → ^{20}Ne
^{20}Ne → ^{16}O
^{16}O → ^{28}Si
^{28}Si → ^{56}Ni
Ni–Fe Core
Collapsing Core
^{28}Si
^{16}O ^{24}Mg ^{23}Na
^{16}O ^{20}Ne ^{23}Na ^{24}Mg
^{12}C ^{16}O 2% ^{20}Ne
^{1}H ^{4}He 2% ^{14}N
^{4}He 2% CNO
0.1% Fe
Principle Elements of each Shell

Figure 1.5. The various burning processes occurring in a Red Giant Star and the various elements produced during a supernova (adapted from [Rol88]).

The second method uses a thick target. The primary beam passing through the target interacts with the target atoms via fragmentation, spallation, and fission reactions (see Fig. 1.6 for examples of these processes). The products are trapped by the target matrix and they lose energy to it. The target is kept hot, the exact temperature is dependent on the isotope one wishes to extract. The produced radioisotopes diffuse through the hot target matrix and emerge as gases. These gases are then sent to an attached ion source to be ionized. After ionization the low energy ion beam is then magnetically separated. This method has the advantage of higher yields due to increased target thickness. The better beam quality from the ion source is another advantage. One disadvantage is that the beam is very low energy and thus requires a post-accelerator. As well the diffusion/transfer process is complicated and requires a long time compared to the shortest half-lives.

TISOL is a thick target Isotope Separator On Line (ISOL) facility. It produces radioactive isotopes using technology similar to that employed by ISOLDE at CERN. ISOLDE was the world's first full scale production/experimental facility for radionuclides. The radioisotopes at TISOL are produced by the interaction of TRIUMF's primary proton beam (E_p= 500 MeV) with a target of thickness ~10 g/cm^2.

The production yield of any product, y_i, can be calculated by the simple formula:

$$y_i = \rho_p \sigma_i N_t , \qquad (1.1)$$

where ρ_p = proton or other primary beam current in particles/second, σ_i is the total production cross section for isotope i and N_t is the target thickness in atoms/cm^2.

Fragmentation Process

$$^{238}_{92}\mathrm{U} + p \longrightarrow \begin{bmatrix} ^{104}\mathrm{Ag}, & ^{50}\mathrm{Ca}, \\ ^{26}\mathrm{Ne}, & ^{30}\mathrm{Si}, \\ ^{4}\mathrm{He}, & ^{20}\mathrm{C}, \\ p, & 4n \end{bmatrix}$$

Spallation Process

$$^{238}_{92}\mathrm{U} + p \longrightarrow \begin{bmatrix} n,\ p, \\ ^{6}\mathrm{He}, \\ ^{231}\mathrm{Th} \end{bmatrix}$$

Fission Process

$$^{238}_{92}\mathrm{U} + p \longrightarrow \begin{bmatrix} ^{140}\mathrm{Xe}, \\ ^{94}\mathrm{Sr}, \\ 4n,\ p \end{bmatrix}$$

Figure 1.6. Examples of fragmentation, spallation, and fission reactions.

In general σ is a complicated function depending on the energy and type of primary beam, the target material, and the required product. At present there is no purely theoretical method to calculate production cross section. However, phenomenological estimates are available from a computer code (SILT) [Dau90], based on the Silberberg–Tsao fitting of all available measured cross sections [Sil85]. An example of the results of SILT can be found for the Neon isotopes in Fig. 2.5 in section 2.5.

1.3 The TISOL Facility at TRIUMF

The TRIUMF Isotope Separator On Line (TISOL) facility was started in 1985 by J.M. D'Auria as a test/engineering facility for the front end of the proposed TISAC (TRIUMF Isotope Separation and Acceleration) Radioactive Beams Facility [TRI85]. The initial purpose of TISOL was to explore the technology needed to produce radioactive ions, develop the necessary engineering experience for the production and handling of radioactive isotopes, and to engage in target studies. Since then TISOL has gone through many changes [Oxo87, Dau89, Dau92]. Two important changes have resulted in its growth from an engineering test site to a facility capable of supporting a modest experimental program. The first improvement was the successful installation of an ECRIS (Electron Cyclotron Resonance Ion Source) [McN89] coupled to the production target. This made TISOL the world's first thick target isotope production facility with an ECR ionizer and gave it a world lead in the production of nitrogen and noble gas radioisotopes. The second change was the extension of the ion beamline into a low background experimental area in the summer of 1991. This included the addition of a switchyard magnet to allow the ion beams to be sent to one of three experimental endstations. As the experimental area was completely new, all services routinely available in other experimental area at TRIUMF, or elsewhere, from electrical power to cable trays had to be designed and assembled. I played a major part in the installation of equipment and making it a productive area for physics research. The acquisition of the new low background experimental area is of primary importance to TISOL's future. The previous experimental area was heavily contaminated by both thermal neutrons and γ–rays from neutron capture reactions, making high precision measurements there impossible. Additionally, the new area is highly visible to the other scientists at TRIUMF and has served to increase awareness of both the existence of TISOL and the exciting work being carried out there.

TISOL is located on beamline 4A on the proton side of the TRIUMF cyclotron (see Fig. 1-7). Beamline 4A is rated for proton beam currents ≤ 10 μA, but for safety reasons the current used at TISOL has never exceeded 1.5 μA, except in short test runs. The facility can be divided into three main sections: the target/ion source (TIS), the mass separator and ion beamline, and the user endstations.

The target/ion source (TIS) is the heart of any Isotope Separator. At present all production targets at TISOL are limited to solid materials. There are two oven designs. The most frequently used oven is a hollow graphite cylinder (1 cm diameter x 8 cm long) supporting a graphite chimney and a tantalum transfer tube leading to the ECRIS [McN89, McN89b, McN90, Buc92]. This oven can be raised to 2000 °C by resistive heating. The maximum temperature obtainable is currently limited by the power supply and not by the oven design itself. To prevent arcing, the oven is held at the same potential as the ion source (+12 kV). The target material is loaded into a perforated graphite crucible that is inserted into the oven (the crucible is electrically isolated from the oven by boron nitride rings). It is impossible to completely seal the oven and hot graphite is porous, so a fraction (<20%) of the gaseous radioisotopes produced escape into the surrounding vacuum chamber and are lost.

The second oven type was developed for use with the Red Giant Experiment [Buc91, Azu94]. It consists of a stainless steel tube (2 cm diameter x 20 cm long) that, after being loaded with the target material, is sealed by welding the end cap in place. The oven is then connected to the transfer line. This oven can be heated to temperatures of 600 °C. The volume of target material contained in this target is greater than in the graphite oven. Both target assemblies are designed to be mounted on a flange that contains all the gas, water, and electrical connections so that targets may be changed quickly.

Figure 1.7. The TRIUMF experimental beamlines. The TISOL facility is visible at the end of beamline 4A.

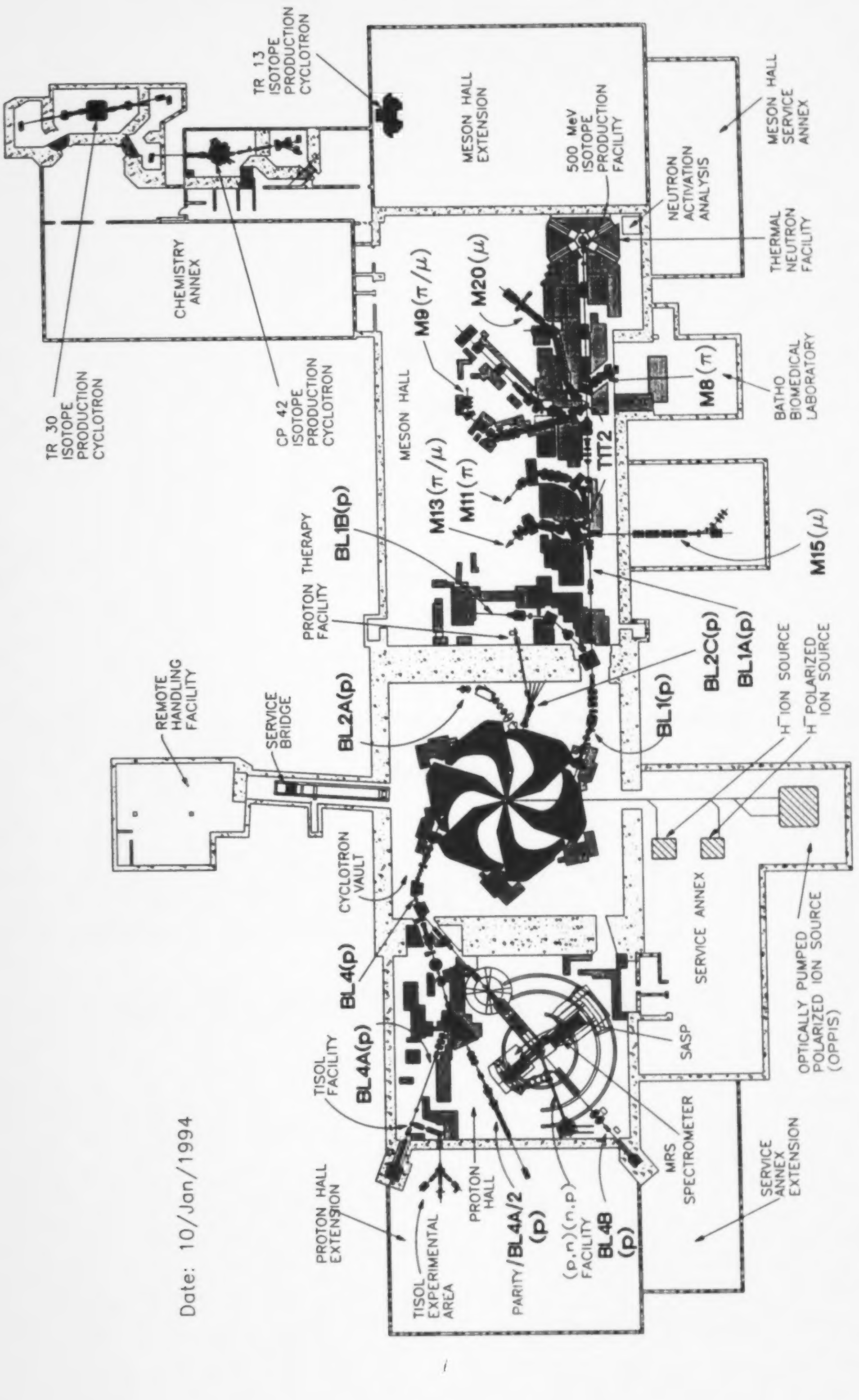
TR 30 ISOTOPE PRODUCTION CYCLOTRON
CP 42 ISOTOPE PRODUCTION CYCLOTRON
TR 13 ISOTOPE PRODUCTION CYCLOTRON
CHEMISTRY ANNEX
MESON HALL EXTENSION
500 MeV ISOTOPE PRODUCTION FACILITY
MESON HALL SERVICE ANNEX
NEUTRON ACTIVATION ANALYSIS
THERMAL NEUTRON FACILITY
MESON HALL
M9(π/μ)
M20(μ)
M8(π)
BATHO BIOMEDICAL LABORATORY
TI T2
M13(π/μ)
M11(π)
M15(μ)
PROTON THERAPY FACILITY
BL1B(p)
BL2C(p)
BL1A(p)
BL1(p)
BL2A(p)
REMOTE HANDLING FACILITY
SERVICE BRIDGE
H⁻ION SOURCE
H⁻POLARIZED ION SOURCE
CYCLOTRON VAULT
SERVICE ANNEX
OPTICALLY PUMPED POLARIZED ION SOURCE (OPPIS)
BL4(p)
BL4A(p)
TISOL FACILITY
SASP
MRS SPECTROMETER
PROTON HALL EXTENSION
TISOL EXPERIMENTAL AREA
PROTON HALL
PARITY/BL4A/2 (p)
(p,n)(n,p) FACILITY
BL4B (p)
SERVICE ANNEX EXTENSION

Date: 10/Jan/1994

BEAMLINES AND EXPERIMENTAL FACILITIES

■ EXISTING □ PROPOSED

Radioisotopes produced in the hot target material gradually diffuse out of the target, and move through the transfer tube to the ECRIS where they are ionized. Since the ECRIS will ionize any atom that reaches it, to eliminate problems of ion beam purity, a cold trap which eliminates all non-gaseous elements is located in the transfer line between the target and ECR. Use of a heated transfer line would permit ionization of metallic elements.

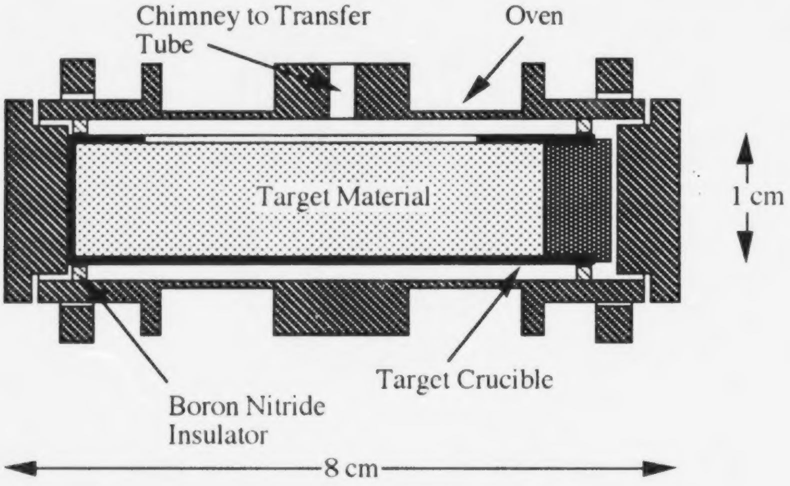

Figure 1.8. A schematic diagram of the TISOL graphite target/oven is shown. The figure is not drawn to scale.

TISOL also has available a surface ionization source designed by M. Dombsky [Dau89, Dom92]. The source is designed to replace the entire ECRIS/target assembly on the ion beamline. It uses the same graphite oven as the ECR. Surface ionization sources are highly efficient (>80%), but only for certain elements, mainly the alkali metals. Regardless of the method of ionization, the ions are extracted at a potential of +12 kV and injected into the ion beamline for mass-separation and transfer to the experimental area on the proton hall extension floor (see Figs. 1.7 and 1.9).

The TISOL ion beamline consists of steering/focusing elements, a mass spectrometer, a switchyard magnet, and a number of diagnostic devices (see Fig. 1–9). After extraction, the ion beam passes through an einzel lens, a quadrupole magnet doublet and a magnetic steerer before entering the mass spectrometer. The mass resolution of the magnet is 1/2400 in the Rb 85–87 mass region. This is sufficient to separate cleanly the isotopes (^{26}Ne, ^{27}Ne, ^{28}Ne), but cannot resolve the isobars (^{15}O, ^{15}C, ^{15}N). After mass analysis, the ion beam passes through a series of electrostatic quadrupoles and an electrostatic bender. There are also electrostatic steerers after most of the electrostatic quadrupole focusing elements (see Fig. 1.9). The steerer just before the electrostatic bender can be biased to +10 kV to deflect the ion beam. The tuning of the electrostatic line is rather time-consuming but the ion beam on the collection station tends to be stable.

After passing through the ion transport line, the ion beam enters the low background experimental area. There is a simple switchyard magnet to select one of three experimental lines. After the switchyard magnet is a quadrupole/steerer box for final focusing. There are a number of diagnostic devices in the beamline. Four faraday cups located along the beamline measure the current. As well, located just before each experimental station, is a faraday cup and wire scanner to allow the beam profile to be monitored. The transmission through the system is good (see Table 1.1) but there are plans for more calculations to be done on various elements plus changes to be made to the mass spectrometer to improve transmission and beam quality.

The whole TISOL operation is controlled by a personal computer running the TRIUMF Instrument Control System program (TICS). From the control station it is possible to monitor and change the settings of all the focusing/steering elements, also, a number of interlocks have been defined to prevent most foreseeable accidents. The interlocks are designed to prevent the malfunction of one element of the system from damaging the others, for example, the oven power supply is interlocked with the vacuum in the target box. Loss of the target box vacuum will turn off the oven power supply preventing thermal damage to both the oven and the target box. The other interlocks prevent the operator from activating equipment by accident, for example, the gate valve between the ECRIS and the beam line cannot be opened unless there is a good vacuum on either side of it. There is a repeater station in the experimental area that allows remote access to the TICS program. Unfortunately, at this time the TISOL beam line elements must all be configured manually as no auto-load capabilities have been built into the system.

Table 1.1. The currents at the various faraday cups during the tuning process for the E597 [top half] and E589 (Red Giant) [bottom half] experimental runs.

m/q	Beamline	Faraday Cup #	Current (μA)
28	Line C	3	45
		4	27
		5C†	28
		EXP Station	17
30	Line B	3	2.6
		4	2.0
		5B†	2.5
		Red Giant (5)*	1.1
		Red Giant (8)*	1.3

*Red Giant (5): the collimator diameter in front of the collection foil was 5 mm . For Red Giant (8): the collimator diameter was 8 mm. This faraday cup was located in the collection assembly described in Chapter 3.

†the letter indicates on which of the three experimental lines after the switchyard magnet that the faraday cup was located.

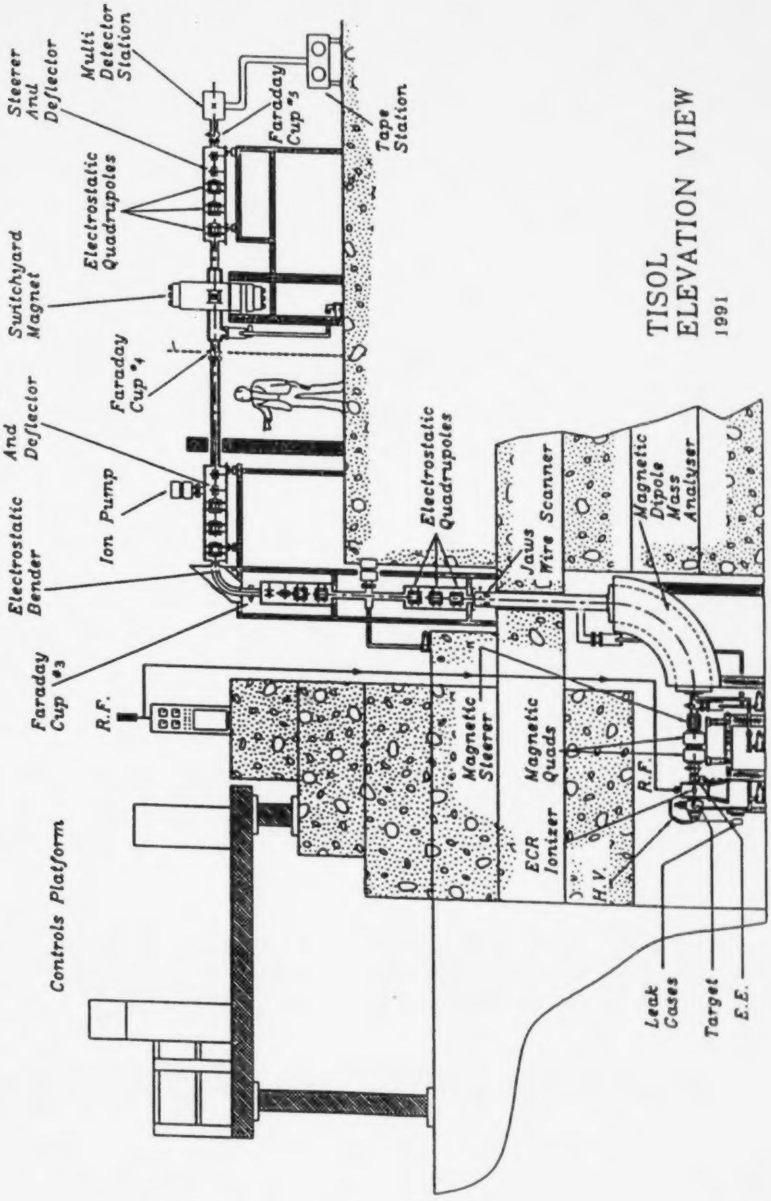
Controls Platform
Faraday Cup #3
R.F.
Electrostatic Bender
Ion Pump
Electrostatic Quadrupoles
Steerer And Deflector
Faraday Cup #4
Switchyard Magnet
Electrostatic Quadrupoles
Steerer And Deflector
Multi Detector Station
Faraday Cup #5
Tape Station
TISOL
ELEVATION VIEW
1991
Electrostatic Quadrupoles
Jaws
Wire Scanner
Magnetic Steerer
Magnetic Quads
ECR Ioniser
R.F.
H.V.
Magnetic Dipole Mass Analyser
Leak Cases
Target
E.E.

Figure 1.9. Side view of the TISOL facility showing all its major components.

1.4 Thesis Goals

The TISOL facility is currently changing its emphasis from engineering/prototype testing and development to that of being a production facility supporting both a growing user community and physics program. This thesis work began with the designing of the low energy ion beamline which extends into the new low background experimental area and ended with the data collection run for feasibility study on parity violation in the decay $^{18}N(\beta\alpha)^{14}C$. The commissioning of the new line, the development of the basic electronic system, and the implementation of the data acquisition software was an important contribution to TISOL. Details of this work are described throughout the thesis

The primary physics goal of this thesis was to carry out a preliminary nuclear physics experiment to investigate the β, and γ decays from $^{25,26,27}Ne$ (more details on the motivation for this is provided in Section 2.4), and demonstrate the usefulness of the new TISOL facility. As this experiment was to be the first $\beta\gamma$ spectroscopy work carried out in the new experimental area, extensive development of experimental support services was carried out. From the beginning it was intended that the experimental apparatus should be usable in future works, so a modular design was implemented to allow for customization by later users (see Section 3.1 for details). It had been recognized early on in the target development work at TISOL that the ion beam from the ECRIS was not isotopically pure and there would often be long-lived contaminants. A tape transport system was designed and built to overcome this problem by stopping radioactive ions of interest and later removing the contamination from the measurement region. Extensive development of a data acquisition system was carried out, both in terms of hardware and software. The final system is presented in detail in Section 3.4. As the TISOL facility had not previously used a CAMAC-based data acquisition system, it was one of the first facilities at TRIUMF to utilize the new site-standard on-line analysis system NOVA [Gre91] and therefore served as a useful debugging tool in NOVA's development. The experience gained during the Ne experiment will indicate which components worked well, and which will require future development. This thesis will also address the capabilities of TISOL in producing isotopes with short (< 1 s) half-lives as all three neon isotopes are relatively short-lived.

The second part of the thesis describes a study that was conducted to determine the feasibility of performing an experiment to measure the parity non-conserving alpha decay from ^{18}O. The evaluation of the data collected and the identification of of the principle elements crucial to the successful completion of the experiment is described in Chapter 5. The importance of studies into parity non-conservation (PNC) is provided in Section 5.3. This PNC study was a by-product of the highly successful Red Giant experiment performed at TISOL [Azu94, Pow95] which was described briefly in Section 1.1. It used the same apparatus (see Section 3.2) and data acquisition system (implemented by me — see Section 3.5) developed for use in the Red Giant experiment. As there were no substantive changes in either the apparatus or data acquisition system, the information gained in the analysis of the Red Giant experiment [Azu94] was directly transferable to the PNC study.

Chapter 2: The Heavy Neon Search

This chapter deals with the theoretical background necessary to follow the analysis of the Ne decay data. Sections 2.1 and 2.2 cover the dominant decay modes — the beta (β) decay and gamma (γ) transitions. Section 2.3 covers the nuclear shell model, since this theory was used by Wildenthal *et al.* [Wil83] to predict the energy levels of ^{25,26,27}Ne. Section 2.4 explains why the Ne isotopes were chosen for this study. The final section 2.5 deals with the limited comparisons that can be made using the present data to the theoretical expectations for ^{25,26,27}Ne and previous measurements.

2.1 Theory of Beta Decay

Nuclear beta decay is the process by which all radioactive nuclei which do not possess sufficient energy in their ground states to emit heavy particles (p, n, α) decay towards stability. There are three forms which beta decay can take:

$n \rightarrow p + e^- + \bar{\nu}$ (β^- emission)

$^{11}\mathrm{C} \rightarrow {}^{11}\mathrm{B} + e^+ + \nu$ (β^+ emission)

$^{7}\mathrm{Be} + e^- \rightarrow {}^{7}\mathrm{Li} + \nu$ (K capture)

Nuclei on the neutron-rich side of stability always decay via β^- emission. Those on the proton-rich side, however, can decay via either β^+ emission or orbital electron capture. In some cases for proton-rich nuclei, both processes occur and compete with one another.

Beta decay has given nuclear physics two of its most interesting puzzles. After it was confirmed that the beta rays emitted by decaying nuclei were ordinary electrons, there was great confusion. The decay of the nucleus was thought to be similar to the decay of an excited atom with the electron taking the place of the emitted photon. However, in the decay of an atom the photon is monoenergetic since it corresponds to the transition between two discrete quantum states. The electron energy from nuclear β–decay on the other hand varies from decay to decay and has a continuous spectrum from zero up to a certain energy E_{max} which depends on the parent and daughter nuclei. Since it was known that β-decays are between two definite states — in the parent and daughter nuclei respectively — this appears to violate simultaneously the conservation of energy, momentum, and angular momentum. Angular momentum seems to be not conserved since it was routinely observed that $\Delta J = 1$ transitions occur while the spin of the electron is 1/2. These problems were resolved in the 1930s by Pauli [Pau34] when he proposed the existence of a massless, neutral, spin–1/2 particle — the neutrino. The existence of the neutrino was confirmed experimentally in the early 1950's [Cow53].

The second puzzle discovered through beta decay was parity non–conservation (PNC). Until 1956 it had been assumed *a priori* that parity conservation, the invariance of the phenomenon in question to *mirror* reflection of the coordinate system, was always true. (For more on parity and parity non–conservation see Chapter 5.) In 1956, based on the decay of the θ and τ mesons, Lee and Yang proposed [Lee56] that the weak interaction did not conserve parity. Beta decay is a form of semi–leptonic decay (*i.e.* both leptons and hadrons take part) and therefore should *not* conserve parity. In 1957, an experiment by Wu *et al.*[Wu57] confirmed Lee and Yang's prediction by observing that in the decay of polarized ^{60}Co the emitted direction of the electron is preferentially opposite to the nuclear spin direction. Hence the expectation value of $<\boldsymbol{v} \cdot \boldsymbol{J}>$, where $\boldsymbol{v}$ is the electron velocity and $\boldsymbol{J}$ is the nuclear spin, is *not* zero, which can only occur if parity is not conserved.

In 1934, Fermi proposed his theory of β–decay [Fer33, Fer34]. His theory is still valid at low energy although the introduction of both relativity and field theory have modified the details of the formalism. For our purposes, as the electrons are of low energy, the original formalism is all that is needed. It allowed the following to be explained [Seg77, Rei72, Kra88]:

(1) the form of the β–decay electron spectrum,

(2) the relationship between the mean life and the maximum decay energy, and

(3) the classification of β–transitions and the establishment of selection rules.

The transition probability, w is written

$$w = \frac{2\pi}{h} \left| H_{if} \right|^2 \rho_{state} , \tag{2.1}$$

where ρ_{state} is the density of states and H_{if} is the matrix element between the two states in question. To expand this expression we must use the following approximations:

(1) the electron may be considered a plane wave and only the first term in the expansion of the exponential term $e^{i\mathbf{k}\cdot\mathbf{r}}$, that is 1, is important;

(2) the energy lost in the nuclear recoil $[E_{rec} << T_e]$ can be ignored;

(3) H_{if} can be replaced with

$$g \frac{M_{if}}{\Omega} , \tag{2.2}$$

where M_{if} is a purely radial integral of the nuclear wave functions, g is a coupling constant and Ω is a volume (introduced for normalization purposes only); and

(4) the mass of the neutrino is zero.

Applying these to eq. 2.1 one obtains

$$w\,(T_e) = \frac{g^2 m_e^5 c^4}{2\pi^3 h^7} \left| M_{if} \right|^2 F\,(Z',T_e)\,(E_{max} - T_e)^2 (T_e^{\,2} + 2T_e m_e c^2)^{1/2} (T_e + m_e c^2) dT_e \;, \tag{2.3}$$

where T_e is the electron kinetic energy, Z' is charge of the daughter nucleus and $F(Z',T_e)$ is a complicated function which includes the effects of the coulomb interaction between the outgoing electron and the nucleus. This latter function can be approximated by [Bla91]

$$F(Z',T_e) \cong \frac{4\pi(1+s)}{\left|(2s)!\right|^2}(2p\kappa)^{2s-2}(s^2+\eta^2)^{s-1/2}\exp\left[2\phi\eta-2s+\frac{s}{6(s^2+\eta^2)}\right], \quad (2.4)$$

where

$$s=\left[1-(Ze^2/hc)^2\right]^{1/2},$$

$$\kappa={}^{Rm_ec}/_{h},$$

$$\eta=+Z'e^2/hv_e, \text{ and}$$

$$\phi=\arctan({}^{s}/_{\eta}).$$

Here R is the nuclear radius, p is the electron momentum in units of m_ec and v_e is its speed. The function $F(Z', T_e)$ does not take into account the screening of the outgoing electron by the atomic electrons but does take into account relativistic effects.

If the constant terms at the beginning of eq. (2.3) are ignored and only the terms dealing with energy are kept the shape of the β–spectrum can be calculated. The terms can then be reorganized into the form

$$\sqrt{\frac{N(T_e)}{F(Z',T_e)(T_e^2+2T_em_ec^2)^{1/2}(T_e+m_ec^2)}}\ \alpha\ (E_{max}-T_e), \quad (2.5)$$

where $N(T_e)$ the number of observed counts at energy T_e replaces $w(T_e)$. If the left side of eq. 2.5 is plotted versus T_e, the intercept of a linear fit is E_{max}, the maximum allowed beta energy. This graph is known as a Fermi–Kurie plot.

Since in general it is not easy to calculate M_{if}, experimental data is analyzed in terms of the ft value given by

$$ft=\frac{const}{\left|M_{if}\right|^2}=f(Z',E_{max})\,t_{1/2}, \quad (2.6)$$

where $f(Z',E_{max})$ is the function $F(Z',E_{max})$ corrected for screening, and $t_{1/2}$ is the partial half-life. The partial half-life is equal to the observed half-life multiplied by the branching ratio to the level which corresponds to the observed E_{max}. It is generally quoted as $\log_{10}(ft)$ or $\log_e(ft)$.

For allowed β–decay there are two selection rules:

$\Delta J = 0$ [no change in parity] Fermi Selection Rule

$\Delta J = \pm 1$, or 0 (except $0 \rightarrow 0$) [no change in parity]

Gamow–Teller (G–T) Selection Rule

It is known that beta decay does not conserve parity. The name 1st-forbidden decay is given to the observed β-decays for which either the Fermi or G-T selection rules for $\Delta J = 0, 1, \ldots$ would be satisfied except for a change in parity, or for a change in spin $\Delta J = 2$, but with a change in parity. Mathematically the transition rate, w, is determined by including additional terms to the electron plane wave exponential expansion. The first term ($\boldsymbol{ik \cdot r}$) is included for 1st-forbidden decays. For the case of 1st-forbidden decays there are also two selection rules:

$\Delta J = \pm 1$, 0 (except $0 \rightarrow 0$) [change of parity]

$\Delta J = \pm 2, \pm 1, 0$ (except $0 \rightarrow 0$, $\frac{1}{2} \rightarrow \frac{1}{2}$, $0 \rightarrow 1$) [change in parity] .

These are completely analogous to the Fermi or G-T selection rules for allowed decays. If the next term is also added then one describes 2nd-forbidden decays and so on. Decays for $\Delta J = 2, 3$ with no change in parity are forbidden by both the allowed decay and the 1st-forbidden selection rules and so are named 2nd-forbidden. The transition rate in this case is calculated by adding in the second term in the electron plane wave expansion. The same naming convention can be continued for 3rd-forbidden decays, and so on for higher orders.

2.2 Theory of Gamma Transitions

The emission of gamma rays (γ) is a common method of de-excitation for nuclei in the light- to medium-mass range. Particle emission begins to compete when the nuclei in question lie far from the valley of stability. The study reported in this thesis is focused on γ-ray transitions following β-decay of Ne isotopes.

The theory behind the emission of a γ-ray from an excited nucleus has been covered in many books. The description which follows is adapted from [Seg77, Bla91]. The transition probability between two states is given by a combination of

$$\lambda_E\,(l, m) = \frac{8\pi\,(l+1)}{h\,l\,[(2l+1)!!]^2}\left(\frac{\omega}{c}\right)^{2l+1}\left|\,Q_{lm} + Q'_{lm}\right|^2 , \tag{2.7}$$

and

$$\lambda_M\,(l, m) = \frac{8\pi\,(l+1)}{h\,l\,[(2l+1)!!]^2}\left(\frac{\omega}{c}\right)^{2l+1}\left|\,M_{lm} + M'_{lm}\right|^2 , \tag{2.8}$$

where λ_E is the emission probability for electric multipole radiation, λ_M is the emission probability for magnetic multipole radiation, c is the speed of light, and ω is the angular frequency of the radiation. The terms Q_{lm} and M_{lm} are the parts of the matrix element of the initial and final nuclear wave functions that involve only the ordinary coordinates while the terms Q'_{lm} and M'_{lm} are the parts of the matrix element which contain the intrinsic magnetic moment. They may be written formally as [Segre77]

$$Q_{lm} = e\sum_{k=1}^{Z}\int r_k^l\,Y_l^{m*}\left(\theta_k, \varphi_k\right)\psi_f^*\,\psi_i\,d\tau , \tag{2.9}$$

$$M_{lm} = -\frac{1}{l+1}\frac{eh}{Mc}\sum_{k=1}^{Z}\int r_k^l\, Y_l^{m*}\left(\theta_k, \varphi_k\right) \nabla\bullet\left(\psi_f^* L_k \psi_i\right) d\tau \quad , \tag{2.10}$$

$$Q'_{lm} = -\frac{i\left({}^{\omega}/_{c}\right)}{l+1}\frac{eh}{2Mc}\sum_{k=1}^{A}\int \mu_k\, r_k^l\, Y_l^{m*}\left(\theta_k, \varphi_k\right) \nabla\bullet\left(\psi_f^* \boldsymbol{r}_k \times \sigma_k\, \psi_i\right) d\tau \ , \tag{2.11}$$

$$M'_{lm} = -\frac{eh}{2Mc}\sum_{k=1}^{A}\int \mu_k\, r_k^l\, Y_l^{m*}\left(\theta_k, \varphi_k\right) \nabla\bullet\left(\psi_\phi^*\, \sigma_\kappa\, \psi_\iota\right) d\tau \ . \tag{2.12}$$

Where i, f indicate initial and final states; k is the nucleon index: 1 to Z for protons, $Z+1$ to A for neutrons; ψ is the wavefunction of the nuclear states; the vector operator $\boldsymbol{L}_k$ is $-i\boldsymbol{r}_k \times \nabla_k$; the μ_k are the magnetic moments of the nucleons in units of $eh/2Mc$ [Seg77].

In principle these formulae allow the transition rates to be calculated. In practice, since these equations depend strongly on the matrix elements of the nuclear wave functions, only in rare cases can they be calculated explicitly. An order of magnitude estimate can be made if the following assumptions about the values of Q_{lm} and M_{lm}, are made:

(1) $\dfrac{M_{lm}}{Q_{lm}} \approx \dfrac{h}{McR}$, M is the nucleon mass ;

(2) $\dfrac{\left|M_{lm} + M'_{lm}\right|^2}{\left|Q_{lm}\right|^2} \approx 10\left(\dfrac{h}{McR}\right)^2$; and

$$(3)\quad \frac{Q'_{lm}}{Q_{lm}} \approx \frac{hk}{Mc} = \frac{h\omega}{Mc^2} \sim 10^{-3} \quad .$$

The ratio (3) can therefore be set to zero for γ-rays of energy $E_\gamma \leq$ a few MeV. All that is left is to estimate the value of Q_{lm}. This requires that a specific model be used. The one frequently applied is the Independent Particle Model [Pre75]. In the Independent Particle Model, it is assumed that the magnetic moment of the nucleus is determined by the orbital of the last unpaired nucleon. The matrix elements will vanish unless the two nuclear states are different only in the quantum numbers of a single nucleon. This model does not have sufficient accuracy to give exact values of the transition rates but does allow estimates to be carried out to a precision of one to three order of magnitude. This model gives

$$Q_{lm} = (4\pi)^{-1/2}\, eC_l \,, \tag{2.13}$$

where

$$C_l = S_l \int_0^\infty r^l\, u_f(r)\, u_i(r)\, r^2\, dr \,, \tag{2.14}$$

where S_l is the statistical function to cover the change in angular momentum and has the form

$$S_l = (2l_i + 1)(2l_f + 1)(2l + 1)^2(2J_f + 1)\left[C_{l_i l_f}(l\,,0\,;0{,}0)\right]^2\left[W(l_i J_i l_f J_f\,;\tfrac{1}{2},l\,)\right]^2 . \tag{2.15}$$

The $C_{l_i l_f}(l,0;0,0)$ term is a Clebsch–Gordan coefficient while W is a Racah coefficient. S_l reduces to 1 if $l_f = 0$. Finally, if we let $u(r)$, the radial wave function, be a step function such that

$$u(r) = \begin{cases} A & r \leq R \\ 0 & r \geq R \end{cases}$$

with A becoming $(3/R^3)^{1/2}$ from normalization, then $C_l \sim \dfrac{3R^l}{l+3}$.

This expression can be considered an upper bound and the actual values of C_l should be lower than this estimate by a factor of 10–1000. However, this does give us a way to estimate the transition probabilities [Bla91]:

$$\lambda_E(l) \approx \frac{2(l+1)}{l\,[(2l+1)!!]^2}\, S_l \left(\frac{3}{l+3}\right)^2 \frac{e^2}{hc} \left(kR\right)^{2l} \omega$$

$$= \frac{4.4(l+1)}{l\,[(2l+1)!!]^2}\, S_l \left(\frac{3}{l+3}\right)^2 \left(\frac{h\omega}{197\,MeV}\right)^{2l+1} R^{2l}\, 10^{21}\ \mathrm{s}^{-1}, \qquad (2.16)$$

and

$$\lambda_M(l) \approx \frac{20(l+1)}{l\,[(2l+1)!!]^2}\, S_l \left(\frac{3}{l+3}\right)^2 \frac{e^2}{2\pi hc} \left(\frac{h}{McR}\right)^2 \left(kR\right)^{2l} \omega$$

$$= \frac{1.9(l+1)}{l\,[(2l+1)!!]^2}\, S_l \left(\frac{3}{l+3}\right)^2 \left(\frac{h\omega}{197\,MeV}\right)^{2l+1} R^{2l-2}\, 10^{21}\ \mathrm{s}^{-1}, \qquad (2.17)$$

where R is in fermi and $h\omega$ is in MeV.

To be able to use these formulas one must know what transitions are possible. The selection rules are summarized in Table 2.1. The selection rules given in the table must be combined with the triangular relation $|J_i - J_f| \le l \le |J_i + J_f|$ to determine if a transition is possible. Clearly a transition from $J_i = 0$ to $J_f = 0$ is always forbidden for a single γ–ray as l cannot equal zero. An $l = 0$ transition is possible by other channels such as the emission of 2 γ–rays or a γ-ray and a conversion electron. By knowing the spin states of the levels in question it is possible to determine the multipolarity of the emitted radiation. For most γ–decays the assumption is made that the lowest possible order of transition ($l = |J_i - J_f|$) will dominate. The ground state of ^{26}Na is known to be 3^+ and the two energy levels at 83 keV and 233 keV are assumed to be 1^+[End90]. This implies that l = 2, 3, or 4 and $\Delta\pi = 0$. From Table 2.1 this means that $E2$,$M3$, $E4$ transitions are possible. The possible cascade between the 83 keV and 233 keV levels has l = 0, 1, or 2 and $\Delta\pi = 0$ and is therefore a mixture of $M1$ and $E2$. Using formulae 2.16 and 2.17, it is possible to calculate the expected transition rates between the levels as given in Table 2.2.

Table 2.1. Selection rules for Electromagnetic (El) or Magnetic (Ml) Transitions of angular momentum l. $\Delta\pi$ is the change in parity.

	$E1$	$E2$	$E3$	$E4$	$M1$	$M2$	$M3$	$M4$
$\Delta\pi$	1	0	1	0	0	1	0	1
l	1	2	3	4	1	2	3	4

Table 2.2. Expected transition rates for the γ–decay of ^{26}Ne. The Statistical Factor S_l has not been included.

Level Transition (keV)	Transition Rate $E2$ (s^{-1})	Transition Rate $M1$ (s^{-1})
83 → g.s.	1.58×10^4	—
233 → 83	4.44×10^5	1.07×10^{11}
233 → g.s.	2.73×10^6	—

The angular distribution of the gamma rays is important since there is every reason to believe the decay of ^{26}Ne will be a gamma cascade from the 233 keV level to the 83 keV level and finally to the ground state. In such a case the distribution of the second gamma ray relative to the first, $W(\theta_{12})$, is given by the formula [Fra65]

$$W(\theta_{12}) = \sum_{k\ even} A_{kk} P_k(\cos\theta_{12}) \ . \tag{2.18}$$

In the case of ^{26}Ne the assumption is made that the first transition between the 233 keV level ($J_i = 1$) and the 83 keV ($J_{int} = 1$) level is purely $M1$ in nature as justified by the rates in Table 2.2. This approximation simplifies the calculations and given the large difference in transition probability is quite reasonable. The transition between the

83 keV ($J_{int} = 1$) level and the ground state ($J_f = 3$) is purely $E2$. The maximum value that k can take in eq. 2.18 is the lesser of ($2J_i$, $2J_{int}$, $2J_f$) or 2. Therefore the expression for $W(\theta_{12})$ is

$$W(\theta_{12}) = A_{00} + A_{22} P_2(\cos\theta_{12}) \; . \tag{2.19}$$

The coefficient A_{00} is 1 while the coefficient A_{22} is given by

$$\begin{aligned} A_{22} &= F_2(L_1 L_1 J_i J_{int}) F_2(L_2 L_2 J_f J_{int}) \\ &= F_2(1\ 1\ 1\ 1) F_2(2\ 2\ 3\ 1) \\ &= (-0.354)(-0.101) = 0.0358 \end{aligned} \tag{2.20}$$

The functions $F_2(l_1 l_1 J_i J_{int})$, and $F_2(l_2 l_2 J_f J_{int})$ are complicated functions of Clebsch–Gordan and Racah coefficients tabulated in [Fra65]. The second order Legendre polynomial $P_2(\cos\theta)$ is

$$P_2(\cos\theta_{12}) = \frac{1}{2}\left(3\cos^2\theta_{12} - 1\right) \; . \tag{2.21}$$

Thus the overall expression for $W(\theta_{12})$ is

$$W(\theta_{12}) = 0.9821 + 0.0538 \cos^2\theta_{12} \; , \tag{2.22}$$

and this is plotted in Fig. 2.1. The distribution in Fig. 2.1 shows that for an angle between the detectors of 180° the angular distribution is at a maximum indicating a good probability for observing $\gamma\gamma$ events.

2.3 The Shell Model Theory of Nuclear Structure

From the inception of nuclear physics it has been the goal to be able to explain and predict the observed properties of nuclei. A great deal of effort has been expended to this end. Unfortunately, the nucleus is a complicated many-body system. For some simple cases, $A \approx 2$–6, the wave functions used in the calculations are known sufficiently well and the number of bodies is small enough that the calculations can be

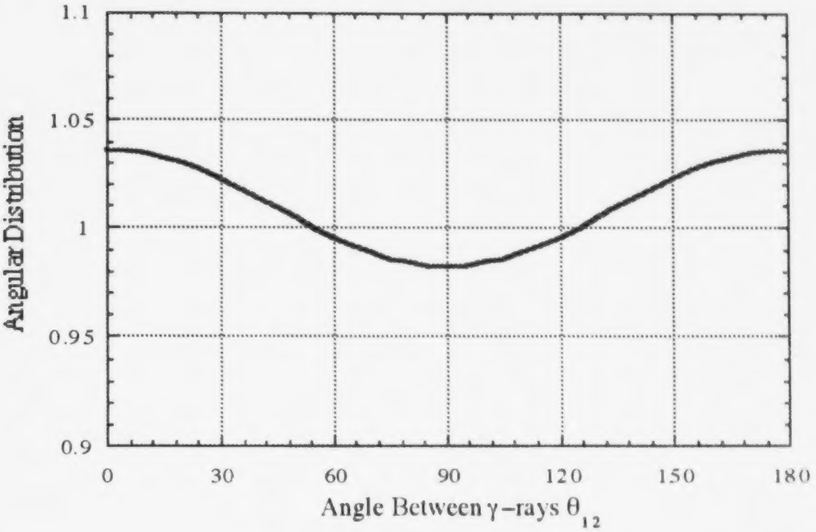

Figure 2.1. The angular distribution of gamma ray intensity for an *M*1 transition followed by an *E*2 transition.

explicitly carried out and the bulk properties of the nucleus predicted.

There have been a number of theories formulated to explain the observed structure and bulk properties of the nucleus (*eg*. the liquid drop model, the alpha cluster model). In general, no model can fully explain all observed properties and each model tends to predict some particular feature better than the others. All models are constrained by a number of symmetry rules. These are [Bri70]:

(1) Conservation of energy, momentum, and angular momentum.

(2) Galilean Invariance: The *NN* interaction should be invariant under the Lorentz transformation. Since nucleons in a nucleus are not moving at relativistic energies it is in general not necessary to invoke relativity, Galilean invariance is often sufficient.

(3) Conservation of Parity: It is well known that the *Strong* interaction conserves parity, therefore the *NN* interaction must as well. It was in the beta decay of ^{60}Co,

however, that the first evidence of parity violation was found and it is now known that the NN interaction has a small part which does *not* conserve parity.

(4) Time Reversal Invariance: this implies that a reaction should proceed independent of a specific direction in time.

(5) Charge Independence (and Charge Symmetry): this basically states that, excluding the coulomb interaction, there should be no difference in the nn, pp, and np interactions. It is known that charge independence and charge symmetry are broken by a very small amount.

Certain bulk properties of the nucleus are known and must be dealt with by any nuclear model. The first property is the saturation of the binding energy per nucleon. This quantity lies in the narrow range

$$7.4 \text{ MeV} \leq B(N,Z)/A \leq 8.8 \text{ MeV} ,$$

where the binding energy, $B(N,Z) = -M(N,Z) + ZM_H + NM_N + Zm_e$. M_H and M_N are the masses of a hydrogen atom and a neutron respectively. $M(N, Z)$ is the mass of the atom, and N is the number of neutrons. There are a few exceptions to these limits if $A \leq 10$. The second property is that the nuclear radius, R, should vary as

$$R \cong r_o A^{1/3} , \tag{2.23}$$

where $r_o \approx 1.2$ fm. Since the volume is proportional to A, it can easily be concluded that the $\rho_N(r)$, the nuclear density, is approximately constant.

Using these properties and the liquid drop model it has been possible to develop a partly theoretical description for $B(N,Z)$ which is normally known as the semi–empirical mass formula (SEMF)

$$B(N, Z) = a_v A - a_s A^{2/3} - a_c \frac{Z^2}{A^{1/3}} - a_a \frac{(N-Z)^2}{A} \pm \delta . \tag{2.24}$$

Here a_v is the volume energy, a_s the surface energy, a_c the coulomb energy, a_a the asymmetry energy, and δ the pairing energy. These coefficients are determined by fitting the known binding energies of many nuclei to the formula. The accuracy of the predictions depends on the precision of the mass measurements of the stable nuclei. The SEMF is of great utility in determining whether a particular nucleus will be particle stable, (*i.e.* inside the drip lines), how it might decay, and what decay products it can be expected to have. An example of its usefulness is shown in Table 2.3.

In Table 2.3 the experimental values for the mass difference, Δ, are compared with the predictions for all the neon isotopes from $A = 15$ to $A = 30$. The mass difference is defined as $\Delta = M\,(Z,N\,)\,-A{*}\mathrm{u} - Zm_e$, where u is the atomic mass unit (amu). The agreement is reasonable given the simplicity of the formula. The SEMF can be used to give indication of the particle stability of the isotope. The Q value of a reaction which emits a neutron or proton is given as

$$Q_N = M(Z,\ N) - M(Z',\ N') - M_N \ . \tag{2.25}$$

In this situation the total number of neutrons and protons is unchanged so the formula simplifies to the difference of the binding energies

$$Q_N = B(Z',\ N') - B(Z,\ N). \tag{2.26}$$

Substitution of the SEMF formula for B into the above equation leads to two separate equations, one equation which describes proton decay and another equation for neutron decay. For the case of proton emission A' = A − 1, Z' = Z − 1, and N' = N and explicitly substituting eq. 2.24 gives

$$Q_p = -a_v + a_s\,((A-1)^{2/3} - A^{2/3}) + a_c\left(\frac{(Z-1)^2}{(A-1)^{1/3}} - \frac{Z^2}{A^{1/3}}\right)$$
$$+\,a_a\left(\frac{(N-Z+1)^2}{A-1} - \frac{(N-Z)^2}{A}\right). \tag{2.27}$$

For neutron emission A' = A − 1, Z' = Z, and N' = N − 1 and again substitution into eq. 2.24 yields

$$Q_n = -a_v + a_s\left((A-1)^{2/3} - A^{2/3}\right) + a_c Z^2\left((A-1)^{-1/3} - A^{-1/3}\right)$$

$$+a_a\left(\frac{(N-1-Z)^2}{A-1} - \frac{(N-Z)^2}{A}\right) . \qquad (2.28)$$

The results for these two equations (eqs. 2.27, 2.28) can be found for Ne in Table 2.3. These calculations indicate that the isotopes ^{15,16}Ne are unbound for proton emission while no Ne isotopes (A ≤31) should be neutron unstable. The onset of neutron emission from Ne appears to begin at A ≥ 33, although ^{32}Ne may be neutron unbound as well, given the small (–0.2 MeV) value for Q_n.

The third bulk property that should be described by nuclear models is the ratio of the nuclear density, ρ_N, to that of the closest possible packing density of neutrons (such as in a neutron star), ρ_{cp}. If one assumes a hard-core repulsion distance d = 0.5 fm then

$$\frac{\rho_N}{\rho_{cp}} \cong \left(\frac{d}{2r_o}\right)^3 \cong 0.01 , \qquad (2.29)$$

where r_o is as previously defined. Combining this with experimental cross section data it is possible to calculate the mean free path for a nucleon inside a nucleus. The value obtained is larger than the size of a typical nucleus [Bri70]. If we assume that the nucleus is a degenerate fermi gas then

$$\rho_N = \frac{A}{V} = \frac{3}{4\pi r_o^3} = \frac{2}{3\pi^2}\kappa_F^3 , \qquad (2.30)$$

where κ_F is the fermi momentum of the nucleon and equals

$$\kappa_F = \left(\frac{9\pi}{8}\right)^{1/3}\frac{1}{r_o} . \qquad (2.31)$$

The corresponding nucleon fermi energy is

$$T_F = \frac{2\pi^2 h^2 \kappa_F^2}{M} \cong 40 \text{ MeV} \ . \tag{2.32}$$

Adding the typical binding energy per nucleon of 8 MeV implies that the potential well should have a depth of ~50 MeV.

Table 2.3. The predictions of the Semi-Empirical Mass Formula (SEMF) as compared to experiment for the Neon (Z=10) isotopes from A=15 to A=30. The Q-values for neutron and proton emission are also given.

A	N	$B(Z,N)$ [MeV]	Q_p [MeV]	Q_n [MeV]	Δ [MeV] (SEMF)	Δ [MeV] (exp)
15	5	63.20	3.54	-28.30	50.05	
16	6	93.39	1.05	-23.80	27.93	
17	7	113.06	-1.37	-20.11	16.33	16.48
18	8	134.80	-3.70	-17.04	2.67	5.32
19	9	147.72	-5.92	-14.45	-2.19	1.75
20	10	163.47	-8.02	-12.26	-9.87	-7.04
21	11	171.57	-10.02	-10.38	-9.89	-5.73
22	12	182.93	-11.91	-8.77	-13.18	-8.03
23	13	187.46	-13.69	-7.36	-9.64	-5.15
24	14	195.50	-15.38	-6.14	-9.61	-5.95
25	15	197.33	-16.98	-5.06	-3.37	-2.04
26	16	202.80	-18.49	-4.11	-0.77	-0.44
27	17	202.54	-19.92	-3.27	7.56	6.96
28	18	205.99	-21.27	-2.52	12.19	11.00
29	19	204.08	-22.56	-1.85	22.17	
30	20	205.90	-23.78	-1.24	28.42	
31	21	202.67	-24.93	-0.71	39.72	
32	22	203.16	-26.04	-0.22	47.30	
33	23	198.87	-27.09	0.23	59.67	

To predict details of nuclear structure a more precise description of the nucleus and the interaction of the nucleons inside it is necessary. A standard procedure used to calculate level information in the shell model requires a four-step process. The first step is to determine the form of the potential for the nucleon–nucleon interaction. Then one decides which shells contribute to the calculation. The third step is to include the effect of a two-body interaction, usually this interaction is considered to be a small perturbation to the main interaction. The final step is to diagonalize the hamiltonian of the system to extract the eigenfunctions, the nuclear wavefunctions and the eigenvalues — the nuclear energies.

The form of the nucleon–nucleon potential is model dependent. It is common to choose the independent particle shell model for calculations. The assumption that the nucleons move in the nucleus independent of each other is prompted by the fact that the fermi gas model of the nucleus was very successful in describing the bulk properties of the nucleus as is indicated above. The *NN* potential must also be a scalar, attractive potential, and must conserve isospin, total angular momentum, and parity[Des74]. These considerations restrict the form of the potential. Based on these restrictions, the independent-particle potential used to describe the nucleus is given by the following form

$$V(r) = V_o(r) + V_S(r)\vec{s}_1 \cdot \vec{s}_2 + V_{LS}(r)\vec{L} \cdot (\vec{s}_1 + \vec{s}_2) + V_{Ten}(r)\left[Y_2(r) \otimes \left[\vec{s}_1 \otimes \vec{s}_2 \right]_2 \right]_0^0$$

$$+ \text{ other terms accounting for isospin.} \qquad (2.33)$$

The first term, the central potential, is often chosen to be a harmonic oscillator potential for ease of calculation. The second term is the spin coupling term which accounts for the spin interaction dependence between the two nucleons. The $\vec{s}_i$ are the Pauli spinors. The third term is to describe the interaction depending on the nucleon intrinsic spins and the orbital angular momentum of their shell levels. The final term incorporates the tensor force between the nucleons. The isospin terms are identical to the ones in eq. (2.23) except that the potential, $V_i^{\tau}(r)$, may be different and each term has a factor $\vec{\tau}_1 \cdot \vec{\tau}_2$ included. The τ are the isospin analogues to the Pauli spinors.

Except for very simple nuclei, any attempt to perform calculations quickly becomes computationally difficult due to the large number of nuclear states available to the nucleons. Recently it has become possible, with the use of high speed computers, to solve the shell model equations for the transition of one nucleus to another via β–decay. Such a study has been published by Wildenthal *et al.* [Wil83] and includes predictions on the decay of neutron-rich nuclei in the *sd* shell region.

Wildenthal *et al.* proceeded as follows. They calculated the seven density matrix elements, $D_{kk'}$, for their generated wave functions, $\Psi^{NTJ\nu}$, given by

$$D_{kk'} = (2\Delta J+1)^{-1/2}(2\Delta T+1)^{-1/2}\left\langle \psi^{N_f T_f J_f \nu_f} \,|||\left[a^{\dagger}(k)\otimes a(k')\right]^{\Delta J=1,\ \Delta T=1} |||\psi^{N_i T_i J_i \nu_i}\right\rangle, \tag{2.34}$$

where $N = A-16$, T is the total isospin, J is the total spin, ν is the counting index identifying a particular eigenstate of the NTJ set, k designates a particular single—particle nucleon state $\rho(n,\ l,\ j)$, nlj are the quantum numbers associated with that state, $a^{\dagger}$ and a are the creation and annihilation operators, and the symbol $|||$ stands for reduction in both isospin and spin. This is then combined with the single nucleon matrix element $S^{GT}_{kk'}$,

$$S^{GT}_{kk'} = \left\langle \rho\,(nlj)\,|||O_{GT}|||\rho\,(n'l'j')\right\rangle, \tag{2.35}$$

where O_{GT}, the Gamow–Teller operator is

$$O_{GT} = \left|\frac{g_A}{g_V}\right| \vec{\sigma}\,\vec{\tau}\,. \tag{2.36}$$

$S^{GT}_{kk'}$ gives the amplitude of the GT process when nucleons convert from one state to another. Thus the total GT matrix element is defined as

$$B(GT)^{1/2} = \left(\sqrt{2(2J_i+1)}\right)^{-1} \begin{Bmatrix} T_f & 1 & T_i \\ -T_{Z_f} & \Delta T_z & T_{Z_i} \end{Bmatrix} \times \sum_{k,k'} D_{kk'} S^{GT}_{kk'}\,. \tag{2.37}$$

The term in the {} is a $6j$ symbol. From the value of $B(GT)^{1/2}$ it is possible to predict the half-life, Q value, and branching ratios of the decay in question. The half-life for the decay is given by the formula

$$t_{1/2} = (6170 \pm 4) f_A^{-1} / B(GT) \ . \tag{2.38}$$

Here f_A is a phase-space factor depending on the electron end-point energy for the particular decay.

There are several limitations imposed on these calculations. The wave functions, for example, are generated such that the ($0d_{5/2}$-$1s_{1/2}$-$0d_{3/2}$) model space gives a least-squares fit of the Hamiltonian eigenvalues to the experimentally known energies of levels with well-understood spin and isospin. The energy levels chosen for the fit tend to be from stable nuclei for which $N=Z$. Additionally, the Hamiltonian must conserve isospin, and is limited to 1- and 2-body operators. In particular the Hamiltonian has a single set of one-body operators and a single set of two-body operators which are scaled to the particular A in question. Examples of the predictions will be given in Section 2.5 for the Neon isotopes.

2.4 Motivation for Study of the Neon Isotopes

In Chapter One the rationale for the study of radioactive nuclei as an important and worthwhile physics endeavor was discussed. The reasons why ^{26}Ne was chosen as the isotope studied can be divided, as one might expect, into experimental and theoretical concerns.

The existence of sophisticated models of the nucleus and powerful computers to perform calculations allows research into the decays of nuclei far from stability to be undertaken with predictions of the possible decay schemes. However, no matter how comprehensive the model, the complexity of the nucleus means that many assumptions must be made and a number of simplifications introduced. Since the best knowledge exists for nuclei closest to the line of stability, an experimental goal of systematic studies of nuclei far from stability is the confirmation of basic assumptions and parameters of the various models which describe stable nuclei adequately.

Quoting from Wildenthal, Curtin, and Brown [Wil83],

> "Comparisons between predictions and experiment for systems lying outside the domain of data for which the Hamiltonian was determined provide crucial tests of the ultimate utility of this type of theoretical formulation."

By comparing theory with experiment it is possible to determine the adequacy of the model space for nucleons with large neutron excess, a region of considerable interest. It also allows for checks on the appropriateness of the Hamiltonian when used on systems that are very different from those used to fit it — those nuclei lying on or close to the valley of stability. Finally, any such tests need to be on nuclei outside those previous studied since, as Wildenthal points out [Wil86],

> "...the existence of comprehensive and internally consistent model predictions for a wide range of phenomena in *sd* shell nuclei creates a positive feedback loop for experimental studies in these systems."

It is the goal of this study to make a limited test of the Shell Model (S.M.) predictions for the energy levels of ^{26}Ne and ^{27}Ne.

There are important experimental / technical considerations for the choice of ^{26}Ne. The calculations of [Wil83] cover 37 isotopes of O, F, Ne, Na, Mg, Al, Si, and P — any of which would be a valid candidate to study. The combination of production target and ECR ionizer, however, preclude some nuclei based either on target chemistry or the ion source efficiency. Since it was intended to use a UOC (Uranium Oxide Carbide) target, the yield of heavy oxygens released from the target matrix was expected to be low due to chemical bonding occurring during the diffusion process. The ECR has a cooled transfer tube; metals cannot be ionized since they would be trapped before reaching the ion source. This leaves only the isotopes of F and Ne. No evidence of fluorine or any fluoride compound has been seen at TISOL — mainly because fluorine is very reactive. Other methods produce F^- beams while the ECR would have to produce a F^+ beam, which is difficult to make. However, HCl^+ has been observed so it may be possible to produce beams of HF^+. A significant amount of ion source development would be required to achieve reasonable yields. For this study Ne was the only remaining choice. As a choice for study, Ne has some advantages which would make it the preferred selection even in the case of viable alternatives. It is a noble gas, hence it is released by the target and not absorbed by the transfer tube. Offline tests [McN89] indicate a satisfactory ionization efficiency for Neon of ~20%. SILT calculations [Dau90] (see section 2.5) have indicated a good yield for Ne isotopes from a UOC target. The half-lives of both ^{25,26}Ne are long enough that a sizable fraction of the produced isotopes arrive at the collector station after the expected total transit time on the order of 1-2 seconds [Dom94]. Unfortunately, the short half-life of ^{27}Ne ($\tau_{1/2}$ = 32±2 ms) is a problem for transit times of that size. In this thesis, an experimental study of the $\beta\gamma$ decay of ^{26,27}Ne has been completed similar to the one done for ^{25}Ne[Goo73].

2.5 Theoretical Predictions and Previous Data

When this project began there existed only one brief report on the properties of ^{26}Ne [Duf87]. The information is given in Table 2.4. A definitive work had been completed on ^{25}Ne[Goo73] and its decay was well known. Primarily for this reason it was to be used as a calibration in this work. During the course of the investigation, work done at ISOLDE at CERN on β–delayed neutron emission was published which gave both the half-lives and neutron emission probabilities (P_n) of ^{26,27}Ne and others [Ten92]. This information is also shown in Table 2.4.

As mentioned previously in Section 2.4, there exists a theoretical calculation of the expected G-T β–decays of ^{25,26,27}Ne. As well, the energy levels of ^{25,26,27}Na are known experimentally [End90]. By combining this knowledge it is possible to produce

Table 2.4. Known decay properties of ^{26}Ne before completion of our study from [Duf87, Ten92].

Gamma Decay Energy	82.9	233 keV
Branching Ratio	92.7	7.3 %
Half-life, $t_{1/2}$	197±1 ms	
Neutron Emission Probability, P_n	0.13±0.03 %	

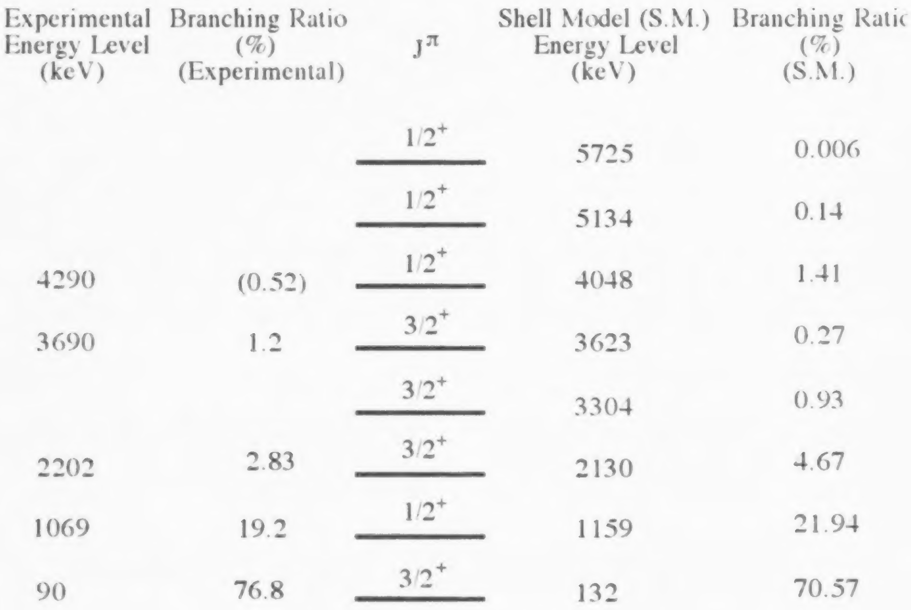

Experimental Energy Level (keV)	Branching Ratio (%) (Experimental)	J^π	Shell Model (S.M.) Energy Level (keV)	Branching Ratio (%) (S.M.)
		$1/2^+$	5725	0.006
		$1/2^+$	5134	0.14
4290	(0.52)	$1/2^+$	4048	1.41
3690	1.2	$3/2^+$	3623	0.27
		$3/2^+$	3304	0.93
2202	2.83	$3/2^+$	2130	4.67
1069	19.2	$1/2^+$	1159	21.94
90	76.8	$3/2^+$	132	70.57

Figure 2.2. A comparison between the Shell Model (S.M.) predictions of [Wil83] and the experimental results of [Goo73] for ^{25}Ne(β)^{25}Na.

predictions for the expected $\beta\gamma$–decay of ^{26,27}Ne. Fig. 2.2 shows the comparison between the predicted and observed decays for ^{25}Ne. There is generally good agreement in terms of the energy levels and beta branching values.

In Fig. 2.3 a comparison between the published data for the ^{26}Na [End90] energy levels and the [Wil83] predictions is shown. The predictions in this case are not so clear cut. Since the predictions for the energy levels are uncertain within ±200 keV groups of known levels are compared to the predicted values. Also shown are the predicted β–branching values.

Examining Fig. 2.3 it is now possible to make some predictions on expected γ–transitions. The first prediction is the easiest; in addition to direct decay of the 233 keV level to the ground state it very likely that there should be a decay to the 83 keV level followed by a subsequent decay to the ground state. The first new γ–ray thus should have an energy of ~150 keV. The next higher known energy level at ~2000 keV (indicated by **I** in Fig. 2.3) has three possible decay modes (ignoring from now on the unobserved 420 keV level) with approximate energies: 1800, 1900, and 2000 keV. For the next energy level at ~2100 kev (**II**) there are four possible decays: 100, 1900, 2000, and 2100 keV. The third level at ~2500 keV (**III**) gives five possibilities: 400, 500, 2300, 2400, and 2500 keV. The highest energy level at 4100 keV (**IV**) has six possibilities: 1600, 2000, 2100, 3900, 4000, and 4100 keV. If the possible decays are considered together, the largest number of possible decays is in the region of 1900–2100 keV. The highest energy transitions are on the order of 4 MeV. Both of these are good regions for the search for new γ–rays since there will be both low background and very few possible contamination gamma lines.

For ^{27}Ne there exists only the measurement of its half-life and P_n value in [Ten92]. These values are given in Table 2.5. A comparison between the known energy levels of ^{27}Na[End90] and the predictions of [Wil83] for ^{27}Ne(β)^{27}Na is shown in Fig. 2.4.

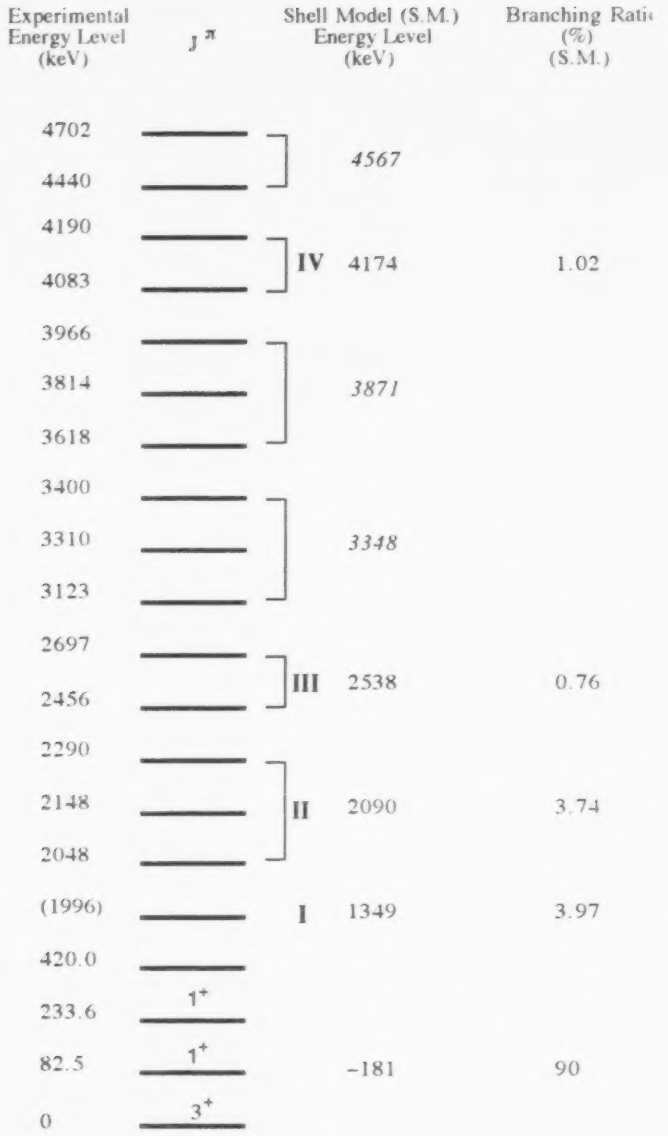
Experimental Energy Level (keV)
J π
Shell Model (S.M.) Energy Level (keV)
Branching Rati
(%)
(S.M.)
4702
4440
4567
4190
4083
IV
4174
1.02
3966
3814
3618
3871
3400
3310
3123
3348
2697
2456
III
2538
0.76
2290
2148
2048
II
2090
3.74
(1996)
I
1349
3.97
420.0
233.6
1+
82.5
1+
-181
90
0
3+

Figure 2.3. Comparison between the known energy levels of ^{26}Na [End90] and the predicted levels obtained by [Wil83] for ^{26}Ne(β)^{26}Na. The Roman numerals indicate levels expected to be populated by β–decay from which previously unobserved γ–rays may be emitted. The numbers given in italics indicate states where theoretical predictions indicate no β–decay. The shown J^{π} values are experimental values. All of the β–decays predicted by [Wil83] are to 1^+ levels

Table 2.5. The half-life and P_n values of ^{27}Ne. The theoretical half-life as predicted by [Wil83] is also given.

Half-life (exp)	32±2 ms
Half-life (theory)	35 ms
P_n	2.0±0.5 %

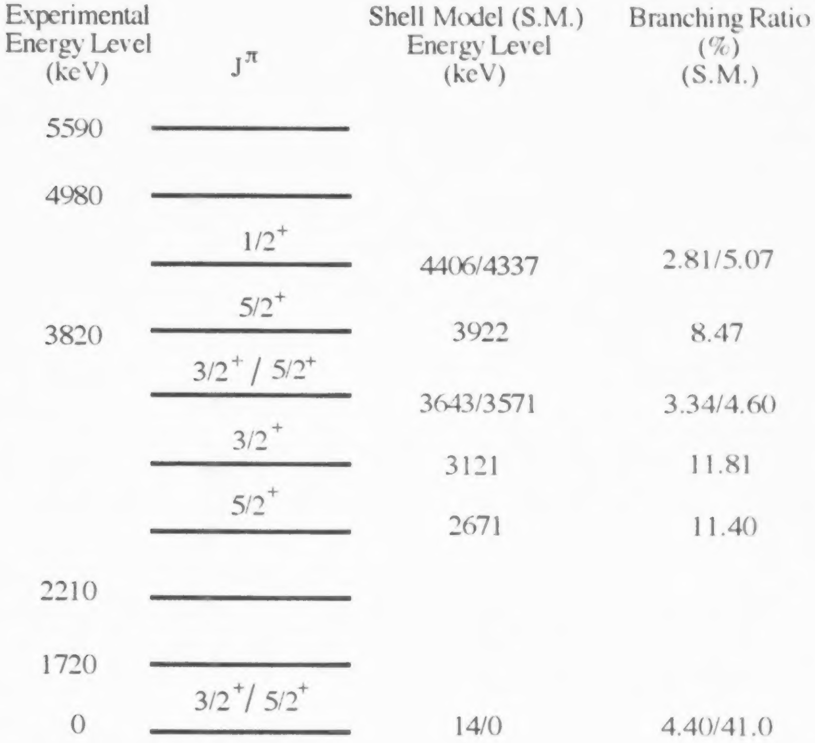
Experimental Energy Level (keV)
J$^\pi$
Shell Model (S.M.) Energy Level (keV)
Branching Ratio (%) (S.M.)
5590
4980
1/2$^+$
4406/4337
2.81/5.07
5/2$^+$
3820
3922
8.47
3/2$^+$ / 5/2$^+$
3643/3571
3.34/4.60
3/2$^+$
3121
11.81
5/2$^+$
2671
11.40
2210
1720
3/2$^+$/ 5/2$^+$
0
14/0
4.40/41.0

Figure 2.4. A comparison between the known energy levels of ^{27}Na [End90] and those predicted by [Wil83]. Only those levels for which the predicted β–branching ratio was greater than 1% are shown. Where two levels were very close they are shown as one line with the two energies separated by a slash. The only experimentally known J$^\pi$ value is for the ground state (5/2$^+$) all other shown values are from the predictions by [Wil83].

Examining the predictions for ^{27}Ne and taking only the four levels with the highest predicted branching ratios, a similar procedure to what was described for ^{26}Ne yields some predictions of the possible gamma transition energy. There are four regions of interest: $E_\gamma = 0.5 - 1.5$ MeV, ~2 MeV, ~3 MeV, and ~4 MeV.

The β-decay energy spectrum provides a clearer situation. In Table 2.6 the shell model predictions of [Wil83] for the Q value of the decay are compared to the existing experimental values. The Q value is the maximum possible electron kinetic energy corresponding to the difference

$$Q = M(Z,N) - M(Z+1,N-1) - [B(Z+1,N-1) - B(Z,N)].$$

Where M is the atomic mass and B is the binding energy (eq. 2.18) of the nuclei.

Table 2.6. The predicted Q values for ^{25,26,27}Ne [Wil83] compared to experimental values when possible from [Goo73].

Isotope	Exp Q–value [MeV]	S.M. Q–value [MeV]
^{25}Ne	7.4 ± 0.3	7.5
^{26}Ne	—	7.2
^{27}Ne	—	12.8

The final theoretical prediction that was required for this experiment was the expected yield. Using the SILT program from Los Alamos provided by J.M. D'Auria [Dau90], a calculation was performed to determine the expected yield from a Uranium target. The results are shown in Fig. 2.5. The graph shows the normalized production yield for a target thickness of 1 g/cm^2 and 1 μA production current. To convert to expected values it is necessary to multiply by the target thickness and the beam current. The predicted production yield for the Ne isotopes is tabulated in Table 2.7. When the actual target thickness and the maximum allowed beam current factors are included, the second column of Table 2.7 is derived. Assuming a one second diffusion time (which is consistent with estimates from ISOLDE for this type of target), the known half-lives of the isotopes, a 10% ionization efficiency for the source, a time of 50 ms for the transit time through the TIS, and a 90% transmission through the ion beamline, one obtains the expected detectable yields for ^{23,25,26,27}Ne shown in the final column of the table.

The high expected yield of 2.7 x 10^4 atoms/s for ^{25}Ne at the detector station translates into a count rate of about 20 counts/s once the detector efficiency [~10^{-3}] (see Section 3.3.1.4) is taken into account. The yield of ^{26}Ne is lower due to its shorter half-life. The yield is ~300 atoms/s at the detector station. Folding in the detector efficiency reduces this to 0.3 counts/s. These low count rates indicate that great care should be taken to reduce all possible sources of background. The outlook for detecting ^{27}Ne is not optimistic. The yield at the detector station is expected to be nearly indistinguishable from zero. However, at ISOLDE, ^{27}Ne was observed with a production setup that is not significantly different from the TISOL system, so that the possibility for observing some activity cannot be ruled out. A more detailed description of predicted production values as compared to the observed yields is given in Section 4.8.

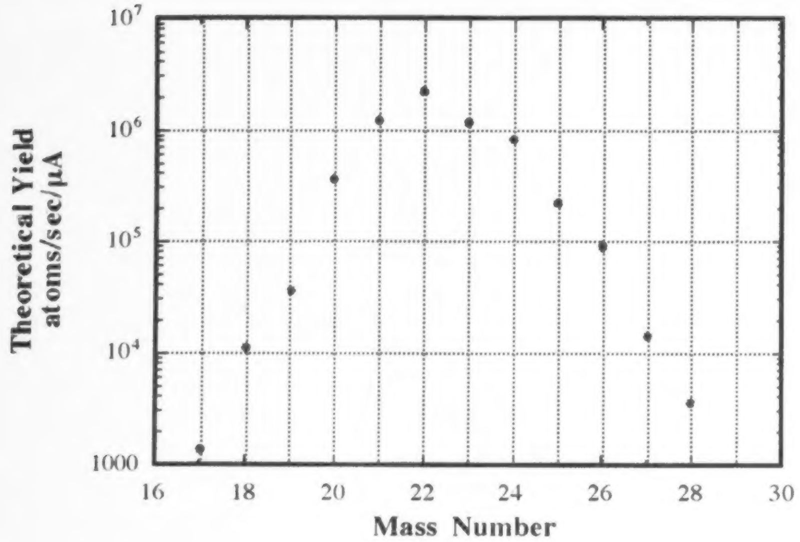

Figure 2.5. The theoretical yield in the target for a target thickness of 1 g/cm^2 for production of Neon isotopes from a Uranium (Z=92, A=238) target using a 500 MeV proton beam.

Table 2.7. The calculated yield for a 1 g/cm^2 target for production of Neon isotopes from a Uranium (Z=92, A=238) target using a 500 MeV proton beam. The Expected Production Yield at the target takes into account a 10 g/cm^2 thick target and a production current of 0.75 μA. The Expected Detectable Yield takes into account the diffusion time from the target, transit time through the TIS, ionization efficiency in the ECR, and transmission through the ion beamline.

Isotope	Normalized Theoretical Yield (atoms cm^2/g/s/μA)	Expected Production Yield (atoms/s)	Expected Detectable Yield (atoms/s)
17	1.36E+03	1.02E+04	
18	1.09E+04	8.18E+04	
19	3.52E+04	2.64E+05	
20	3.63E+05	2.72E+06	
21	1.24E+06	9.30E+06	
22	2.20E+06	1.65E+07	
23	1.17E+06	8.78E+06	7.68E+05
24	8.29E+05	6.22E+06	5.57E+05
25	2.24E+05	1.68E+06	2.70E+04
26	8.96E+04	6.72E+05	2.93E+02
27	1.45E+04	1.09E+05	9.16E-10
28	3.62E+03	2.72E+04	

Chapter 3: The Experimental Apparatus

3.1 Experimental Endstation Hardware

The detector endstation used in experiment 597 was designed so that it could accommodate a number of different experimental configurations with only minimal changes. The station is intended to be used with a moving tape transport system. In the configuration used for this experiment, the tape transport system removes radioactive materials after each counting interval is completed to reduce the build-up of long-lived daughter nuclei and other unwanted contamination.

The heart of the endstation is a box frame (the standard ISIS 10" diagnostic box) onto which a variety of aluminum flanges can be mounted to hold detectors. Since each flange can be individually machined to the users' requirements, the endstation is very flexible and able to accommodate different experimental configurations.

For these measurements the endstation was separated by a gate valve from the rest of the ion beam line. A faraday cup and wire scanner were mounted before the gate valve to allow the TISOL operator to optimize beam transmission and the beam profile. A two-part collimator followed the gate valve . The first part was a lead slug with a 0.5" diameter hole in the center to provide shielding from γ-ray activity associated with the majority of radioisotopes deposited on the collimator. The beam collimation was done by an aluminum plate with a 0.5" long x 0.375" wide slot milled into it which was mounted on the upstream side of the lead slug. The shape of the slot was chosen to maximize beam deposited on the tape while minimizing the contamination on the surrounding detector elements. Behind the gate valve a TORR 7 cryopump (pumping speed: 5000 l/s) was located to provide the high vacuum. A cold cathode ion gauge gave a vacuum reading. Since it could see the pump, this gauge provided a reading on the vacuum in the collection station that is probably an order of magnitude

magnitude too low. The target box itself also held a Convectron gauge used for initial (low) vacuum readbacks and interlocks. A roughing pump was connected to the tape transport line to provide initial pumping out of the endstation.

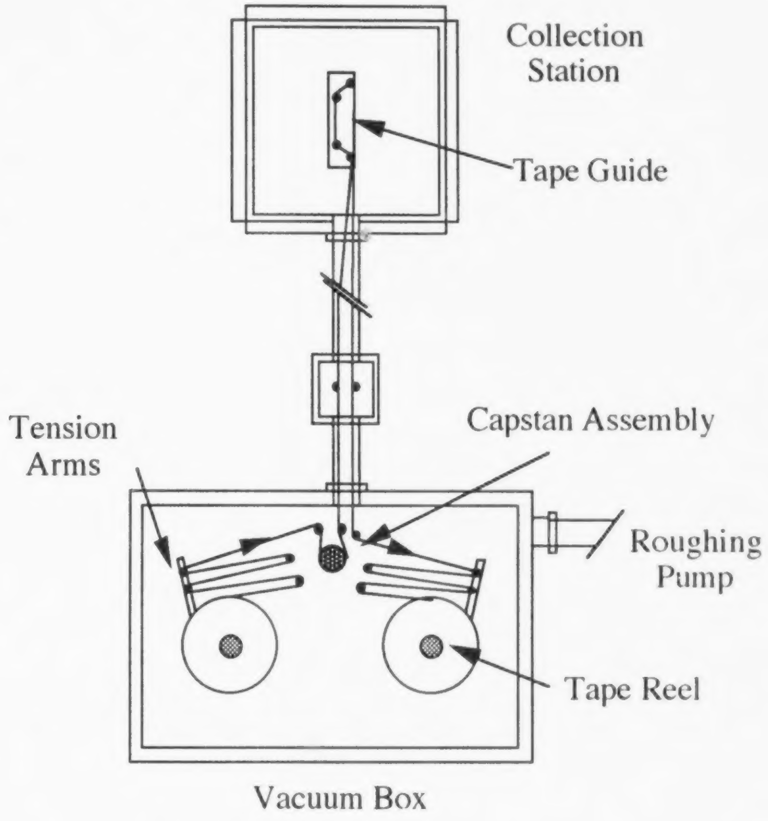
Collection Station
Tape Guide
Tension Arms
Capstan Assembly
Roughing Pump
Tape Reel
Vacuum Box

Figure 3.1. The vacuum box containing the TISOL tape transport system. The tape path used for the experiment is shown.

The tape transport system has three elements: the tape box, the controller, and the transport piping. The tape box consists of a vacuum case, two reels, and their motors. The box also has a capstan which is used to control the distance the tape moves under the command of the controller by determining how long the tape has been running. Each reel is turned by a reversible electric motor. Fig 3.1 shows a schematic of the vacuum box and the transport system with the tape path shown.

The controller was built by the University of Alberta Center for Subatomic Research technical support staff using parts taken from a 9-track magnetic tape drive (the schematic of the control system is shown in Fig 3.3). The controller determines both the direction and time during which the motors turns the reels. Initially, it was intended to use a PC computer with a specialized control program, however, it turned out to be more convenient to set up a system of NIM modules to control the tape motion since this allows for the integration of ion beam deflection and tape movement. The tape speed is ~1.5 m/s, and the distance the tape moves can be controlled by adjusting a time setting on the front panel of the controller. For all of the experimental runs in this thesis the time of tape movement was set to 0.9 s. A start pulse was provided by the NIM control electronics at the appropriate time (see Fig 3.2). An output from the tape controller is normally used to disable data acquisition while the tape is in motion.

The transport piping is a series of 2" stainless steel tubing and aluminum boxes which can be assembled in a variety of ways to guide the tape from the tape box to the ion beam collection point and back to the tape box again. For the final configuration the tape was merely run straight up from the vacuum box to the endstation and then straight back down again.

The detector configuration for the final runs is shown in Fig. 3.4. The heart of the detector system was the three beta paddles ($\beta1$,$\beta2$,ΔE) which form the beta trigger. Two of the paddles, $\beta1$ and $\beta2$, are 1.5 mm thick x 70 mm square, while the third paddle, ΔE, is 1.5 mm thick x 40 mm square. The three paddles were ORed together to cover as much of the solid angle as possible surrounding the ion beam collection point (~ 50% of 4π). Installed as closely as possible to these paddles were mounting ports for the Hyper-Pure Germanium (HPGe) detectors. The entrance windows were 1.5 mm thick Al to reduce γ attenuation. Behind the tape position was a thick (50 mm square x 70 mm long) plastic scintillator which when combined with the ΔE β paddle provided a good ΔE–E telescope. By combining detectors in different ways it was possible to configure the data acquisition system to be sensitive to different decay combinations: $\beta\gamma$, $\gamma\gamma$, γ–singles, *etc*. Details on the detectors is provided in Table 3.1. A faraday cup was placed in front of the ion collection point as a final diagnostic device which could be manually raised or lowered to give a signal during beam tuning.

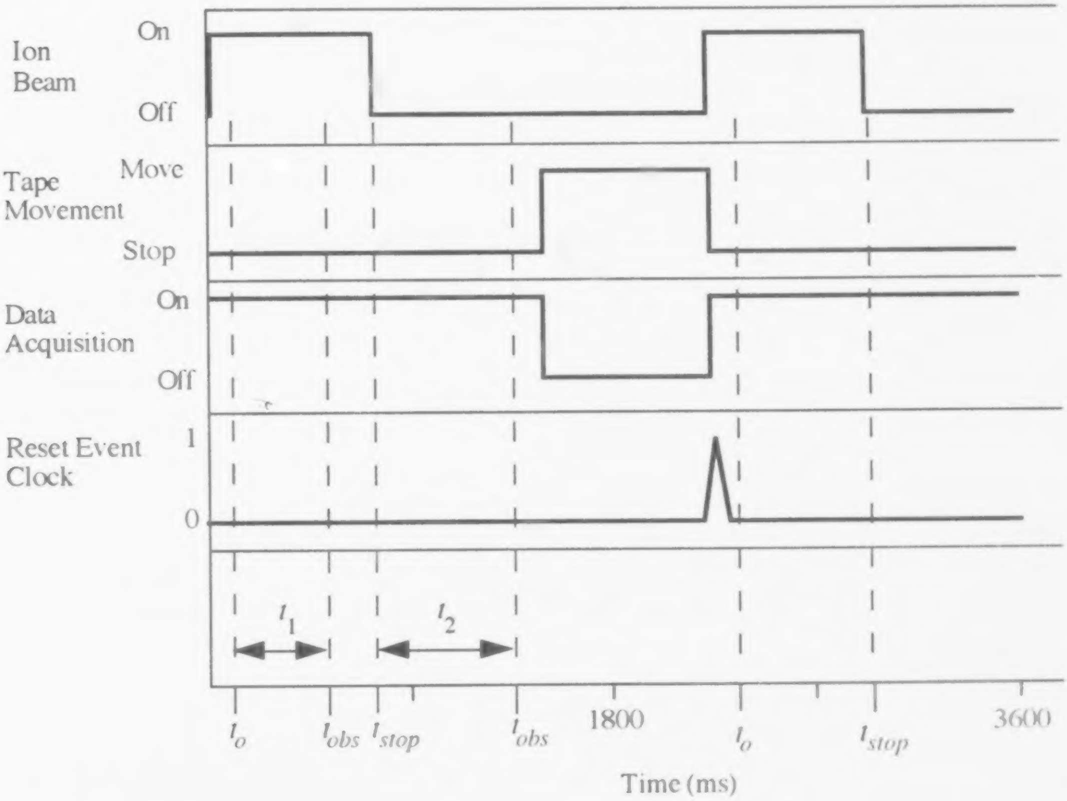
Ion Beam
On
Off
Tape Movement
Move
Stop
Data Acquisition
On
Off
Reset Event Clock
1
0
t_1
t_2
t_o
t_{obs}
t_{stop}
t_{obs}
1800
t_o
t_{stop}
3600
Time (ms)

Figure 3.2. The timing pulses controlling the tape transport system. Also shown are the timing points which were used in the half-life data analysis in Chapter 4. t_o is the time required for the power supply to ramp down and t_{stop} marks the end of the ion beam collection period. t_{obs} marks the position of an event. The adjusted times t_1 and t_2 are also shown. The clock starts at the beginning of the graph and is later reset.

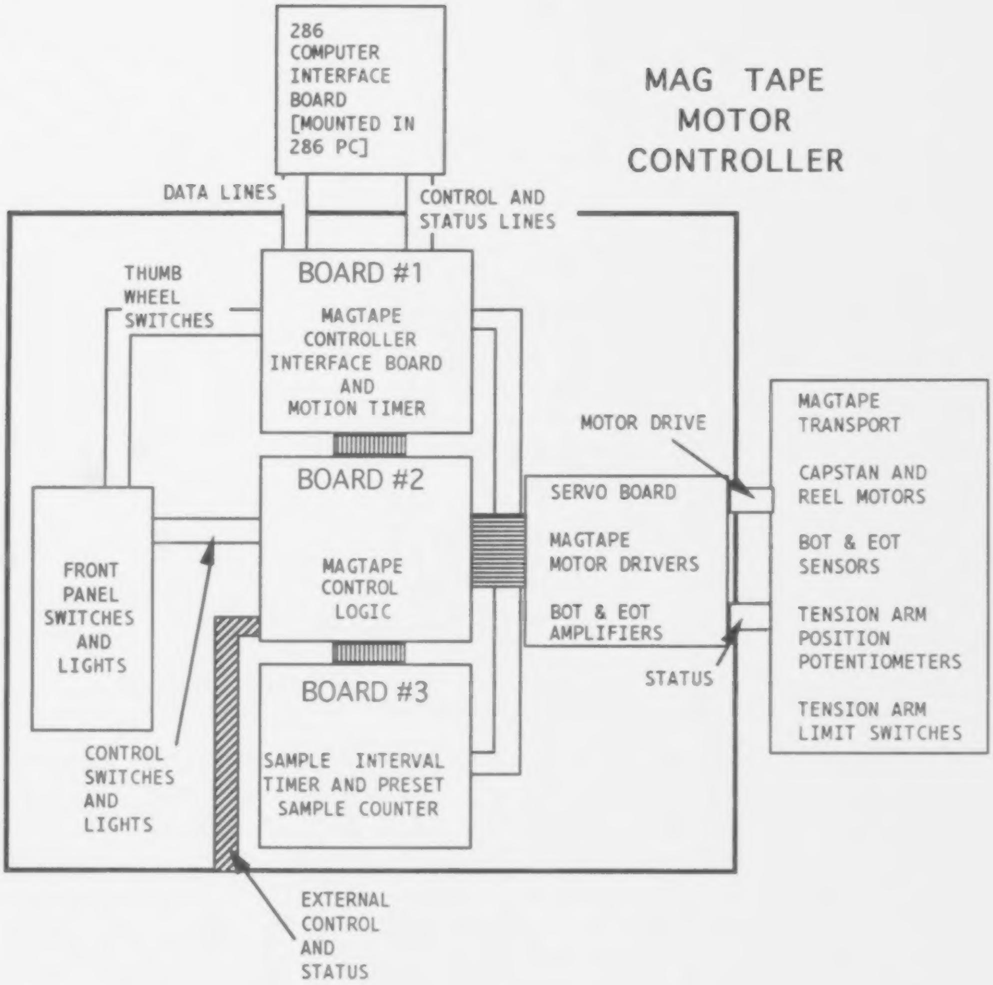
286 COMPUTER INTERFACE BOARD [MOUNTED IN 286 PC]
MAG TAPE MOTOR CONTROLLER
DATA LINES
CONTROL AND STATUS LINES
THUMB WHEEL SWITCHES
BOARD #1
MAGTAPE CONTROLLER INTERFACE BOARD AND MOTION TIMER
BOARD #2
MAGTAPE CONTROL LOGIC
BOARD #3
SAMPLE INTERVAL TIMER AND PRESET SAMPLE COUNTER
FRONT PANEL SWITCHES AND LIGHTS
CONTROL SWITCHES AND LIGHTS
EXTERNAL CONTROL AND STATUS
MOTOR DRIVE
SERVO BOARD
MAGTAPE MOTOR DRIVERS
BOT & EOT AMPLIFIERS
STATUS
MAGTAPE TRANSPORT
CAPSTAN AND REEL MOTORS
BOT & EOT SENSORS
TENSION ARM POSITION POTENTIOMETERS
TENSION ARM LIMIT SWITCHES

Figure 3.3. The schematic of the tape controller electronics.

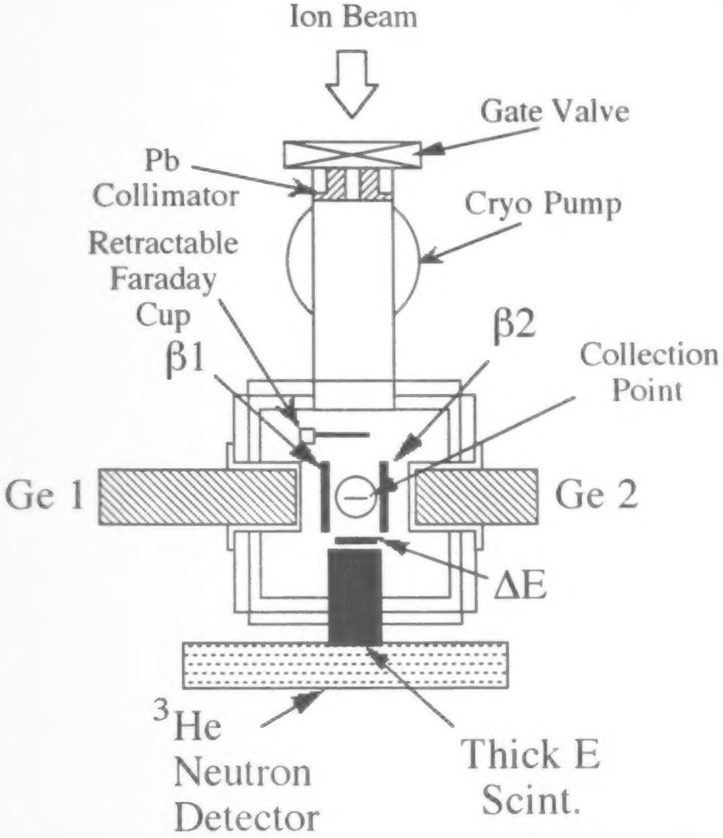
Ion Beam
Gate Valve
Pb Collimator
Cryo Pump
Retractable Faraday Cup
β1
β2
Collection Point
Ge 1
Ge 2
ΔE
^{3}He Neutron Detector
Thick E Scint.

Figure 3.4. A top view of the final detector configuration for E597. The ^{3}He detector is located below the mid-plane of the collection station.

Table 3.1 The known physical properties of all detectors described in Sections 3.1 and 3.4 are given below.

Plastic Scintillators		
Detector	Material	Dimensions
$\beta1$, $\beta2$	NE102A	70 mm x 70 mm x 1.5 mm
ΔE	NE102A	40 mm x 40 mm x 1.5 mm
E	NE102A	50 mm x 50 mm x 700 mm
HPGe Detectors		
Detector	Material	Crystal Dimensions
Coaxial (Ge1)	HPGe	Unavailable[†]
Planar (Ge2)	HPGe	400 mm^2 x 10 mm thick
Neutron Detectors		
Detector	Material	Dimensions
^{3}He Proportional	^{3}He gas	50 mm (dia) x 300 mm long
NE213	liquid Scintillator	127 mm (dia) x 51 mm thick

[†] The documentation for this detector is lost. The manufacturer has been contacted.

3.2 Experimental Apparatus Used for the ^{18}N Study

The equipment used for the study of $^{18}N(\beta\alpha)^{14}C$ experiment (TRIUMF E628) was the same as used in Experiment 589 (Red Giant) [Azu94]. The Red Giant target wheel assembly is fully described in reports [Azu94, Buc92b]. It is described only briefly here. Two views of the detector station are shown in Fig. 3.5 and Fig. 3.6.

The target wheel was used to hold the thin (10-35 $\mu g/cm^2$) self-supporting collection foils. The foils were chosen to be sufficiently thin such that they stopped the 12 keV ^{18}N ion beam but still allowed the recoiling ^{14}C to escape with minimal energy straggling. There were three detector stations and a collection point. In front of the collection point there was a collimator wheel with different sized apertures to define the beam spot more precisely. A faraday cup was located behind the wheel. Using the combination of the collimator and faraday cup it was possible to achieve very precise beam tunes which maximized the ^{18}N yield.

Each detector station consisted of two lead cups, each of which held a silicon surface barrier detector (SSB). The lead shielded the detectors from any external electron background. The detectors were mounted facing one another and were positioned as close as possible to the foil (~ 5 mm separation between the detectors). It was possible to rotate a Gadolinium source through the detector positions to calibrate the detectors. Specifications for the detectors are given in Table 3.2.

The target wheel was connected to a stepping motor. A system of two Ortec 471(S) timer-counters was used to control the dwell time and the number of motor steps. The system was set to rotate the target wheel through 90°. Thus, for a user-set period, the ion beam would be collected on a particular target foil, then the wheel rotated this foil between the first detector pair, stopped for a fixed time, then rotated to the next detector pair. This was repeated so that on the fourth stop the foil returned to the collection point. The wheel rotation time was ~0.25 seconds, fixed by the stepping motor.

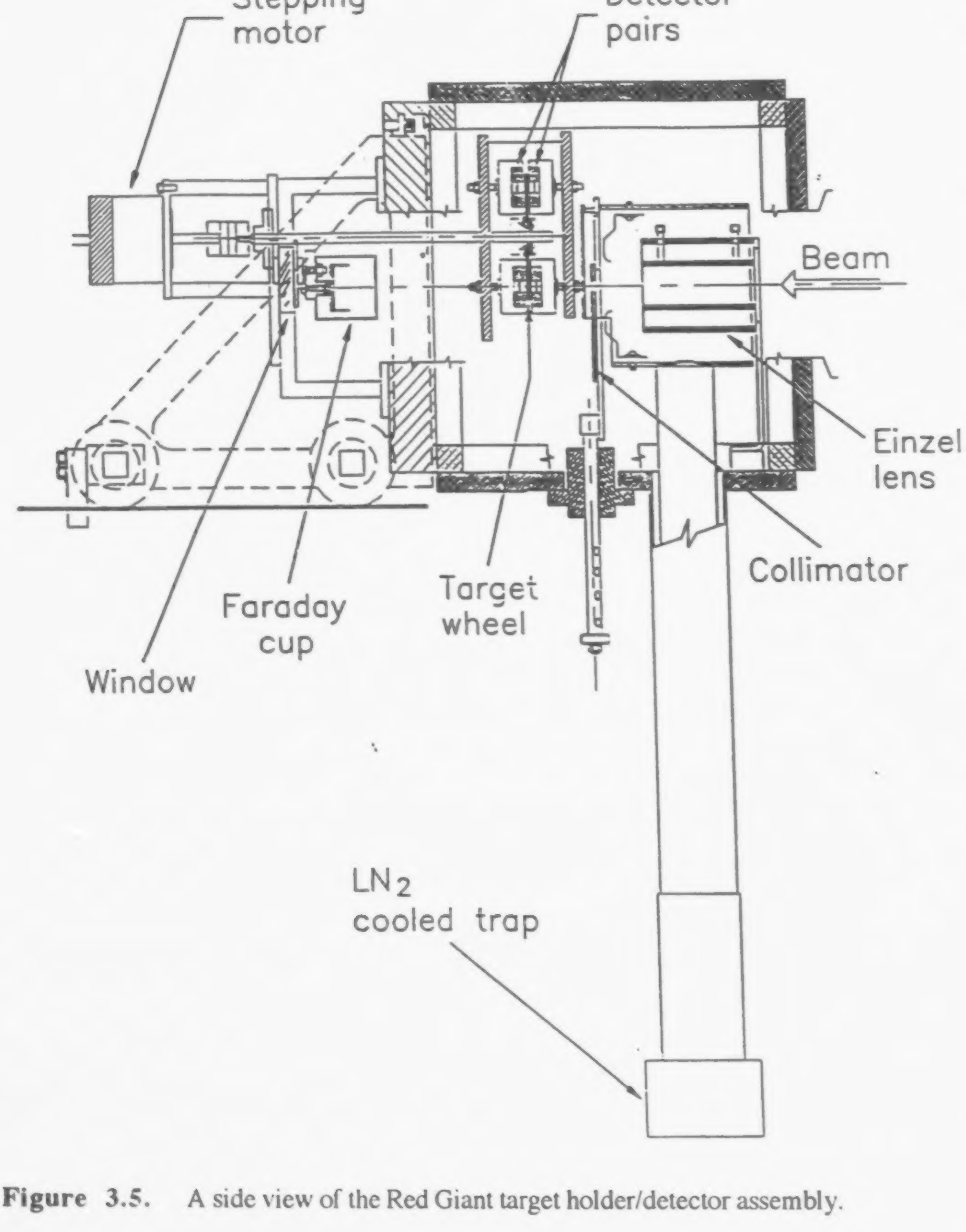
Stepping motor
Detector pairs
Beam
Einzel lens
Collimator
Target wheel
Faraday cup
Window
LN$_2$ cooled trap

Figure 3.5. A side view of the Red Giant target holder/detector assembly.

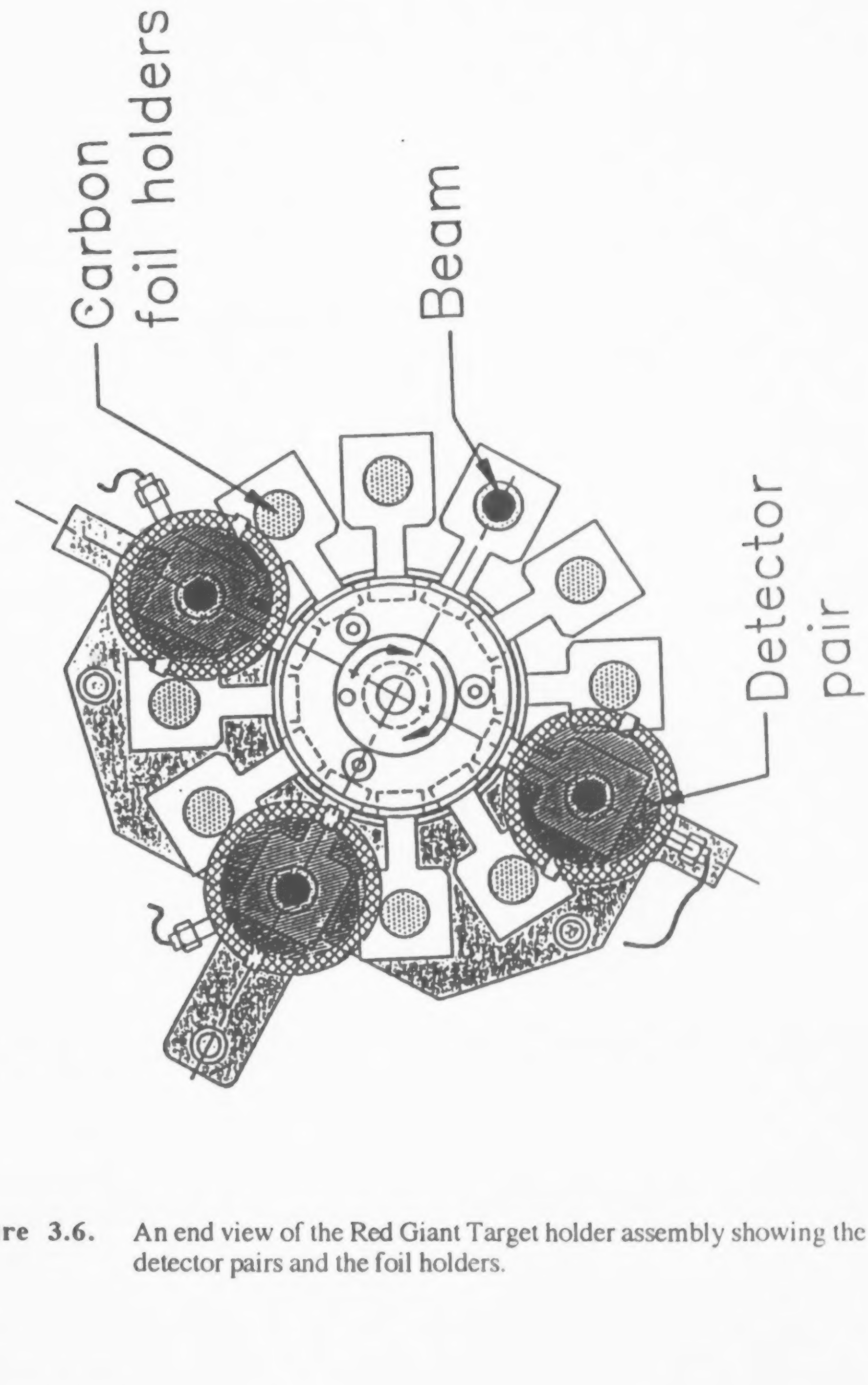
Carbon foil holders
Beam
Detector pair

Figure 3.6. An end view of the Red Giant Target holder assembly showing the detector pairs and the foil holders.

Table 3.2: The specifications on the detectors used in the experimental runs. The first half of the table is for the 1992 run while the second half is for the 1993 run.

Detector	Serial Number	Depletion Depth [μm]	Bias Voltage [V]	Noise [mV]
1	31-448E	10.6	5.5	4.0
2	23-694F	50	22.0	3.5
3	27-125C	12.9	6.5	4.5
4	31-448J	12.3	7.0	5.0
5	31-448D	13.3	6.5	3.0
6	31-168L	15.8	9.0	6.0
7	†	500‡	30.0	2.5
1	31-448E	10.6	†	†
2	31-448J	12.3		
3*	†	30		
4*	†	28		
5	27-125C	12.9		
6	31-168L	15.8		
7	†	500‡		
8	†	2000‡		

* These detectors have areas of 100 mm^2. All other SSB detectors had 50 mm^2 areas.

†Information not recorded in run log book.

‡The 500 μm detector was an SSB but the 2000 μm detector was a HPGe crystal.

The target wheel assembly was mounted on a thick plastic plate to insulate it electrically from the ion beam line to prevent detector ground loops and to reduce vibrations from the target box and the rest of the beamline. The stepping motor was also mounted on plastic rods to insulate the detectors from any vibration of the motor during the periods it was not turning. Pumping for the whole assembly was provided by a 400 l/s turbo pump connected via a 4" pipe to the target box. A gate valve separated the target box from the TISOL ion beam line. To prevent the build-up of hydrocarbons on the target foils, a LN_2 cold trap was located in front of the collection point. An einzel lens was incorporated in the cold trap to help focus the beam.

3.3 Detector Properties

The purpose of this section is to give a brief introduction to the properties and operating principles of each of the detectors used in the data acquisition systems described in Sections 3.4 and 3.5 First the detectors used in E597 will be discussed. This experiment used primarily two types of detectors: HPGe (Hyper Pure Germanium) γ detectors, and plastic scintillators. A ^{3}He neutron detector was in place during the experiment, but as no useful data was collected with it, the properties of neutron detectors will only be briefly discussed. The second experiment, the $^{18}N(\beta\alpha)^{14}C$ PNC search, used Silicon Surface Barrier (SSB) detectors. The operating principle behind each of the detectors and some specific characteristics which were determined during the experiment will be given. The calibration data for the detectors used can be found in the Sections 3.3.1.3, 3.3.1.4 and 3.3.2.1. The information in this section is from [Leo87]

3.3.1 Hyper Pure Germanium Detectors

The most important detectors used in the experiment were the HPGe γ detectors. A HPGe detector is a solid state semiconductor detector which works by detecting the ion pairs created by the passage of charged particles through its volume. A charged particle passing through the detector interacts with the valence electrons of the solid state lattice. The interaction raises the valence electrons to the conduction band forming electron–hole pairs. If an electric field is applied, the electrons/holes can be collected at opposite sides of the field. Since the amount of energy required to create each electron/hole pair is approximately constant, the charge collected is proportional to the total energy lost in the detector. Table 3.3 gives some of the important physical properties of Germanium.

To reduce the effect of random noise caused by thermal excitation of electrons in the crystal, the detector volume is cooled to liquid nitrogen temperature. The great advantage of HPGe detectors over the earlier lithium-drifted germanium [Ge(Li)] detectors is that although they must be cooled to operate they do not have to kept cool at all times to prevent the lithium from diffusing throughout the crystal, thereby destroying the depletion layer.

The signal timing from an HPGe, or any other solid state detector, is not precise due to the slow rise time and a long (~μs) tail of the signals. This complicates the electronics necessary for integration of solid state detectors with the very fast (~ns) plastic scintillators. The signal processing requires a fast-slow interface with the timing information for the solid state detectors being generated by constant fraction discrimination (CFD) of a timing filter amplifier. The logic output from a constant fraction discriminator is generated at a constant fraction, k, of the incoming signals peak height. This discrimination is achieved by splitting the incoming signal into two parts. One part is delayed by the rise time from the constant fraction level to the peak of the signal. The other part is inverted and attenuated by the factor k. The two parts are summed together to give a bipolar pulse with a zero-crossing point that is at a constant fraction *k* of the original signal.

Table 3.3. Some of the important physical properties of Germanium related to detection of charged particles.

Atomic Number (*Z*)	32
Atomic Weight (*A*)	72.6
Density (ρ)	5.32 g/cm^2
Dielectric Constant [relative]	16
Intrinsic Resistivity	45 Ω–cm
Energy gap (300 K)	0.7 eV
Energy gap (0 K)	0.785 eV
Electron mobility (300 K)	3900 cm^2/Vs
Hole mobility (300 K)	1900 cm^2/Vs
Average Energy to form an Electron–Hole pair	2.96 eV

3.3.1.1 Photon Interactions

To explain how HPGe detectors work it is first necessary to explain briefly how photons interact with matter. The information given in this section is adapted from [Leo87]. Photons interact by three processes: the photoelectric effect, Compton scattering, and pair production. Each of these processes will remove a photon from the initial flux. Thus, passage through matter does not degrade the energy of a photon beam, but reduces its intensity as the distance traversed increases.

$$I(x) = I_o \exp(-\mu x) \ , \tag{3.1}$$

where I_o is the initial intensity and $\mu = \sigma N_a \rho/A$. Here N_a is Avogadro's number, ρ is the density, A is the atomic number of the material, and σ is the total cross section for photon interaction given by

$$\sigma = \Phi_{photo} + Z\sigma_c + \tau_{pair} \ . \tag{3.2}$$

The photoelectric effect is the absorption of a photon of energy $h\nu$ (ν is the frequency) by a bound electron which is then emitted with an energy

$$E = h\nu - B.E. \ , \tag{3.3}$$

where $B.E.$ is the binding energy of the electron. The cross section for K–shell interactions (which dominate for photon energies >100 keV) is given by

$$\Phi_{photo} = 4\alpha^{2}\sqrt{2}\,Z^{5}\,\phi_o\,(m_e c^{2} / h\nu)^{7/2} \text{ per atom} \ . \tag{3.4}$$

Here $\phi_o = (8/3)\ \pi r_e^2 = 6.651 \times 10^{-25}\ \text{cm}^2$, r_e is the classical electron radius, and $\alpha = 1/137$ is the fine structure constant. Below ~0.1 MeV, depending on Z, this process dominates the total cross section.

Compton scattering occurs when the initial photon is scattered by free electrons and a lower energy photon and the recoil electron are emitted as shown in Fig. 3.7. Using the notation of Fig. 3.7 and relativistic mechanics, the kinematic parameters are

$$h\nu' = \frac{h\nu}{1+\zeta(1 - \cos\theta)} \ , \tag{3.5}$$

$$\cos\theta = 1 - \frac{2}{(1+\zeta)^{2}\tan\phi + 1} \ , \tag{3.6}$$

$$T = h\nu - h\nu' = h\nu \left(\frac{\zeta(1-\cos\theta)}{1+\zeta(1-\cos\theta)} \right) \ , \tag{3.7}$$

$$\cot\phi = (1+\zeta)\tan(\theta/2) \ , \tag{3.8}$$

where $\zeta = h\nu/m_e c^2$. The maximum energy transfer to the electron occurs for back-scattered photons giving

$$T_{max} = h\nu\left(\frac{2\zeta}{1+2\zeta}\right). \tag{3.9}$$

This energy is known as the Compton edge. This is the apparent energy deposited in the detector if the scattered photon subsequently escapes from the detector. The differential cross-section for Compton scattering can be derived using Q.E.D. and is known as the Klein–Nishina equation. When integrated this equation yields the total Compton cross-section

$$\sigma_c = 2\pi r_e^{\,2}\left\{\frac{1+\zeta}{\zeta^2}\left[\frac{2(1+\zeta)}{1+2\zeta} - \frac{1}{\zeta}\,ln\,(1+2\zeta)\right] + \frac{ln\,(1+2\zeta)}{2\zeta} - \frac{1+3\zeta}{(1+2\zeta)^2}\right\}. \tag{3.10}$$

The contribution to the total cross section from Compton scattering is most important between energies of 0.1 — 10 MeV.

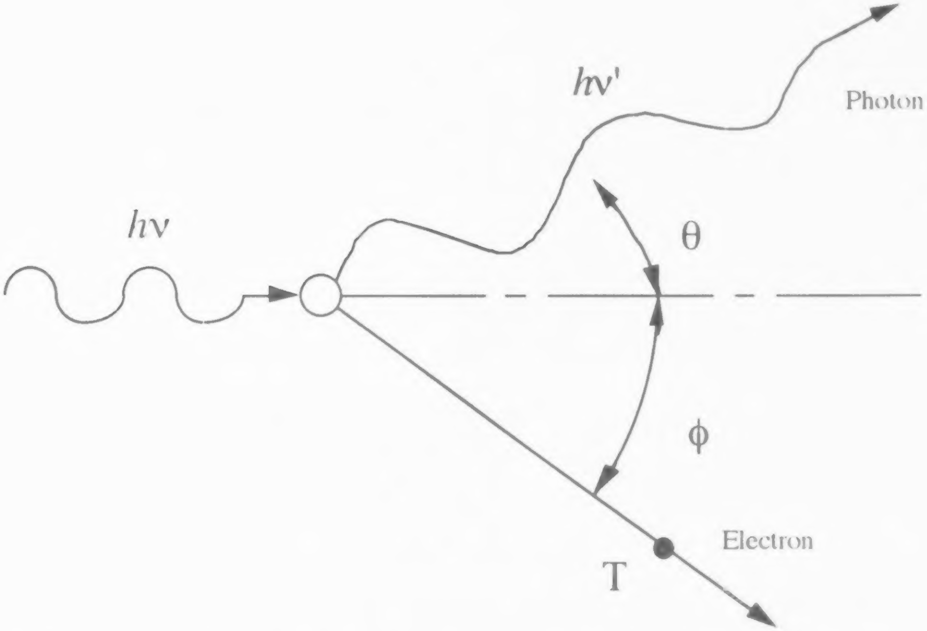

Figure 3.7. Diagram defining the kinematic variables for Compton scattering.

The third process is pair production. This process only occurs if the energy of the photon is above 2 m_ec^2 or 1.022 MeV. For energies of interest (E_γ < 10 MeV) the cross section for pair production is given by

$$\tau_{pair} = 4Z^2 \alpha r_e^2 \left[\frac{7}{9}\left(\ln\frac{2h\nu}{m_ec^2} - f(z)\right) - \frac{109}{54}\right]. \tag{3.11}$$

Here $f(z)$ is a correction term which takes into account the coulomb interaction of the emitted electron and the nucleus. For $a = Z/\alpha$, $f(z)$ is given by

$$f(z) = a^2\left[(1+a^2)^{-1} + 0.20206 - 0.0369a^2 + 0.0083a^4 - 0.002a^6\right]. \tag{3.12}$$

The pair production cross-section begins to dominate at E_γ > 5 MeV. Fig. 3.8 shows the contributions of the three processes to the linear absorption coefficient of Ge and Si. The linear absorption coefficient is the cross-section multiplied by a constant, so the figure also shows how the cross-sections for the three processes vary with energy.

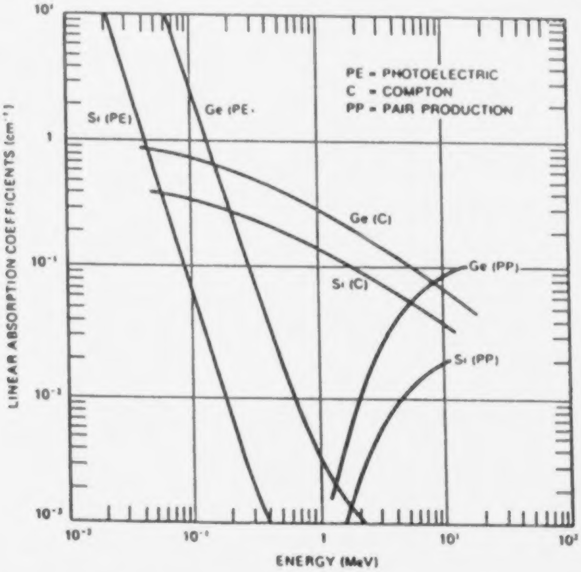

Figure 3.8. The linear absorption coefficient for photon scattering in Ge and Si. Shown are the contributions of the three processes. The linear absorption coefficient is the cross-section multiplied by a constant. Thus the figure shows, as well, the variation of the process cross-section with energy.[Ort92]

The problem with detecting photons arises because they are neutral particles. One must detect the charged particles produced by interactions as the photon moves through the detector. This is complicated since all three processes (photoelectric effect, Compton scattering, pair production) can occur for any single photon. In all observed spectra there is a peak corresponding to total absorption of the gamma energy (the photopeak). Additionally, if $E_\gamma > 1.022$ MeV there is the possibility that in the advent of pair production one or both of the γ–rays produced by the positron annihilating may escape the detector. Therefore two additional peaks are formed 0.511 MeV and 1.022 MeV below the main photopeak. These are known as the single-escape and double-escape peaks respectively. There also is the Compton scattering associated with the main peak which results in a broad continuum up to the Compton edge. Contributing to this continuum are geometrical effects which arise when the interactions occur too close to the end or edge of the active volume for the full energy of the photon to be absorbed. A simple example of all these processes is shown in Fig. 3.9. If, as is common, the nucleus has several γ-rays associated with it, the spectrum can become quite complicated.

3.3.1.2 Charged Particle Interactions

An electron moving through matter loses energy by two methods: direct collisions with atomic electrons and electron bremsstrahlung. The energy loss of electrons due to atomic collisions is given by a modified Bethe–Bloch formula [Leo87] (neglecting here a few correction terms which are not significant at low energies)

$$-\frac{dE}{dx} = 2\pi N_d r_e^2 m_e c^2 \rho \frac{1}{\beta^2}\left[\ln \frac{\tau^2(\tau+2)}{2(I/m_e c^2)} + F(\tau)\right] . \qquad (3.13)$$

Here I is the mean ionization potential for the stopping medium, and for electrons

$$F(\tau) = 1 - \beta^2 + \frac{\frac{\tau^2}{8} - (2\tau + 1)\ln 2}{(\tau^2 + 1)} \quad . \tag{3.14}$$

Here $\beta = v_e/c$, and τ is the electron kinetic energy in units of m_ec^2.

Bremsstrahlung is the emission of photons due to the acceleration of a charged particle. It begins to dominate energy losses at electron energies >25 MeV in Ge and >100 MeV in plastic scintillator. It is not a significant effect at the low energies where HPGe detectors are commonly used. Therefore the electron energy loss is dominated by collision losses for the purposes of this experiment.

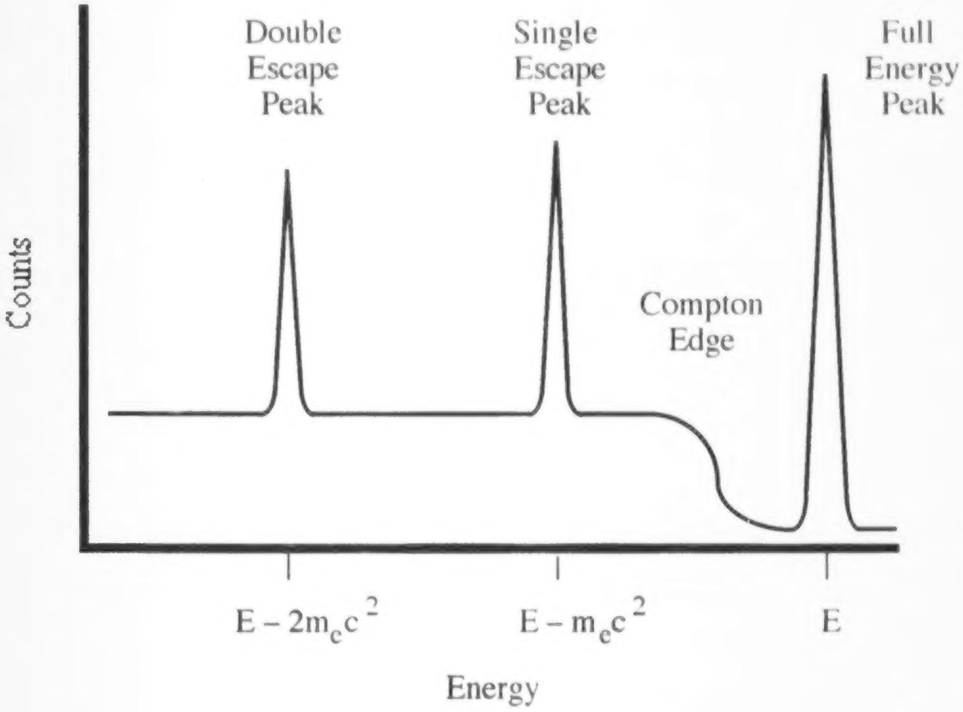
Double Escape Peak
Single Escape Peak
Full Energy Peak
Compton Edge
Counts
$E - 2m_ec^2$
$E - m_ec^2$
E
Energy

Figure 3.9. The various processes occurring for a high energy γ-ray and what the pulse height spectrum would look like.

3.3.1.3 Energy Calibration of the Germanium Detectors

To calibrate the energy response of the HPGe detectors a simple procedure was followed. ^{133}Ba and ^{60}Co sources (for which information can be found in Table 3.4) were placed near the detectors and runs were performed until sufficient events had been collected for all the peaks of the sources to be clearly visible. The data analysis program NOVA [Gre91] was used to find the centroid and width of each peak. These results were then plotted against the known energy of the peak. The resulting calibration curve was used to generate the correspondence between energy and ADC channel in the subsequent NOVA analysis of the γ–ray data. Shown in Fig. 3.10 is the energy calibration curve for Ge1 taken during run 25. Fig. 3.11 shows the energy calibration curve for Ge2 also taken during run 25. In Fig. 3.12 the deviations from the calibration curves and the observed γ–ray data are given for both detectors. From Fig. 3.12 the data appear to lie very close to the fit with the only significant deviation being for the ^{133}Ba 81 keV peak for the planar HPGe (Ge2). The reason for this deviation is the unresolved weaker 79.6 keV γ–ray in the decay of ^{133}Ba. The presence of this γ–ray in conjunction with the 81 keV γ–ray will shift the effective peak centroid towards a lower ADC channel value. This shift will introduce a systematic error in the energies around 80 keV, the magnitude of which can be estimated during the ^{25}Ne(β)^{25}Na analysis by comparing the observed γ–ray energy with the known 89.5 ± 0.1 KeV γ-ray. This calibration procedure was repeated as necessary during the run if there were changes to the electronics of the acquisition system. Based on Fig. 3.12, estimated systematic error in energy determination is about ±0.1% for energies between 200 keV – 1 MeV, increasing to ±0.3 keV near 80 keV.

Table 3.4. Calibration information for the sources used to calibrate the HPGe detectors.

Isotope	γ—Ray [keV]	Strength [γ/100 decays]	$t_{1/2}$ [s]	Source ID #	Activity† [μCi]
^{133}Ba	79.6	2.43	3.267×10^{8}	1R646	9.1
	81.0	32.8	"	"	"
	276.4	7.29	"	"	"
	302.9	18.6	"	"	"
	356.0	62.3	"	"	"
	383.9	8.84	"	"	"
^{60}Co	1173.2	99.9	1.662×10^{8}	1U762	7.16
	1332.5	100	"	"	"

†activity as of January 1, 86

3.3.1.4 Efficiency Calibration of the Germanium Detectors

To generate branching ratios from the data it is necessary to know the efficiency of the detector at a particular energy. Using the standard calibration sources that were also used to energy calibrate the detectors (see Section 3.3.1.3) a small off-line experiment was carried out to determine the detector efficiency. The two HPGe detectors were already in their respective run positions.

The principle behind the measurement is simple: measure a known source for a fixed period of time. It is possible to calculate the expected number of counts and by comparison to the observed number of counts determine the efficiency for that energy.

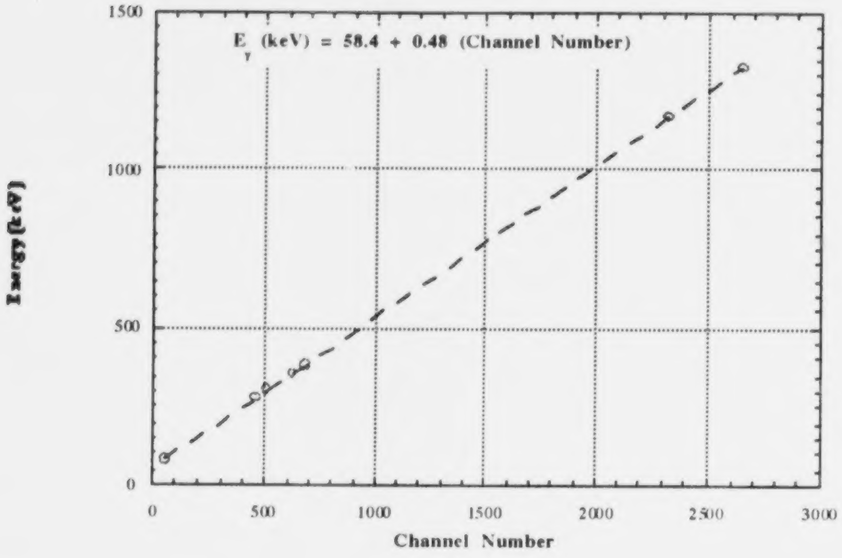

Figure 3.10. The calibration curve for Ge1 using data collected during run 25.

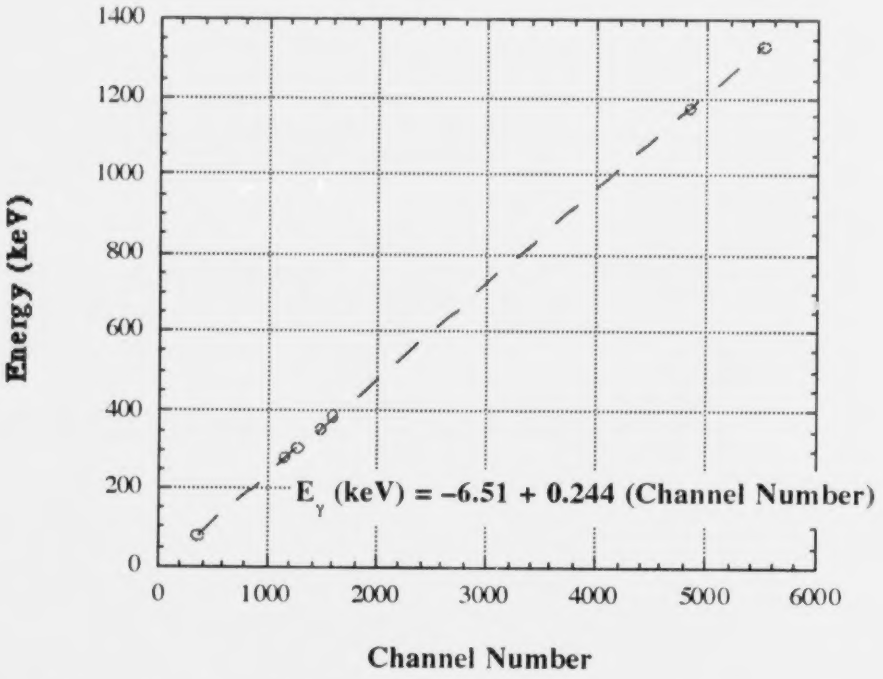

Figure 3.11. The calibration curve for Ge2 using data collected during run 25.

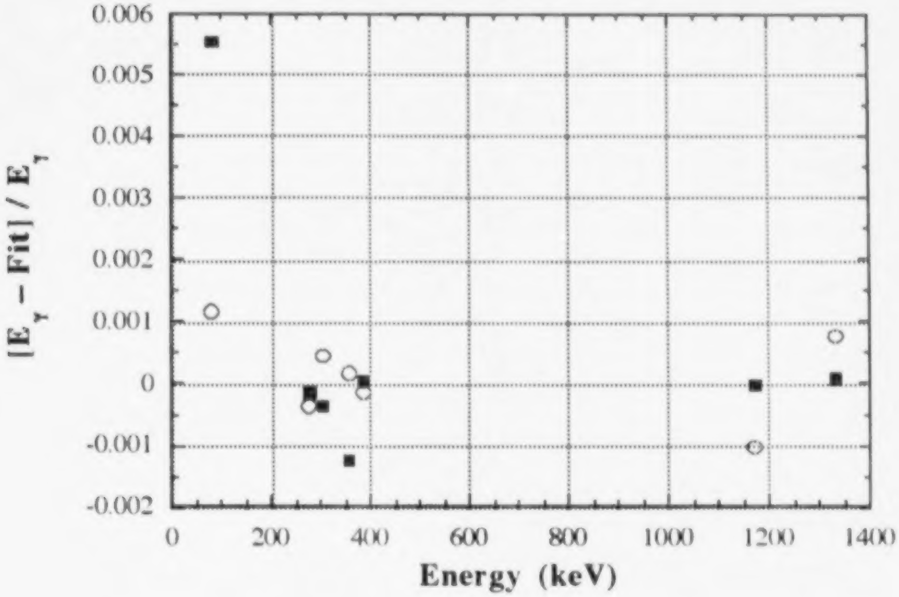

Figure 3.12. The deviation of the fits to the calibration data from the known energies of the γ-rays included in the fit. The circles are for the Coaxial HPGe (Ge1), while the squares are for the Planar HPGe (Ge2).The data is from run 25 for each detector and thus corresponds to the two previous graphs.

The sources were placed in two positions. The first is denoted the *far* position where the source was placed in the left downstream corner of the collection box. The second was the *tape* position where the source was placed between the detectors in the same position as the expected ion beam collection point during the run (see Fig. 3.4).

The TISOL PCAII data acquisition system was used to acquire the spectral data.

This system was chosen since it could be easily preset to count for a specific period of time and had an automatic dead-time correction. A run time of 600 s was chosen to ensure reasonable levels of statistics were collected. Before beginning to collect efficiency data a background run of 600 s was performed for each detector. The pumping station on Line B is radioactive and ^{60}Co contamination of the spectra was expected but could be compensated for because of the background spectra taken before data collection. As ^{60}Co is one of the calibration sources it was necessary to subtract from the collected spectra those counts contributed by the pump. Data was collected in a series of six runs. For Ge1 the ^{60}Co source was measured at both the *tape* and *far* positions and the ^{133}Ba source was measured at only the *far* position. For Ge2 the ^{133}Ba source was measured at both the *tape* and *far* positions while the ^{60}Co was measured only at the *far* position.

The purpose was to measure the efficiency over the range 80—1300 keV with the *far* measurements. The *tape* measurements would then be used to scale the *far* results to correct for geometric efficiency. In principle this would then yield the absolute efficiency curve.

The spectra were analysed by the following method. For each run the spectrum was segmented isolating the particular peak (or peaks) of interest. For Ge1 the corresponding section of background spectrum was subtracted. For Ge2 the background was not removed since the generally low levels of background counts in the detector meant that often subtraction would introduce a large number of channels with negative counts.

The resulting peak(s) was analysed with a modified version of the peak-fitting routine (MUL_PEAKFIT) to be described in Section 4.2.1. The modifications were necessary due to the shape of the peaks in the calibration spectra (see Fig. 3.13). Each peak rather than being a single gaussian was composed of two sets of symmetric wings. These are indicative of either noise in the system or else jitter in the ADC.

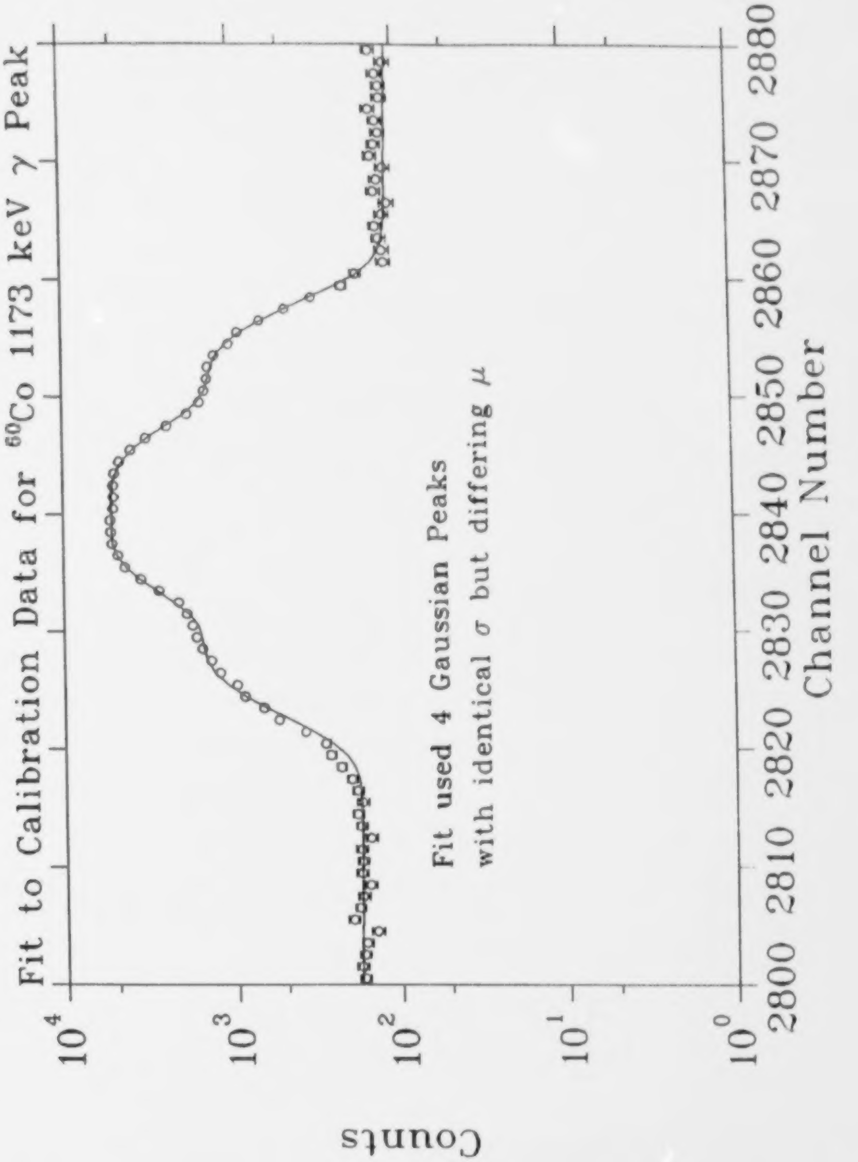

Figure 3.13 The fit to the 1173 keV γ peak for the efficiency calibration of the coaxial HPGe (Ge1). Clearly visible in the peak shape are the two pairs of gaussian peaks symmetric about the main centroid at 2840 channels. Each peak has a σ of 3.23 ± 0.02 channels. The first pair of peaks is offset from the main centroid by 3.30 ± 0.02 channels, while the second pair of peaks is offset by 12.34 ± 0.04 channels.

To compensate for this peak distortion, the fitting program was modified by changing the fitting function so each peak was formed by four gaussian peaks arranged in two symmetric pairs. The standard linear background was kept along with the step background but the short and long range tails were removed from the fit. The two pairs of peaks visible in the data (see Fig. 3.13) were obviously symmetric about a common centroid. The combination peak was modeled by giving these four gaussian peaks a common width, σ, but each pair of peaks had a different separation centered about the overall centroid, μ. This procedure improved the quality of the fit significantly over either a single peak or a single peak with a single set of symmetric wings. The total counts in each peak was then the sum of four peaks. No systematic error in evaluating the peak centroid is introduced by this procedure.

The peaks of the four higher energy ^{133}Ba peaks were fit simultaneously since it seemed reasonable to assume that their Compton tails would influence one another. For Ge2, since the number of counts in the spectrum for ^{60}Co was so small, no peak fitting was done. All counts in the clearly visible peaks were counted and assumed to be from ^{60}Co.

The net counts for each peak were then fed into an EXCEL spreadsheet which calculated the efficiency for that energy (see Table 3.5). The spread sheet calculated the expected number of events by applying the standard radioactive decay law to the source activity on 1 January 1986 and then multiplying by 600 s to account for collection time. The effect of the various amounts of absorber material between the source and the detector were accounted for (for calculations of the linear absorption coefficient μ see Appendix 2). The final efficiency was found by the following formula

$$\varepsilon_{eff}(E) = \frac{N_{obs}}{A_s \bullet 600\ \mathrm{s} \bullet e^{-\sum_i \mu_i x_i}} . \qquad (3.15)$$

The error is given by

$$\delta\varepsilon_{eff}(E) = \varepsilon_{eff}\left[\left(\frac{\delta N_{obs}}{N_{obs}}\right)^2 + \frac{1}{A_s \bullet 600\ \mathrm{s}} + (0.05)^2\right]^{1/2} , \qquad (3.16)$$

where μ_i is the absorption coefficient for material i, x_i is the thickness of material i, A_s is the expected source activity, and N_{obs} is the observed number of counts. An additional 5 % error was added in to the error formula to cover the possible small errors in μ, x, the exact date that the source was initially measured, and the error in that measurement.

The only modification to the above procedure was for the 81 keV peak efficiency in ^{133}Ba. In the energy calibration described in Section 3.3.1.3 it was found that the 79.6 keV peak could not be resolved. For the efficiency calibration the superposition of the two peaks can be compensated for by simply adding the intensity of the 79.6 keV peak (2.43 %) to the intensity of the 81 keV peak (32.8 %) to generate a combined intensity of (35.23 %) for the 81 keV peak.

To generate the scaling factor between the *far* and *tape* positions, the efficiency at the tape position was divided by the efficiency at the far position. The factor was then averaged. The scaling factor for Ge1 was 10.56±0.23 for the two measurements available. The scaling factor was not very constant for Ge2 unfortunately, ranging from 56 to 103 (four data points). Since the data would primarily be analysed for branching ratios for which has the geometric correction in each term would cancel, the data was fit to the unscaled *far point* efficiency. This is the efficiency used in the analysis in Chapter 4. One deficiency in this technique is that the material traversed is not identical for the near and tape positions. Priority should have been given to the *tape* position data, but was not.

Table 3.5. The table showing the data and calculations used to determine the efficiency of each detector.

Calibration Source	Initial Activity (atoms/sec)	Half Life (s)	InitialDate	Observed Date	Time Difference (s)	Expected Activity (atoms/sec)
Ba-133	3.36700E+05	3.26646E+08	01/1/86	26/11/92	2.17814E+08	1.72841E+05
Co-60	2.64920E+05	1.66226E+08	01/1/86	26/11/92	2.17814E+08	7.14556E+04

Detector and Position	Energy (keV)	Branching Ratio (%)	Observed Activity (atoms)	Error in Obs. Activity (atoms)	Linear Att. Coeficient μ-Al (cm-1)	Linear Att. Coeficient μ-CH (cm-1)	Transmission (%)	Adjusted Counts	Efficiency	Error in Efficiency
Ge 1	81	35.23	34101.1	355.8	0.5009	0.1724	32.08	106313.6	2.910E-03	1.49E-04
Far Position	276.4	7.29	3474.6	131.7	0.2863	0.1217	52.21	6655.6	8.804E-04	5.52E-05
	302.9	18.6	7937.5	146.7	0.2746	0.1177	53.61	14805.8	7.676E-04	4.09E-05
Ba-133	356	62.3	24166.9	212.6	0.2551	0.1107	56.04	43127.9	6.675E-04	3.39E-05
	383.9	8.84	2825.2	84.4	0.2465	0.1075	57.14	4944.1	5.393E-04	3.14E-05
Ge1 Far Position	1173.2	99.9	6270.7	152.8	0.1482	0.0652	71.44	8778.1	2.050E-04	1.14E-05
Co-60	1332.5	100	5432.8	120.9	0.1398	0.061	72.80	7462.4	1.741E-04	9.53E-06
Ge1 Tape Position	1173.2	99.9	87776.7	439.9	0.1482	0.0652	96.83	90631.7	2.116E-03	1.06E-04
Co-60	1332.5	100	78113.4	501.6	0.1398	0.061	97.03	80502.3	1.878E-03	9.47E-05
Ge2	81	35.23	2107.0	79.9	0.5009	0.1724	30.46	6917.5	1.893E-04	1.19E-05
Far Position	276.4	7.29	182.4	19.1	0.2863	0.1217	50.33	362.4	4.793E-05	5.35E-06
	302.9	18.6	352.4	27.9	0.2746	0.1177	51.75	681.0	3.530E-05	3.31E-06
Ba-133	356	62.3	884.9	41.6	0.2551	0.1107	54.21	1632.5	2.527E-05	1.73E-06
	383.9	8.84	87.3	15.8	0.2465	0.1075	55.33	157.8	1.721E-05	3.24E-06
Ge2 Far Position	1173.2	99.9	127.0	11.3	0.1482	0.0652	70.05	181.3	4.233E-06	4.31E-07
Co-60	1332.5	100	109.0	10.4	0.1398	0.061	71.48	152.5	3.557E-06	3.84E-07
Ge 2	81	35.23	555638.8	1116.5	0.5009	0.1724	90.39	614688.0	1.682E-02	8.4E-04
Tape Position	276.4	7.29	19218.8	234.4	0.2863	0.1217	94.06	20431.8	2.703E-03	1.39E-04
	302.9	18.6	42136.4	335.5	0.2746	0.1177	94.28	44690.6	2.317E-03	1.17E-04
Ba-133	356	62.5	108575.6	604.9	0.2551	0.1107	94.66	114700.4	1.775E-03	8.9E-05
	383.9	8.84	15471.1	335.0	0.2465	0.1075	94.83	16314.9	1.780E-03	9.70E-05

The efficiencies obtained were plotted and then fitted with the function

$$\varepsilon_{eff}(E) = k\,E^{a}\ , \tag{3.17}$$

which is a straight line on a log–log plot.. Fig. 3.14 is the fitted efficiency for both detectors for the *far* data. Table 3.6 has the fitting parameters and their errors along with some other information on the detectors. The fit was to the data for ^{60}Co and the two strongest peaks of ^{133}Ba (E_γ = 302.9 keV and 356.0 keV). For both HPGe detectors the lowest energy point was known to be in a region where the detector efficiency is non-linear so the 81 keV data was not included in the fit. Even by eye it was evident that the highest energy point at E_γ = 383.9 keV was poorly fit by the peak fitting routine and thus the number of events in the peak was suspect. For this reason it was not included in the linear fit to determine the efficiency curve.

Table 3.6. The results of the efficiency fit for each detector along with other important identifying information.

Detector	Manufacturer	Serial #	Model #	Bias Voltage [V]	Fitting Parameter a	Fitting Parameter k
Ge1 [Co-axial]	Canberra	1086779	7600S	(–)3000	-1.0001 ±0.0158	0.236 ±0.025
Ge2 [Planar]	Aptec	1041	PS4010	(–)1500	-1.5187 ±0.0357	0.195 ±0.045

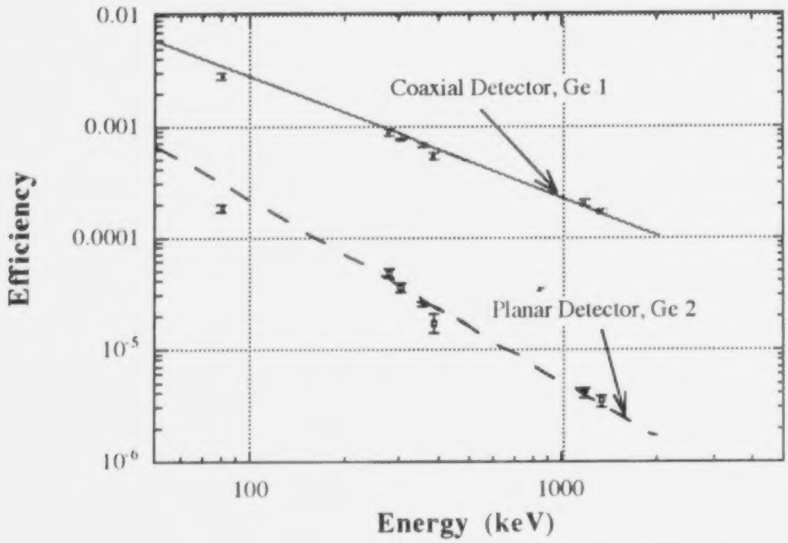

Figure 3.14. The fit to the efficiency data for detectors Ge1 and Ge2 from data taken at the far position.

3.3.2 Plastic Scintillator Detectors

Plastic scintillators were used for β detection. Plastic scintillators operate by absorbing energy from the charged particles passing through them. This energy excites some scintillator atoms to a higher energy state. The atoms de-excite releasing energy mainly through heat and lattice vibrations. However some energy is emitted in the form of photons (λ_n = 425 nm, for NE102A). The scintillation efficiency (the amount of light released as a fraction of the amount of energy deposited in the scintillator) of all plastic scintillators is quite low, about 2.3% for NE102A. The emitted photons are transmitted via total internal reflection through a light guide to a photomultiplier tube (PMT). The photons strike the surface of the PMT photocathode, knocking out electrons which are then accelerated and focused on the first in a series of dynodes in the tube. The dynodes are made of material which release a large number of secondary electrons under electron bombardment. This process is repeated 12 times for the RCA 8575 PMT used here, each successive stage increasing the number of electrons. The net result is an amplification of the initial signal by a factor of about 10^7. The properties of the scintillator and PMT used in the experiment are given in Table 3.7 [Fer90].

The two β–paddles and the ΔE–E telescope were fabricated out of NE102A scintillator. For the detection of electrons this material offers some advantages. It has a fast response time since the main time-decay component is 2.4 ns. This allows the timing gate for an ΔE–E coincidence to be set very tightly. Unfortunately, since the time response of the HPGe detectors is quite slow, this introduces some complications in the $\beta\gamma$ coincidence circuits (see Section 3.3.3.5).

Table 3.7. The properties of NE102A scintillator and the RCA 8575 photomultiplier.

NE102A Scintillator		RCA 8575 PMT	
Light Output[a]	58—70 %	Useful Diameter	46 mm
λ	423 nm	Gain	14×10^6
Attenuation Length	250 cm	λ peak response	385 nm
Rise Time	0.9 ns	Quantum Efficiency	31 %
Decay Time	2.2—2.5 ns	Rise Time	2.5 ns
Pulse FWHM	2.7—3.2 ns	Transit Time (1800V)	40 ns

[a] as a percentage of anthracene

Another advantage of NE102A is the almost 100% detection efficiency for electrons. However, there exists a significant probability that the electron will undergo large-angle scattering and exit the detector before depositing all its energy. Backscattering is an extreme case of this. Since electrons have a very low mass, there exists the possibility that they will be "reflected" back out from the surface instead of penetrating into the detector, depositing only minimal energy in the detector. Fortunately, carbon, the main constituent of plastic, has a low backscattering coefficient. The fraction backscattered is about 2% of the incident flux at 1 MeV. For 10 MeV electrons this fraction drops to 1%.

An important property of plastic scintillators is that the light output is linear with electron energy (1 photon/100 eV energy loss) for $T_e > 125$ keV. The β–paddles and the ΔE scintillator were only 1.5 mm thick. For electron energies >1 MeV the energy deposited in the scintillator was almost constant. To examine the situation more quantitatively, it is necessary to calculate the most probable energy loss, W_{MP}, given by

$$W_{MP} = \xi \left(\ln \frac{\xi}{\varepsilon} + 0.198 - \delta \right) . \tag{3.18}$$

Here ξ is

$$\xi = 2\pi N_a r_e^2 m_e c^2 \rho \frac{Z}{A} \left(\frac{z}{\beta} \right)^2 x , \tag{3.19}$$

z is the charge of the particle, and x is the absorber thickness, and numerically one has $2\pi N_a r_e^2 m_e c^2 = 0.1535$ MeV cm^2/g.

The quantity ε is defined by

$$\ln \varepsilon = \ln \left[\frac{(1-\beta^2) I^2}{2 m_e c^2 \beta^2} \right] + \beta^2 . \tag{3.20}$$

The final term, δ, is the relativistic correction term of the Bethe–Block equation. For electrons between 1 and 7 MeV in scintillator it can be approximated by

$$\delta = 4.6052\Pi - 3.20 + 0.1610(2.49 - \Pi)^{3.24}, \tag{3.21}$$

where $\Pi = \log_{10}(\beta\gamma)$, and $\gamma = (1-\beta^2)^{-1/2}$. The dependance of W_{MP} on electron energy for the scintillator used in the experiment is shown in Fig 3.15. From the graph it is clear that the energy loss is essentially flat over the whole range of interest although a clear deviation is evident for $T_e < 2$ MeV (β=0.98). Even with this deviation the energy loss varies by only 50 keV between 1 MeV [W_{MP} = 250 keV] and 7 MeV [W_{MP} = 200 keV].

Detailed drawings of the scintillators used in the experiment are shown in Figs. 3.16 and 3.17. To accommodate both the PMTs for β1 and β2 and the tape system it was necessary to mount the PMTs in the corners of the top box plate. This required a complicated shape for the connecting light guides. The same was true of the ΔE light guide as can be seen in Fig. 3.10.

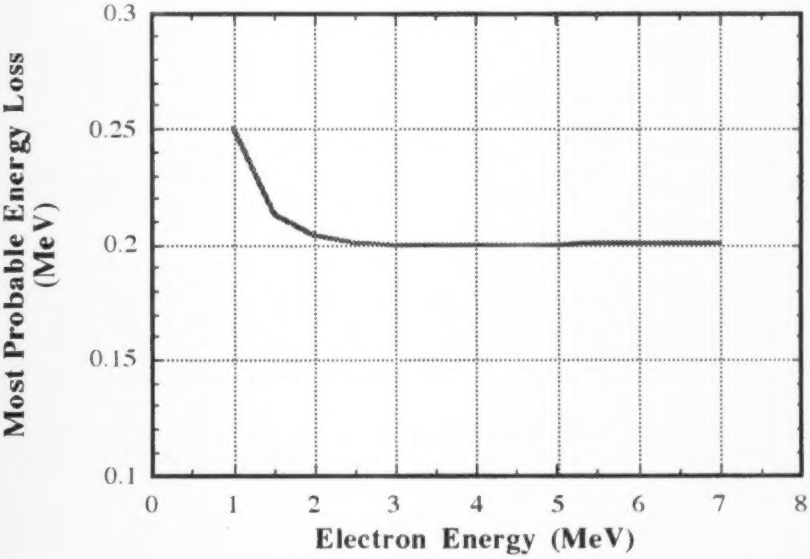

Figure 3.15. The most probable energy loss W_{MP} for electrons in the plastic scintillator (ΔE) of thickness 1.5 mm used in the experiment.

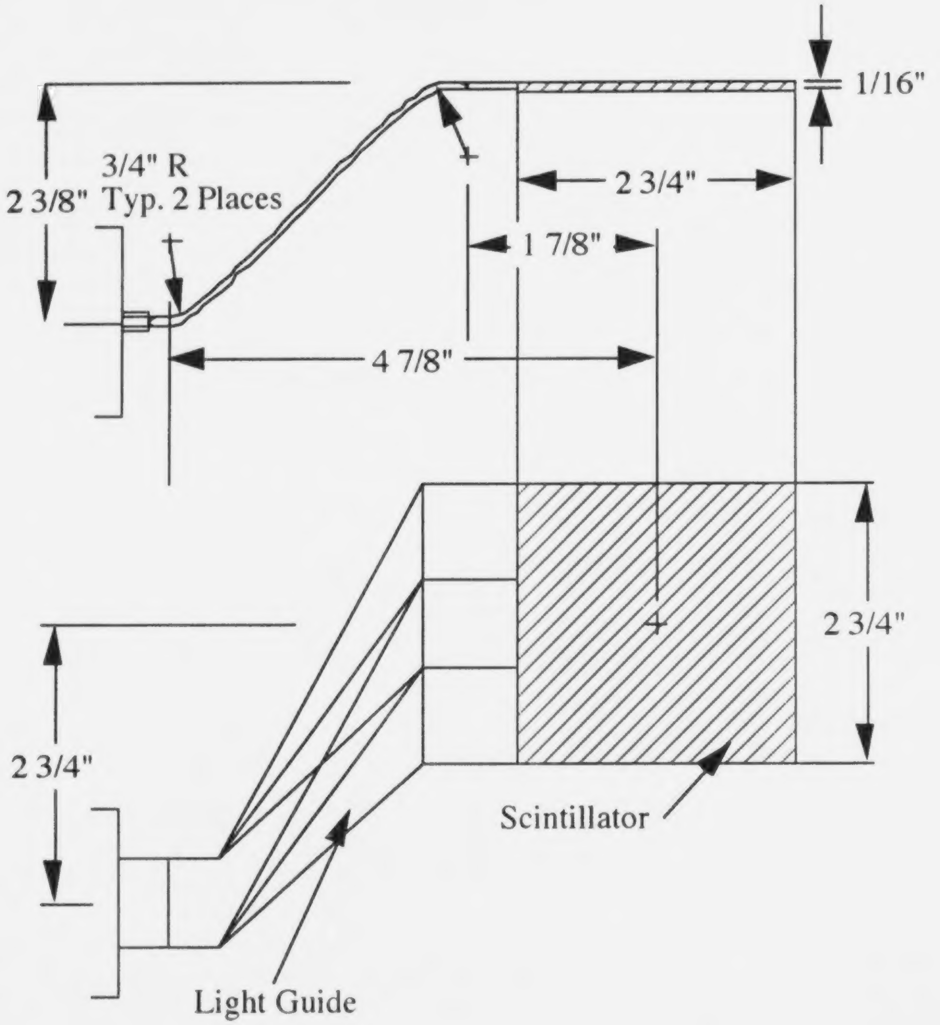
1/16"
3/4" R
Typ. 2 Places
2 3/8"
2 3/4"
1 7/8"
4 7/8"
2 3/4"
2 3/4"
Scintillator
Light Guide

Figure 3.16. The details of the scintillators used in the β paddles, $\beta1$ and $\beta2$.

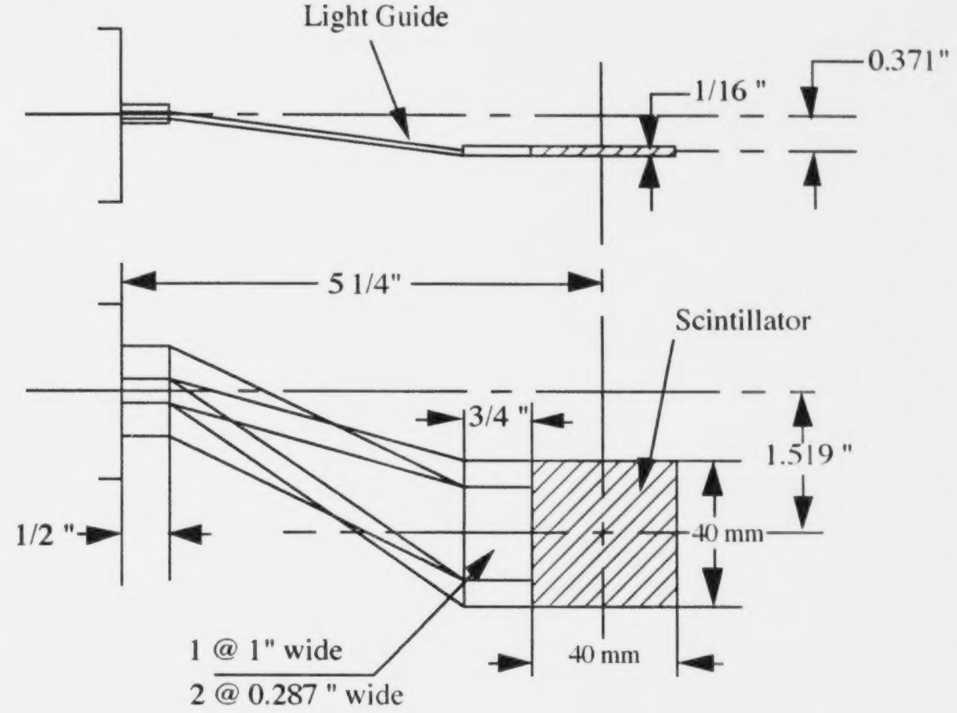

Figure 3.17. The details of the scintillator used in the ΔE detector.

3.3.2.1 Calibration of the Beta Telescope

A usual method employed in calibrating a β detector is to use a monoenergetic electron source[Bea86] (the best being a variable energy electron linac). Since no source of this type was available at TRIUMF an alternative method was employed.

Taking advantage of TISOL's ability to produce different isotopes, a series of additional runs were undertaken during the experiment to collect data from ^{6}He, ^{8}He and ^{23}Ne. This data covered a wide range of beta endpoint energies as shown in Table 3.8. Unfortunately, the voltage setting on the PMT for the thick E scintillator was set too high, resulting in a signal that saturated the ADC for electrons with energies $T_e >$

$T_e > 5$ MeV. The fault was not noticed by the people running the experiment at the time and the result is that the data are of mixed quality. Examination of Table 4.1 will reveal that the calibration runs occurred after the ^{25,26}Ne data collection periods and only just before the termination of the experiment. Although it was immediately obvious upon review that the voltage was too high there was nothing that could be done about the situation and the data had to be analysed with this important flaw. As an example of the spectra collected, Fig. 3.18 shows the ^{6}He β spectrum. Unlike a monoenergetic source, all β energies are possible up to the endpoint energy. This complicates the calibration procedure since one must try to determine the energy of events where the rate approaches zero.

A computer code DECAYFIT was written to fit the data. The knowledge of the channel corresponding to the detector pedestal was used to give the zero energy point. The fitting program used this and the known endpoint energy to determine the linear energy calibration. The calibration is assumed to be a simple linear relationship. Based on an initial estimate of the endpoint channel and the channel corresponding to the ADC pedestal it was a simple matter to calculate the slope and intercept of calibration. The energies used in determining the theoretical value for the number of counts observed were then calculated from the center of the bin corresponding each data point. This was the energy corresponding to an electron at the exit of the ΔE scintillator. To determine the total initial energy of the electron, T_{tot}, the energy loss in the ΔE scintillator had to be accounted for. The energy loss for electrons in a 1.5 mm thick plastic scintillator was calculated using tabulated electron energy losses in the TRIUMF Kinematics Handbook [Gre87]. A localized linear fit was performed on these data at 2 to 7 MeV. The energy loss is non-linear below ~2 MeV so the experimental data were cut at this value. The total energy of the electron before entering the detector was calculated as

$$T_{tot} = \frac{T_{obs} + \Delta E_{int}}{(1 - \Delta E_{slope})} = \frac{T_{obs} + 0.266 \text{ MeV}}{(1 - 0.6333 \times 10^{-2})} , \tag{3.22}$$

where T_{obs} is the observed energy deposited in the thick E scintillator, ΔE_{slope} is the slope of the linear energy loss fit in the ΔE scintillator, and ΔE_{int} is the intercept of the fit.

The program generated the theoretical shape of the β energy distribution from zero energy to the known β endpoint energy (see eq. 2.3). This function was then convoluted by a gaussian function whose width was given by:

$$\sigma = A + B^{*}\mathrm{sqrt}\,(energy)\ , \tag{3.23}$$

where A and B are fitting parameters. The convoluted function was then normalized to the total number of observed counts in the data spectrum. Additionally, a factor, F, was used to scale the resulting spectrum. This factor was to compensate for difficulties in fitting the shape of the spectra caused by known physical processes such as scattering of the electrons out of the sides of the detector before they had deposited their full energy as well as the assumption that the decay is only to a single level. The closer this value is to unity the better the theoretical expression in eq. 2.3 describes the data and the more valid the fit. If the value of F is ≥ 1.5 then this indicates that the spectrum is poorly defined by eq. 2.3 and the validity of the results for the fit is questionable. The final component of the fit was the addition of a constant background.

The program executed a χ^2 minimization using MINUIT. The value of the channel corresponding to the β–endpoint, the pedestal value, A, B, F, and the magnitude of the constant background were allowed to vary during the fitting procedure. The results of the runs are summarized in Table 3.9. The fit for ^{8}He was very poor. This is not surprising for ^{8}He since the detector is gain-adjusted for observing only the central region of the decay spectrum and thus the program had to extrapolate a great distance to the endpoint. The fitted values of A, and B for the decays other than ^{6}He all terminated at the upper limit of the allowed ranges of variation. Poor convergence also is not unexpected as the program was approximating the second decay component of these decays as a flat line. When the β endpoints are not well separated this will result in an increase in the width of the spectrum. A flat background under a peak shifts the peak upwards, but a curved background under the same peak not only shifts it upwards but also widens the peak itself. This widening is exactly what is seen in the fit results. For ^{23}Ne, where the majority of the spectrum shape is visible, and where it is known that there is a second decay component, the program was rerun with wider limits on the values of A, and B. The χ^2/DOF decreased slightly (–0.2) if the values were allowed to increase to $A=1$, $B=4$. However, the values for A, and B are a function of the detector itself and should not vary depending on the isotope being studied. As the increase of the values of A, and B could be understood in terms of the superposition decay curves, the parameter values were fixed to those given by ^{6}He for all further work since it had a visible endpoint energy.

The intercepts of the energy calibration agree within error between ^{6}He and ^{23}Ne. The slope does not. A variety of adjustments to the fitting procedure were carried out using the available spectra. Typical variations in the endpoint energies obtained from the different slope parameters were ±300 keV. This gives an estimate of the systematic error in any determined endpoint energy. Based on the body of fits, the energy calibration adopted for the detector was: slope = 4.43 keV/channel, offset = +110 keV. It would be expected that the values determined from a fit using this calibration value would have a systematic error of about ±300 keV at 5 MeV

3.3.3 Silicon Surface Barrier Detectors

For the study of the β–delayed α–emission of ^{18}N, silicon surface barrier (SSB) detectors were used to detect both the alpha and the recoiling ^{14}C. This type of detector consists of n–type silicon with a thin layer of gold deposited over it to form the diode. The contact potential generated by their differing Fermi levels results in the band levels of the silicon being lowered thereby forming a depletion zone extending into the silicon.

Table 3.8. This table gives the half-life and maximum beta energy of the isotopes used as input data in the calibration fits.

Isotope	Half-life [ms]	β Endpoint [MeV]
^{6}He	807	3.56
^{8}He	119	10.65
^{23}Ne	$3.72\text{x}10^{4}$	4.376

Table 3.9. This table gives the results for each isotope used in the calibration showing fitting parameters, χ^2, and the calibration values determined from them.

Isotope	Slope [keV/ch]	Intercept [MeV]	A	B	F	χ^2	χ^2/DOF
^{6}He	4.13±0.01	−0.103±0.009	0.296 ±0.064	3.024 ±0.003	1.32±0.01	1226	1.77
^{8}He	5.39	−0.13	$0.36^{\dagger}$	$3.048^{\dagger}$	1.01±0.01	2663	2.68
^{23}Ne	4.43±0.02	−0.110±0.028	$0.36^{\dagger}$	$3.048^{\dagger}$	1.10±0.00	1426	1.66

†after ^{6}He was fit these values were then constrained by the value and error given in that fit. The value chosen by the program for all other runs was the maximum for the range. This means the MINUIT generated errors for A and B are meaningless so are not quoted.

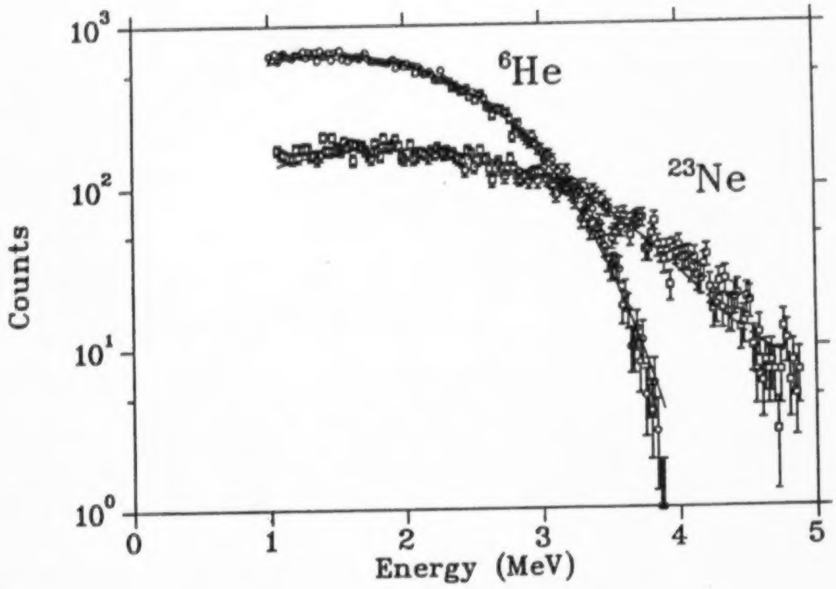

Figure 3.18. The fit to the ^{6}He and ^{23}Ne beta decays showing the fit determined for each. Only every 5th data point is shown for clarity.

To increase the depth of the depletion zone a reverse bias can be applied across the detector. The depletion zone does not have any mobile charge carriers. As an electric field is applied across this zone any electrons produced in it by energy loss of the particles of interest will be swept out, causing a current proportional to the energy loss. The detectors produce very low currents so preamplification is necessary. Noise can be a problem since they operate at room temperature and are sensitive to ambient light.

3.3.4 Neutron Detectors

Two different neutron detectors were available for use with the experiment: a NE213 liquid scintillator detector and a high-pressure ^{3}He proportional detector. The two detectors served different purposes. The NE213 detector was useful in determining the number of neutrons emitted by the decaying isotope but gave very poor energy information. The ^{3}He detector had a very low efficiency ($\sim 10^{-5}$ for a source located at the wall of the detector) but could give an accurate energy spectrum of the observed neutrons. The neutron, like the photon, is difficult to detect since it is a neutral particle and one must look for the products of interactions with the detector medium. The neutron is even more difficult to detect than the photon as it must interact via the strong force which has a much shorter interaction range than the electromagnetic force. Both detectors look for the presence of the fast, charged recoil nucleus from elastic scattering reactions to detect the neutron.

The NE213 detector detects the recoil nucleus in the manner described in Section 3.2.2. To differentiate the neutron events from γ–events pulse shape discrimination (PSD) is used. Pulse shape discrimination uses the fact that different energy loss mechanisms result in different decay processes for the excited molecules of the detector. The time for a pulse to decay to a certain fraction of its peak value is different for the n–events and γ–events.

The ^{3}He detector is a proportional gas detector. The recoiling nucleus loses energy to the surrounding gas by ionizing the molecules. The electrons produced, if formed in the presence of a specific electric field shape, undergo avalanche photomultiplication and produce a signal proportional to the energy lost to the gas. More information on neutron detection and proportional counters can be found in [Leo87].

3.4 Experimental Endstation Data Acquisition System

The online data collection and analysis system for TISOL consists of a standard TRIUMF computer system normally used for such tasks. The host computer, named 4ADAC, is a VaxStation 3200. Connected to this is a 8 mm tape drive for data storage and a J11 Starburst CAMAC Controller/Data Interface. The J11 is loaded with a compiled TWOTRAN[1] program to control the CAMAC crate. The data acquisition process is controlled by the site standard VDACS data acquisition program [Lud88]. The purpose of VDACS is to control the data flow from the CAMAC crate through the J11 to 4ADAC, and finally to the tape. It allows the experimenter to control the acquisition process, and to view the data as it is collected.

The preliminary online analysis is carried out by the TRIUMF standard data acquisition program NOVA written by P.W. Green [Gre91]. NOVA monitors VDACS and will attempt to analyse as much data from the data stream as the event rate allows. NOVA allows for the display of data in histograms specified by the user. Calculated variables also can be defined from the incoming new data and displayed. There are also NOVA routines which will display scaler data in either "Total-to-Date" or "Rate" form. The NOVA execution is determined by a Command file containing variable, histogram, and test definitions and a logical analysis chain called the Operating Sequence

---

[1] TWOTRAN is a programming language loosely based on FORTRAN which is used to control the event processing structure of the data acquisition system. The TWOTRAN code will specify which modules are to be accessed, depending on the LAM received by the J11.

(OPSEQ). The Command file specifies the relationship between the user-defined analysis elements and the raw incoming data. The Operating Sequence defines the conditions when the spectra are to incremented. For more information on either NOVA or VDACS refer to either the NOVA or VDACS user references [Lud88, Gre91].

The CAMAC crate configuration and the electronics hardware setup for the experiment are shown in Figs. 3.19 and 3.20. In the description of the detector branches and logic systems which follow items in italic print refer to particular entities named in Fig. 3.20.

The detector system and its associated electronics used in the experiment were configured for $\beta\gamma$, $\gamma\gamma$, ΔE–E, and ^{3}He neutron event types. The requirement for a master trigger to occur was any of these event types. The primary focus of the experiment was on γ–decay, so three separate γ–detection systems were in place. Two HPGe detectors were in use: Ge1 was a coaxial HPGe and Ge2 was a planar HPGe. Each of these detectors was individually coupled to the beta detection system surrounding the collection point to make an $\beta\gamma$ event type. The two detectors were also used to form a $\gamma\gamma$ event type to search for evidence of gamma cascades. The ΔE–E β–telescope was used to observed the β–energy spectrum and for half-life information. As it was known that ^{27}Ne would emit neutrons, the ^{3}He neutron detector was in place to determine their energy spectrum. Data were collected in event-by-event mode with all detectors being read independent of which event type gave the master gate.

3.4.1 The CAMAC Digital Electronics

The CAMAC crate organization is shown in Fig. 3.19. The C212 Event Register (CAMAC N=3) is used to determine which of the possible coincidence branches (see below) has set the master gate. It is read for each event and this information is used by NOVA to determine which histograms should be incremented.

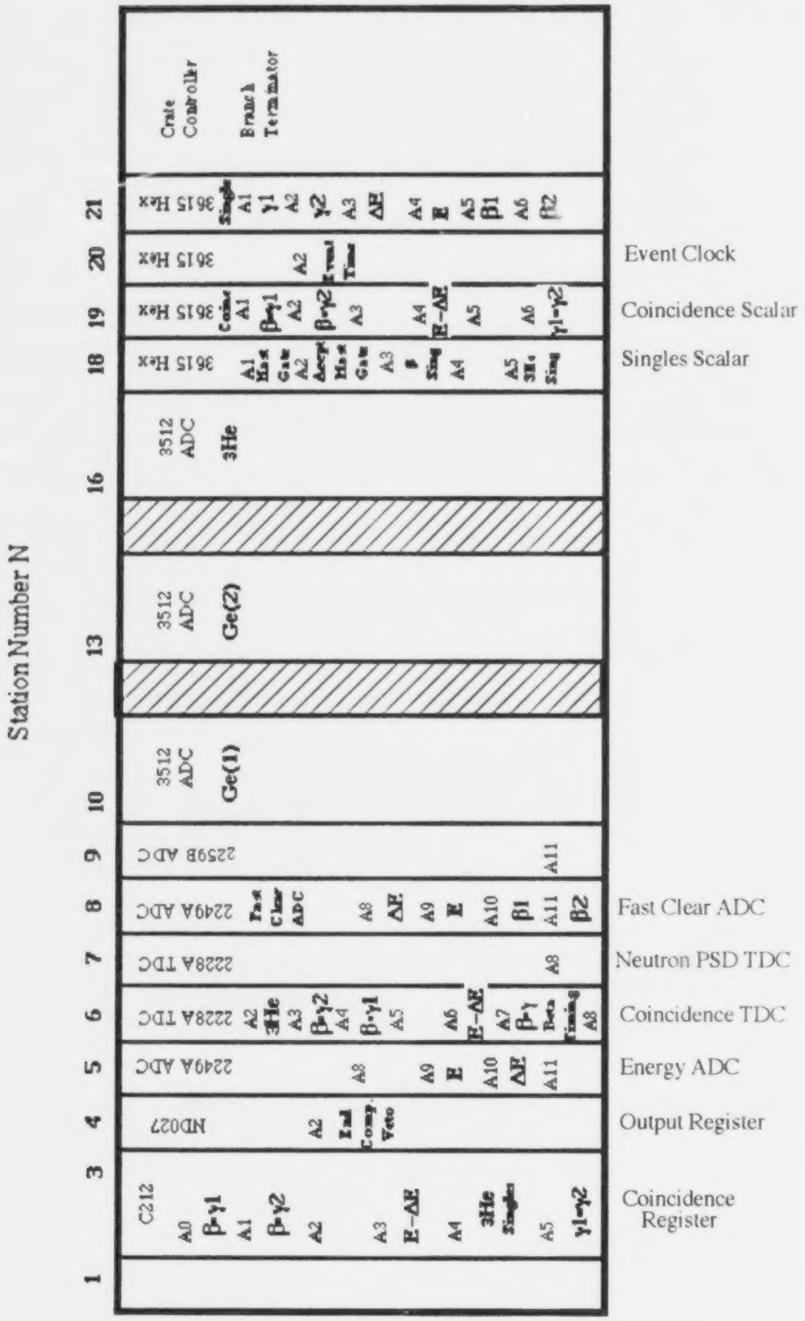
Station Number N
1
3
4
5
6
7
8
9
10
13
16
18
19
20
21
C212
A0
β-γ1
A1
β-γ2
A2
A3
E-ΔE
A4
3He Singles
A5
γ1-γ2
ND027
Ext Comp. Veto
2249A ADC
A8
A9
E
A10
ΔE
A11
2228A TDC
3He
β-γ2
β-γ1
A6
A7
β-γ
Beta Timing
Fast Clear ADC
β1
β2
2259B ADC
3512 ADC
Ge(1)
Ge(2)
3615 Hex
Singles
γ1
γ2
E-ΔE
Crate Controller
Branch Terminator
Event Clock
Coincidence Scalar
Singles Scalar
Fast Clear ADC
Neutron PSD TDC
Coincidence TDC
Energy ADC
Output Register
Coincidence Register

Figure 3.19. The configuration of the CAMAC crate for the experiment.

The ND027 (CAMAC N=4) is a NIM output register which allows the J11 to clear the Busy Veto Latch (see below) when the computer is finished processing an event. A 2249A ADC (CAMAC N=5) was used to determine the energy deposited in the ΔE, E, and NE213 scintillators. The 2228A TDC (CAMAC N=6) was used for most of the coincidence timing and had its conversion gain set to 250 ps/ch. The 2228A TDC (CAMAC N=7) was used exclusively for the NE213 pulse shape discrimination analysis and had its conversion gain set to 50 ps/ch. The 2249A ADC (CAMAC N=8) was used for the *Fast Clear Beta* ADC readout. Signals from ΔE, E, $\beta 1$, and $\beta 2$ were always read out by this ADC but it also included a clear input signal which would clear the ADC in the event no $\beta\gamma$ coincidence was detected. There were three LeCroy 3512 ADC's used to read out the two HPGe and the ^{3}He detectors (slots 10, 13, and 16 respectively). These ADCs were used because they can handle a +10V signals, and have 13-bit resolution. There were four 3516 hex scalars used in the experiment. The first (CAMAC N=18) recorded the singles data: *Master Gate*, *Accepted Master Gate*, β–singles, NE213 singles, ^{3}He singles. The second (CAMAC N=19) was for coincidence data: $\beta\gamma$, $\gamma\gamma$, β–n, ΔE–E. The third scaler (CAMAC N=20) recorded the number of pulser counts since the tape was last moved and formed the event clock. The final scaler (CAMAC N=21) recorded the number of events in each detector during each collect/count cycle. It was cleared at the same time as the clock.

3.4.2 Master Gate Logic

The master gate circuitry for processing an event can be found in the box at the center of Fig. 3.20. Events were processed in the following manner. A valid coincidence is formed in one of the detector branches. A valid coincidence is either a $\beta\gamma$(planar), $\beta\gamma$(coaxial), ΔE–E, βn(NE213), $\gamma\gamma$, or βn(^{3}He). The signal passes to a model 429 Logic Fan In/Fan Out (LoFIFO), the *Master Gate*, which ORs the various coincidence branches. The single output from this goes into the busy veto, a

Figure 3.20. The electronics layout for experiment 597.

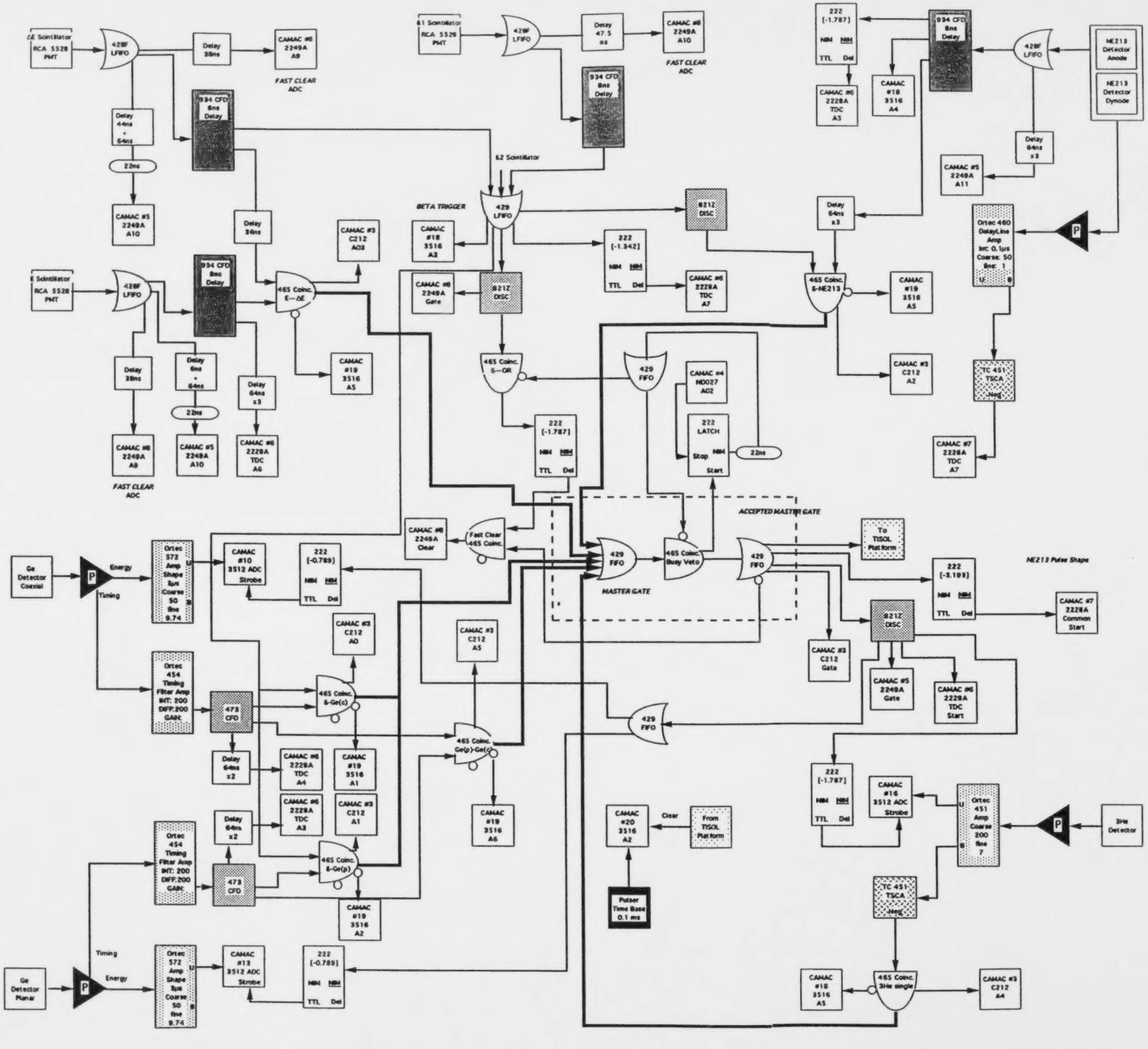
ΔE Scintillator RCA 5528 PMT
428F LFIFO
Delay 38ns
CAMAC #8 2249A A9
FAST CLEAR ADC
934 CFD 8ns Delay
Delay 44ns + 64ns
22ns
CAMAC #5 2249A A10
Delay 36ns
CAMAC #3 C212 A03
E Scintillator RCA 5528 PMT
428F LFIFO
934 CFD 8ns Delay
465 Coinc. E—ΔE
Delay 38ns
Delay 6ns + 64ns
22ns
Delay 64ns x3
CAMAC #19 3516 A5
CAMAC #8 2249A A9
CAMAC #5 2249A A10
CAMAC #6 2228A TDC A6
FAST CLEAR ADC
ß1 Scintillator RCA 5528 PMT
428F LFIFO
Delay 47.5 ns
CAMAC #8 2249A A10
FAST CLEAR ADC
934 CFD 8ns Delay
ß2 Scintillator
BETA TRIGGER
429 LFIFO
CAMAC #18 3516 A3
821Z DISC
222 [-1.342] NIM NIM TTL Del
CAMAC #6 2228A TDC A7
CAMAC #8 2249A Gate
821Z DISC
465 Coinc. ß—OR
429 FIFO
CAMAC #4 NO027 A02
222 [-1.787] NIM NIM TTL Del
222 LATCH Stop NIM Start
22ns
222 [-1.787] NIM NIM TTL Del
CAMAC #6 2228A TDC A5
934 CFD 8ns Delay
CAMAC #18 3516 A4
428F LFIFO
NE213 Detector Anode
NE213 Detector Dynode
Delay 64ns x3
CAMAC #5 2249A A11
Delay 64ns x3
465 Coinc. ß-NE213
CAMAC #19 3516 A5
CAMAC #3 C212 A2
Ortec 460 DelayLine Amp Int: 0.1µs Coarse: 50 fine: 1 U B
P
TC 451 TSCA Neg
CAMAC #7 2228A TDC A7
ACCEPTED MASTER GATE
CAMAC #8 2249A Clear
Fast Clear 465 Coinc.
429 FIFO
465 Coinc. Busy Veto
429 FIFO
MASTER GATE
To TISOL Platform
NE213 Pulse Shape
222 [-3.193] NIM NIM TTL Del
CAMAC #7 2228A Common Start
821Z DISC
CAMAC #3 C212 Gate
CAMAC #5 2249A Gate
CAMAC #6 2228A TDC Start
Ge Detector Coaxial
P
Energy
Timing
Ortec 572 Amp Shape 3µs Coarse 50 fine 9.74 U B
CAMAC #10 3512 ADC Strobe
222 [-0.789] NIM NIM TTL Del
CAMAC #3 C212 A0
Ortec 454 Timing Filter Amp INT: 200 DIFF: 200 GAIN:
473 CFD
465 Coinc. ß-Ge(c)
Delay 64ns x2
CAMAC #6 2228A TDC A4
CAMAC #19 3516 A1
CAMAC #3 C212 A5
465 Coinc. Ge(p)-Ge(c)
CAMAC #19 3516 A6
429 FIFO
Delay 64ns x2
CAMAC #6 2228A TDC A3
CAMAC #3 C212 A1
Ortec 454 Timing Filter Amp INT: 200 DIFF: 200 GAIN:
473 CFD
465 Coinc. ß-Ge(p)
CAMAC #19 3516 A2
CAMAC #20 3516 A2
Clear
From TISOL Platform
Pulser Time Base 0.1 ms
222 [-1.787] NIM NIM TTL Del
CAMAC #16 3512 ADC Strobe
Ortec 451 Amp Coarse 200 fine 7 U B
P
3He Detector
TC 451 TSCA Neg
CAMAC #18 3516 A5
465 Coinc. 3He single
CAMAC #3 C212 A4
Ge Detector Planar
P
Timing
Energy
Ortec 572 Amp Shape 3µs Coarse 50 fine 9.74 U B
CAMAC #13 3512 ADC Strobe
222 [-0.789] NIM NIM TTL Del

model 465 coincidence unit set up for self-coincidence running. One output from the busy veto goes to the busy latch, a model 222 Gate and Delay generator (G&D) operating in LATCH mode. This signal sets the latch on which then sets the veto input of the busy veto high, thereby inhibiting any further master gate signals until the computer is finished event processing. Another output from the busy veto goes into the *Accepted Master Gate*, another 429 LoFIFO. It is from here that multiple signals diverge.

3.4.3 Data Acquisition System Logic

The most important signal from the *Accepted Master Gate* is the one which strobes the C212, thereby generating the LAM and beginning the CAMAC event processing. Another signal goes to the TISOL platform to give the operator some indication that events are occurring. This signal was normally used by feeding it into a visual scaler. A third signal goes to an Ortec 222 G&D. The delayed output from this unit provides the common start for the NE213 neutron detector *Pulse Shape* TDC (CAMAC N=7). The fourth signal is regenerated in an 821Z discriminator and is used to gate the 2249A "Energy" ADC (CAMAC N=5) to convert the E and ΔE scintillator signals and to common start of the "Coincidence" TDC (CAMAC N=6). Another output from this discriminator is fanned out using a 429 LoFIFO and feeds three 222 G&D generators. The TTL outputs from these 222s then gate the three 3512 ADCs. The rates of both the *Master Gate* and the *Accepted Master Gate* are recorded by the "Singles Scaler", a 3516 Hex Scaler, (CAMAC N=18). The final step of TWOTRAN event processing is for the J11, using the ND027 output register, to send a signal to the busy latch STOP input clearing the latch enabling the circuitry to accept another event.

The *Fast Clear* Beta ADC reads all of the plastic scintillators when there is any event, not just a ΔE–E, and thus the energy deposited in the plastic scintillators is always known. An output of the LFIFO for each of the E, ΔE, β1, and β2 is delayed and sent to the *Fast Clear* ADC (CAMAC N=8). The ADC is gated or cleared depending on if there is a valid event in the master gate. The event clock scaler (CAMAC N=20) contains the event time (since last time it had been cleared) by counting pulses from a logic scaler operating at 10 kHz. The event clock clear signal is sent from the TISOL control platform and is a regenerated signal from the tape controller to indicate the end of tape movement.

3.4.3.1 Beta Trigger Electronics

The *Beta Trigger* determines if an electron has passed through any of the scintillator paddles. The three paddles, $\beta 1$, $\beta 2$, and ΔE, are all configured in the same way. The signal from the PMT goes to a 428F Linear Fan In/Fan Out (LFIFO). From here the signal has two routes. The signal used to form the *Beta Trigger* goes to a 934 CFD (for a description of constant fraction discrimination see Section 3.2.1) which has an 8 ns external delay, and a discriminator setting of 30 mV. Constant fraction discriminators are chosen for all coincidence timing operations of the experiment since they provide highly accurate timing information. The three discriminator outputs are sent to a 429 LoFIFO which is the *Beta Trigger*. Signals from here then go through delays and into the various coincidence branches where they serve as the Beta signal. One signal goes to the "Singles Scaler", (CAMAC N=18, A3) and is used as the Beta singles rate. Another signal goes to a 222 G&D and the delayed output gives the $\beta\gamma$ timing in the "Coincidence" TDC (CAMAC N=6, A7). The other output from the *Beta Trigger* LFIFO is delayed and then goes to the *Fast Clear* ADC (CAMAC N=8). A signal from the *Beta Trigger* is regenerated in an 821Z discriminator with one output going to the gate of the *Fast Clear* ADC and the other to a 465 coincidence module. The coincidence module is operating in stand-alone mode so that its veto capability can be used. The fast clear veto signal is supplied by the Veto Latch NIM output after delay. The output of the coincidence unit starts a 222 G&D and the delayed output is sent to another 465 coincidence module along with the

NOT signal from the *Accepted Master Gate*. The logical AND of these two signals then goes on to form the *Fast Clear* pulse when there is only a beta signal in the gate.

3.4.3.2 The ΔE–E β Telescope

The ΔE–E β–telescope is used to detect electrons and the coincidence discriminates against γ–rays in the thick E scintillator. The ΔE signal comes from a 934 CFD, is delayed, and then goes into the 465 [ΔE–E] coincidence module. The signal from the LFIFO is delayed and input to the "Energy" ADC (CAMAC N=5, A10). The E–signal goes into a LFIFO with one output going into a 934 CFD whose output is sent to the ΔE–E coincidence module. Another output is delayed and sent to the Fast Clear ADC. A third output is delayed and sent to the "Energy" ADC (CAMAC N=5, A9). For timing information, the signal from the E–CFD is delayed and sent to the "Coincidence Timing" TDC (CAMAC N=6, A6).

3.4.3.3 The Liquid Scintillator Neutron Detector

The NE213 liquid scintillator neutron detector is intended to give an estimate of the rate of neutrons emitted from the target that are in coincidence with β's. To identify neutrons as opposed to γ–rays pulse shape discrimination [PSD] (see Section 3.2.4) is used. The signal from the NE213 anode goes to a LFIFO and from there the signal is split. One signal goes to a 934 CFD, is delayed, and then sent to a 465 coincidence module where it is ANDed with a signal from the *Beta Trigger*. This then forms a βn (NE213) coincidence event. The event signal goes to the master gate, to the C212 "Coincidence Register" (CAMAC N=3, A2), and to the "Coincidence Scaler" (CAMAC N=19, A5). The second signal is delayed and is sent to the "Energy" ADC (CAMAC N=5, A11). A signal from the CFD is sent to a 222 G&D where the delayed output is sent to the "Coincidence" TDC (CAMAC N=6, A5) to give the βn(NE213) timing.

The third signal from the CFD goes to the "Singles Scalar" (CAMAC N=18, A4) to give the neutron singles rate.

The signal from the NE213 dynode goes first to a Ortec 113 preamplifier and from there to a Ortec 460 delay-line amplifier. The bipolar signal from the delay-line amplifier goes into a TC451 timing single channel analyser (TSCA). The negative output from this is sent to the "stop" input of the neutron "Pulse Shape" TDC (CAMAC N=7). The start signal for the TDC is sent by the *Accepted Master* gate.

3.4.3.4 The ^{3}He Neutron Detector

The ^{3}He neutron detector is intended to give an accurate value of the energy of the observed neutrons. Since its efficiency is so low ($\sim 10^{-5}$) it was very difficult to set up a coincidence with the β's visually with an oscilloscope so the decision was made to leave it in singles mode. The signal from the detector preamplifier energy output is sent to an Ortec 451 shaping amplifier. The bipolar output pulse is input to a TC451 TSCA. The negative TSCA output acts as sole output to a 465 coincidence module whose output goes to the *Master Gate*, and to the C212 coincidence register (CAMAC N=3, A4), and to the "Singles Scaler" (CAMAC N=18, A5). The Unipolar output from the shaping amplifier goes to a 3512 ADC (CAMAC N=9) for energy information.

3.4.3.5 The HPGe Detector Electronics ($\beta\gamma$)

This detector system gathers information on the energy of the observed γ–ray, as well as the relative timing between the β and γ signals, which can be vital for removing random backgrounds. By use of the Fast Clear ADC system, the signals in the various plastic scintillators ($\beta1$,$\beta2$,ΔE, and E) are read out to facilitate data cuts and analysis on the gamma data. The electronics for the planar HPGe and the coaxial HPGe systems were identical. Only the coaxial HPGe, $\beta\gamma1$, system will be described in detail. The differences in the CAMAC module input numbers can be seen in Fig.

3.12. The signal from the timing output of the coaxial HPGe preamplifier is sent to an Ortec 454 timing filter amplifier (TFA). From here the signal is sent to an Ortec 473 CFD. One of the outputs from the CFD goes to a 465 coincidence module to be ANDed with the signal from the *Beta Trigger* to form the $\beta\gamma 1$ (coaxial) coincidence event. The output from the coincidence module goes to the *Master Trigger*, to the C212 coincidence register (CAMAC N=3, A0), and to the "Coincidence Scaler" (CAMAC N=19, A1). Another output from the CFD goes to the “stop” of the "Coincidence Timing" TDC (CAMAC N=6, A4). The energy output of the HPGe preamplifier goes to an Ortec 572 shaping amplifier. The unipolar output from the shaping amplifier is sent to a 3512 ADC (CAMAC N=10).

3.4.3.6 Coaxial — Planar HPGe Coincidence ($\gamma 1\gamma 2$)

The $\gamma\gamma$ [coaxial HPGe ($\gamma 1$)–planar HPGe ($\gamma 2$)] system was intended to detect cascades of γ-rays. It was intended to supplement the $\beta\gamma$ information by providing energy and timing information on the γ-rays observed in coincidence. The system begins at the CFD's for the TFAs used in the two $\beta\gamma$ systems described in Section 3.3.3.5. The outputs from each are sent to a 465 coincidence module to form the $\gamma 1\gamma 2$ coincidence event. The output of the the coincidence module is sent to the *Master Gate*, the C212 "Coincidence Register" (CAMAC N=3, A5), and to the "Coincidence Scaler" (CAMAC N=19, A6). The timing information is provided by the same system used for the $\beta\gamma$ timing in Section 3.3.3.5.

3.5 Data Acquisition System for the ^{18}N Parity Non-Conservation Feasibility Study

Since the SSB detectors produce very small signals (~μA) they are very susceptible to noise. Every effort is made to shield them from external noise sources. In addition to isolating the detector mounting itself the leads from the detectors to the preamplifiers are kept as short as possible, and the preamplifiers themselves are shielded and connected to a common ground.

A schematic of the electronic layout is shown in Fig. 3.21. The signal from the detector is sent to an Ortec 142B preamplifier. The timing output of the preamplifier is connected to a Tennelec 241 amplifier with 1 μs shaping time. The bipolar output is

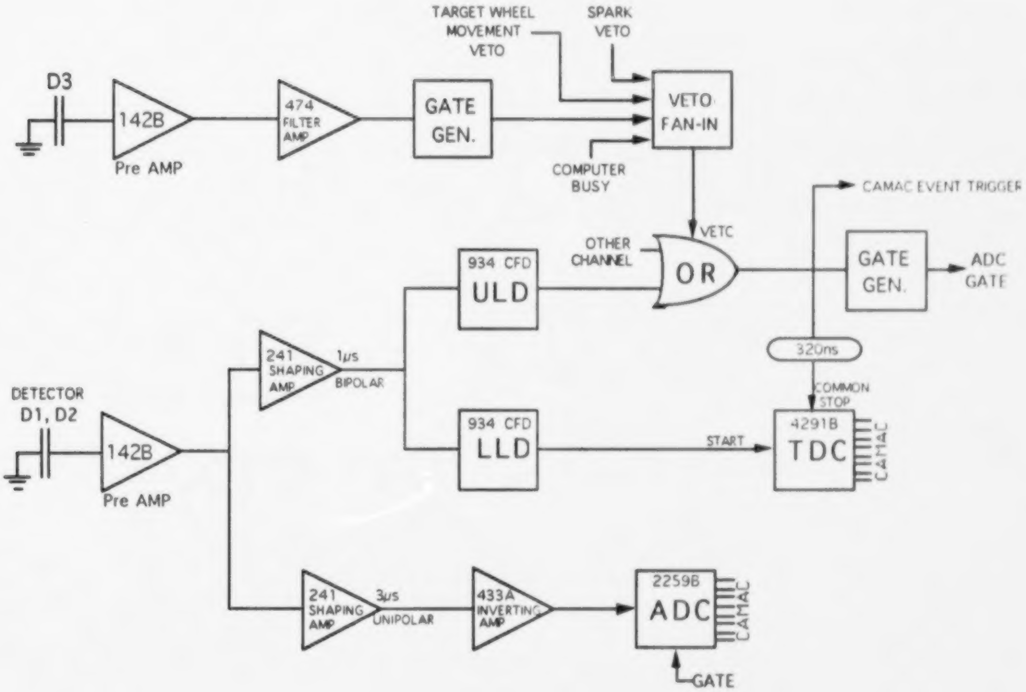
TARGET WHEEL MOVEMENT VETO
SPARK VETO
D3
142B
Pre AMP
474 FILTER AMP
GATE GEN.
VETO FAN-IN
COMPUTER BUSY
CAMAC EVENT TRIGGER
VETO
OTHER CHANNEL
OR
GATE GEN.
ADC GATE
934 CFD
ULD
241 SHAPING AMP
1μs BIPOLAR
320ns
COMMON STOP
DETECTOR D1, D2
142B
Pre AMP
934 CFD
LLD
START
4291B
TDC
CAMAC
241 SHAPING AMP
3μs UNIPOLAR
433A INVERTING AMP
2259B
ADC
CAMAC
GATE

Figure 3.21. The schematic of the electronics used for the ^{18}N study.

sent to a pair of Ortec 924 CFDs which provides lower level (LLD) and upper level discriminator (ULD) thresholds. The LLD is set to just below the noise threshold (50 keV) while the ULD is set to (300 keV). The signals from the ULD's are ORed together and the output is sent to an Ortec 222 G&D generator to furnish the ADC gate and the strobe for the C212 event trigger. The signal is also delayed and sent to the TDC to function as a common stop. Each LLD output is sent to the TDC to start the timing sequence. A pulser is also used to feed signals to each of the detectors simultaneously to monitor their gains on-line. A signal is sent to the C212 so pulser events can be identified in later analysis.

There are two possible vetoes attached to the master gate. The first is a "computer busy" veto which was set high during event processing. The second is a "wheel turn" veto which is set for the period of wheel motion plus 300 μs to allow the system to recover. Also at the end of the wheel rotation settling time the event clock is cleared and reset. The event clock marks each event with the time since the clock was last cleared.

The CAMAC system for the experiment consists of a C212 module, an Ortec 2259B (12 bit) ADC, and the LeCroy 4290 TDC system. Additional scalars to monitor rates are present as is an event clock. A much more detailed description can be found in [Pow95].

During the 1993 run two additional detectors were mounted behind detectors 1 and 2. These new detectors were very thick (500 μm and 2000 μm) and were useful in monitoring the ion beam intensity provided by the mass separator. Since they were sensitive to the β activity of the ^{16}N, they gave the operator immediate feedback on the effects of any changes to the tune of the beamline. The 500 μm detector was a SSB while the 2000 μm detector was a HPGe crystal purchased for use as a β–energy spectrometer.

Chapter 4: Decay of the Heavy Neon Isotopes

This chapter deals with the analysis of the data collected during the last experimental run in November 1992. Section 4.1 contains the history of the experiment which outlines the development of the experimental system and notes the important limitations which affected the overall quality of the data and subsequent analysis. Sections 4.2 to 4.4 describe the analysis methods as well as the details of difficulties which were encountered due to the poor quality of the data available. The beta decay of ^{25}Ne analysis is in Section 4.5. A comparison between the existing data [Goo73] and the present results is used as a check on the equipment and the calibrations of the detectors. Section 4.6 deals with the beta decay of ^{26}Ne. Section 4.7 contains the results obtained for the attempt to observe the beta decay of ^{27}Ne. In each of the analysis sections the γ-ray information obtained is presented first. Next, the branching ratios for the observed γ-rays are discussed followed by the experimentally determined half-life. Finally, the β endpoint energy results are reported.

The calibration information is included in Sections 3.3.1.3, 3.3.1.4 and 3.3.2.1. These sections describe in detail the energy and efficiency calibrations for the HPGe detectors and the energy calibration of the plastic scintillator telescope.

4.1 Experiment 597 Historic Overview

Experiment 597 had four proton beam running periods allocated to it. The first was a 24-hour run in July 1991. The second period was in December 1991 and lasted 48 hours. These two test runs were intended to optimize yields and detector arrangements. The final two runs were for data collection. The third run in January 1992 was 72 hours long. The final run of 120 hours duration was scheduled in November 1992.

The July 1991 run proved that the combination of the new, low-background experimental area and the utilization of $\beta\gamma$ coincidence electronics allowed for the clean observation of the ^{26}Ne γ–rays.

For the second run the DAS had evolved significantly towards the system described in Chapter 3. However, the tape drive system for the movable ion collection target was not available. Data taking was limited to a 1.5-hour period at the very end of the allocated beam time due to a combination of problems involving TISOL and the DAS. However, two significant advances occurred during this running period. In this run, the 151 keV γ–ray from the decay of ^{26}Ne, inferred in the decay scheme shown in [Duf87], was clearly identified, . In addition to the observation of the new γ–ray, the run marked the first time beam deflection was utilized to allow half-life information to be collected.

The January 1992 run utilized the DAS described in Chapter 3 and the tape drive system was available for the run. Unfortunately no useful data were collected because of two experimental difficulties encountered. The first problem was a vacuum leak in the tape system reel motor feed-through. This meant that the tape could not be moved without destroying the vacuum in the collection station and the ion beam line. The second difficulty was the existence of an unacceptably high level of ^{208}Rn^{8+} contamination which has nearly the same m/q setting as ^{26}Ne. ^{208}Rn has a half-life of 24 m and its daughter ^{208}At has a half-life of 98 m. The vacuum in the collection station was poor because there was no direct pumping on the collection station itself and the nearest pump was about 3 m away. This poor vacuum caused the ion beam to disperse as it entered the collection station so that deposition of activity was not confined to the tape. As the tape could not be moved without ruining the vacuum in the ion beam line it took only about an hour and half before the ^{26}Ne($\beta\gamma$)^{26}Na activity started to be overwhelmed by ^{208}At γ activity. The data collection in the December 1991 run had been relatively short, so the contamination problem had not been noticed. The January 1992 run also had the first attempt at setting up a $\gamma\gamma$ coincidence using a coaxial and a planar HPGe detectors. The planar detector turned out to be defective. Energy spectra collected using it indicated an energy resolutions that were more like that of a plastic scintillator than a HPGe device.

For the final run in November 1992 the vacuum leak problems with the tape drive were corrected and the vacuum improved by installing a cryo-pump directly to the collection station. There were additional changes in the detectors used in this run. The NE213 liquid scintillator was removed as it had shown no neutron events from ^{26}Ne, in the previous runs. In any case, the ^{3}He detector would provide more useful energy information on neutrons emitted from ^{27}Ne. The coaxial HPGe used in the previous three runs had been damaged and was unavailable. Scheduling problems also meant that the new high efficiency coaxial HPGe, now available at TRIUMF, was in use by another experimental group. Therefore, an older coaxial detector was substituted shortly before the run. The planar HPGe detector used in the third run was also replaced with the newly-repaired TISOL planar HPGe detector. As a result information obtained in understanding the detectors employed in earlier runs was not usable. As will become evident in the data analysis, the properties of the HPGe detectors used in the final run were not understood and measured as well as one would have liked because of time pressure before they were put into use. Since the thesis frequently refers to data collected by run number, table 4.1 gives a summary of the experimental runs during the final beam period along with a brief description of the purpose of the run.

Data collection was halted at the mid-point of the scheduled running period by the seizure of the feedthroughs on the tape drive reel motors. This problem was fixed quickly, but in the interim the tape controller developed an unrepairable fault. The experiment was terminated just as the last changes to the DAS were completed and more time was becoming available to study the data as it was collected on-line. No time was available to correct the problems which will be described in detail in Section 4.2.2.

Table 4.1. The run number and purpose for each of the runs in the November 1992 beam period.

Run Number	Purpose [Comments]
1 — 14	Off-line set up of electronics
15	^{25}Ne collection [problem Ge2 ADC]
22	^{25}Ne collection [low proton current]
24	^{26}Ne tuning [data not collected on tape]
25	^{133}Ba and ^{60}Co source calibration
26	^{26}Ne collection
28	^{26}Ne collection [tape dereeled, very short]
29	^{25}Ne collection [very short]
30	^{26}Ne collection
31	^{26}Ne collection
32	^{23}Ne collection [calibrate β–telescope]
33	^{23}Ne collection [adjust gain of Ge1 amplifier]
35	^{26}Ne collection [Ge1 now views $\leq$ 4 MeV]
37	^{133}Ba and ^{60}Co source calibration
38	^{26}Ne collection
39	^{8}He collection [calibrate β–telescope]
40	^{6}He collection [calibrate β–telescope]
41	^{92}Kr collection [calibrate β–telescope]
42	^{93}Kr collection [calibrate β–telescope]
43	^{27}Ne collection [mass 27?]
44	^{27}Ne collection [mass 27?]
45	^{27}Ne collection [tape drive failure]

4.1.1 Experimental Difficulties

In addition to the tape drive failure encountered during data collection two problems with the experimental set-up were discovered early in the offline data analysis. The first problem was in the $\beta\gamma$ coincidence timing circuits. One expects a broad peak in the time spectrum due to timing inaccuracies inherent to HPGe detectors. A sharp time peak was observed since, effectively, the same signal was used to both start and stop the TDC. Starting the TDC was the responsibility of the coincidence circuit. The signal which defined the coincidence time was the beta trigger signal. Unfortunately, this was also the signal sent to the TDC as a stop. This error meant that a powerful tools for removing background was not available. There had been evidence in previous runs that good timing information could significantly reduce the background and so the discovery of this error was disappointing.

The second problem was similar in nature. For the $\gamma\gamma$ coincidence circuit there is evidence that the timing circuitry was inappropriately set up. The gates were set too wide, resulting in too many random coincidences. Most of the data appeared to be random coincidences. Since two functioning HPGe detectors were available only in the last running period and there was very little time to test the electronics before the run, the system was not optimized before the experiment terminated. There may be good events in the data collected, but analysis was not been able to extract them from the much larger random background.

A partial solution to these problems, which allowed for a reasonably complete $\beta\gamma$ analysis to be carried out, was to look for the γ signal in coincidence with a β-ΔE–E event. Since all of the detectors were read out for any specific event trigger, this proved possible. Unfortunately, this method of analysis gives no information on the time relationship between the β-ΔE–E event and the γ–ray. An attempt was made to look for possible $\gamma\gamma$–ΔE–E events but such events are very rare and were indistinguishable from random background.

4.2 Gamma Ray Data Analysis

The γ-ray spectra to be analysed were generated by the NOVA analysis package [Gre91] from the data gathered by the DAS. A number of cuts were applied to the raw data. The first cut selected only those events with a ΔE–E trigger (see section 3.4.3.2). The next cut ensured that the event was a good ΔE–E event — that the ΔE signal was in a valid region (between 80 and 1300 keV), and that the time difference between the E and ΔE signal was also in a valid region (between 75 and 105 ns). The NOVA analysis program also checked that electrons which entered the HPGe detector were not counted by vetoing events with a signal in the beta paddle in front of the HPGe detector.

The RAW data (data for which no specific gate signal was required) spectra for both HPGe detectors were also analysed. For run 29 (^{25}Ne data) the effects of the cuts can be seen in Figs. 4.1 and 4.2 for the coaxial HPGe, Ge1, and the planar HPGe, Ge2, respectively. The RAW planar HPGe spectrum is relatively background-free, with only peaks associated with ^{25}Ne appearing in it. The ^{26}Ne spectra were similar in nature. For this reason, and because the statistical precision available from the RAW spectrum is much better than from the data after the cuts were applied, the RAW data were fit for the planar HPGe during the analysis. Comparison of results from the RAW data to those from the data with cuts applied also serves to check that the cuts have not effected the branching ratio.

4.2.1 Peak Fitting Procedures

A fitting package was developed based on the χ^2-minimization code MINUIT [Jam89]. MINUIT is a CERN Library program which varies the input parameters of a

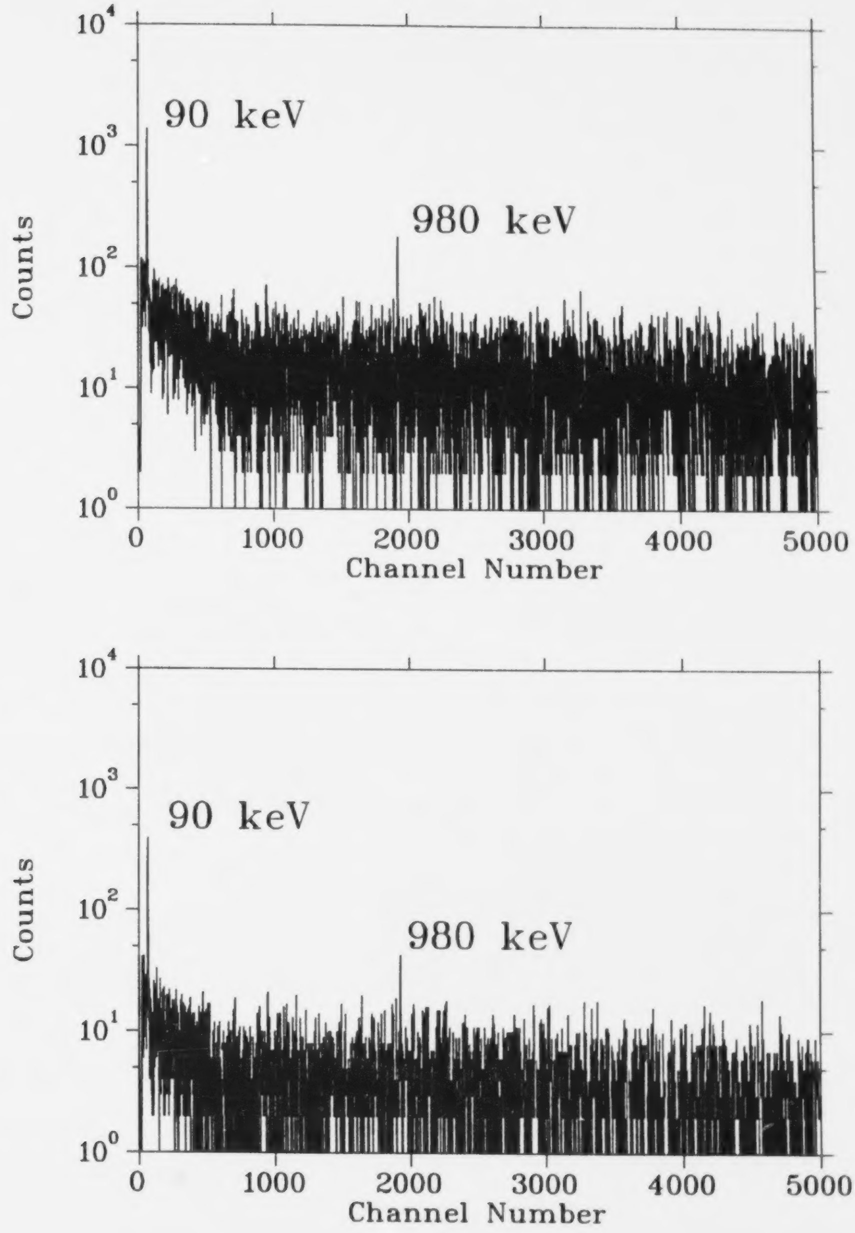

Figure 4.1. Spectra showing the effects of the cuts in the data analysis for the coaxial HPGe, Ge1. The top spectrum is the RAW data while the bottom spectrum shows those events which passed all levels of cuts. Data are from run 29 for ^{25}Ne.

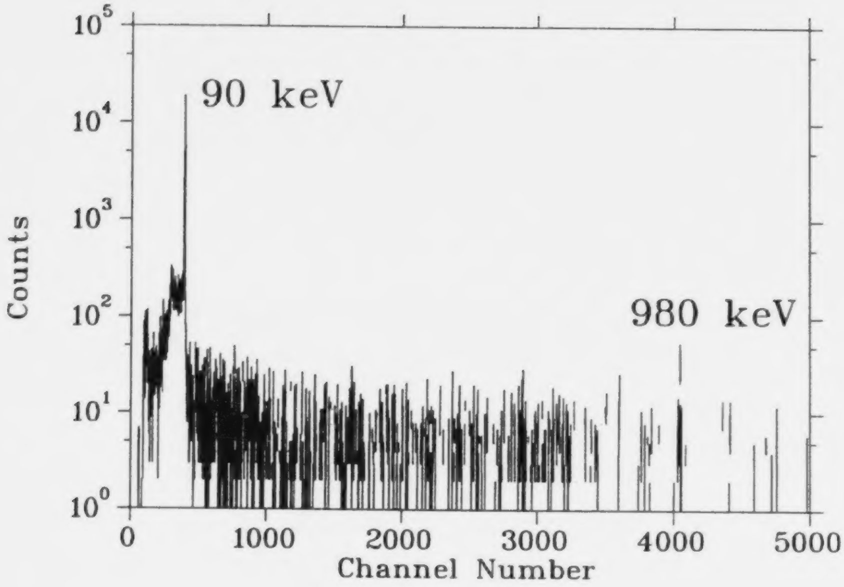

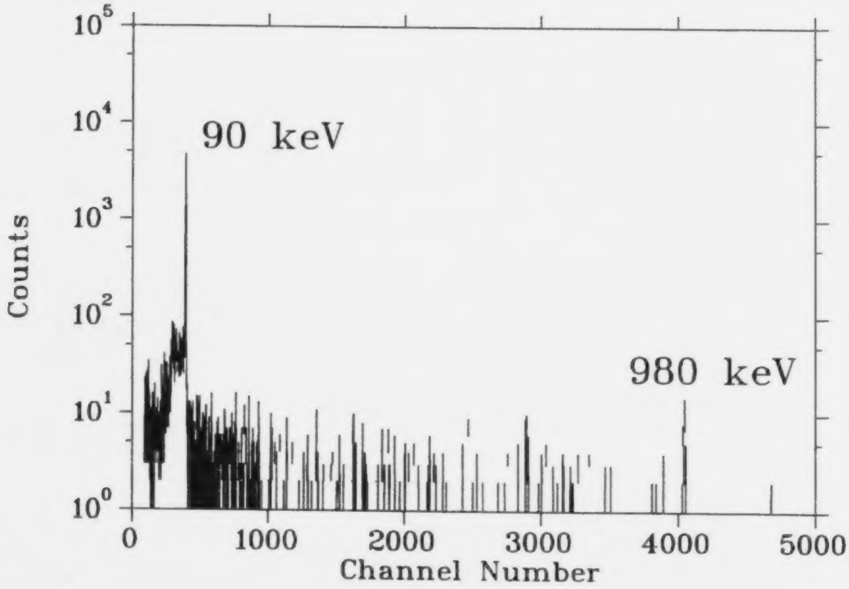

Figure 4.2. Spectra showing the effects of the cuts in the data analysis for the planar HPGe, Ge2. The top spectrum is the RAW data while the bottom spectrum shows those events which passed all levels of cuts. Data are from run 29 for ^{25}Ne.

user-defined function to achieve the lowest χ^2. The program, using the parameter values passed to it, calculates predictions which are then compared to the data. Additionally, the exact form of the χ^2 is user-defined. For the program developed to do peak fitting the standard definition of χ^2 was used

$$\chi^2 = \sum_{i=1}^{bins} \left(\frac{Observed\ Value - Fit}{Error\ in\ Observed} \right)_i^2 . \tag{4.1}$$

MUL_PEAKFIT is the program written for this analysis. It allows for the fitting of spectra with up to 10 gamma peaks in close proximity to one another. The form used for the shape of the peak was provided by the review article of Helmer and Lee [Hel80]. Based on the recommendations in the article the following form was adapted in the fitting.

$$FIT = BG_L + \sum_{npeaks} \left[BG_S + P_G + T_S + T_L \right] , \tag{4.2}$$

where BG_L is a linear background,

BG_S is a step function background associated with a particular gamma peak,

P_G is a normalized Gaussian function for the main part of the gamma peak,

T_S is a short range tail of the Gaussian peak, and

T_L is a long range tail of the Gaussian peak.

The linear background term is

$$L_B = a + bE + cE^2 , \tag{4.3}$$

where E is the energy, a is the intercept, b is the slope, and c is a possible quadratic term. Normally c is set to zero. The gaussian term for the peak is

$$P_G = \frac{N}{\sigma\sqrt{2\pi}} \exp\left[- \frac{(E-\mu)^2}{2\sigma^2} \right] , \tag{4.4}$$

where N is the total number of counts in the gaussian portion of the peak, μ is the gaussian centroid, and σ is its standard deviation. The step background associated with the gaussian term is

$$BG_S = 0.5\,N_S\,\mathrm{erfc}\left(\frac{E-\mu}{\sigma\sqrt{2}}\right), \tag{4.5}$$

where erfc is the complimentary error function and N_S is the normalization factor. This form of the step function background was chosen since it depended only on the parameters of the Gaussian peak (E, μ, σ) and thus added only one additional parameter to the fit. The short range tail term is

$$T_S = P_1\exp[-P_2(E-\mu)] \bullet \{1 - \exp[-P_3 \bullet (E-\mu)^2/2\sigma^2]\}, \tag{4.6}$$

where P_i are normalization and shape fitting parameters. This tail is limited to the energy region below the gaussian centroid, *i.e.* $E < \mu$.The long range tail term is

$$T_L = P_4 \bullet \exp[(E-\mu)/P_5] \bullet \mathrm{erfc}[(E-\mu)/\sqrt{2}\sigma P_6 + \sqrt{2}\sigma P_6/2P_5], \tag{4.7}$$

where P_i are normalization and shape fitting parameters. The short range tail is the same as is used by the commercial fitting program GAMANAL [Gun72] and the long range tail is the same as is used by the commercial fitting program HYPERMET [Phi76].

To analyse the calibration data (see Section 3.3.1.4) a modified version of the program was used where the single gaussian and two tail structure was replaced by a function with two pairs of gaussian peaks (for a total of four peaks). Each of the four peaks had the same σ. Each peak in a pair had the same height. The separation of the peaks was different for each pair, but both pairs had a common centroid. The common centroid is the same as what would have been obtained for a fit using a single peak.

During analysis of the Ne γ-energy spectra, structure was observed on the high energy side of the peaks in the planar HPGe data. To compensate for this the program was modified by the addition of another gaussian peak with the same σ as the main peak but shifted ahead of the centroid by a few keV. This secondary peak was probably due to a small amount 60 Hz noise in the electronic chain. As there did not appear to be a symmetric contribution on the other side of the main gaussian peak the effect of noise was not sinusoidal in nature. This structure was not observed in all peaks in a systematic manner. It had a contribution <10% of the main peak and introduces a small systematic error in the estimates of the peak centroid. This error is addressed again later.

4.3 Summary of the Half–life Analysis Techniques

Using NOVA, an event time spectrum was generated containing the time of each event after the arrival of the ion beam on-target. This was determined by feeding a scaler with a 10 kHz logical pulser and reading the scaler with each event. Using this spectrum and the fitting routine MINUIT, it was possible to fit the data to the expected growth and decay curves. In fitting the total β–decay data it was assumed that both the parent and daughter nuclei were present along with a constant background. It was unnecessary to include the effects of other contaminants, which indicates that any long-lived material present (*i.e.* ^{208}Ra and its daughters), was carried away by the tape and not deposited on the surfaces surrounding the collection point. The user-written function supplied to MINUIT fitted the data using two time intervals. The ***collection interval*** contains a ***background–only phase*** where there is only background activity (before the beam arrives on-target), plus a phase where the beam deposits radioactive material onto the tape. The ***background–only phase*** coincides with the physical time when the deflecting power supply was ramping-down from 10 kV to 0 volts.

A typical beam cycle is indicated in Fig. 3.2 The time point when the deflection power supply has dropped to zero, allowing the beam to hit the tape, is labelled t_o. The program was allowed to vary the parameter t_o (the average fit value was 246±37 ms). After this time the ion beam would pass through the collimator and reach the collection point. This meant that the time which corresponded to an event, t_{obs}, had to be adjusted by subtracting t_o when fits to the decay curves were made. The deflection of the ion beam away from the target was more rapid since the deflection element was located many meters from the collimator and it did not take much deflection to ensure that the ion beam did not pass through the slit in the collimator.

The time interval during which collection occurred, t_{coll}, was also allowed to vary. The time when collection stopped, $t_{stop} = t_o + t_{coll}$, was then determined. These times can be seen in relation to the collection and count cycles in Fig. 3.2. The relevant time for an event observed during the collection interval is t_1, the time since beam arrived on-target, and the relevant time for an event which is observed after the collection interval is t_2, the time since beam deflected off-target,

$$\begin{aligned} t_1 &= t_{obs} - t_o \ , \\ t_2 &= t_{obs} - t_{stop} \ . \end{aligned} \tag{4.8}$$

During the second phase of the first interval (*collection interval*) the parent (neon) activity was modelled with the formula

$$A_{Ne} = S(1 - \exp(-\lambda_{Ne} t_1) \ , \tag{4.9}$$

where S is the rate of deposition of the neon, and λ_{Ne} is the decay constant. The daughter (sodium) activity produced by the decaying parent (neon) was then included using

$$\begin{aligned} A_{Na} = S[&(1 - \exp(-\lambda_{Na} t_1)) + \\ &(\lambda_{Na}/(\lambda_{Na}-\lambda_{Ne}))(\exp(-\lambda_{Na} t_1) - \exp(-\lambda_{Ne} t_1))] \ , \end{aligned} \tag{4.10}$$

with λ_{Na} being the decay constant for sodium. S, λ_{Ne}, λ_{Na} were also allowed to vary during the fitting procedure.

After the collection period the beam was deflected and the decay curve was observed. In this pure decay interval the parent (neon) activity was modelled with the simple formula

$$A_{Ne} = \lambda_{Ne} N_o \exp(-\lambda_{Ne} t_2) \,, \tag{4.11}$$

where $N_o = (S/\lambda_{Ne})\,(1 - \exp(-\lambda_{Ne}\, t_{stop}))$. For the daughter (sodium) there is a more complicated expression

$$A_{Na} = (\lambda_{Ne}\, \lambda_{Na}\, N_o/(\lambda_{Na}\text{-}\lambda_{Ne}))[\exp(-\lambda_{Ne}\, t_2) - \exp(-\lambda_{Na}\, t_2)] + \lambda_{Na}\, n_o \exp(-\lambda_{Na}\, t_2) \,, \tag{4.12}$$

where $n_o = (S/\lambda_{Na})\,[(1 - \exp(-\lambda_{Na}\, t_{stop})) + (\lambda_{Na}/\,(\lambda_{Na} - \lambda_{Ne}))(\exp(-\lambda_{Na}\, t_{stop}) - \exp(\lambda_{Ne} t_{stop}))]$. The first term in eq. 4.12 is for the decay of the daughter (sodium) activity produced during the decay of the parent (neon). The second term is for the decay of the daughter (sodium) activity produced during the collection phase. In either case N_o and n_o represent the number of parent or daughter atoms available to decay at the beam-off time, respectively.

Two refinements were made to the fitting procedure in defining the relevant χ^2 function. The first was to incorporate the existing data for the half-life of the daughter and its error into the χ^2 calculation. This immediately constrained the solution near to physical values of λ_{Na}. The second was to employ the knowledge of the intended total collection time as input into the NIM scalar gate module, T_{stop}, to the sum of the t_o and t_{coll}. The final χ^2 value was then evaluated as

$$\chi^2 = \sum_{\text{ndata}} \frac{(obs - fit)^2}{\Delta obs^2} + \frac{(t_{1/2}(^{26}Na) - fitted\,[t_{1/2}(^{26}Na)])^2}{[\Delta t_{1/2}(^{26}Na)]^2} + \frac{(T_{stop} - (t_o + t_{coll}))^2}{(1/120\text{ s})^2} \,, \tag{4.13}$$

where *obs* are the counts observed in the time interval, *fit* are the corresponding counts determined by the fitting procedure, and $\Delta t_{1/2}$ is the error in the existing value for the half-life of the daughter. The value of 1/120 s in the denominator of the third term is a pessimistic estimate of the possible error in the scaler gate which provided the collection/count timing.

Although the discussion above used the elements Ne (parent) and Na (daughter), the formulae are generally applicable to any parent and daughter isotopes. To give an illustration of the results of the program, the various components of a decay curve are illustrated in Fig. 4.3 for the ^{8}He(β)^{8}Li decay. The figure shows the total fit and the three components corresponding to the growth and decay of the parent and daughter activity as described above. The pure ^{8}He (parent) activity, labeled 1, can be seen to grow and then decay exponentially. There are three components of ^{8}Li (daughter) decay. The earliest term, labeled 2, corresponds to ^{8}Li activity which was produced during the collection period by the decay of the ^{8}He being deposited at the target. This curve also has a contribution (labeled 3) corresponding to the decay of the surviving of ^{8}Li after the collection period. The later ^{8}Li curve, labeled 4, is the activity of the ^{8}Li produced by the decay of the ^{8}He remaining after the ion beam was deflected off-target.

The γ–ray half-lives were easier to fit since only the parent activity must be included — any daughter activity occurs at a different energy and can be eliminated. Only two formulae were necessary. The growth was defined by

$$A_{Ne} = S(1 - \exp(-\lambda_{Ne} t_1) \, , \tag{4.14}$$

and the decay was defined by:

$$A_{Ne} = \lambda_{Ne} N_o \exp(-\lambda_{Ne} t_2) \, , \tag{4.15}$$

where the symbols are as previously defined. For γ–ray fitting a similar adjustment to the definition of χ^2 was made with the exception that the second term with the daughter's half-life was irrelevant.

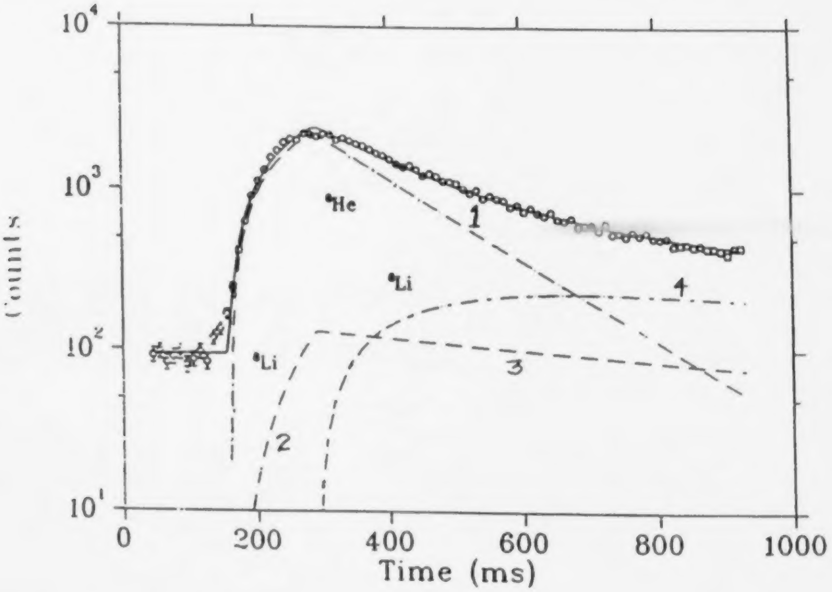

Figure 4.3. The decay ^{8}He(β)^{8}Li. The total fit to the data is shown as a solid line. The various growth/decay components described in the text are indicated by broken lines. The growth and decay of ^{8}He is indicated by [— · —] and labeled 1. The ^{8}Li produced during the deposition is indicated by [— —] and labeled 2 and 3. The ^{8}Li produced during the decay of ^{8}He after the ion beam has been redeflected is indicated by [— - —] and labeled 4.

4.4 Summary of the Beta Spectrum Analysis Techniques

The goal of this analysis was to determine the maximum allowed beta energy for the decay, Q_β. To accomplish this, the program DECAYFIT was written. The program used the routine MINUIT to fit the data from the thick E scintillator to the spectral shape given by eq. 2.3. This same program had been used to calibrate the thick E scintillator (see Section 3.3.2.1), except that in this case the determination of the β–endpoint was the goal of the fit.

The following procedure was used to fit the data. The calibration, derived in Section 3.3.2.1, was used to convert ADC channel to observed energy which was then corrected for the energy loss in the plastic scintillator as described in eq. 3.22. The fitting program then calculated the expected theoretical shape (using the energy terms of eq. 2.3). To simulate the detector response the program convoluted the theoretical shape with a gaussian resolution function whose width was given by $A + B\sqrt{Energy}$. The values of A and B were determined during the calibration (see Section 3.3.2.1). The effect of including a low energy tail in the resolution function was tested and found to have negligible effect on the fits (except to greatly increase the time needed for the fitting procedure). The normalized, convoluted, theoretical shape function was then multiplied by the observed number of counts. To generate the final fit function this was then multiplied by an additional scaling term. The scaling term was introduced to help the fit compensate for effects such as backscattering and loss of particles out of the sides of the detector before they deposit their full energy. When the theoretical shape is a good approximation to the shape of the spectrum this additional scaling term should be close to unity. If its value became >1.5 then the shape of the spectrum was inconsistent with the simple assumptions of the fit (a single decay curve and simple background) and the validity of the fit is suspect. The value of Q_β , a linear background term, and the additional scaling term were allowed to vary during the fit.

4.5 The ^{25}Ne(β)^{25}Na Reaction

The experimental results of this experiment for ^{25}Ne are compared to existing data in this section. Particular attention is paid to the branching ratios of the observed γ-rays, the half-life of the decay, and the β–endpoint energy. The results obtained for ^{25}Ne provide a check to ensure the analysis is correct. Two runs were analysed, Run 22 (total length 10 218 s) and Run 29 (total length 1 983 s).

The cycle for isotope collection and decay observation was the same in each run. The beam was on the collection target for 1800 msec, it was then deflected away and the decay was observed for an additional 2000 ms. Finally, the tape was moved for 900 msec and the cycle repeated. The data acquisition was disabled during the tape movement. An improved experimental technique would incorporate the collection of background data during this time since this proved to be a weak point in the analysis.

4.5.1 ^{25}Ne(β)^{25}Na Gamma Ray Energies and Branching Ratios

The known γ-rays emitted by the ^{25}Ne(β)^{25}Na reaction are listed in Table 4.2 along with their expected intensities [Reu83]. This experiment is able to produce results for only the strongest decays — the 90 keV and 980 keV γ-rays due to the relatively low number of events collected.

The observed γ-ray transitions are listed in Table 4.3, which gives the fitted centroid energies and the standard deviation of the peaks. The values should be compared with the values from [Goo73] of 89.5 ± 0.1 keV and 979.8 ± 0.2 keV. The agreement is within error for the observed 89.7 ± 0.3 keV γ–ray. The higher energy γ–ray at 981.4 ± 0.8 keV does not agree with [Goo73] within our estimated error, which was taken from the sample fluctuation of the various measurements. If the energy calibration uncertainty is included, ±1 keV at 980 keV, the agreement seems reasonable.

Systematic error in the peak determination is difficult to estimate. The fits are only slightly biased (estimate ±0.2 keV) by the structure in the peaks mentioned earlier. More seriously, the spectra have what appears to be a non-statistical behaviour (point-to point fluctuations are too large) which was not noticed during data collection and cannot be explained or corrected. The energies from the coaxial HPGe (Ge1) are uniformly high, indicating a possible systematic error in the energy calibration. The magnitude of the deviation from [Goo73] increases with increasing γ–ray energy from 0.3 keV at 89.7 keV to 1.6 keV at 981.4 keV.

Table 4.2. The intensities of the known γ-rays from the decay $^{25}\mathrm{Ne}(\beta)^{25}\mathrm{Na}$ [Reu83].

Energy [keV]	Intensity [γ's/100 decays]
89.5	95.5
979.8	18.1
1069.3	2.0
1132.8	0.6
2112.5	0.5
2202.1	1.2
3598.	0.2
3687.	1.0

The deviation of the planar HPGe (Ge2) from [Goo73] is at low energy in the energy region where the linear fit value deviated the most from the expected energy (see Fig. 3.12). This deviation was explained in Section 3.3.1.4 as resulting form the superposition of two γ-rays in the decay of ^{133}Ba, but is small compared to the apparent discrepancies noted here. The magnitude of the deviation of the fitted γ–ray from the known energy of ^{25}Ne is indicative of the systematic error in energy determination (< 1 keV at 89 keV and about 2 keV at 980 keV).

Table 4.3 The results of the fits for the energy of the observed γ-rays from ^{25}Ne.

Run	Detector	Energy [keV]	σ [keV]
22	Ge1	90.30	0.69
	Ge1	982.40	0.68
	Ge2	89.10	0.32
	Ge2†	979.82	0.94
29	Ge1	90.12	0.67
	Ge1	982.03	0.84
	Ge2	89.19	0.33
	Ge2†	—	—‡
	Sample Error and	89.7 ± 0.3	
	Error of the Mean	981.4 ± 0.8	

† Fit is in region where χ^2 fitting procedure is not valid due to too few counts in peak.

‡ Value is at limit of allowed range in MINUIT — no valid error can be generated.

The spectra with their fits can be found in Fig. 4.4, and Fig. 4.5. The shape of the peaks were fit reasonably well by the program MUL_PEAKFIT but the overall χ^2 was poor. The background region was hard to fit as can be seen in Figs 4.4 (b,c) and 4.5 (b,c). This contributed to the large χ^2/DOF values.

The calculations for the intensities based on the fit results are shown in Table 4.4. The transmission was calculated assuming 1.5 mm of scintillator and 1.5 mm of aluminium between the collection point and the detector. The absorption coefficient is calculated as described in Appendix 2. The efficiency was calculated using the formula (eq. 3.17) given in Section 3.3.1.4. The efficiency used is a relative value and is from the *far point* data collected in the calibration experiment. The use of the relative efficiency is justified since the interesting quantity to be calculated is the ratio of the number of observed 980 keV γ–rays to the 90 keV γ–rays so the geometric efficiency, which is unaffected by the γ–ray energy, will cancel. Therefore it is not necessary to use the scaled efficiency calculated from the incomplete measurements at the *tape position.*

In [Goo73] the intensity of the 90 keV γ–ray was measured to be 95.5±0.6% while the intensity of the 980 keV γ–ray was measured to be 18.1±1.9%. This gives an expected ratio of the 980 keV γ–ray to the 90 keV γ–ray of 0.19±0.02. To compare with these results the relative intensity ratio between the 980 keV transition and the 90 keV transition was calculated using

$$R = \frac{N_{obs}(E\ 980)}{N_{obs}(E\ 90)} \frac{T(E\ 90)}{T(E\ 980)} \frac{E_{ff}(E\ 90)}{E_{ff}(E\ 980)} \quad , \qquad (4.16)$$

where $N_{obs}(Ei)$ is the observed counts at energy Ei,

$E_{ff}(Ei) = E_i^a\, 10^b$ is the *far point* efficiency at energy Ei,

a, b are the slope and intercept of the relative efficiency calibration respectively,

and $T(Ei)$ is the transmission of γ's at energy Ei.

Table 4.4. The intensity of the observed γ-rays along with the information used to calculate the intensities. The relative efficiency (ε_{ff}) for both detectors is adjusted for the low energy drop off by using the measured value of the far point efficiency at 81 keV. Note: the error in the number of counts is probably underestimated, but no better value is available.

Run	Detector	Energy [keV]	Observed Counts	χ^2/DOF	Relative ε_{ff}	Trans $T(E_\gamma)$	Intensity†
22	1	90	1953±44	2.31	2.9E-03	0.91	100
	1	980	214±16	1.95	2.4E-04	0.97	124 ± 22
	2	90	18034±134	3.03	1.9E-04	0.91	100
	2	980	53±7	—‡	5.6E-06	0.97	9 ± 3
29	1	90	1709±41	4.38	2.9E-03	0.91	100
	1	980	179±13	2.35	2.4E-04	0.97	119 ± 21
	2	90	16291±128	4.18	1.9E-04	0.91	100
	2	980	90±9	—‡	5.6E-06	0.97	18 ± 6

† Normalized to the 90 keV peak for each detector.

‡ No fit was done; all of the counts in the region 970 keV to 985 keV were added together from the data.

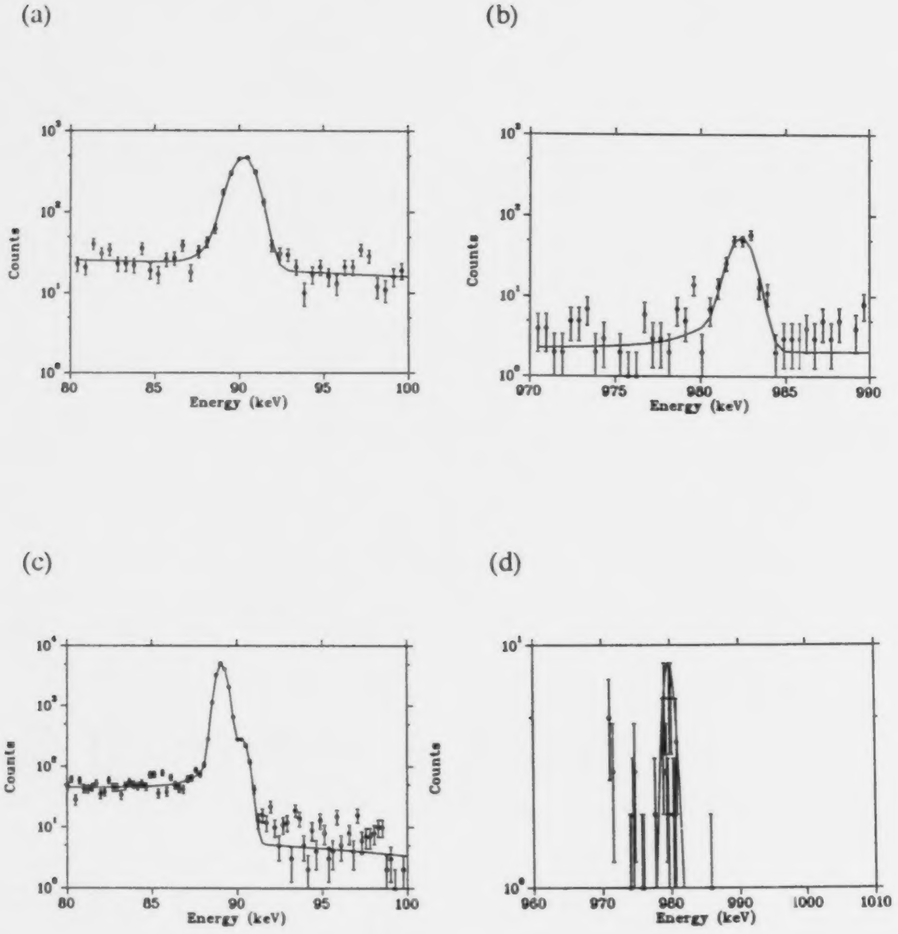

Figure 4.4. The fit to the data for the 90 and 980 keV γ-rays from run 22. The upper pair (a,b) is from the coaxial HPGe, Ge1, while the lower pair (c,d) is from the planar HPGe, Ge2.

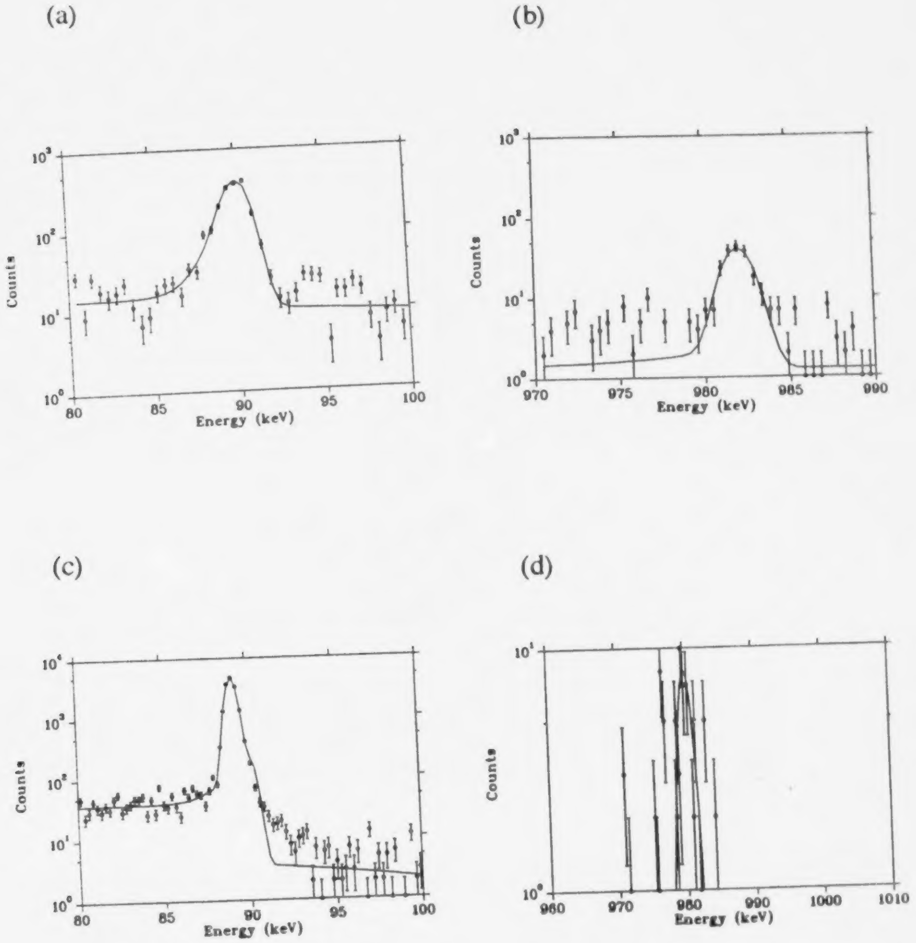

Figure 4.5. The fit to the data for the 90 and 980 keV γ-rays from run 29. The upper pair (a,b) is from the coaxial HPGe, Ge1, while the lower pair (c,d) is from the planar HPGe, Ge2.

The error in the relative intensity ratio was determined with the formula

$$\frac{\Delta R}{R} = \left[\left(\frac{\Delta N_{obs}(Ei)}{N_{obs}(Ei)} \right)^2_{i=1,2} + \left(\frac{\Delta T(Ei)}{T(Ei)} \right)^2_{i=1,2} + \left(\ln(980)\,\Delta a \right)^2 + \left(\ln(10)\,\Delta b \right)^2 + \left(\frac{\Delta E_{ff}(90)}{E_{ff}(90)} \right)^2 \right]^{\frac{1}{2}} \tag{4.17}$$

The results for the intensity ratio from runs 22 and 29, and for both HPGe detectors, are given in Table 4.5. In determining the error it is assumed that the error in the transmission are very small (<<4%) and thus can be ignored. The error in the observed counts is the square root of the number of counts in the sum of the components of the MUL_PEAKFIT fitting. Given the poor quality of the fits, this is likely an under-estimate. The value for the efficiency at 90 keV used in the calculations for both Tables 4.4 and 4.5 is the measured detector efficiency at 81 keV (see Section 3.3.1.4). The energy dependence of the efficiency between the 90 keV and 80 keV is almost flat, given the expected fall off shown in Fig. 4.6.

Table 4.5. The results for the relative intensity ratio of the 980 keV peak to the 90 keV peak for both HPGe detectors and the comparison with the expected value [Goo73].

Run	Detector	Expected Ratio ±0.02	Observed Ratio
22	Ge1 [coaxial]	0.19	1.24±0.22
	Ge2 [planar]	0.19	0.09±0.03
29	Ge1 [coaxial]	0.19	1.19±0.21
	Ge2 [planar]	0.19	0.18±0.06
	Weighted Average		0.14 ± 0.03

Although the weighted average for the intensity ratio is reasonable, a problem is obvious for data involving the coaxial HPGe Ge1 detector. The determined intensity ratio is > 1, which is totally inconsistent with existing results even though the statistical error is large.

The possibility that the error in the intensity ratio was caused by an error in the efficiency prompted further investigation into the low energy properties of HPGe detectors and revealed that below about 100 keV the efficiency is no longer linear. The efficiency curve for a typical 15% Canberra coaxial HPGe detector is illustrated in Fig. 4.6. HPGe detectors are rated by their detection efficiency compared to a 3"x3" NaI detector, so a 15% detector is one that has 15% of the efficiency of a standard NaI detector for the ^{60}Co 1.33 MeV γ-ray. The coaxial HPGe detector in this work was probably only a 10% detector (the specification sheets have been lost and detailed information on the detector is not available), but the shape of the curve is expected to be similar. It is clear from Fig. 4.6 that the efficiency begins to fall off near 100 keV.

For HPGe detectors the photopeak efficiency decreases with increasing photon energy since it becomes less likely that all of the energy of the photon will be collected. For $E_\gamma < 120$ keV the HPGe detector will almost always collect all the energy of the photon so the efficiency should then become constant. Further complications are introduced when dealing with very low energy γ–rays. The coaxial detector has a 700 μm dead layer which causes the efficiency to decrease as the low energy photons are absorbed before reaching the active volume. This is not as much of a problem in the case of the planar HPGe since the dead layer is thinner. Both detectors also have a thin Be window, but for the energies of interest to this work, the transmission through this window is essentially 100%. To determine the efficiency of either HPGe at 90 keV for use in Tables 4.4 and 4.5 it is assumed that the efficiency is constant and is equal to the measured value at 81 keV from a ^{133}Ba source (see Section 3.3.1.4).

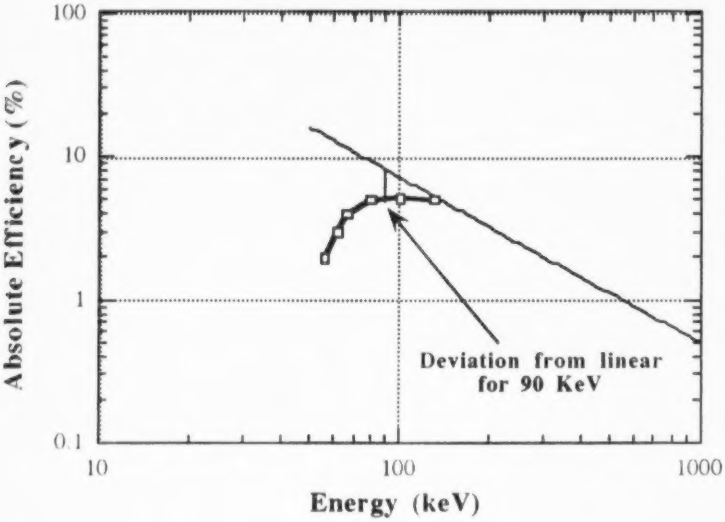

Figure 4.6. The efficiency for a typical 15% Canberra HPGe detector. The solid line indicates the efficiency fit to data above 200 keV. The squares are measured efficiency in the region where the detector has a non linear response. The deviation at low energy from the linear fit is clearly visible. NOTE: All data points are estimated from a graph published in the Canberra catalogue (ninth edition).

The planar HPGe detector has a number of important factors to be considered when interpreting the relative branching ratios given in Table 4.5. This detector was chosen because it has excellent energy resolution and reasonable efficiency for the low energy γ-rays expected in ^{26}Ne. This type of detector is intended for observation of low energy γ–(<80 keV) and X-rays. The 980 keV γ-ray is an order of magnitude above the energy the detector is intended to observe, as is clearly indicated by the efficiency curve (see Section 3.3.1.4, Fig. 14). The detector has an efficiency of 5.6 x 10^{-6} for the 980 keV γ-rays while for the 90 keV γ-ray the efficiency is 2.1 x 10^{-4}. This leads to a huge imbalance in the number of observed events, with 16K at 90 keV compared to 80 events at 980 keV. The poor statistics of the observed 980 keV events,

<100 in either run, thus make an accurate determination of the relative intensity ratio for ^{25}Ne difficult.

The thin crystal of the planar detector also has a sizable low energy tail (very clear in the fits) for the high energy γ's. There were insufficient counts in the 980 keV peak during either run to perform a MINUIT fit similar to what was done for the 90 keV peak. Examining Figs 4.4(d) and 4.5(d) reveals that the region around the peak is very clean with no background. As the detector is thin, a number of the γ-rays will be observed with less than their full energy. It is therefore reasonable to assume that all the events in the region 970 keV to 985 keV are from the decay of ^{25}Ne. This sum is number of observed events used in Table 4.3.

The number of counts observed in the coaxial HPGe (Ge1) was small compared to the planar HPGe (Ge2) for the energies of interest to the ^{26}Ne investigation. This is contrary to what would be expected from the efficiency calibration done before the experiment using a different electronic setup. The results for the calibration for the coaxial HPGe (Ge1), when scaled to correct for geometry, indicate a similar efficiency to the measured value for the planar HPGe (Ge2) in the tape position. The overall efficiency of the coaxial HPGe (Ge1) is not understood even though the energy dependence of the *far point* efficiency measurements seems reasonable (the slope being similar to what is published by Canberra, compare Figs. 4.6 and Fig. 3.14) and the ratio of the ^{60}Co data from the *far point* and *tape* position is stable for the limited data available.

One of the most important checks on the analysis procedure and the efficiency calibration is the relative intensity ratio between the 980 keV and the 90 keV γ-ray. It is clear that for the coaxial HPGe (Ge1) there is no agreement with the previous measurement. This indicates that not all of the properties of this detector and possible its associated electronics chain were well understood. Although postulating small errors in the efficiency calibration process is reasonable, the change in the efficiency that would be required to bring the intensity ratio in line with the results of [Goo73], a factor of 5.5, is very clearly not. There is reasonable agreement between the run 29 results for the planar HPGe detector (Ge2) and the previous measurement.

Some other facts are indicated by closer examination of Fig. 4.5. There are lower levels of background found in the planar HPGe (Ge2) as compared to that observed for the coaxial HPGe (Ge1). The planar HPGe (Ge2) detector also has a much better energy resolution.

Based on all of the above observations, it was decided that only the planar HPGe (Ge2) would be used for determining branching ratios in the ^{26}Ne investigation. The fact that the intensity ratio for the coaxial HPGe (Ge1) is in error strongly effects this decision. The coaxial HPGe (Ge1) was still useful for determining γ-ray energy and searching for previously unobserved high energy γ-rays.

4.5.2 ^{25}Ne(β)^{25}Na Half–life

The half-life of the ^{25}Ne(β)^{25}Na decay was obtained both from the β– and γ–decay spectra. For the beta decay, a time spectrum for every valid ΔE–E event was incremented, thereby generating the growth and decay curve. For the γ–rays, a window was set around each of the 90 and 980 keV γ–ray peaks and similar time spectra were generated. The spectra for the β–decay half-life obtained in runs 22 and 29 are shown in Fig. 4.7. The spectra for the half-life from the 90 keV γ–ray from the planar HPGe for runs 22 and 29 are shown in Fig. 4.8. Although half-life data were collected with the coaxial HPGe, there were insufficient counts per channel to allow reliable fitting to be performed.

The half-life results and their errors are shown in Table 4.6. There is marginally acceptable internal agreement between the observed values of the half-life from both β and γ decays, but good agreement with the accepted value of 602±8 ms [End90]. This is shown graphically in Fig. 4.9. The sample average and standard error of the mean of all the data [604 ± 15 ms] is used as the result from this experiment because of the marginal internal consistency. The fits can be affected by fluctuations in the proton beam intensity during the collection phase. This introduces a small, but unknown systematic error which can only be estimated from run-to-run fluctuations. There is also good agreement with the accepted value of the half-life of ^{25}Na (59.1 ± 0.6 s) [End90] although this is expected since the accepted value was included in the fit.

Table 4.6. The results for the half-life of $^{25}\text{Ne}(\beta)^{25}\text{Na}$ from both β and γ decays.

Run	Detector	^{25}Ne Half-life [ms]	^{25}Na Half-life [ms] ±50 ms	χ^2 for fit	χ^2 /DOF for fit
22	Beta	569 ± 9	59 102	368.4	1.16
	Ge2	641 ± 7	—	173.9	2.29
29	Beta	595 ± 15	59 102	339.5	1.07
	Ge2	609 ± 13	—	193.9	2.52
Sample average ± SEOM		604 ± 15			

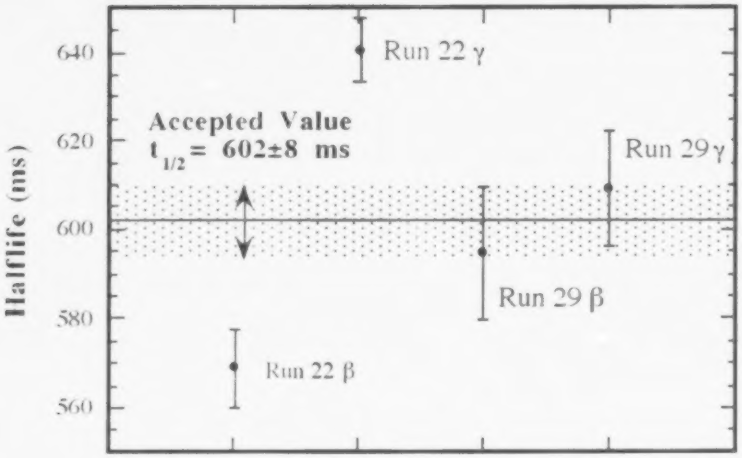

Figure 4.9. The comparison between the observed half-lives of $^{25}Ne(\beta)^{25}Na$ for the different runs and detectors and with the previous work [End90].

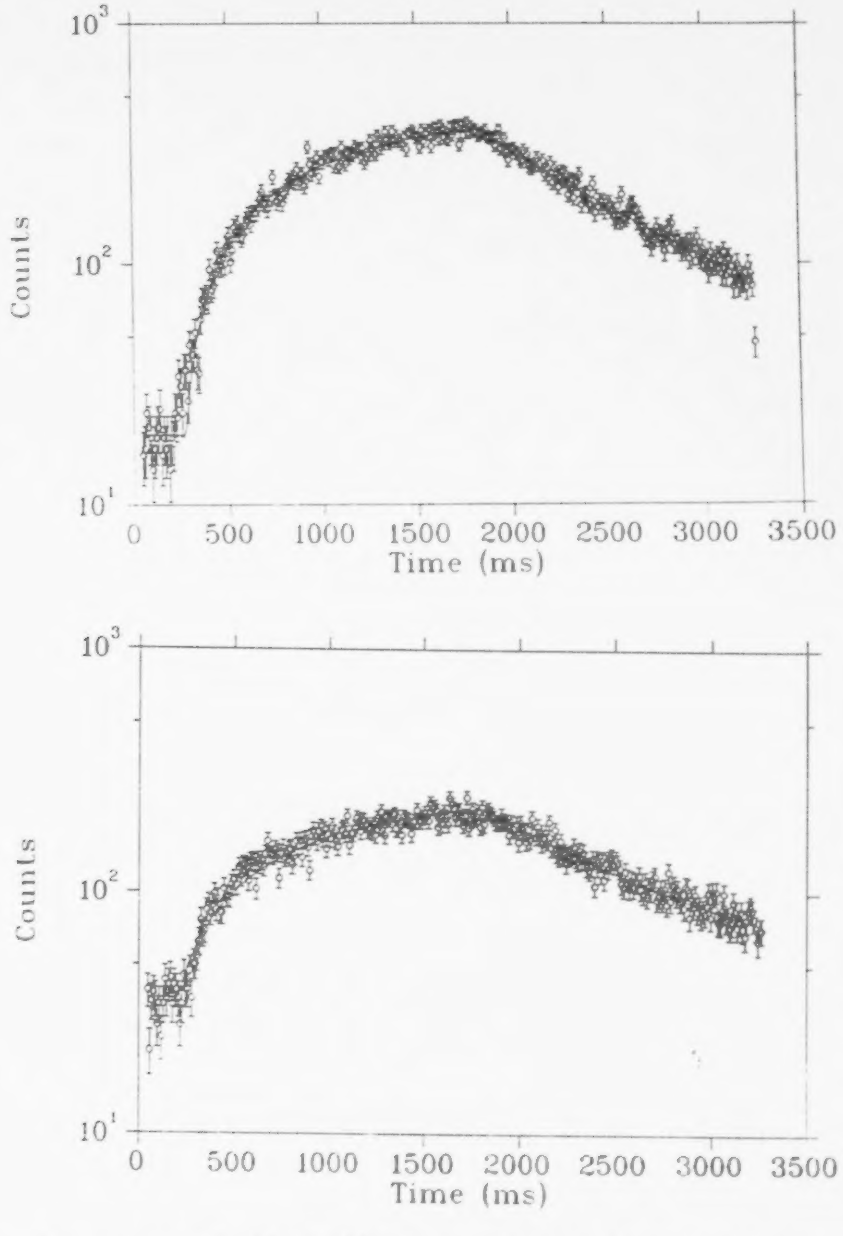

Figure 4.7. The fit to the ^{25}Ne(β)^{25}Na β–decay half-life determined by the event time of the ΔE–E events. The upper spectrum is for run 22 while the lower is for run 29.

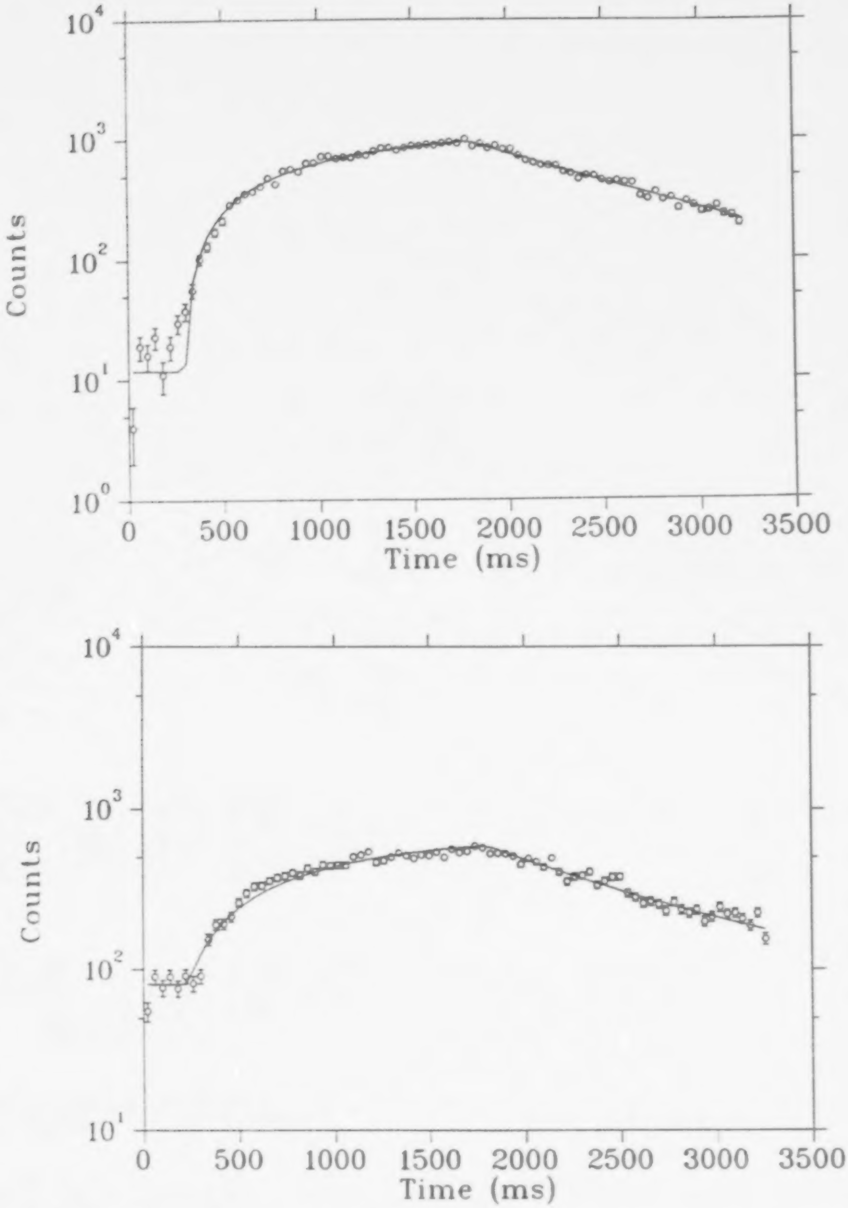

Figure 4.8. The ^{25}Ne(β)^{25}Na half-life fits to the 90 keV γ- ray peak for the planar HPGe (Ge2) from both runs. The upper spectrum is for run 22 while the lower is for run 29.

4.5.3 ^{25}Ne(β)^{25}Na Beta Energy Endpoint

An estimate of the ^{25}Ne β-energy endpoint, Q_β, was found using the simple program DECAYFIT . The determination of the β-energy endpoint is seriously hampered because the β-energy data is cut off at 5 MeV due to the saturation of the ADC (see Section 3.3.2.1). This requires the fitting procedure to make a large extrapolation to the known endpoint at 7.3 MeV. Fig. 4.10 shows the results from DECAYFIT for runs 22 and 29. The value of Q_β for each run is given in the top half of Table 4.7. The present value is in better agreement with the existing data [Goo73] than at first it might appear (5.9 MeV compared to 7.3 MeV). There are two dominant decay branches in ^{25}Ne(β)^{25}Na. The strongest is to the 90 keV level and has a measured beta transition energy of 7.3 ± 0.3 MeV [Goo73] while the second is to the 1.07 MeV level which has a measured transition energy of 6.3 ± 0.3 MeV [Goo73]. The program assumes that there is only one possible decay branch and a flat background. Effectively it treats the superposition as a lower transition energy decay curve on top of a flat background provided by the second decay. For this simple hypothesis the fit is biased towards the transition energy of 6.3 MeV because the high energy end of the spectrum was not recorded. The proper comparison to make with the 5.9 MeV fitted endpoint energy for the decay is some average of the two values 7.3 and 6.3 MeV, the 1.07 MeV level having more weight than normal. The errors for the endpoint from the fitting program were unrealistically small due to the simplistic nature of the fit. Based on an estimated resolution of 0.5 MeV for a plastic scintillator and a mono-energetic 5.9 MeV electron beam, and the observed uncertainty of the calibration fit to ^{6}He (see Section 3.3.2.1), one might expect that the error in the fit to the endpoint would be about 300 keV. Systematic error due to the simplistic assumptions could be larger. No good estimate is available. There is an additional systematic error in the endpoint of about 300 keV introduced by the energy calibration. Given the large overall uncertainty, the usefulness of these data is questionable.

Table 4.7. The results of the fits to the observed β–decay energy spectra to determine the endpoint energy. The first half of the table contains the data from the computer fit. In the second half the data from the Kurie plots is shown. HER stands for High Energy Region, T_e>3.5 MeV. The two numbers in the existing data column indicate the expected energy in the decay to the 90 keV (1070 keV) energy levels [Goo73].

Run	Q_β [MeV]	χ^2	χ^2/DOF	Existing Data [MeV]	$\text{Log}_{10} ft$
22	5.9	629	1.05	7.3 (6.3)	4.63±0.18
29	5.9	587	0.98	7.3 (6.3)	
22	6.4 ± 0.2	180	1.24	6.3 ± 0.3	4.82 ± 0.07
22 (HER)	6.8 ± 0.4	78	1.00	7.3 ± 0.3	4.30 ± 0.13
29	6.5 ± 0.2	116	0.99	6.3 ± 0.3	4.85 ± 0.07
29 (HER)	6.8 ± 0.4	50	0.82	7.3 ± 0.3	4.30 ± 0.13

As a further method to determine the endpoint energy, Kurie plots were generated for each of the runs using data for energies greater than 2.5 MeV (see Fig. 4.11) and fits were made. The results are also shown in Table 4.7. The values (labelled 22 and 29) obtained are also more consistent with a transition to the 1.07 MeV level. To further check the assumption that the discrepancy arises from the different endpoint energies of the two decays the data was re-fit and replotted, but this time for energies above 3.5 MeV (see Fig. 4.12). The new fits (22HER and 29HER) give higher values for Q_β that just agree within errors with the previous measurement [Goo73] for the expected transition to the 90 keV level. This indicates that the assumption made about the decays to two levels was reasonable. Without the endpoint visible in the data a more precise value for Q_β for either transition is hard to achieve. The errors quoted for Q_β in the second half of Table 4.7 are calculated from the errors in the slope and intercept of the linear fit, but clearly there are large systematic errors. The 300-400 keV difference between the Q_β values achieved by varying the energy regions in the fit is a reasonable estimate of the systematic error.. Again a 300 keV scale uncertainty from the calibration should be included as an additional systematic error. The overall uncertainty for the value of Q_β is dominated by systematic errors.

Combining the data in this section with the value for the half-life in section 4.4.2 allows for the calculation of the log *ft* value for the decays. They are given in the final column of Table 4.7.

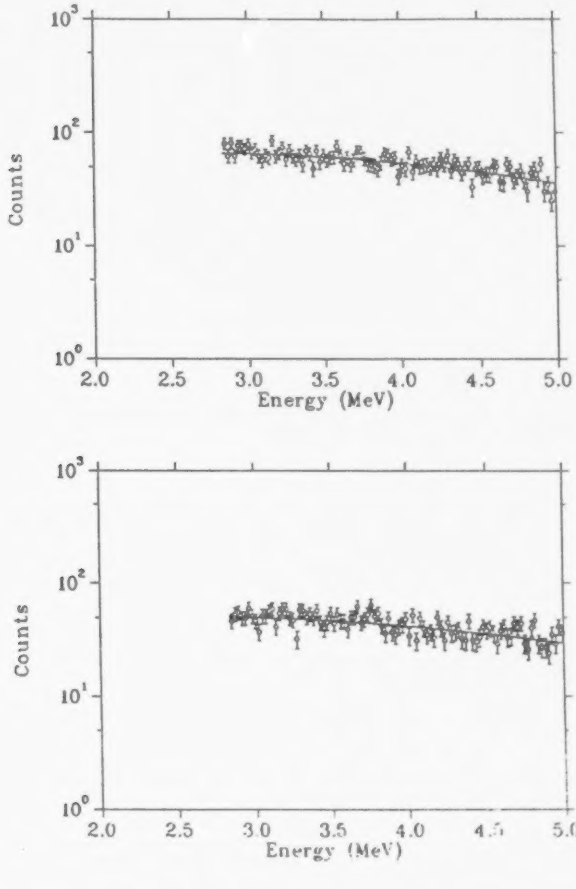

Figure 4.10. The fit to the beta decay energy in the thick E scintillator. Only every fifth data point is shown to prevent confusion. The upper is for run 22 while the lower is for run 29.

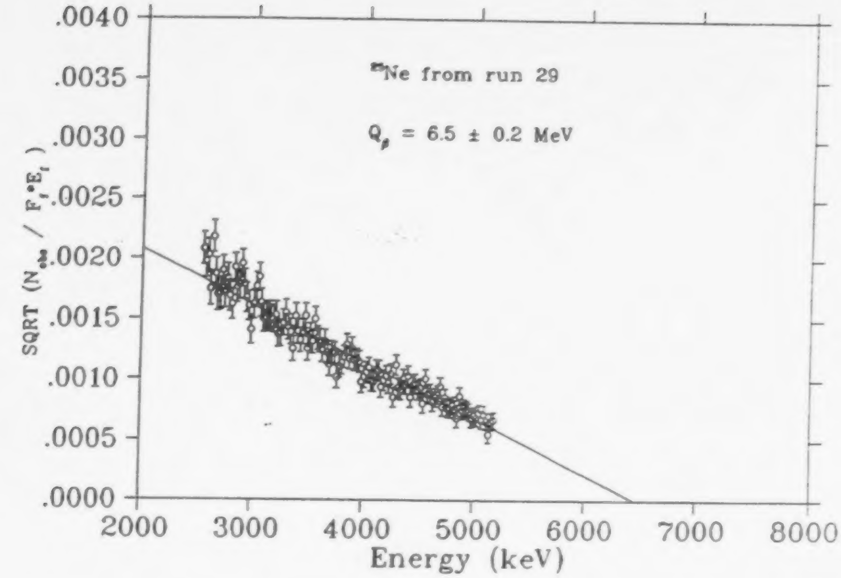

Figure 4.11. The Kurie plot of the data from run 29 for ^{25}Ne.

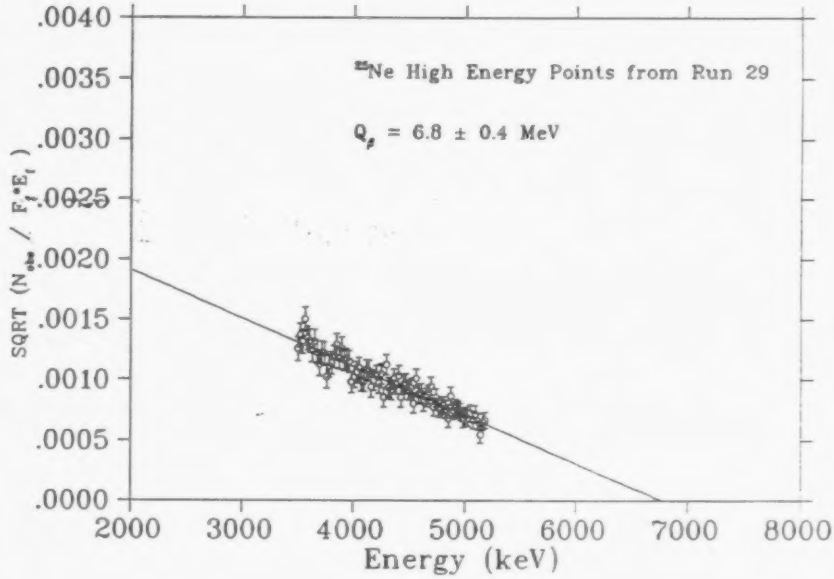

Figure 4.12. The Kurie plot to the beta decay data in the thick E scintillator from run 29 for ^{25}Ne for the region $T_e > 3.5$ MeV. Only every fifth data point was plotted.

4.6 The ^{26}Ne(β)^{26}Na Reaction

This section describes the experimental results obtained for ^{26}Ne and the comparison to existing data and theoretical predictions. As with ^{25}Ne, the focus is on the observed gamma rays and their branching ratios. The measured half-life and maximum β–energy are also reported.

The runs were divided into three groups based on the amplifier settings of the coaxial HPGe detector. The first three runs (26, 30, and 31) had the amplifier set so that the maximum observable γ–ray energy was 2 MeV. In run 35 this was increased to 4 MeV. However, the lowest peak (83 keV) was lost due to the adjustment of the amplifier and the discriminator levels of the 3512 ADC. The last run, run 38, corrected this problem and all γ–ray energies up to 4 MeV were visible. The first three runs were combined and analysed together. The other two runs were analysed separately.

The data collection for ^{26}Ne consisted of repeated sequences of 600 ms collection time, 1000 ms decay observation time, and 900 ms tape movement time. The run lengths were: run 26 (8 539 s), run 30 (13 716 s), run 31 (20 541 s), run 35 (17 875 s), and run 38 (17 246 s).

4.6.1 ^{26}Ne(β)^{26}Na Gamma Ray Energies and Branching Ratios

Prior to this experiment previous measurements [Duf87] had observed two γ-rays associated with the decay of ^{26}Ne(β)^{26}Na (see Section 2.5) with energies of 82 and 234 keV. The predictions reported in Section 2.5 indicated that higher energy γ-rays might also be expected. This experiment confirmed the existence of the two previously-observed γ-rays and also revealed the presence of a third new γ-ray at 151 keV. It seems a reasonable assumption that this is a transition γ–ray from a γ–cascade as was indicated in [Duf87]. To completely confirm the existence of a cascade, one of two pieces of additional evidence is necessary. The first is an accurate measurement of the β–endpoint energy for each gamma transition and the observation that the β–endpoints were the same for the 234 keV and 151 keV γ–ray. The other piece of evidence would be a $\gamma\gamma$ coincidence measurement which sees both the 234 and 151 keV γ's and the 151 and 82 keV γ's in coincidence. Poor statistics for β–decays in coincidence with the γ–rays precludes the first, and the timing problems mentioned earlier in Section 4.2.2 did not allow the $\gamma\gamma$ coincidences to be seen.

Table 4.8 summarizes the results for the energies of the observed γ–rays as determined by the fitting procedure described in Section 4.2. Due to the existence of the third γ–ray, the branching ratios determined from this experiment do not agree with those reported in the literature[End90]. Table 4.9 contains the data on the observed γ transitions in ^{26}Ne($\beta\gamma$)^{26}Na with the final adjusted number of counts for each γ-ray in each run.

The fits to the γ–energy spectra can be seen in Figs. 4.13 to 4.17. The anomalously high χ^2/DOF values in Table 4.9 needs clarification. A closer examination of any of the fits in Figs. 4.13 to 17 will reveal the cause. The data seem to have non-statistical fluctuations, particularly in the background regions, which give a very large contribution to the χ^2 value. These variations exists in the untreated ADC data before energy calibration, so it is not a result of binning problems in the Nova analysis program. This was the first time either of the HPGe detectors had been used so previous experience cannot be used to make an informed judgement. The data from the other attempts at the ^{26}Ne measurements, obtained with a different coaxial HPGe, indicated that large channel to channel fluctuations in the number of observed counts from also occur. The fits to the peaks themselves are clearly in reasonable agreement with the data. Based on this observation the centroid and peak widths are well determined, but the best estimate of the error in the centroids is obtained from the run-to-run variations. In addition to the statistical error for the 83 keV γ–ray, there is a ±0.3 keV systematic error in the energy calibration for this energy region.

The channel-to-channel fluctuations also generate spurious peaks in the data as can be seen in Figs. 4.16, and 4.17 for the 233 keV γ–ray. The fitting program was not measurement of the β–endpoint energy for each gamma transition and the observation that the β–endpoints were the same for the 234 keV and 151 keV γ–ray. The other piece of evidence would be a $\gamma\gamma$ coincidence measurement which sees both the 234 and 151 keV γ's and the 151 and 82 keV γ's in coincidence. Poor statistics for β–decays in coincidence with the γ–rays precludes the first, and the timing problems mentioned earlier in Section 4.2.2 did not allow the $\gamma\gamma$ coincidences to be seen.

Table 4.8 summarizes the results for the energies of the observed γ–rays as determined by the fitting procedure described in Section 4.2. Due to the existence of the third γ–ray, the branching ratios determined from this experiment do not agree with those reported in the literature[End90]. Table 4.9 contains the data on the observed γ transitions in ^{26}Ne($\beta\gamma$)^{26}Na with the final adjusted number of countsfor each γ-ray in each run.

The fits to the γ–energy spectra can be seen in Figs. 4.13 to 4.17. The anomalously high χ^2/DOF values in Table 4.9 needs clarification. A closer examination of any of the fits in Figs. 4.13 to 17 will reveal the cause. The data seem to have non-statistical fluctuations, particularly in the background regions, which give a very large contribution to the χ^2 value. These variations exists in the untreated ADC data before energy calibration, so it is not a result of binning problems in the Nova analysis program. This was the first time either of the HPGe detectors had been used so previous experience cannot be used to make an informed judgement. The data from the other attempts at the ^{26}Ne measurements, obtained with a different coaxial HPGe, indicated that large channel to channel fluctuations in the number of observed counts from also occur. The fits to the peaks themselves are clearly in reasonable agreement with the data. Based on this observation the centroid and peak widths are well determined, but the best estimate of the error in the centroids is obtained from the run-to-run variations. In addition to the statistical error for the 83 keV γ–ray, a +0.3 keV systematic error has been observed in the ^{25}Ne data for this energy region.

The channel to channel fluctuations also generate spurious peaks in the data as can be seen in Figs. 4.16, and 4.17 for the 233 keV γ–ray. The fitting program was not designed to perform peak searches. The existence of a peak was determined visually. The fitting program was then constrained with bounds on the values of μ and σ. These bounds were set by observation of the properties of the individual detectors. The coaxial HPGe (Ge1) was allowed values of the centroid, μ, which varied from the estimated mean by ±3 keV. The standard deviation of the peak, σ, was allowed to take values between 0.25 and 1 keV. The planar HPGe (Ge2) had a much better energy resolution so the constraints were tighter. For the planar HPGe (Ge2) the centroid was allowed to vary by ±0.5 keV from the expected and the σ of the peak was allowed to vary between 0.2 and 0.4 kev. Note that these ranges are much larger than the errors quoted in Table 4.8. The fits were stable if these limits were relaxed and there were no problems with the convergence of the fits. Because of the poor χ^2 values and the non-statistical channel to channel fluctuations mentioned earlier it was felt that the error estimates from the fitting procedure were unreliable, so the sample mean and error were used for the γ–ray energies.

Although no direct evidence for the cascade could be found, indirect evidence suggests that it is the more likely alternative. If the cascade is assumed, then the intensity of the γ–rays are as given in Table 4.11. If there is no cascade then the intensity corresponds to the branching ratio given in Table 4.10. As well as the β–branching ratio, the gamma branching ratio of the 234 keV level can be calculated as shown in Table 4.12. The result is that the γ–ray decays to the ground state or the 82 keV level about equally. As evidence of the existence of the cascade, Table 4.13 shows the difference between the value obtained from the fit for the energy of the 151 keV γ–ray as compared to the difference in the 82 and 234 keV γ–ray energies. It is hard to believe that such good agreement is mere coincidence.

Table 4.8. This table shows the results for the γ–ray energies determined for each run and each observed γ–ray. The average of all runs and the standard error of the mean (S.E.O.M) are quoted at the bottom. Note that systematic errors in the energy calibration are larger than the statistical fluctuations quoted here.

Run	Peak Centroid [keV]	σ [keV]
26,30,31	82.30	0.31
	151.69	0.33
	234.00	0.20
35	82.33	0.28
	151.79	0.32
	234.12	0.27
35 RAW	82.41	0.28
	151.53	0.22
	234.18	0.29
38	82.32	0.31
	151.68	0.30
	234.12	0.27
38 RAW	82.39	0.30
	151.76	0.30
	234.22	0.31
Run Average and sample error	82.35 ± 0.03[†]	
Run Average and sample error	151.69 ± 0.05	
Run Average and sample error	234.13 ± 0.04	

[†] A systematic error of +0.3 keV must be included with this error.

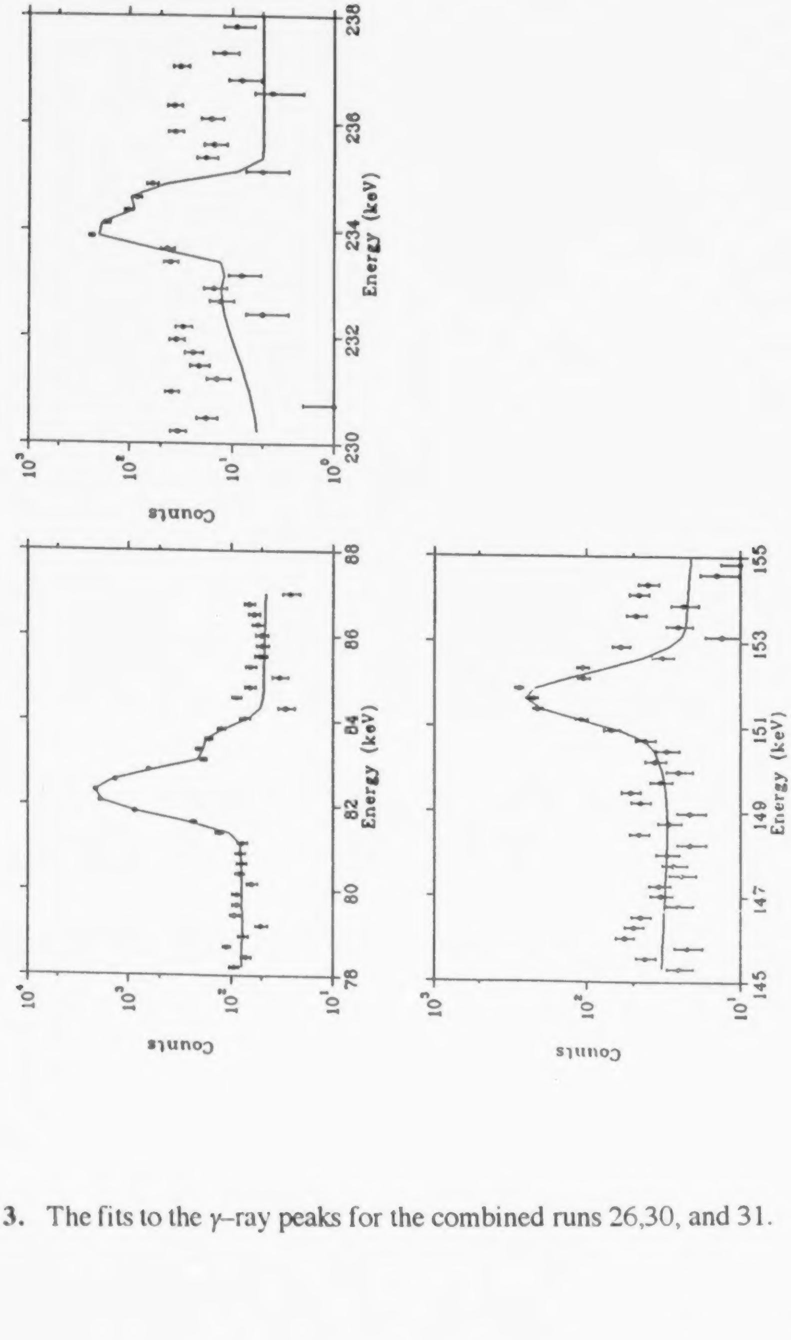

Figure 4.13. The fits to the γ–ray peaks for the combined runs 26,30, and 31.

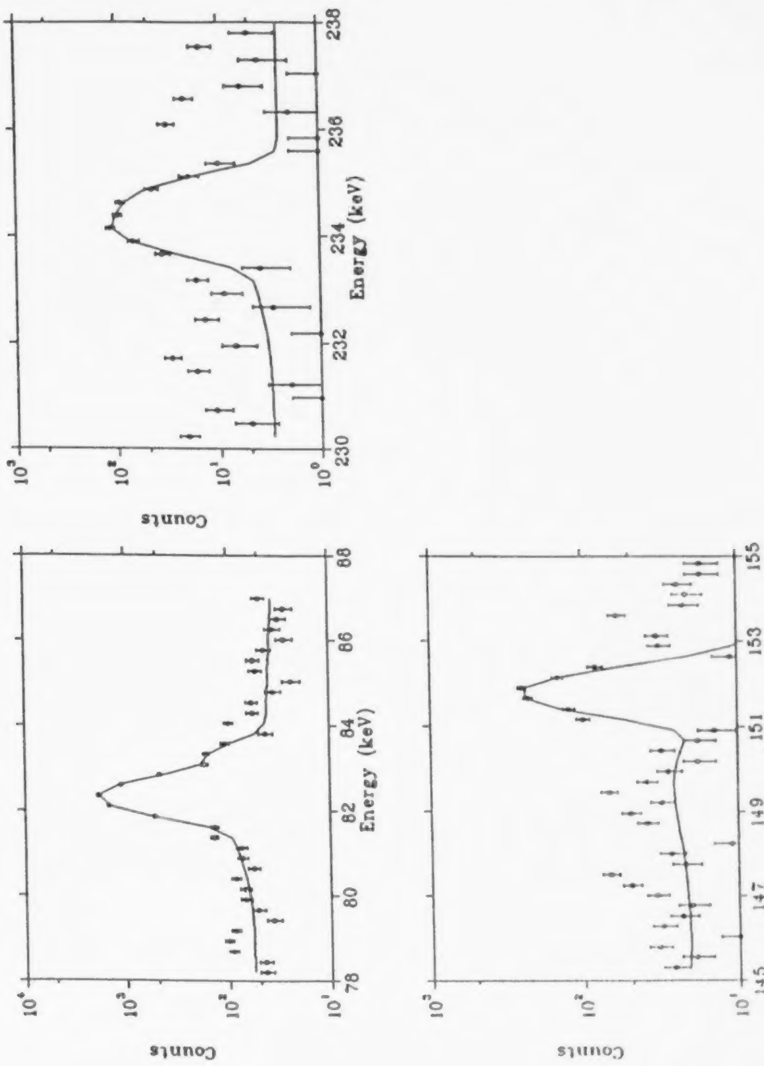

Figure 4.14. The fits to the γ–ray peaks for run 35.

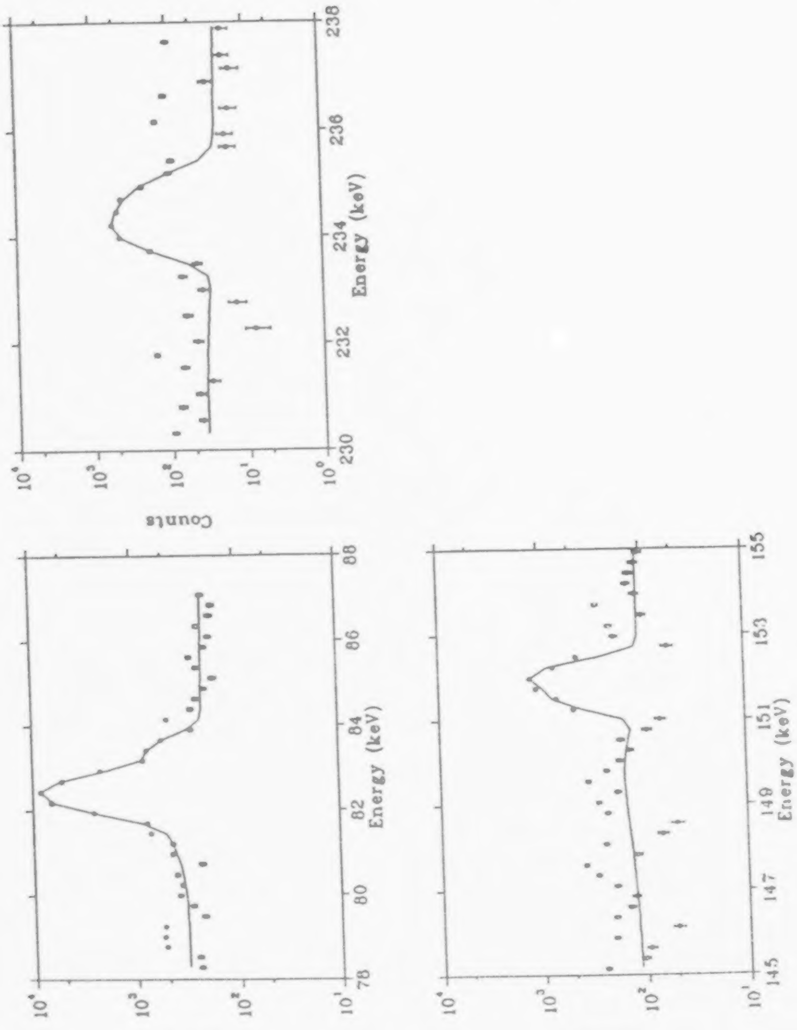

Figure 4.15. The fits to the γ–ray peaks for the RAW data from run 35.

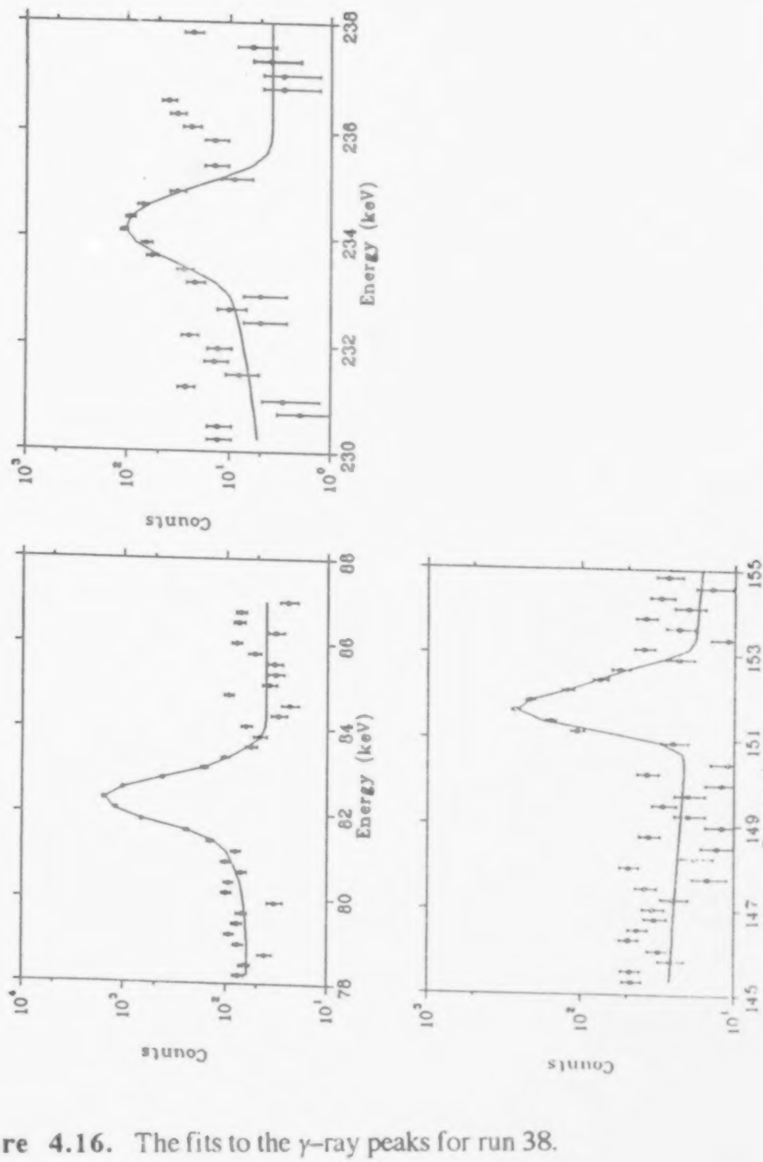

Figure 4.16. The fits to the γ–ray peaks for run 38.

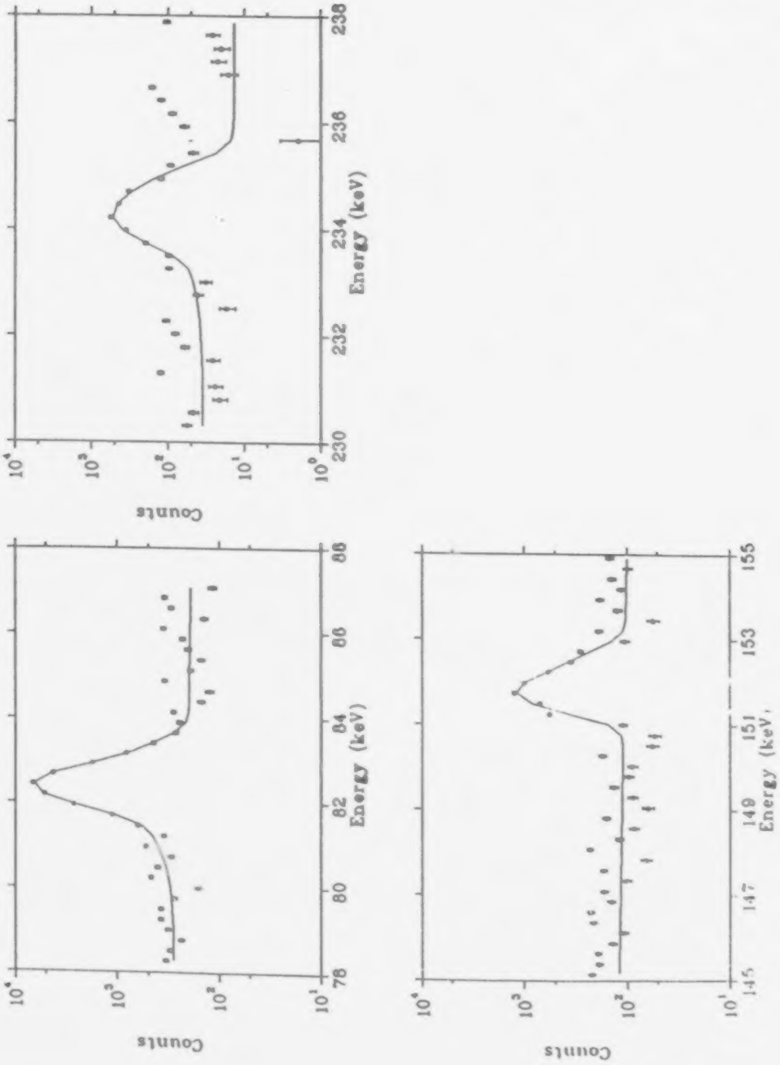

Figure 4.17. The fits to the γ–ray peaks for the RAW data from run 38.

To determine the branching ratios, assumptions about the decay scheme had to be made. It was not possible to determine if there was a gamma cascade so two possible decay schemes are given (they are illustrated in Fig. 4.18). The first decay scheme assumes no cascade and the existence of a new level at 151 keV. The second decay scheme assumes that a cascade exists between the 234 and 82 keV levels. This was implied in [Duf87], but no 151 keV γ was observed [End90]. The results for each of these assumptions are shown in Table 4.10. For the "no cascade" decay scheme the branching ratio [B.R.(E)] was calculated as

$$\mathrm{B.R.}(E) = \frac{N_{adj}(E)}{\sum N_{adj}(E)} , \tag{4.18}$$

where $N_{adj}(E)$ is the final adjusted counts for energy E. The "cascade" decay scheme used the formulas

$$\mathrm{B.R.}\ (82) = \frac{N_{adj}(82) - N_{adj}(151)}{N_{adj}(82) + N_{adj}(234)} , \tag{4.19}$$

and

$$\mathrm{B.R.}\ (234) = \frac{N_{adj}(234) + N_{adj}(151)}{N_{adj}(82) + N_{adj}(234)} . \tag{4.20}$$

The error formulae for these calculations are mathematically complex and would require the inclusion of the error in the number of counts which was not well determined. To avoid this the sample average and standard deviation were determined by averaging the branching ratios determined from the different runs.

Table 4.9. The data on the observed counts and the adjusted counts used in calculating the branching ratios. The efficiency used for the 82 keV γ-ray is the measured value for 81 keV from the calibration. The other two efficiencies are calculated from the linear efficiency fit.

Run	Average Energy [keV]	Relative Efficiency ε_{ff}	Trans T(E_γ)	Observed Counts	Adjusted Counts [x10^7]	χ^2	χ^2/DOF
26,30,31	82.35 ± 0.03	1.89×10^{-4}[†]	0.90	7 260	4.24	150	6.3
35				5 880	3.43	183	7.6
35 RAW				26 170	15.28	603	31.8
38				5 220	3.05	210	8.8
38 RAW				22 030	12.87	776	32.4
26,30,31	151.69 ± 0.05	9.52×10^{-5}	0.92	950	1.09	185	6.6
35				1 040	1.19	370	13.2
35 RAW				4 400	5.24	1 553	55.5
38				870	0.99	200	7.1
38 RAW				3 880	4.43	818	29.2
26,30,31	234.11 ± 0.04	4.92×10^{-5}	0.93	710	1.55	330	16.5
35				470	1.02	174	8.6
35 RAW				2 380	5.24	781	32.5
38				470	1.02	196	9.8
38 RAW				2 050	4.49	781	41.1

[†] This value for efficiency is the measured value at 81 keV for the ^{133}Ba spectrum. The other efficiency values are derived from the linear fit to the data.

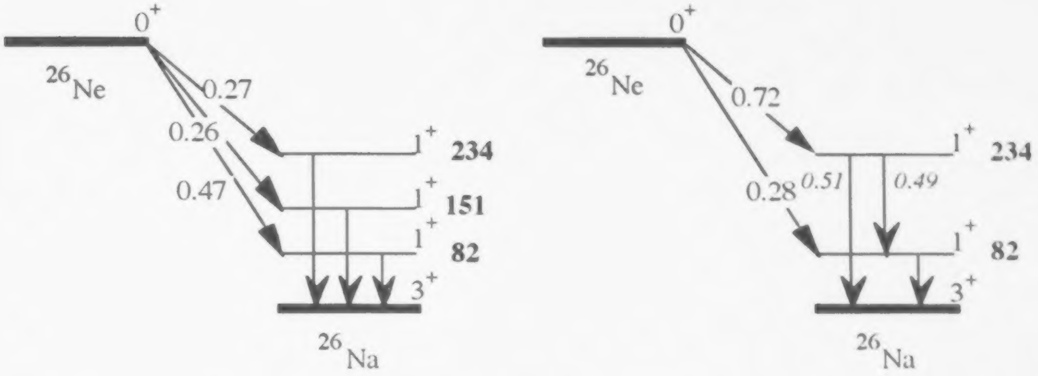

Figure 4.18. The energy level diagrams for the two possible decay schemes. The cascade scheme, on the right, also shows the γ branching ratio for the 234 keV level.

Table 4.10. The branching ratios determined for the ^{26}Ne(β)^{26}Na Decay. The first three columns are for the decay scheme with no cascade, and the final two columns are assuming a cascade does occur. The run average and standard error of the mean is given at the bottom of each column.

Run	B.R. (No Cascade) 82 keV	B.R. (No Cascade) 151 keV	B.R. (No Cascade) 234 keV	B.R. (Cascade) 82 keV	B.R. (Cascade) 234 keV
26,30,31	0.474	0.240	0.286	0.308	0.692
35	0.469	0.275	0.256	0.267	0.733
35 RAW	0.463	0.265	0.270	0.270	0.730
38	0.465	0.265	0.269	0.272	0.728
38 RAW	0.459	0.269	0.271	0.260	0.740
Average	0.466 ± 0.003	0.263 ± 0.006	0.271 ± 0.005	0.275 ± 0.008	0.725 ± 0.008

Table 4.11. The average intensity [γ's observed per 100 decays of ^{26}Ne] of the observed gamma rays under the assumption of a gamma cascade for all the runs (26, 30, 31, 35, 35 RAW, 38, and 38 RAW). The sample average and standard error of the mean are given.

Intensity 82 keV γ	Intensity 151 keV γ	Intensity 234 keV γ
63.3 ± 0.4	35.7 ± 1.1	36.7 ± 0.4

Table 4.12. The average gamma branching ratio for the 234 keV level to the ground state or the 83 keV level under the assumption of a gamma cascade for all runs (26, 30, 31, 35,35 RAW, 38 and 38 RAW). The sample average and standard error of the mean are given.

B.R. to Ground State [%]	B.R. to 83 keV Level [%]
49.3 ± 1.0	50.7 ± 1.0

Table 4.13. The average difference in energy between the 234 and 83 keV energy level as compared to the average energy of the observed intermediate gamma ray for all runs (26, 30, 31, 35, 35 RAW, 38, and 38 RAW). The sample average and standard error of the mean are given.

Observed Intermediate γ–ray Energy [keV]	Level Separation [keV]	Difference Level Separation and γ–ray [keV]
151.69 ± 0.04	151.79 ± 0.03	0.10 ± 0.05

4.6.1.1 High Energy γ's from ^{26}Ne(β)^{26}Na

The experiment also searched for the existence of any higher energy γ–rays. In Section 2.5 the predicted [Wil83] β–branching ratios for transitions from ^{26}Ne to high energy states in ^{26}Na, as well as possible γ decay energies were given . Based on these predictions, the gain of the the coaxial HPGe detector was adjusted in Runs 35 and 38 to observe γ–ray energies up to 4 MeV. No significant peak was observed other than the three low energy peaks, the 511 keV annihilation radiation peak, and an 1808 keV peak from the decay of the daughter ^{26}Na (see Fig. 4.19). Data from the coaxial HPGe and the planar HPGe detectors conclusively rule out any new gamma rays below 1 MeV with a branching ratio > 1%. For the region 1-2 MeV, the lack of any visible peak in the planar HPGe indicates a branching ratio for the decay < 5%, based on the observed number of 83 keV gammas and the detector efficiency. For energies above 2 MeV only the coaxial HPGe can provide any data. Given that the known weak (branching ratios ~2%) high energy γ–rays in the decay ^{25}Ne(β)^{25}Na (see Table 4.2) were not observed by the coaxial HPGe (Ge 1), it is clear that branching ratios of the same strength as those high energy γ–rays could not be observed in ^{26}Ne(β)^{26}Na, so it is possible that such decays may exist.

This experiment is able to add new information on the decay ^{26}Ne(β)^{26}Na. The observation of a new γ–ray at 151 keV has changed the decay scheme from that given in [End90]. Indirect evidence suggests that this is an intermediate γ–ray from a cascade between the 234 keV level and the 83 keV level. To strengthen the argument for the cascade the data on nearby nuclei [End90] was examined to determine if a similar decay scheme could be found. The decay ^{24}Ne(β)^{24}Na shown in Fig. 4.20 duplicates some of the properties of ^{26}Ne(β)^{26}Na. Both parent nuclei have 0^+ ground states and β–decay to two 1^+ levels in the daughter nucleus. The ground state of the daughter nucleus in both cases has a large value of J^π (3^+ for ^{26}Na and 4^+ for ^{24}Na). For the case of ^{24}Ne an *M*1 cascade γ–ray has been observed. Therefore it is reasonable that a similar *M*1 transition in ^{26}Ne would also occur.

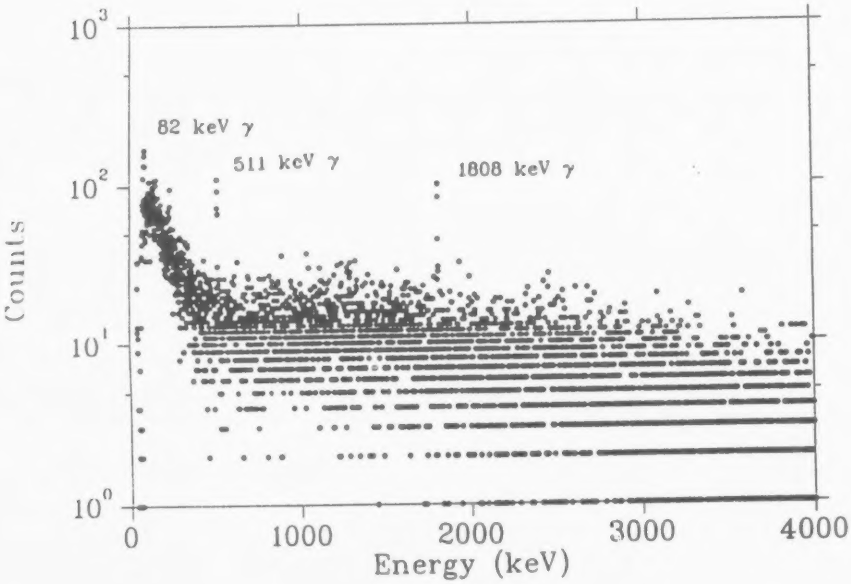

Figure 4.19. The spectrum from the coaxial HPGe (Ge 1) for ^{26}Ne from run 38 showing the high energy region. The 1808 keV peak is from the decay of the daughter ^{26}Na.

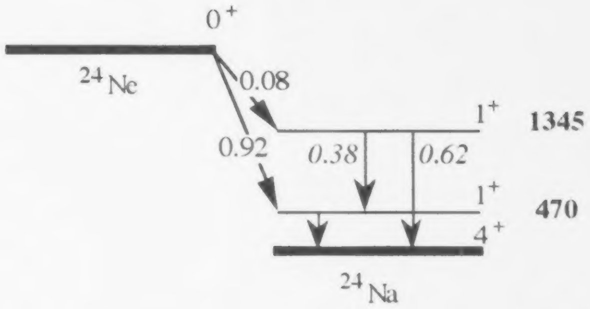

Figure 4.20. The level scheme for the decay $^{24}Ne(\beta)^{24}Na$ from [End90].

4.6.2 $^{26}Ne(\beta)^{26}Na$ Half-life

The procedure followed was the same as for ^{25}Ne (see section 4.5.2). The β–decay half-life data were summed over all runs (26,30, 31, 35, and 38) and fit. The result for the half-life for ^{26}Ne is shown in Table 4.14. Fig. 4.21 shows the time spectrum of the β–decay and its fit. The resulting half-life of 199.4 ± 1.1 ms agrees extremely well with the previous works [End90, Ten92]. It is significantly greater than the value of 162 ms predicted by [Wil83], which indicates that their calculated value for the total Gamow–Teller matrix element B(GT) is too large. As was the case for ^{25}Ne, the fitting procedure contained the known value of the half-life of the daughter (1 070 ± 30 ms [End90]). The result for the fit is a value for the half-life of ^{26}Na of 1 072 ± 1 ms which is, as expected, in good agreement with the known value.

Table 4.14. The results of the half-life data analysis for all runs for the β–decay of ^{26}Ne with a comparison to the existing data from the literature. The value from [Wil83] indicates the result for their pure shell model calculation.

Results From	half-life [ms]	χ^2	χ^2/DOF
Sum All Runs	199.4 ± 1.1	321	2.1
[End90]	230 ± 60		
[Ten92]	197 ± 1		
[Wil83]	162		

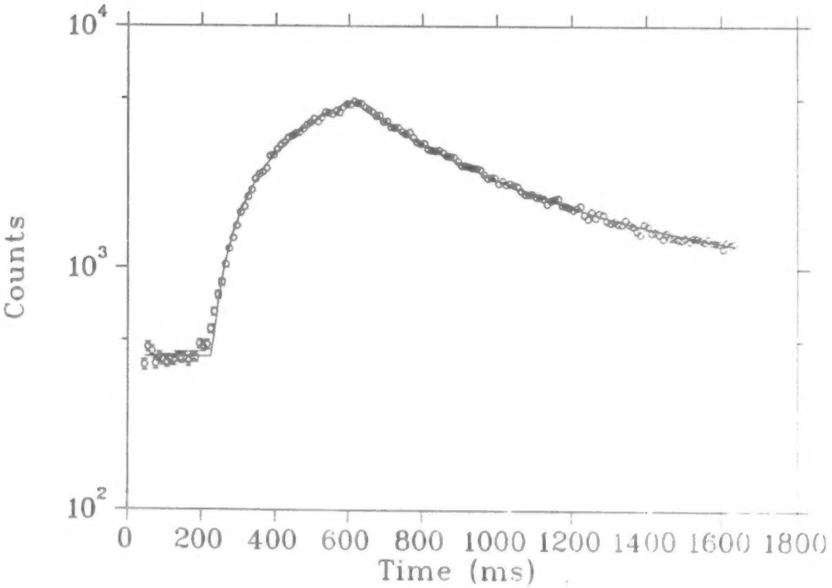

Figure 4.21. The fit to the beta-decay time spectrum to determine the half-life of ^{26}Ne. All runs (26, 30, 31, 35, and 38) were combined.

4.6.3 ^{26}Ne Beta Energy Endpoint

The ^{26}Ne beta energy endpoint energy was found using the program DECAYFIT and by fits to Kurie plots. As for the runs for ^{25}Ne, the spectrum was truncated at 5 MeV by the saturation of the ADC. The results for all the runs summed together can be seen in Fig. 4.22. The value of Q_β observed is presented in Table 4.15. The agreement between this value of 6.8 MeV and the expected value of 6.901 MeV [Wil83] for the dominant decay to the 234 keV level is good. This would seem to indicate that the simple conditions for the fit are satisfied and that the shell model calculations [Wil83] make reasonable predictions for the β decay energy. As for the ^{25}Ne data discussed in Section 4.5.3, a reasonable estimate of systematic error in the endpoint energy is a combination of ±0.3 MeV, based on the detector resolution at 6.8 MeV combined with a systematic error due to the calibration uncertainty of ±0.3 MeV.

The quality of the computer fits for ^{26}Ne was worse than in the case of ^{25}Ne. The fitting routine used an additional scaling factor when calculating the theoretical spectrum during the fitting process (Section 3.3.2.1.). For the ^{25}Ne fits the values of this parameter were nearly unity (1.05 for run 22 and 0.93 for run 29) which indicates that the theoretical shape closely approximated the observed data. The additional scaling term in the case of ^{26}Ne was 1.5. As the two levels are not far apart (200 keV compared to 1 MeV), the shape of the two curves is similar, so the second curve would be poorly approximated by the assumed flat background. The large value in the scaling term attempts to compensate for the discrepancy. The large value of the additional scaling term and high χ^2/DOF freedom are therefore related to the simplicity of the fitting procedure. The endpoint is not included in the data, which for the case of ^{26}Ne contributes to a large uncertainty in the value of Q_β as the data must be extrapolated. The errors generated by MINUIT for Q_β are unrealistically small. Systematic fitting error is more easily estimated from the Kurie plot analysis.

Table 4.15. The data from the fit to the observed beta decay energy of ^{26}Ne summed over all runs. The first value is the result obtained by the DECAYFIT program fit of the decay curve while the bottom two results are based on Kurie plot analysis. The two values in the theoretical prediction are for transitions to the 82 keV and 234 keV levels. The *ft* values were calculated by assuming a γ–cascade.

Fit Value of Q_β [MeV]	χ^2	χ^2/DOF	Theoretical Q_β [MeV]	$\text{Log}_{10} ft$
6.8	958	1.6	6.901 (234 keV)	3.81 ± 0.17
6.5±0.1	351	1.73	7.053 (82 keV)	4.29 ± 0.03
6.9±0.2	71	0.97		3.84 ± 0.06

A Kurie plot analysis was performed as described in Section 4.5.3. Two plots were obtained (see Figs. 4.23 and 4.24). For the data above 2.5 MeV, the value of Q_β determined is 6.5±0.1 MeV. There is clearly a distinct curve in the data, as can be seen in Fig. 4.23. The simple one-state fit obviously underestimates the real endpoint and systematic error dominates the fitting error. If only the data above 3.5 MeV is fit, as is also shown in Fig. 4.24, then a much better result is obtained. The value of 6.9±0.2 MeV for Q_β agrees with the DECAYFIT calculation and with the theoretical calculations of [Wil83]. As before the calibration uncertainty adds a systematic error of 0.3 MeV to the values quoted above.

The lower endpoint determined from Fig. 4.23 cannot be due to the superposition of the decay to 234 keV and 83 keV levels as these two levels have similar endpoints their slopes should be nearly indistinguishable in this data. It cannot be from the decay of ^{26}Na as the Q_β value is 7.4 MeV for the dominant decay so it would not contribute to a lower value of Q_β. The result from Fig. 4.23 could indicate a branch to a higher energy level in ^{26}Ne or might be due to energy loss non-linearities in the detector.

The $\log_{10}$ *ft* values in Table 4.15 were calculated under the assumption of a γ–cascade and can be compared to the shell model value of 3.708 calculated by

[Wil83] for a branching ratio of 90.5% and half-life of 162 ms. The agreement is not surprising since the $\log_{10}ft$ value is dominated by the value of $\log_{10}f$ and both the Kurie plot and the [Wil83] calculation have similar values for Q_β. The ft values given are indicative of an allowed G–T decay so $\Delta J = 1$, and $\Delta\pi = 0$. It is therefore reasonable to assign $J^\pi = 1^+$ to the 82 keV and 234 keV levels. As the ground state of ^{26}Na is 3^+, a ground-state to ground-state decay branch would require a second-forbidden β–transition . This is considerably less likely than the allowed decays to the 82 keV and 234 keV levels, so it is safe to propose that it does not exist.

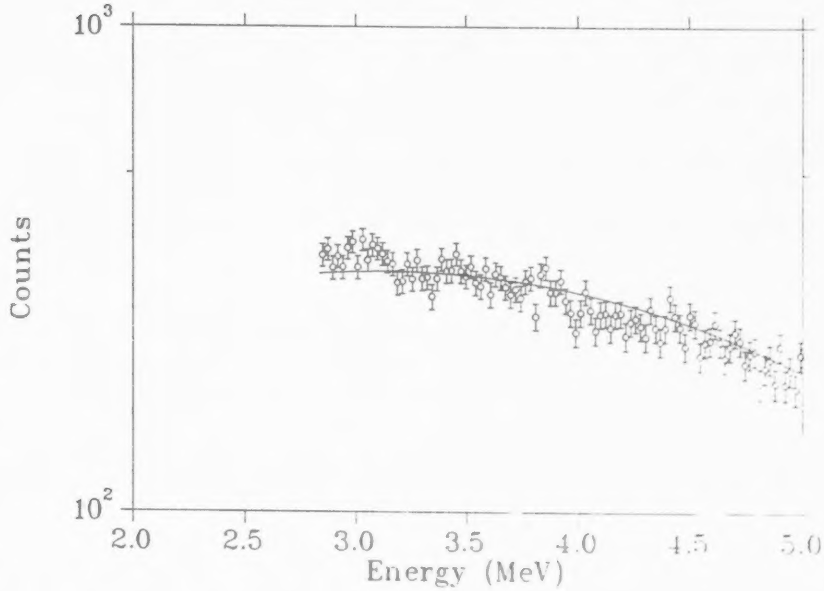

Figure 4.22. The fit from the program DECAYFIT to the β–decay energy spectrum of ^{26}Ne(β)^{26}Na for all runs combined.

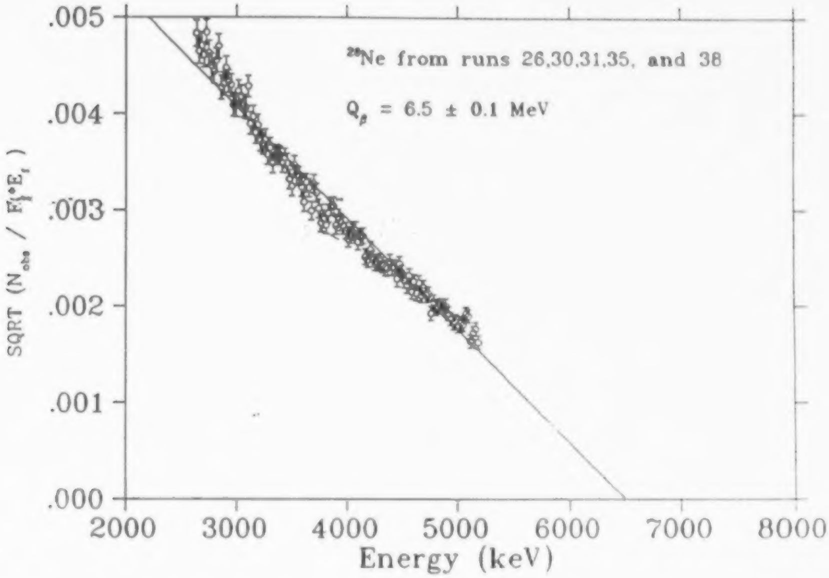

Figure 4.23. The Kurie plot for the β–decay energy spectrum of ^{26}Ne(β)^{26}Na for all runs combined.

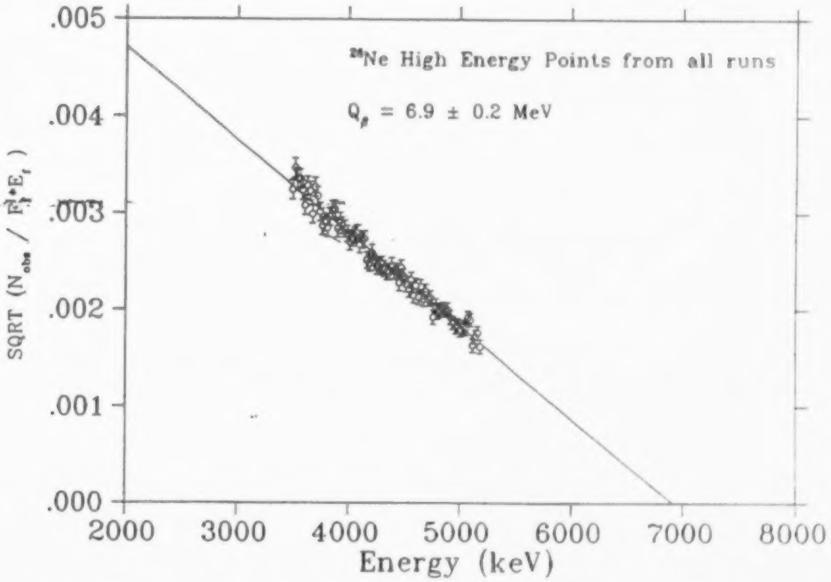

Figure 4.24. The Kurie plot for the β–decay energy spectrum of ^{26}Ne(β)^{26}Na for all runs combined, for $T_e > 3.5$ MeV.

4.7 The Search for ^{27}Ne(β)^{27}Na

The experiment was terminated by the failure of the tape drive during the segment of time allocated to the search for ^{27}Ne, so not much data was collected. There were three very short runs: Run 43 (2 720s), Run 44 (733s) and Run 45 (5 607s). Three very different collection strategies were used. In Run 43, the beam was collected for 200 ms and then the decay was observed for 600 ms. In Run 44, a 1000 ms collection time and a 1 500 ms decay observation time were used to search for evidence of the daughter ^{27}Na. In Run 45, the collection time was 2 000 ms and the decay observation time 400 ms.

4.7.1 Results for ^{27}Ne(β)^{27}Na

There was nothing observed in either the γ–spectrum or the β–energy plot that was significantly different from background in either run 43 or 44. The only γ–ray observed for either run was a 511 keV γ–ray peak in the coaxial HPGe. In both runs, the energy spectrum from the β–telescope was similar to that obtained during a background run taken before the experiment began. For Run 45, some more interesting elements turn up. There is clear evidence of the expected γ–ray at 250 keV for the decay of ^{135}Xe in both the coaxial HPGe and the planar HPGe (Ge 2) (see Fig. 4.25 for the the planar HPGe spectrum). The planar HPGe (Ge 2) also shows γ activity near 30 keV which is also from ^{135}Xe. There is structure in the β telescope energy spectrum (see Fig. 4.26). Clear evidence exists of a peak at ~500 keV superimposed on a spectrum very similar to that for the background run. The maximum expected electron energies for the β–decay of ^{135}Xe are of 0.9 MeV (BR 96.0 %) and 0.55 MeV (BR 3.15 %). These energies are too low to allow a fit to be performed due to non-linearities in the β–detector response. Qualitatively, the peak of

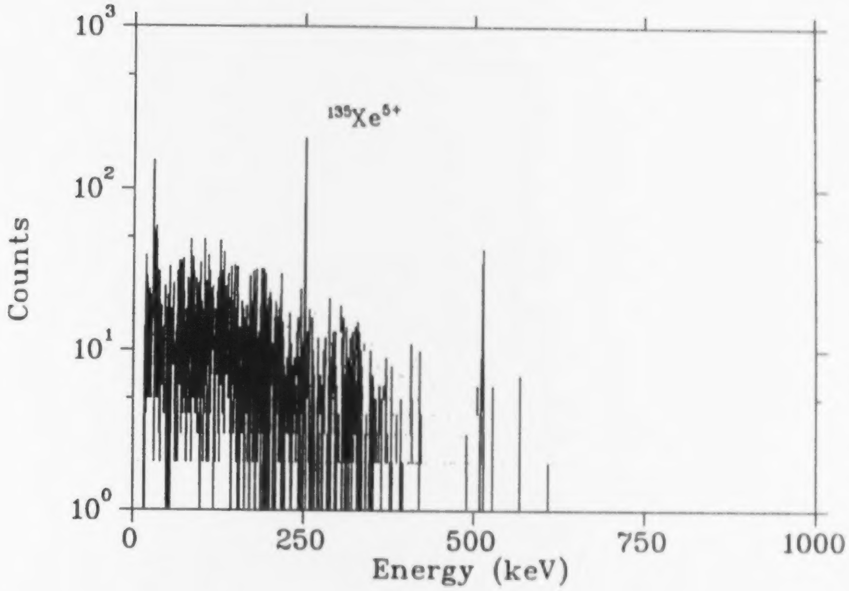

Figure 4.25. The spectrum collected by the planar HPGe during Run 45.

the beta spectrum is usually about half the maximum available electron energy so a peak near 500 keV is consistent with ^{135}Xe. The half-life of ^{135}Xe is 9.10 h, so the collection/count time cycle used does not allow for a fit to be performed. It is most likely that both the 250 keV γ–ray and the β–signal were caused by $^{135}Xe^{5+}$ rather than ^{27}Ne. The data also indicate a large yield for $^{135}Xe^{5+}$ since, given the short decay observation time compared to the long half-life, seeing a signal as small as a count every five seconds requires a large value for the deposition rate (~2.2 x 10^7 atoms/s). Given that the yield decreases, usually by an order of magnitude for each increment in charge state, the singly charged yield is almost certainly very large (~2 x 10^{11} atoms/s).

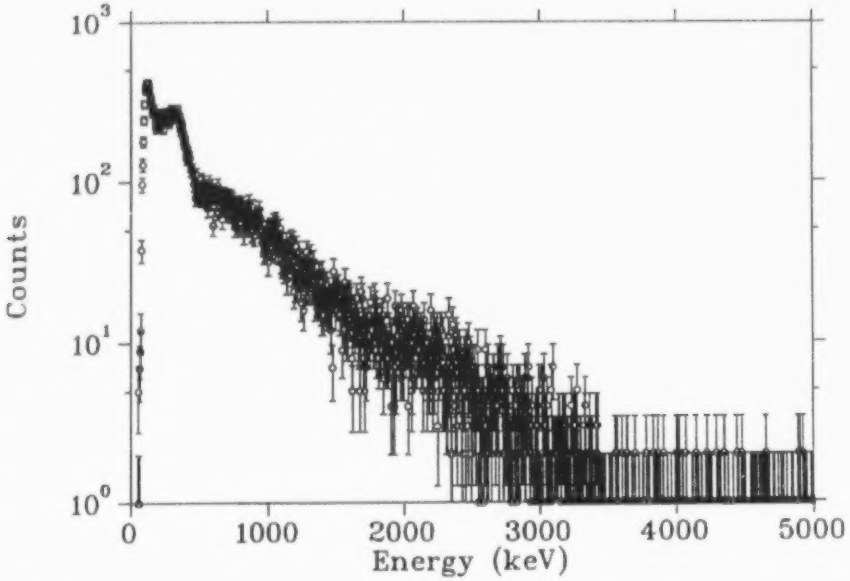

Figure 4.26. The thick E scintillator spectrum collected during Run 45.

The experiment was terminated by the tape drive failure during run 45 after only a very short time on target. It is unclear if ^{27}Ne was produced in sufficient quantity to warrant pursuing the investigation further. However, since ^{27}Ne has been produced at ISOLDE, the possibility of being able to produce ^{27}Ne at TRIUMF still exists. As well, the attempt to observe ^{27}Ne shows the need for a high-quality mass-analysing magnet with known characteristics to allow searches into mass regions where previous information is lacking. The inability of the TISOL system to unambiguously identify the mass region being observed meant that most of the time available was spent verifying that the beam was in fact composed of mass 27 ions. ^{27}Ne has a mass of 27.006 u [End90] whereas ^{135}Xe^{5+} has a mass of 26.981 u [Led78], neglecting the mass of the missing electrons. This gives $\Delta M/M = 1/1080$. In Section 1.3 it was stated that TISOL has a mass resolution of 2400 in the mass region Rb 85–87.

Therefore it should have been possible to separate ^{27}Ne for ^{135}Xe^{5+} — apparently it was not. This indicates that the magnet optics and the transmission through the ion beamline need additional study.

4.8 Production of Neon Isotopes at TISOL

A figure of merit for any ISOL facility is the yield for a particular isotope. As described in Section 1.2, the production in the target is governed by eq. 1.1. Between the yield produced in the target and the detectors at the collection point two important physical processes occur: diffusion through the target material and ionization in the ion source. At TISOL some diffusion studies have been carried out [Dom90] but only for isotopes accessible through the use of the surface ionization ion source [Na, Rb, Cs, and In]. The value of the diffusion times ranged from 1.9 ± 8.2 s for Na isotopes to 507 ± 520 s for Rb isotopes [Dom90]. No similar studies have been performed for the noble gas isotopes available with the ECR ion source. Noble gas elements do not form chemical compounds so their diffusion time is unaffected by losses due to chemical reactions occurring with the surrounding target matrix. For this reason their diffusion through the target material should be fast. Recent studies at ISOLDE have shown their release times to be ~0.5 s [Rav87]. Since our target design is similar to the targets used at ISOLDE, it is a reasonable assumption that the diffusion times would be similar. To arrive at an estimate of the diffusion time, the production yield calculations which follow will be done for both a 0.5 s and 1.0 s diffusion time.

The isotopes released from the target are transferred to the ECR ion source. The most important consideration of the ion source is its ionization efficiency. I studied the ECR ion source both offline [Men90] and, after installation, online [Dau92]. The ionization efficiency was found to be similar, ~20%, in both cases. The ionization efficiency of an ECRIS is influenced by source pressure, RF power, and the magnetic field of the solenoid coils. The most important of these effects is the source pressure.

The ECRIS in its online position is closely coupled to the target chamber and is affected by any pressure fluctuations in the target chamber. The pressure in the target chamber is affected by both the temperature of the target and the proton beam. A sizable pressure increase (up to an order of magnitude) was noted when the proton beam was irradiating the production target. This is a much greater effect than what would be anticipated by an increase in target temperature due to beam heating.

Dedicated beam time was not available to make quantitative measurements of the effects on stable and radioactive ion beams of varying ECR ion source parameters under the normal operating conditions typical of a data collection run. Although extensive target development work, which I participated in, was performed while preparing for the Red Giant experiment, these runs were focused on the production yield and stability of the target rather than the ion source.

Based on my knowledge of the ECR ion source, a reasonable value for Ne ionization efficiency would be 10 ± 5 %. It is unlikely that during an 8-hour data collection period the combination of parameters defining the ionization efficiency would remain stable and at optimal values, so the net ionization efficiency over the total running time would always be below the optimal value. After ionization the effect of transmission through the ion beamline must be taken into account. Based on the data contained in Table 1.1, the transmission through the beamline was about 40 %.

To calculate the theoretical production yield, the SILT program cross section results for ^{25,26,27}Ne are multiplied by the target thickness and production current. The diffusion time, t_D, through the target is combined with the isotope half-life to generate the fraction which decay before escaping the production target. The ionization efficiency, I_{eff}, and the beamline transmission, T_{BL}, are then multiplied by the surviving fraction. To account for the time of transit between the surface of the target and the detector position an additional time factor of 50 ms is included. This delay is ten times longer than it would take an ion with 1800°C thermal energy to travel between the target and ECRIS. The theoretical yield at the detector, $Y_i\,(det)$, for isotope i is

$$Y_i\,(det) = N_t \rho_p \sigma_i\, e^{-t_D \lambda_i}\, I_{eff}\, T_{BL}\, e^{-50\,ms\,\lambda_i} \quad . \tag{4.21}$$

This yield must then be multiplied by the absolute detector efficiency to compare with the observed rate. The results for this equation are listed in table 4.16 for the two target diffusion times.

The half-life fitting of the β–decay data observed in the ΔE–E telescope (Section 4.4.3 and 4.5.3) offer a straight forward way to compare the observed yield with the calculated value in table 4.16. The efficiency of the detector is near unity (90 ± 10 %) for detecting electrons and the solid angle is 5 ± 1 % of 4π. The absolute detector efficiency is calculable (4.8 %) and has an error no worse than ~20% which is sufficient for comparison purposes. Table 4.17 has the data used to calculate the observed yield based on the formula

$$Y_{obs} = S \,/\, (T_R \,/\, T_C) \ , \tag{4.22}$$

where S is the ion beam intensity from the half-life fitting, T_R is the total run time, and T_C is the time for one complete collection/decay/move tape cycle.

Table 4.16 The values used in eq. 4.21 to calculate the theoretical event rate at the detectors.

Isotope	Run	I_{eff} [%]	T_{BL} [%]	ρ_p [nA]	$N_t\sigma\rho_p$ [atoms/s]	λ [s]
^{25}Ne	22	10	40	200	4.5 x10^5	1.16
^{25}Ne	29			400	9.0 x 10^5	1.16
^{26}Ne	Sum All			400	3.6 x 10^5	3.47

Table 4.17 The values used in eq. 4.22 to calculate the observed yield of Ne isotopes based on the results of the half-life fitting.

Isotope	Run	S [atoms/s]	T_R [s]	T_C [s]
^{25}Ne	22	$(4.01 \pm 0.09) \times 10^5$	10 218	4.7
^{25}Ne	29	$(2.19 \pm 0.04) \times 10^5$	1 983	4.7
^{26}Ne	Sum All	$(5.38 \pm 0.01) \times 10^6$	77 917	2.5

The agreement between the calculated and the observed event rates given in Table 4.18 is acceptable. The actual cross section from SILT is the largest uncertainty in the calculation process. The SILT calculation of the cross section is only a guide and could be in error by a factor of two to ten. Thus to make quantitative comments on the diffusion time based on these results is very difficult. The observed event rate for ^{25}Ne agrees with a diffusion time estimate of 1 s. The observed event rate for ^{26}Ne indicates that the diffusion time is probably less than 0.5 s. It is clear from the data that the diffusion time is not significantly longer than than 1 s. It would only require the cross section for the production of ^{25}Ne to be out by less than a factor of 2 for the observed rate to be consistent with a 0.5 s release time.

The search for ^{27}Ne or the possibility of observing very short half-life activity at TISOL is directly affected by the diffusion time. If the diffusion time is as short as 0.5 s, then the intensity of ^{27}Ne at the target for a 400 nA proton beam would be $\approx 10^{-2}$ ^{27}Ne atoms/s, which is significantly better than the 1×10^{-9} atoms/s predicted for a 1 s diffusion time (see Table 2.7). A measurement of the diffusion time by pulsing the primary proton beam is clearly a critical measurement for all targets intended for use in future experiments at TISOL.

Table 4.18 A comparison between the calculated, Y_i (*det*), and observed, Y_{obs}, rates for the intensity of neon isotopes. The observed rate is determined by fitting the half-life spectrum of the ΔE–E telescope. Two different values for the diffusion time from the target were assumed. Systematic errors in the observed yields could be as large as 20%.

Isotope	Run	Observed Yield [atoms/s]	Calculated Yield [atoms/s]	
			T_D [0.5 s]	T_D [1.0 s]
^{25}Ne	22	184	440	250
^{25}Ne	29	519	890	500
^{26}Ne	Sum All	170	100	20

Chapter 5: The $^{18}N(\beta\alpha)^{14}C$ Decay

This chapter deals with the initial feasibility studies done for an experiment to observe the parity non-conserving (PNC) decay in $^{18}N(\beta\alpha)^{14}C$. The chapter begins with an introduction to α–decay and parity violation. This is followed by a section on the analysis of the data collected on July 21–26, 1992 and on June 15–20, 1993. The final section discusses the requirements that must be met for a successful PNC experiment to take place. The experimental apparatus used here has been previously described in section 3.5.

5.1 Introduction to Alpha–Decay

Alpha emission is generally characteristic of the decays of very heavy isotopes $A>150$. However, for lighter nuclei far from stability, β–decay may leave the daughter nucleus in an energy level which is above the α–emission threshold. Usually in these cases α–emission is not the dominant form of decay but must compete with γ–transitions or neutron emission.

The energy of the emitted α is easy to calculate if one knows the energy level and the emission threshold. However, in the case where neither is known, it is possible to calculate an approximate value for the α total energy, ε_α, by using the formula

$$\varepsilon_\alpha = E^*(Z,A) - E\,(Z-2, A-4) + B_\alpha , \tag{5.1}$$

where $E^*(Z,A)$ is the total energy of a nucleus (with charge Z and atomic number A) including the binding energy and the excitation energy above the α-emission threshold. B_α is the α-binding energy of 27.6 MeV. $E^*(Z,A)$ can be calculated using the semi-empirical mass formula (eq. 2.18) if necessary. If the SEMF is used the α energy is only approximate, but if the exact excitation energy is known, as in the $^{16}N(\beta\alpha)^{12}C$ decay, eq. 5.1 gives the exact value of ε_α. In this case ε_α = 1.8 MeV. For the ground state of ^{16}O, eq. 5.1 yields $\varepsilon_\alpha = -7.2$ MeV, that is, the α is bound. This agrees with the observed alpha-emission threshold of 7.162 MeV. If the nucleus ^{16}O is left in a 9.6 MeV excited state after the β–decay of ^{16}N, eq. 5.1 predicts an energy release of 2.4 MeV, which after being reduced by the energy of the recoiling ^{12}C (0.6 MeV) agrees with the observed value of $\varepsilon_\alpha = 1.8$ MeV.

The general theory of α–emission is based on quantum mechanical tunneling [Seg77, Bla91, Pre75, Rei72]. The situation is shown schematically in Fig. 5-1. In order for the α–particle to emerge from the nucleus, it must penetrate a potential barrier whose height is given by

$$V_B = \frac{2Ze^2}{R} + \frac{L(L+1)(2\pi hc)^2}{2M_\alpha c^2 R^2} \quad . \tag{5.2}$$

The first term is the Coulomb potential, V_c, and the second term is the centripetal barrier, V_{cp}, due to the angular momentum (L) of the emitted α-particle. For S-wave (L=0) α-emission from ^{18}O, $V_B = 5.07$ MeV . For P-wave (L=1) emission the barrier is 5.97 MeV, and for F-wave (L=2) emission it is 7.77 MeV.

It is relatively straightforward to calculate the probability of an α penetrating the barrier

$$P = \frac{\Gamma_\alpha}{h} = \omega_o T(\alpha) \ , \tag{5.3}$$

where ω_o is the α-particle collision frequency with the barrier, Γ_α is the width of the state for α-emission, and T(α) is the transmission coefficient. An estimate of ω_o can be made. If R is the nuclear radius and v_α is the alpha velocity inside the nucleus ($v_\alpha \approx c/10 = 3\text{x}10^9$ cm s^{-1}), then the average time between barrier collisions will be $v_\alpha/2R$. It is assumed that the number of alpha particles inside a nucleus, N_α, at

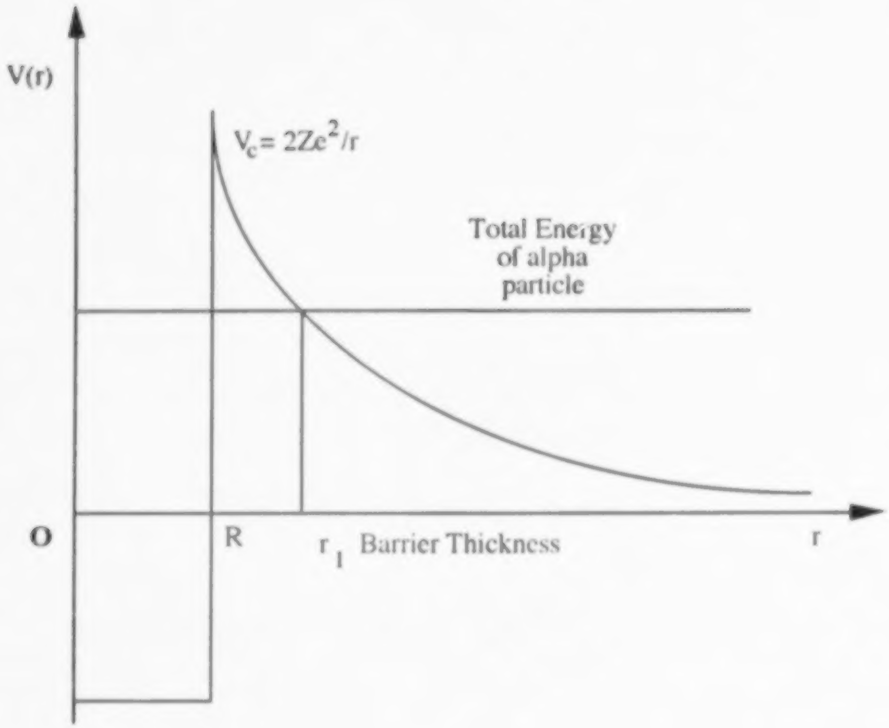

Figure 5.1. A diagram showing the situation facing a *S*–wave α–particle attempting to exit the nucleus. R is the nuclear radius. The centrifugal barrier is zero in this case.

any time is between 1 and 10. For the very light nuclei of interest to this investigation $N_\alpha = 1$ is most likely. Therefore an estimate of ω_o for ^{18}N is

$$\omega_o = N_\alpha v_\alpha / 2R = 4.4 \times 10^{21}\ \mathrm{s}^{-1}. \tag{5.4}$$

In situations where $E << V_c$, the coulomb barrier height, the *S*-wave escape probability can be written as [Rol88]

$$P(\alpha) = \exp(-2\pi\eta) \quad , \tag{5.5}$$

where η is known as the Sommerfeld parameter and is equal to

$$\eta = \frac{Z_1 Z_2 e^2}{\hbar v_\alpha} \ . \tag{5.6}$$

One can also write

$$2\pi\eta = 31.29\, Z_1 Z_2 \left(\frac{\mu}{E}\right)^{1/2} , \tag{5.7}$$

where E is the α *c.m.* energy in keV and μ is the reduced mass in amu. This is known as the Gamow factor. It is then possible to write the cross section for the reaction as

$$\sigma(E) = \frac{1}{E} \exp(-2\pi\eta)\, S(E) , \tag{5.8}$$

where $S(E)$ is the astrophysical S-factor and contains all the nuclear effects.

For narrow resonance reactions the cross section as a function of energy is characterized by the Breit–Wigner formula [Rol88]

$$\sigma(E) = \pi\lambda^2 \frac{2J+1}{(2J_1+1)(2J_2+1)} (1+\delta_{12}) \frac{\Gamma_a \Gamma_b}{(E-E_R)^2 + (\Gamma/2)^2} , \tag{5.9}$$

with $\Gamma = \Gamma_\alpha + \Gamma_\beta + \ldots$, δ_{12} is a delta function which equals 1 for identical entrance particles, E_R is the resonance energy, and $\pi\lambda^2 = 656.6/(\mu E)$ barns.

For broad resonances the situation becomes much more complicated. The overlap of two or more possible states can lead to destructive or constructive interference in the cross section. Also, states below the reaction threshold may have widths broad enough to contribute to the reaction. To properly fit the experimental data, it is necessary to utilize a computer code such as the K-matrix formalism [Fil89]. For simple cases (such as ^{17}N which has only two α states) simple Breit–Wigner or even gaussian fits will often suffice to describe the experimental data.

5.2 Introduction to the Parity Violating Interaction

Some basic ideas concerning parity violation and how it relates to the $^{18}N(\beta\alpha)^{14}C$ decay of interest are presented here. The information in this section is a summary of some recent works and more details can be found in [Ade85].

The Parity operator performs a mirror reflection on a system. This immediately leads to two classes of quantities — those conserved under parity and those that are not conserved. Vectors which are not conserved under parity transformations are known as pseudovectors or axial vectors. For example, angular momentum, torque, and spin are axial vectors. The dot product of a vector and pseudovector is known as a pseudoscalar and the observation of a non-zero pseudoscalar signals parity non-conservation.

In 1927, Wigner proposed parity conservation to explain the radiative transitions between electron levels in atoms [Wig27]. This conservation law was accepted universally. When Fermi postulated his theory of beta decay in 1933 [Fer34], he also assumed that parity would be conserved and this assumption stood until 1956. In 1957, Wu et al. [Wu57] observed a correlation between the spin of an unstable nucleus and the direction of the emitted electron. This appears as a non-zero value for the pseudoscalar quantity $<\boldsymbol{v}\bullet\boldsymbol{J}>$, where $\boldsymbol{v}$ is the electron velocity and $\boldsymbol{J}$ is the nuclear spin in the β-decay of ^{60}Co. This result corroborated the theory of Lee and Yang[Lee56] which predicted that the weak interaction would not conserve parity.

The reason that the parity-violating hadronic weak interaction is so interesting can be summed up by the following statement [Bal84]:

> Parity Violation is, in fact, the only means to study strangeness–conserving purely hadronic weak processes. Theoretically, the problem is usually approached by describing the observed effects of different isospin components of a weak (parity violating) NN potential, and by relating these components to weak meson–nuclear coupling constants... This involves, even for the two nucleon system, the understanding of the strong NN interaction at short distances, a problem of long standing interest by itself.

The parity-violating weak interaction hamiltonian was first introduced by Feynman and Gell-Mann [Fey58] in a current – current formulation. Since then it has undergone many refinements. One of the first was proposed by Cabibbo[Cab63]. In his theory the weak charged-current interaction of hadrons consists of two parts: a hypercharge-conserving current $J_w{}^{o}$ and a hypercharge non–conserving part $J_w{}^{1}$. The total current can be written as

$$J_w^{\ h} = \cos\theta_c\, J_w^{\ o} + \sin\theta_c\, J_w^{\ 1} \quad , \tag{5.10}$$

where the Cabibbo angle is $\theta_c = 0.235 \pm 0.006$ rad. Although this theory is successful in explaining the experimental results for leptonic or semi–leptonic processes, it had to be modified to explain hadronic reactions. As more knowledge has been gained in the areas of field theory, weak leptonic interactions, QED, and finally about quarks and QCD, the old theories have been modified to fit the new knowledge. As an example, the simple Cabibbo interpretation has now been modified so that the $J_w{}^{o}$ current drives the up → down quark transition and the $J_w{}^{1}$ current drives the up → strange quark transition. There is as yet no complete theory to explain all elements of the hadronic weak interaction. However, it is possible to draw a theory–independent diagram of the interaction as shown in Fig. 5.2. In this figure one of the two strong interaction vertices has been replaced by a parity non-conserving weak vertex.

At low or intermediate energies, the exchange of mesons has been very successful in explaining the parity conserving interaction [Pre75]. By replacing a strong-coupling vertex by a weak-coupling one, this description can be extended to the Parity Violating Interaction, *PVI*. Since this description involves a rather large number of exchange particles, the problem of computing the parity-violating potential is in determining which mesons participate, which are forbidden, and which give only small contributions.

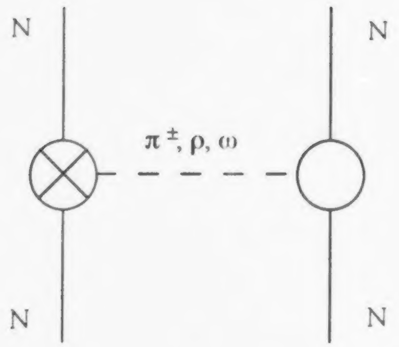

Figure 5.2. All possible one boson exchange contributions to a NN interaction. The weak vertex is indicated by the cross.

In general, the potential may be written as

$$V^{PNC}_{Weak} = V^{\rho\,\Delta T=0,2} + V^{\rho\,\Delta T=1} + V^{\pi\,\Delta T=1} + V^{2\pi\,\varphi\,\omega} \quad . \tag{5.11}$$

The long range part of the potential is contained in the one-pion exchange term V_{π}. This term will vanish if no isospin breaking is allowed [Sch72]. The exchange of the π^0 is forbidden by CP conservation because the π^0 is its own anti-particle. Thus, only charged pions can be exchanged. Of all the *OBEPs* (One Boson Exchange Potentials), pion exchange is the weakest of the terms in eq. 5.11. It is unfortunate that its contribution is so small since it is the one for which the most experimental information is available, as the parity-conserving pion exchange potential is well known.

The most significant terms of the parity non-conserving potential (eq. 5.11) are considered to be those due to ρ ($V^{\rho\Delta T=0,1,2}$) and ω (V^{ω}) exchange. The terms correspond to the exchange of $\rho^{\pm}$, ρ^0 and ω^0 but the actual particle exchanged is highly dependent on the energy of the nucleon. The reason $\rho^{\pm}$ exchanges are highly nucleon energy dependent is that the current-current Lagrangian has a purely charged-current character. The $\rho^{\pm}$ contribution decreases like the $\pi^{\pm}$ terms as these particles can only be exchanged by on-shell nucleons (a nucleon is considered on-mass-shell if E^2-p^2 is equal to the nucleon rest mass). Therefore at high nucleon energies, the contribution is from the exchange of ρ^0 and ω^0 only. These exchanges comprise the short range part of the potential. The ρ and ω contribute to the $V^{\Delta T=0}$ potential. This potential is often used to replace the 2π exchange term. The $V^{\Delta T=2}$ potential is strictly a ρ exchange. Other possible exchange particles are the pseudoscalar η and η', the scalar particles s and δ, and the vector meson ϕ. The exchange of scalar and pseudoscalar is restricted by Barton's theorem [Bar61] which forbids, due to CP invariance, any coupling of neutral $J = 0$ mesons, bosons and on-shell nucleons . This means that η, η', s, and δ^0 exchanges can be excluded to the extent that CP violation is negligible. The only observed case of CP violation is found in the decay of the kaon [Hug85]. It has a strength on the order of 10^{-3} of the weak interaction [Hug85]. As the weak interaction of hadrons causing the observed parity violation is on the order of 10^{-7} of the strong force, the effect of CP violation is negligible. Of the other possibilities, only the 2π exchange is expected to contribute significantly.

The effect of 2π exchange is zero in the limit of strict isospin-symmetry, except for the case of off-mass-shell nucleons [Hen74]. Although the off-mass-shell effect of 2π-exchange is small, it is thought to be the correction required to alleviate the discrepancy between parity-violation experiments and theoretical calculations [Lac68]. The simple Cabibbo theory predicts terms proportional to $\sin^2\theta_c$ and $\cos^2\theta_c$ for the 2π exchange terms. Calculations by Desplanques [Des72] and by Pirner and Riska [Pir73] have shown that the $\sin^2\theta_c$ term is negligible compared to ρ and ω exchange. In many treatments the surviving $\cos^2\theta_c$ term is assumed to be included in the potentials from vector meson exchange. Table 5.1 shows the coupling constants for the various terms in the PNC potential.

Parity violation experiments can be divided into two broad categories: experiments done on complex nuclei and those done on few-body systems. The experiments done on complex nuclei are in general easier to do experimentally and it is possible to find situations where the PNC effect is enhanced, but the theoretical interpretation is often confused by the internal structure of the nucleus, which, as mentioned in Chapter 2, is rarely well known. The experiments done on few-body systems have the problem that the parity-violating effect is generally suppressed by 10^{-7} compared to the parity-conserving interaction and so the experimental difficulty is mainly in reducing the experimental errors to a comparable level.

Another way of categorizing experiments was given by [Ade85] and separates the experiments into three categories. Type I experiments attempt to measure decay rates which should be zero if parity is conserved. The main experiment of this type is parity-violating α-decay. The decay we are interested in, $^{18}N(\beta\alpha)^{14}C$, is of this type. The classic type I example is the $^{16}N[2^-](\beta\alpha)^{12}C[0^+]$ decay studied by [Neu74]. Type II experiments observe non-vanishing pseudoscalar expectation values caused by interference between PC and PNC matrix elements. One type II observable is the circular polarization of gamma rays emitted by an unpolarized nucleus, for example ^{18}F [Eva85].

Type III experiments observe the non-pseudoscalar interference between the PC and PNC matrix elements, resulting in an observable that is second order in the weak interaction. An example is the existence of odd powers of $\cos\theta$ in the angular distribution of γ–rays emitted by an isolated nuclear state. Each one of these experimental types has theoretical and experimental strengths and weaknesses. Since, our interest is in type I experiments, the others will not be discussed further.

There are two major experimental difficulties associated with the observation of PNC β–delayed α–decay. The first is the lack of choice in the nuclear system inherent in an experiment which can only be performed by observing parity-forbidden transitions between energy levels of even–A nuclei. The second problem, even if such levels exists above the alpha-decay threshold, they must be selectively populated at a rate great enough that the PNC decay rate is observable over the background. The major theoretical obstacle is the fact that nuclear state calculations are very difficult to perform accurately. Often, further complications arise due to the level widths, if they are broad enough several energy levels may overlap. The interaction of these levels will then be determined by their respective angular momenta and the signs of the interference terms between them — information that is not always known.

Table 5.1. Weak coupling constants from the "best value" and "reasonable range" results of Desplanques, Donoghue, and Holstein [Des80] for the Glashow–Weinberg–Salam model[a]

Coupling Constant	"Best Value" ($x10^{-6}$)	"Reasonable Range" ($x10^{-6}$)
$(g_{\pi NN} f_{\pi})/\sqrt{32}$	1.08	0 : 2.71
$-(g_{\rho} h_{\rho}^{o})/2$	1.59	-1.59 : 4.29
$-(g_{\rho} h_{\rho}^{1})/2$	0.027	0 : 0.053
$-(g_{\omega} h_{\rho}^{2})/2$	1.33	-1.06 : 1.54
$-(g_{\omega} h_{\omega}^{o})/2$	0.80	-2.39 : 4.29
$-(g_{\omega} h_{\omega}^{1})/2$	0.48	0.32 : 0.80
$-(g_{\omega} h'_{\omega}{}^{1})/4$	0.0	—

[a] with the values: $g_{\pi NN} = 13.45$, $g_{\rho} = 2.79$, and $g_{\omega} = 8.37$.

5.3 Experiment Justification and Background

Recently several parity violation experiments have been proposed and/or carried out [Bal84, Eva85, Els84, Sno78, Lan85, Nag78, Kny84]. These have been very difficult experiments to perform with sufficient accuracy. At this time a *pp* parity violation experiment is underway at TRIUMF (E497) [Roy92]. This experiment, conducted with 233 MeV polarized protons incident on a LH_2 target, should determine the value of the coupling constants (see Table 5.1) of h_ρ and h_ω when combined with the results of other experiments. The experiment proposed here, $^{18}N(\beta\alpha)^{14}C$, is intended to complement it by determining the value of f_π. This coupling constant can not be accessed in the *pp* system since a PNC π^0 exchange would require the violation of both parity conservation and charge conjugation. As mentioned previously, CP violation is at least three orders of magnitude weaker than P violation alone.

It is possible to determine f_π in light nuclei because one often has initial and final states with identical spin but opposite parity. The parity non-conserving part of the nucleon–nucleon interaction allows for mixing through the weak interaction. This mixing can be observed in the laboratory by measurements of P_γ, the gamma ray circular polarization $<\sigma_\gamma \bullet \boldsymbol{p}_\gamma>$ or A_γ, the gamma ray asymmetry. In fact, experiments have been conducted on ^{21}Ne [Sno83], ^{18}F [Eva85], ^{19}F [Els84], and by scattering polarized protons on ^4He [Lan85]. In the latter three cases the situation is complicated by the fact that the experiments are also sensitive to a particular linear combination of f_π, h_ρ, and h_ω — $Af_\pi + B(h_\rho + 0.58h_\omega)$. A and B are determined by nuclear structure calculations. Fortunately, the validity of these calculations for ^{18}F and ^{19}F can be checked by comparison to 1st-forbidden beta-decay experiments. When this is done it leads to a reduction of the meson-nucleon coupling constants by a factor of three over what would be expected from $(L+\hbar\omega)$ shell-model calculations [Kub78]. Although this check is impossible for ^{21}Ne, since the corresponding β-decay does not occur, the reduction in the coupling constants is expected to be of the same magnitude and the same scaling is applied in comparing with other experiments.

The four mentioned experiments give a value of $f_\pi = (3.3 \pm 1.0) \times 10^{-7}$. However, as seen in Fig. 5.3, the experimental values do not have a common overlap due to the ^{18}F experiment. The value of f_π is interesting to theorists since 95% of its value can be attributed to neutral-current diagrams in the quark model. As well, calculations done by Holstein [Hol88] show that the small value of f_π given by the ^{18}F P_γ experiment would require the current algebra quark masses to be increased by a factor of two over the Weinberg values.

As mentioned previously, parity violation can also be observed in the emission of α particles. A classic experiment has been performed in the case of $^{16}N(\beta\alpha)^{12}C$, by Neubeck *et al.* [Neu74]. This experiment measured the parity-violating alpha width and found $\Gamma_{\alpha PNC} = (1.03 \pm 0.28) \times 10^{-10}$ eV. This was an impressive achievement. Unfortunately this particular decay is not dependent on f_π so it can not be used to constrain the possible values of this coupling constant. In the case of the $^{18}N(\beta\alpha)^{14}C$ reaction, it is possible to use a simple two-level model to analyse the data. For a simple case, one chooses a 0^-, $T = 1$ state in ^{18}O which α–decays, violating parity, to a 0^+ state in ^{14}C. It is assumed that this occurs due to mixing with a 0^+, $T = 0$ state. The PNC α–decay width can be written as $\Gamma_{\alpha PNC} = |A|^2\Gamma_\alpha(0^+)$. $\Gamma_\alpha(0^+)$ is the allowed α–decay width and $|A|$ is the amplitude given by

$$A = \frac{\left\langle 0^+\ T=0 \left[V_{PNC}(\Delta T=1) \right] 0^-\ T=1 \right\rangle}{\left(E_- - E_+\right) - 0.5\,i\left(\Gamma_- - \Gamma_+\right)} \qquad (5.12)$$

$E_\pm$, $\Gamma_\pm$ are the energies and total widths of the 0^+, 0^- states respectively. It can be seen that small level separations and/or decay widths can have a great effect in enhancing the mixing amplitude.

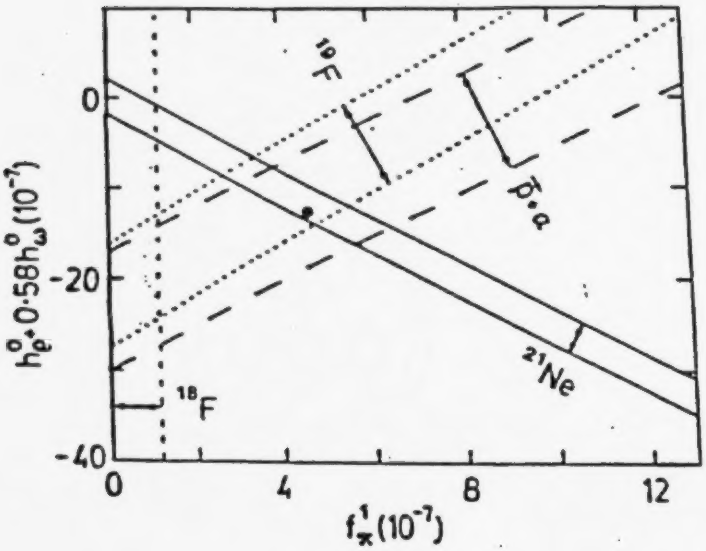

Figure 5.3. The results for the four experiments performed to determine f_π [Els84, Eva85, Lan85, Sno83]. As described in the text, the result for ^{21}Ne has the same scaling factor of 1/3 applied to it as was used for ^{18,19}F.

The intention of the full scale experiment is to measure the PNC α-decay width of the decay of the 0^- state in ^{18}O at 6.88 MeV, by the reaction ^{18}N($\beta\alpha$)^{14}C. Parity is violated in emission of an α from this state for the following reason. The level after β–decay is 0^- while both the α and ^{14}C are 0^+ particles, thus the angular momentum, L, carried by the α must be zero. The parity of an $L = 0$ α is $(-1)^L = +1$, therefore, since the initial parity is negative, it cannot equal the parity of the final state: $(+1)_\alpha \bullet (+1)_C \bullet (-1)^0$, which is positive. The beta decay to the 0^- level has been studied and a 14.8% branching ratio has been assigned [Oln82]. Some preliminary shell model calculations have been done [Zha89], and a PNC α-width is estimated to be of the order 10^{-11} eV.

For this particular reaction both isoscalar and isovector components of the PNC interaction apply, resulting in a PNC effect proportional to $(f_\pi - 0.27\ h_\rho)$[Bro88]. Therefore a further independent confirmation of the value of f_π is possible. The main goal of the experiment performed in this thesis is to determine whether it is possible to collect and accurately analyse the data. To answer this, many elements of the experiment were investigated and the results are presented in the next sections. Before examining the data collected, some relevant background information is required. Fig. 5.4 shows the level diagram of ^{18}O. Table 5.2 gives the expected α and ^{14}C energies for the known α-emitting states in ^{18}O populated by β transitions from ^{18}N and the 6.88 MeV PNC state. The α-emission threshold for ^{18}O is 6.228 MeV [Ajz87].

As PNC events are rare, an important factor to estimate is the expected count rate for the experiment. Under the assumption that most of the decays after PNC transition are via γ–emission, the alpha width of the 6.88 MeV state can be estimated to be

$$\Gamma_\alpha = \frac{\Gamma_\gamma N_\alpha (6.88\ \mathrm{MeV})}{N_\beta (6.88\ \mathrm{MeV})} \quad . \tag{5.13}$$

Here N_α(6.88 MeV) is the number of α-particles observed from this state, and N_β(6.88 MeV) is the number of β-decays to that state. The width of the 7.62 MeV state is dominated by α decay, so $N_\beta(7.62) \approx N_\alpha(7.62)$. Using this relation in eq. 5.13 allows $N_\alpha(6.88)$ to be calculated with respect to the observed α-decay from the 7.62 MeV level

$$N_\alpha(6.88) = \frac{\Gamma_\alpha}{\Gamma_\gamma}\frac{N_\beta(6.88)}{N_\beta(7.62)}N_\alpha(7.62) \quad . \tag{5.14}$$

Referring to table 5.2 for the relevant branching ratios, using the value of 25 fs for the lifetime of the 6.88 MeV state [Oln82] and with 10^{-11} eV for the PNC alpha width [Zha89] one gets

$$N_\alpha(6.88) = 10^{-9} N_\alpha(7.62) \quad . \tag{5.15}$$

Eq. 5.15 can be used to find the required number of PC α–decays from the 7.62 MeV level for a particular rate of PNC α's. For a minimally acceptable rate of one PNC α per day, the rate of α's from the 7.62 MeV level must be of the order 10^4 s^{-1}. An accurate knowledge of the γ–decay lifetime of the PNC level would improve the quality of the estimate since the value of 25 femtoseconds [Oln82] is only an upper limit. Also, it would be desirable to have another check on the expected PNC alpha width using the most modern shell model calculations possible.

5.4 The ^{18}N$(\beta\alpha)^{14}$C Parity Violation Feasibility Study

Two experimental runs were undertaken to study the requirements needed to mount an experiment to observe the the parity violating α-decay of ^{18}N. During the Red Giant experiment it was discovered that there was some ^{18}N contamination of the molecular ^{16}N ion beam. This ^{18}N contamination occurred since ^{18}N^{14}N$^+$ has the same m/q as ^{16}N^{16}O$^+$ which was the form of the molecular ^{16}N ion beam used. Additional short runs (each of duration ~ 2 hours) were carried out to accurately measure the shape of the β-delayed α spectrum from the decay of ^{18}N at the m/q position of 34. During these background runs there appeared to be additional, previously unobserved, high-energy α peaks in the spectrum. The first PNC feasibility study run (July, 1992) had the secondary goal of collecting data on these high energy α particles. The second run (June, 1993) was solely intended for the PNC feasibility study. The next section presents the data gathered in each of these runs and some of the analysis performed to study the background in the region of interest for the PNC decay.. The final section lists the requirements necessary for the successful completion of the experiment.

Table 5.2: A summary of pertinent information for the $^{18}N(\beta\alpha)^{14}C$ decay. The excitation energy (E_x) in ^{18}O, β-branching ratio, and spin/parity assignments are given. As well, the expected energies of the emitted α and ^{14}C in the Laboratory frame are also given. The sub-threshold state at 6.198 MeV is included since it is relevant to the K-matrix fits. Brackets indicate uncertain values.

E_x [keV]	Branching Ratio [%]	J^π	E_α [MeV]	$E_{^{14}C}$ [MeV]
6 198.22 ± 0.40	1.4 ± 0.2	1^-	—	—
6 880.45 ± 0.27	14.8 ± 0.8	0^-	0.507	0.145
7 620 ± 2	6.8 ± 0.5	1^-	1.083	0.309
8 039 ± 2	1.8 ± 0.2	1^-	1.408	0.402
(9 030)	(3.6)	(1^-)	2.179	0.623

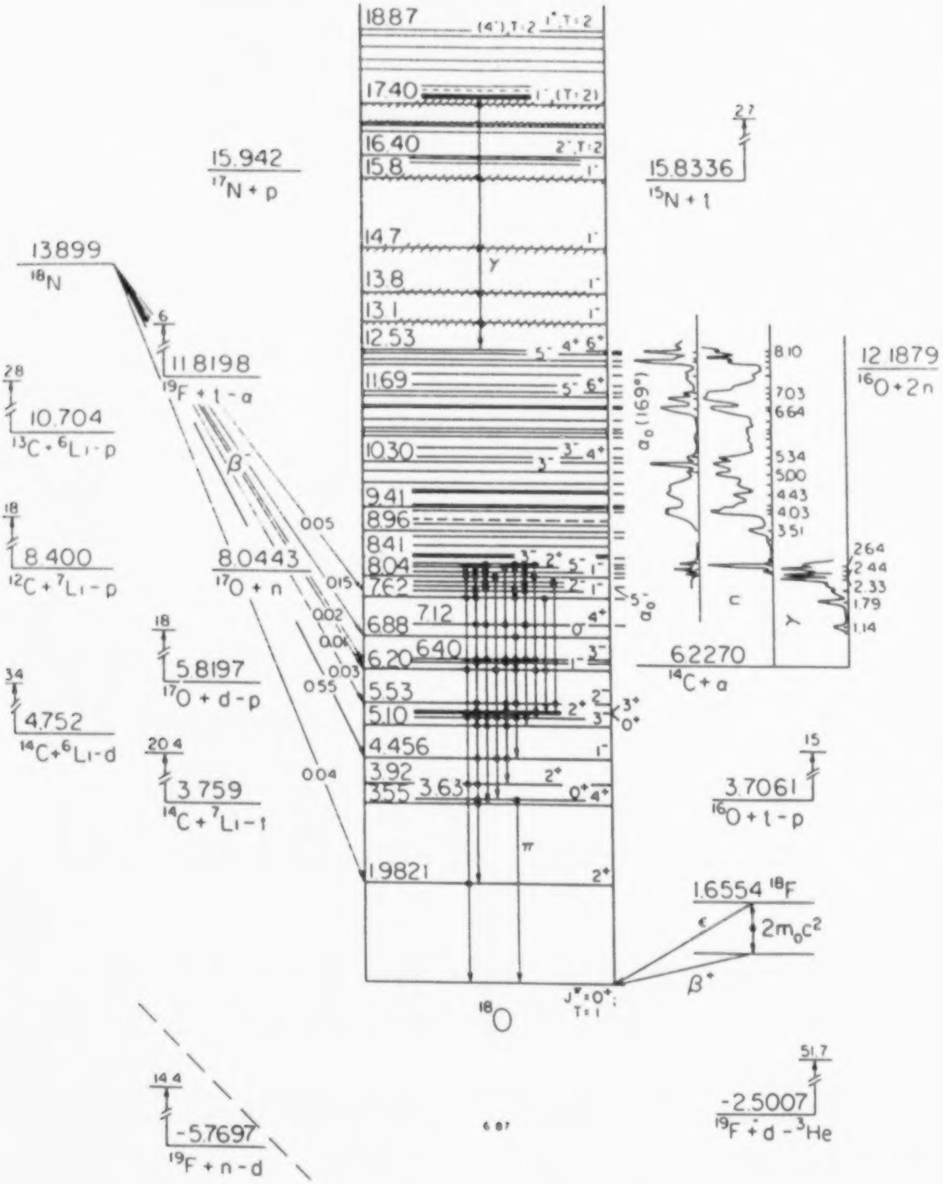
18.87
17.40
16.40
15.8
14.7
13.8
13.1
12.53
11.69
10.30
9.41
8.96
8.41
8.04
7.62
7.12
6.88
6.40
6.20
5.53
5.10
4.456
3.92
3.63
3.55
1.9821
15.942
^{17}N + p
13.899
^{18}N
11.8198
^{19}F + t - α
10.704
^{13}C + ^{6}Li - p
8.400
^{12}C + ^{7}Li - p
8.0443
^{17}O + n
5.8197
^{17}O + d - p
4.752
^{14}C + ^{6}Li - d
3.759
^{14}C + ^{7}Li - t
15.8336
^{15}N + t
12.1879
^{16}O + 2n
6.2270
^{14}C + α
3.7061
^{16}O + t - p
1.6554 ^{18}F
$2m_0c^2$
β^+
β^-
-2.5007
^{19}F + d - ^{3}He
-5.7697
^{19}F + n - d
^{18}O
$J^\pi = 0^+$; T = 1
0.05
0.15
0.02
0.01
0.03
0.55
0.04
γ
π
a_0 (169°)
n
γ
6 87

Figure 5.4. The energy level diagram for ^{18}N(β)^{18}O* from [Ajz87].

5.4.1 The $^{18}N(\beta\alpha)^{14}C$ Decay Data

The data were collected with the apparatus described in Sections 3.4 and 3.5. There were six SSB detectors arranged into three detector stations. Each station had two detectors separated by a narrow gap arranged face to face to view the foil containing the deposited ^{18}N. The data from each of the three pairs of detectors were analysed in the following manner. First the raw data was skimmed to remove all pulser events, all scaler events, and with a very loose criteria to eliminate most non-valid events. The coincidence condition required a signal in both detectors of any pair (1 and 2, 3 and 4, or 5 and 6). The first level skim removed only those events which had more than one detector pair with coincidence events or a coincidence between non-paired detectors. The accepted data consisted of events in which there was a coincidence in one and only one pair of detectors.

The principle cut on the ADC data was on the ratio between the pulse heights of the detector pairs. This ratio was calculated for both combinations of each pair of detectors *i.e.* (detector–1/ detector–2) and (detector–2/ detector–1). The cut required that one or the other of the ratios satisfy the limits, because particles in the detectors were not identified. From kinematics, the ratio of kinetic energies α:^{14}C is 3.5:1. The particles, however, suffer both energy loss and straggling in the carbon collection foil and the gold layer on the detector itself. Using the TRIM [Zie85] Monte Carlo program, the α and ^{14}C energy losses were calculated as shown in Fig. 5.5. As can be seen, at the energies of interest for the PNC decay the 150 keV ^{14}C will lose about 30 keV. A 500 keV α loses a similar amount, ~32 keV. Assuming a gaussian spread for the energy loss, the standard deviation in the TRIM results should be ≤ 2 keV for either material [Leo87]. The energy loss in the foil and gold layer results in an upward shift of the peak of the pulse height ratio spectrum (see Fig. 5.6). Fig. 5.7 shows the distribution of ratios as a function of observed α energy. The effect of varying the ratio cuts can be easily seen. The majority of the valid events lie in a narrow band of ratios, but it is clear that there exist tails extending toward larger values. This is more apparent in the thicker detectors used in the (July, 92) run. For the first level skim, the detector pair pulse height ratio was considered valid if it was between 1 and 10. For the investigation that followed the allowed ratio was set individually for each detector. The lower limit was between 3 and 3.4. The upper limit was set to allow the most events possible and was between 7.5 and 8.5. The ratio cut is the best tool available to reduce the background caused by β–β, β–α, and β–^{14}C coincidences since these in general have either very large or very small ratios.

Energy calibration of the α-spectrum was provided automatically by the two narrow α peaks in the ^{18}O spectrum [E_α = 1.081 ± 0.001, and 1.409 ± 0.001 MeV] [Ajz87]. The Red Giant experiment had previously measured both the electronic resolutions (FWHM = 14–20 keV) and the detector resolutions using a ^{148}Gd source (E_α = 3.182 MeV, with resolution FWHM = 22–28 keV). The ranges reflect variations between the detectors. The resolution for α-particles from ^{18}N($\beta\alpha$)^{14}C was found to be 48 keV. This larger resolution was due to β-neutrino recoil effects which, for a pure G-T decay, would have values of 39 and 43 keV for the two narrow levels, respectively. Adding in the intrinsic 25 keV resolution gives values consistent with the observed 48 keV resolution.

The skimmed data were used to generate two "summed" spectra, one which had no additional cuts and another which passed the tighter ratio cuts mentioned previously. Figs. 5.8 and 5.9 shows these summed spectra for each of the experimental runs. It is apparent from the counts per channel in each spectrum that the cuts have little effect except in the low energy region (~500 keV for the α-particles) (see also Table 5.3). This is the area of interest for the PNC experiment. The effect of the cuts is to reduce the background in that region. The 1992 run (Fig. 5.8) has more background in the PNC region than the 1993 run (Fig. 5.9) due to the use of a thick (28 μm) detector rather than the two thin detectors used in the second experimental period.

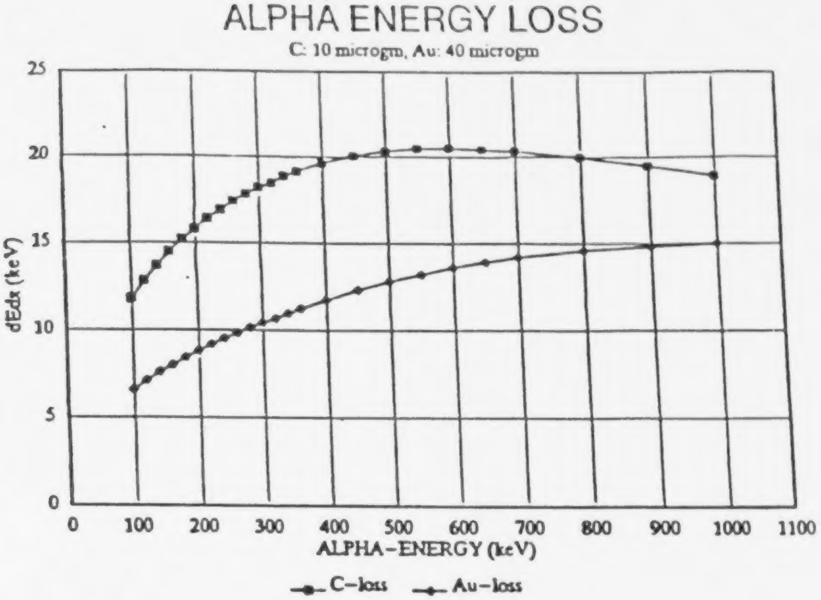

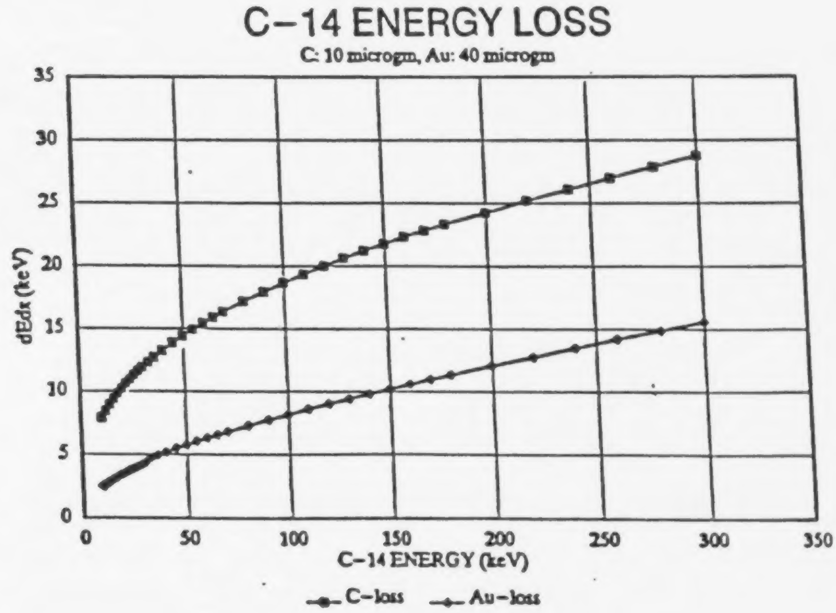

Figure 5.5. TRIM calculations for the sum of the energy loss in both the carbon collector foil and the gold layer of the SSB. Curves are given for both α and ^{14}C particles.

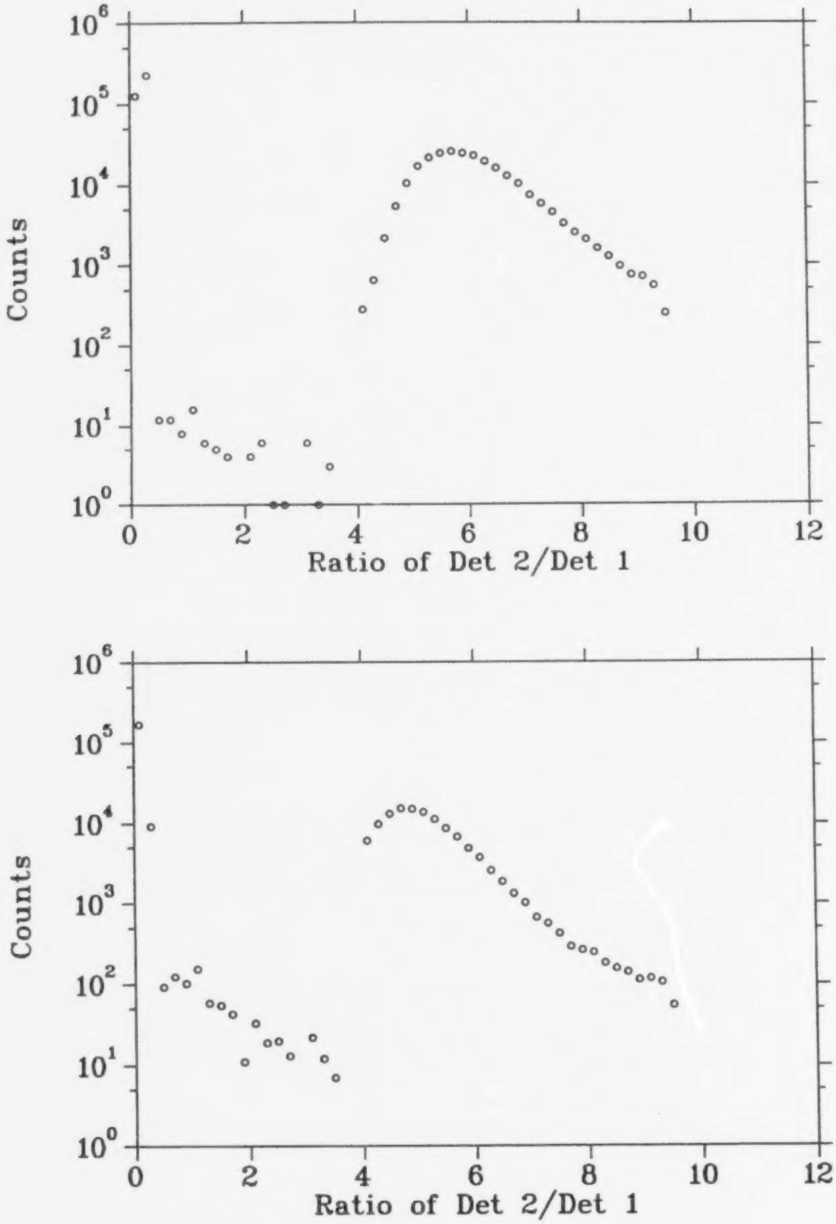

Figure 5.6. The spectra of the observed ratio between the pulse height in Detector 2 to Detector 1 for all the data which survived the first level skim. The upper spectrum is from July 92 and the lower from June 93.

The analysis which is described below depends on information gathered for the Red Giant experiment, the details of which are provided in [Azu94]. From the Red Giant experiment it was known that the coincidence time between two detectors had a FWHM of ~150 ns. This meant that timing information was not a useful tool for vetoing events and so the conditions on the TDC time difference were set very loosely. Fig. 5.10 shows a typical time difference spectrum for detector–1 and detector–2 from each experimental run. The Red Giant experiment also determined the coincidence efficiency (40%) as a function of energy and verified that it was constant down to $E_\alpha \sim 550$ keV. This work also discovered that the rate of purely random coincidences, as determined by examining the data rate for unpaired detectors *e.g.* detector–1 and detector–6, was negligible.

Table 5.3. The number of events seen in the experiment during each of the run periods showing the total number of α particles observed and the number of α particles observed in the 1.081 MeV peak $[N_\alpha(7.62)]$. The figure from which the data were derived is also given with (u) referring to the upper pair of spectra and (l) referring to the lower pair.

Run Period	Total α Events	N_α (7.62 MeV)	Collection Time [s]	Figure
June 92 (skim only)	540 827	273 031	190 110	5.8 (u)
June 92 (tight cuts)	453 839	206 631		5.8 (l)
June 93 (skim only)	304 398	273 512	126 692	5.9 (u)
June 93 (tight cuts)	273 512	124 554		5.9 (l)

Of more interest and utility than the spectra shown in Figs. 5.8, and 5.9 is a two-dimensional energy spectrum for each detector pair. Fig. 5.11 shows the spectra of the first detector pair (detector–1 and detector–2) for each of the run periods. The good events are clustered in intense diagonal bands. The structure observed in the singles spectrum is clearly reproduced and it is apparent that the background is very low. The outer contour represents regions where there are at least two counts per 31 keV energy bin. It is very clear that valid events fall within very narrow regions that are easy to identify and select. Note that the contours span a range of four orders of magnitude.

It is possible to focus in on the PNC region. Figs. 5.12 and 5.13 shows the energy region in which the PNC events are expected to lie for detector pair #1 for each of the running periods. The upper spectra show the region after only the first level skim has been applied. The lower spectra are those events which survive the tighter cuts. All four figures are quite clean. In each set of figures is a box which shows the area where the majority of the PNC events are expected to occur. In each case the limits of the box are adjusted to compensate for energy loss in the carbon foil and gold layer. Using the values given in Table 5.2 for the 0^- level, the expected mean energies are E_α = 475 ± 48 keV and E_C = 115 ± 48 keV for the ^{14}C. The events shown inside the boxes of Fig. 5.12 or 5.13 are not PNC α's but are evidence for background events in the energy region of interest.

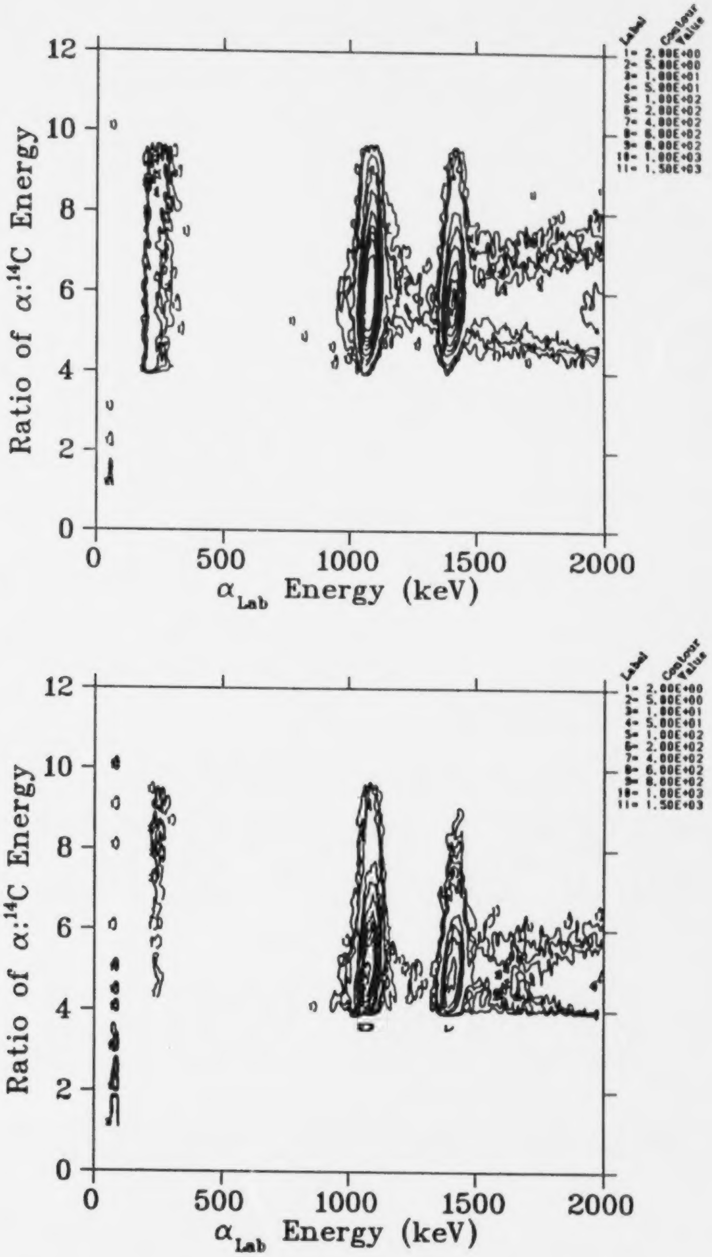

Figure 5.7. The spectra of the energy ratio versus alpha energy for both the July, 92 (upper) and June, 93 (lower) experimental periods. All of the data which survived the first level skim are shown in the graphs.

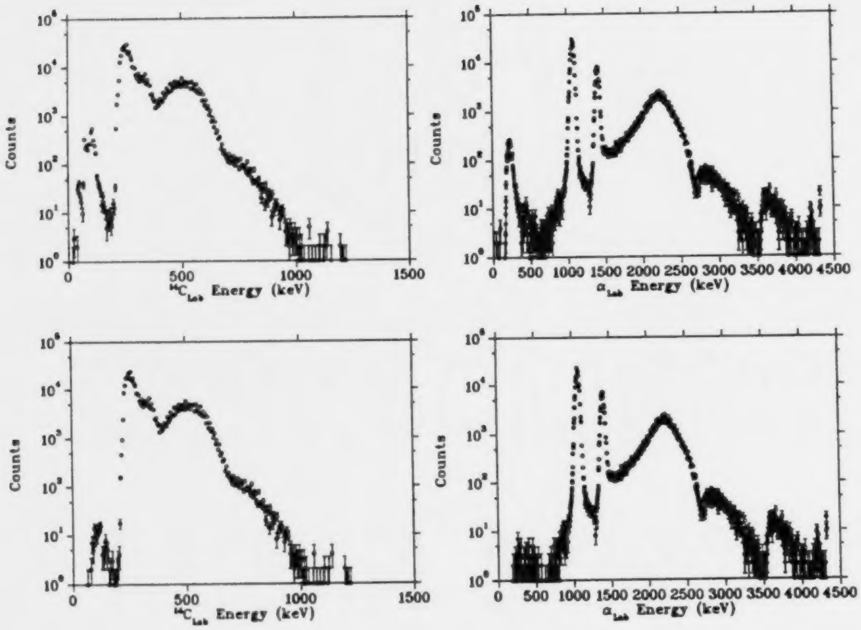

Figure 5.8. The spectra collected during the July 92 running period. The upper two spectra are the α and ^{14}C spectra with only the first level skim cuts applied. The lower two spectra are the α and ^{14}C spectra with the tighter ratio constraints applied.

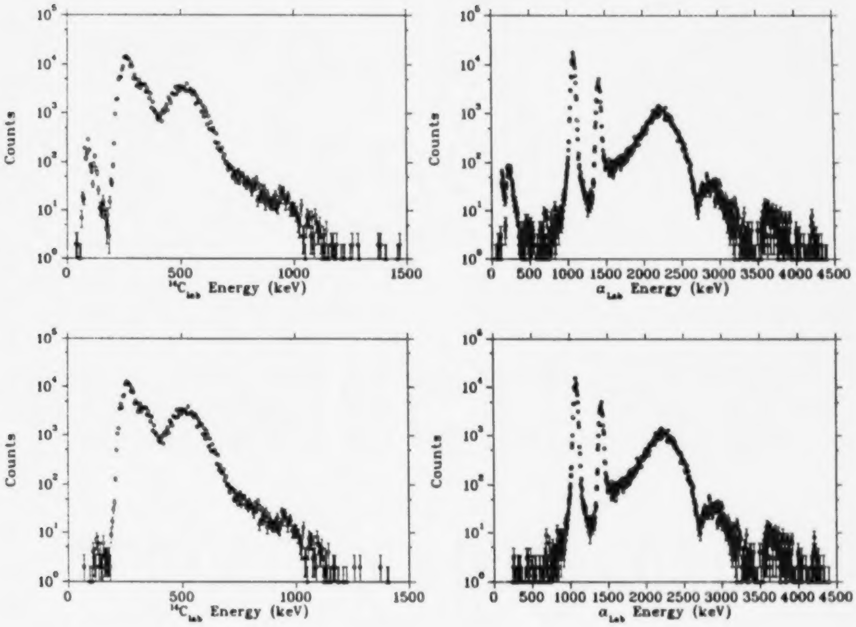

Figure 5.9. The spectra collected during the June 93 running period. The upper two spectra are the α and ^{14}C spectra with only the first level skim cuts applied. The lower two spectra are the α and ^{14}C spectra with the tighter ratio constraints applied.

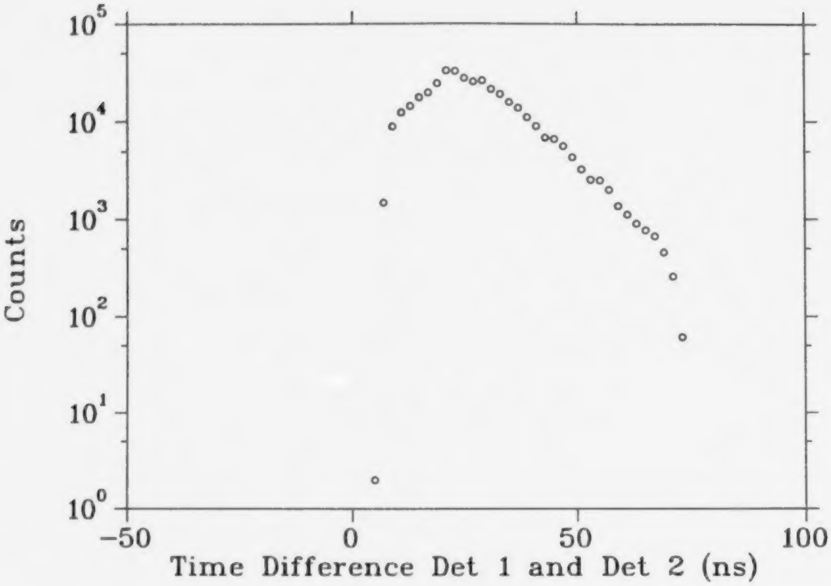

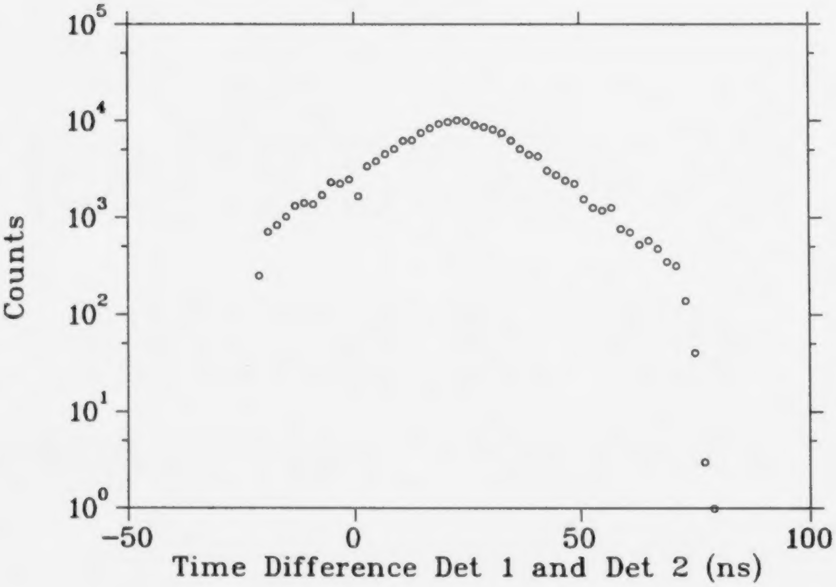

Figure 5.10. The spectra of the time difference between the first detector pair for both running periods. The upper spectrum is from July 92 and the lower from June 93.

The background events visible in Figs. 5.12 and 5.13 in the PNC region are due to two sources which can not be eliminated completely by ratio cuts. The first type of background is due to either to the coincidence between an energy-degraded α and an energy-degraded ^{14}C from one of the higher energy peaks, or else due to the tail of the broad α-peak (at E_α = 2.2 MeV) extending downward into the region of interest (see the α spectra in Fig. 5.9) The chance that an α will be energy-degraded is slight (<0.1% of the main peak α's). The same degradation probability also applies to the ^{14}C. As well, the degradation must leave both particles in the PNC region. As ~50% of the observed α–^{14}C events are from the decay of the 7.620 MeV level, this decay is the largest possible source of energy degraded events. The kinematics for the decay of the 7.620 MeV level give a 1.081 MeV α and a 0.309 MeV ^{14}C (see Table 5.2). If the PNC α peak is assumed to have the same width as for the decay of the 7.620 MeV level (±48 keV), then the chance the degradation places the particle in the PNC region is the ratio of that width to the total available energy assuming a uniform low energy tail. Thus the total probability that both the α and ^{14}C from the 7.620 MeV level would be degraded, in coincidence, and in the required energy region is given by:

Total probability α is degraded: $< 10^{-3}$.

Total probability ^{14}C is degraded: $< 10^{-3}$.

Chance the α is in the PNC region: 0.096 MeV/ 1.081 MeV $\approx 10^{-1}$.

Chance the ^{14}C is in the PNC region: 0.096 MeV/ 0.309 MeV $\approx 3 \times 10^{-1}$.

Coincidence efficiency: 4×10^{-1}.

Total Probability of a α–^{14}C coincidence in the PNC region: $< 1.2 \times 10^{-8}$.

The coincidence efficiency must be included since we are interested in α–^{14}C pairs in this experiment. This estimate is only meaningful for coincidence events since events which are energy degraded singles will not make it through the ratio cuts. The probability that both particles of the pair will be degraded into the PNC area is an effect on the order of probability of the observation of a PNC α–^{14}C pair (one PNC α for every 10^9 α–^{14}C pairs from the decay of the 7.62 MeV level) itself but is smaller than the other possible sources of background.

The possible background due to the tails of the known higher energy α-emitting states is harder to analyse. Fits using the K–matrix formalism [Fil89] to the existing spectra have been performed by Buchmann [Buc94], and Giesen [Gie94]. K–matrix fitting allows one to take into account the interference between the various states, the α-penetrability, and the effects of sub-threshold states into the calculation of the expected spectrum. The initial fits done by Buchmann produced an α contribution in the PNC area from all of the higher energy α-emitting levels that was 100 times the expected number of PNC α's from the 6.88 MeV level. This signal to background ratio is of the same order of magnitude as that observed in the ^{16}N PNC experiment [Neu74]. As the shape of the background will be known from the K–matrix fitting it will be possible to subtract it from the observed spectra. Thus this level of background can be dealt with but further study to determine if this magnitude of background is in fact correct is required.

The second, and more troublesome, form of background is due to β–^{14}C coincidences where the β has lost about 500 keV of energy within the detector. With the thin detectors used the expected energy loss is ~25 keV. Thus the electron would have to lose twenty times the expected value, which does occur. For the relativistic electrons involved in the experiment the detectors are sufficiently thin that Vavilov's energy loss theory [Leo87] applies. The probability of an electron losing ~500 keV can be estimated from the data itself. Assuming that all events in the area of interest are from such β–^{14}C events, then using the gated spectrum in Fig. 5.12 for the thinner detectors of the second run period, one calculates 3.2 x 10^{-5} β–^{14}C events per detected alpha particle in the 1.081 MeV peak. This rate is calculated by taking the four observed number of events in the expected area of the PNC α–^{14}C events for Fig 5.12. and dividing by the observed number of α particles in the 1.081 MeV peak (see Table 5.3). This rate can be directly compared to the expected rate of PNC α particles from eq. 5.15. This is effectively the non-removable background of the experiment. This rate would generate a substantial background if the desired number of

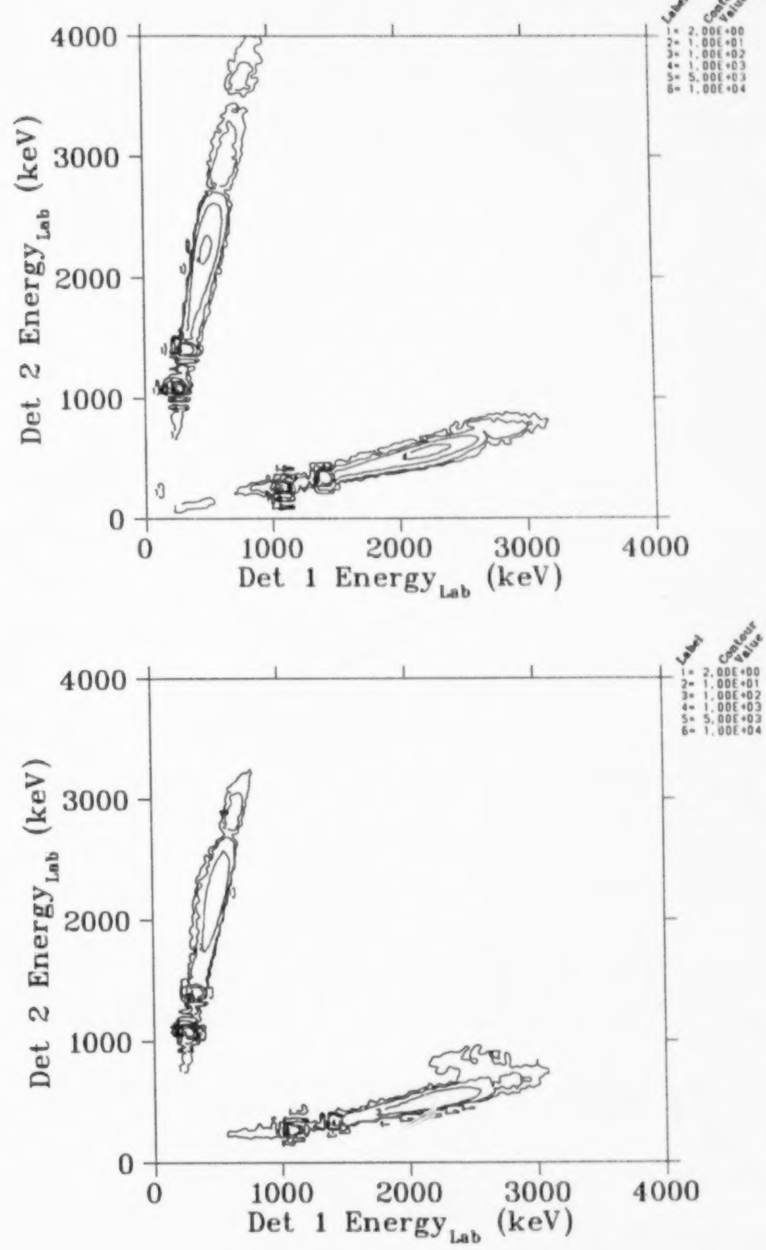

Figure 5.11. The 2D spectra for the first detector pair. The first contour level signifies 2 events in the energy bin. The upper spectrum is from July 1992 and the lower from June 1993.

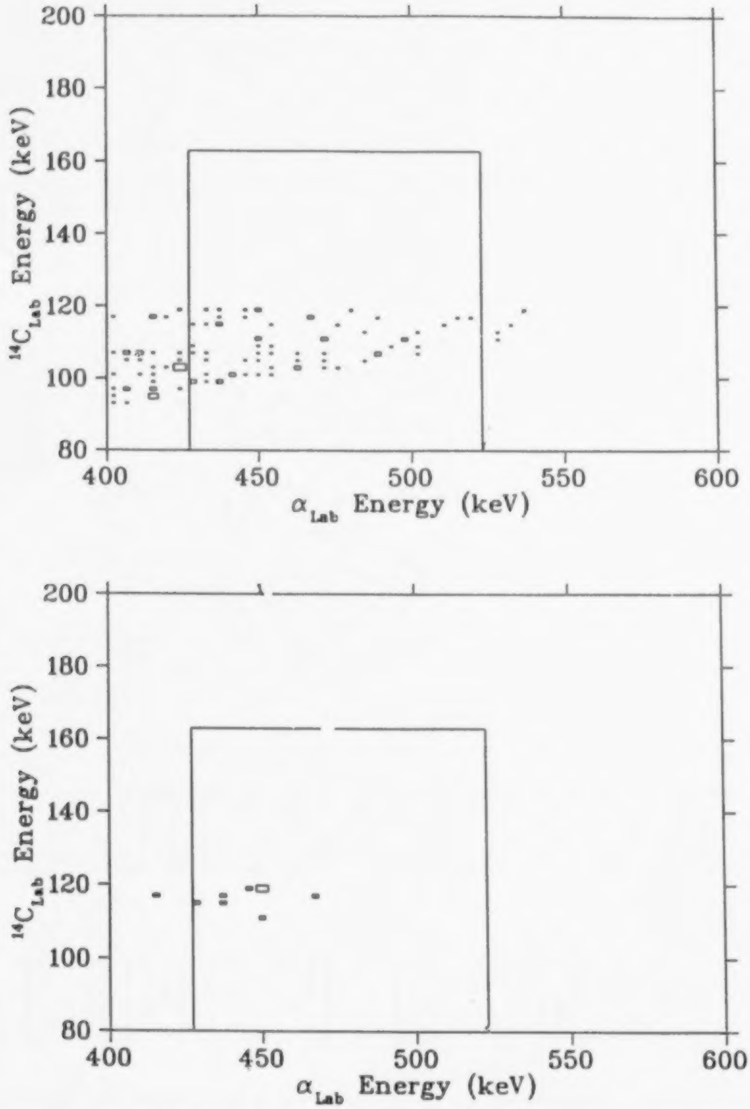

Figure 5.12. The area where parity violating α particles are expected to be observed. The upper spectrum has only the first level skim applied while the lower has the all the tighter constraints applied. The size of the rectangle indicates the number of events in the bin. The smallest rectangle indicates 1 event. The spectra are from the July 1992 running period. The large box indicates the energy region in which the majority of the PNC events are expected.

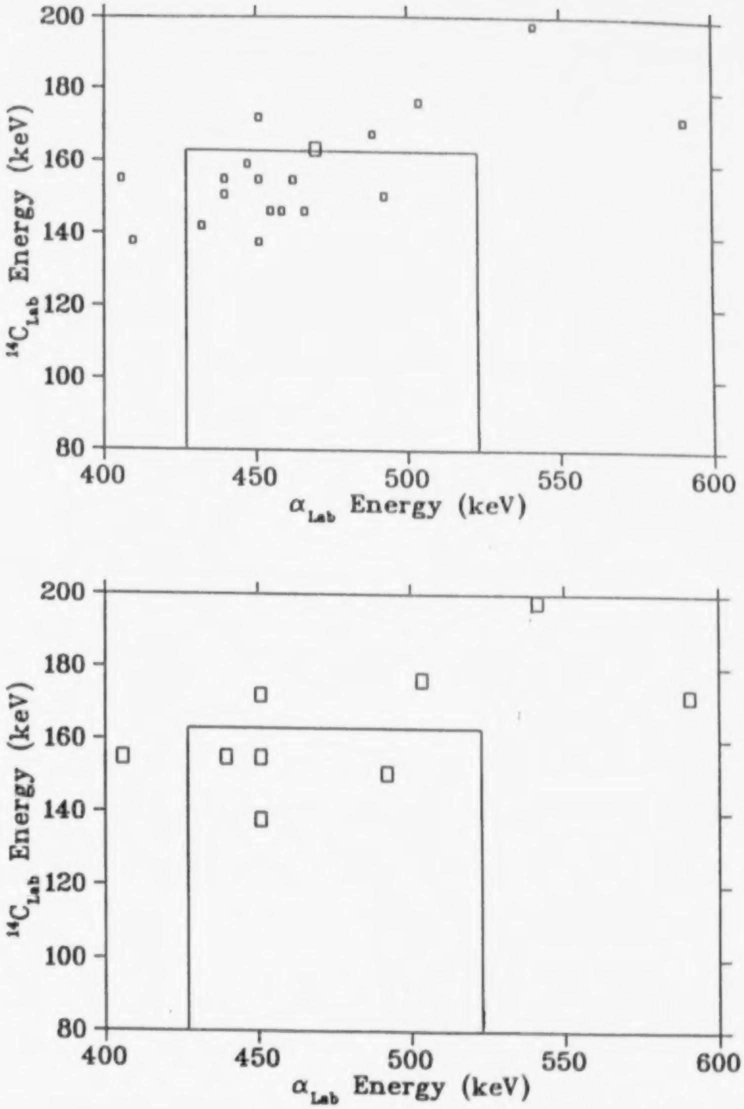

Figure 5.13. The area where parity violating α particles are expected to be observed. The upper spectrum has only the first level skim applied while the lower has the all the tighter constraints applied. The size of the rectangle indicates the number of events in the bin. The smallest rectangle indicates 1 event. The spectra are from the June 1993 running period. The large box indicates the energy region in which the majority of the PNC events are expected.

α particles (~10^9) in the 1.081 MeV peak were obtained. However, closer examination of Fig. 5.12 reveals that most such events are clustered above the expected energy values (shown by the box) for the PNC α/carbon pair. How many background events might leak down into a more tightly constrained PNC region is impossible to predict from the available data.

5.4.2 Comments on Performing the ^{18}N($\beta\alpha$)^{14}C PNC Experiment

To assess the feasibility of the proposed experiment and the requirements for its success three concerns must be addressed. In discussing these concerns the requirements for the experiment will naturally arise and be dealt with.

The first area of concern centers on the experimental apparatus. The successful completion of the Red Giant experiment and the two ^{18}N runs have confirmed that the principles of the detector/collection station and the associated DAS are sound. Some refinements of both systems are necessary to conduct the PNC experiment more efficiently. The first refinement actually results in a simplification of the system. There is little advantage in using more than one detector station since, due to the short half-life of ^{18}N, there was little net contribution to the overall event total from the second and third stations. Using only one station simplifies the electronics as well.

As for the detectors, it would be advantageous to commission a detector manufacturer to produce a pair of custom-designed thin (≤ 7 μm thick), large area (100 mm^2) detectors. This would reduce the contribution of β–^{14}C coincidences and boost the detection efficiency considerably over the 50 mm^2 detectors in current use. Unfortunately, such thin detectors produce more electronic noise. The solution, if the noise level is excessive, would be the development of low-noise preamplifiers. The main amplifiers themselves could be replaced by high-quality spectroscopy amplifiers. A desirable but not essential improvement to the DAS would be the utilization of high-precision 13-bit spectroscopy ADC's. The thinner detectors would not be able to stop the high energy α's ($E_\alpha > 1.5$ MeV) and so could be backed up by a pair of standard SSB detectors to operate in ΔE–E mode. The second detectors could also function as a β–veto.

Beyond the changes mentioned above and some mechanical redesign of the current system, neither the collection station nor the detectors/DAS are a cause for concern with regard to accomplishing the experiment.

The second concern relates to the data analysis and the ability to extract the PNC α peak. The major problems are background and the signal-to-background ratio. As mentioned in Section 5.5.1, there are two backgrounds of importance. The most important is the β–^{14}C background — this is invasive and will have to accepted. However, as this background is of a random nature, it can be estimated and subtracted by fitting the background in a region where one does not expect PNC events to occur. This would require a proper statistical handling of the resulting data, but such techniques are routinely applied in other areas of nuclear and particle physics.

More difficult to quantify is the possible effect of a tail from the known, higher-energy α-emitting states extending down into the PNC area. Work is underway [Gie94, Buc94] to investigate the expected contributions via K-matrix calculations. The work is complicated by the large number of available α-emitting states and the rather poor knowledge of the spins and parities of the high-energy states in ^{18}O. A much better model of the important nuclear states in ^{18}O is vital for the success of the K-matrix fitting and such calculations should be pursued. In the advent that the contribution to the spectra in the PNC area is non-zero, it can be handled in the manner of the β-^{14}C background, however, in this case, it is clear that the K-matrix fit has to be very well understood.

The data collected so far (see section 5.5.1) do not indicate that either of the backgrounds or the data analysis would preclude the completion of the PNC experiment. Further theoretical work would clearly benefit the experiment.

The final and most important concern is the production of ^{18}N at TISOL. As the number of PNC α's is directly related to the number of α's observed in the 1.081 MeV peak, it is vitally important that the number of ^{18}N ions delivered to the collection station be as high as possible. During the two run periods, the ^{18}N production yield was estimated to be about 10^4 s^{-1} based on measurements of γ activity taken at the Faraday cup just ahead of the detector endstation. This rate of ^{18}N atoms is clearly too low.

Based on the run data, the α–^{14}C coincidence event rate from the 7.62 MeV level was about one per second. How does this rate compare with what is expected for an ion beam intensity of 10^4 ^{18}N atoms/s? The number of ^{18}N atoms which are collected on the foil for an intensity of 10^4 ^{18}N atoms/s is given by

$$N(^{18}\mathrm{N}) = \frac{10^4}{\lambda_{(^{18}\mathrm{N})}}\left(1 - e^{-\lambda_{(^{18}\mathrm{N})}0.6s}\right)$$

$$= 4300\ ^{18}\mathrm{N}\ \text{atoms deposited on the foil}\ . \tag{5.16}$$

The ^{18}N atoms on the foil at the end of the collection period are rotated between the first detector pair. This takes 0.25 s during which 25 % of the ^{18}N atoms will decay. The activity, A, of the ^{18}N decaying will give the number of α–^{14}C pairs expected.per second given by

$$A = \lambda_{(^{18}\mathrm{N})}\, N(^{18}\mathrm{N})\, e^{-\lambda_{(^{18}\mathrm{N})}\,0.6s}$$

$$= 1870\ ^{18}\mathrm{N}\ \text{atoms decaying per second}\ . \tag{5.17}$$

The number of α–^{14}C pairs which can be expected from the above activity is

$$= A\, C_{eff}\, BR_{\beta}(7.62)\, E_{SA}$$

$$= 14\ \alpha - {}^{14}\mathrm{C}\ \text{pairs per second}\ . \tag{5.18}$$

where C_{eff} is the coincidence efficiency (40 %), $BR_{\beta}(7.62)$ is the branching ratio to the 7.62 MeV state, E_{SA} is the solid angle the detector pair subtends (37 % of 4π). The calculated rate of 14 α particles/s is a factor of 14 greater than the observed decay rate. This indicates the initial assumption of the average beam intensity was probably incorrect and the current was closer to ~7 x 10^2 ^{18}N atoms/s which gives one α–^{14}C pair per 10^3 ^{18}N ions. This reduction from the single γ measurement is understandable since the proton beam current available from TRIUMF varied with each run, and the transmission through the ion beamline varied due to periodic drifting of the bending magnet field. Thus the expectation is that the average rate would be less than the optimum estimate.

SILT calculations [Dau90] predict a yield of about 10^9 atoms/s/μA for typical TISOL zeolite target thickness (see Fig. 5.14). The desired rate is ≥1 PNC α per day. This requires an α rate in the 1.081 MeV peak of ~10^4 s^{-1}, or an ion beam intensity of >10^7 ^{18}N atoms/s. This rate is 10^3 times greater than what was available during the test runs. As with the Ne yield calculations in Section 4.8, the largest uncertainty in the prediction is the diffusion time for the N isotopes from the Zeolite target. To the extent that one is willing to believe SILT calculations, it may be possible to obtain some idea on the order of magnitude of the diffusion time from a Zeolite target. The ratio of the ion beam intensity between ^{18}N and ^{16}N should depend only of the amount of each isotope produced in the target and different decay losses during the diffusion time due to their different half-lives. Other factors such as ionization efficiency and transmission should be the same. The Red Giant experiment measured a ^{16}N ion beam intensity of 10^6 ^{16}N atoms/s. The ^{18}N beam intensity is 10^3 ^{18}N atoms/s. Fig. 5.14 gives the expected production ratio in the target. The diffusion time can be estimated from

$$\frac{N(^{18}\mathrm{N})\, e^{-\lambda_{(^{18}\mathrm{N})} t_D}}{N(^{16}\mathrm{N})\, e^{-\lambda_{(^{16}\mathrm{N})} t_D}} = \frac{I\,(^{18}\mathrm{N})}{I\,(^{16}\mathrm{N})}$$

$$\frac{3\,x\,10^{9}\, e^{-1.16\, t_D}}{10^{10}\, e^{-0.094\, t_D}} = 10^{-3}$$

$$t_D = 4.37\, s\,. \qquad (5.19)$$

This estimate indicates that the diffusion time could vary from 2 s to 10 s since that is the range of uncertainty in both the cross section and actual ion beam intensity. However, it allows for some estimate of the production rate required to produce the ^{18}N activity for the experiment. As a rate of 10^7 ^{18}N ions/s will be needed, at a minimum the production rate must be on the order of 10^{11}/s in the target. The diffusion time will reduce the intensity by a factor of 200. The ion source has an efficiency of 1–5 % for Nitrogen introducing another reduction by a factor of 20–100. Finally, the transmission is on the order of 50 %. These losses can be compensated by increasing target thickness and proton beam current. It is important to remember that the SILT calculation should only be used a guide. A similar calculation using a different code [Dom93] produced a more pessimistic yield estimate by about a factor of 10.

It is very apparent that such beam intensities are beyond the capabilities of the present TISOL facility. Even with the proposed upgrade to the 20 μA proton beam current at the new TISOL II facility, there is insufficient primary proton beam current to produce such an intense ^{18}N beam. To properly complete the experiment the ISAC facility will be necessary. With the ability to use a target thickness $\geq$100 g cm^{-2} (with a maximum possible target thickness for a U target of ~250 g cm^{-2}) and proton currents of 100 μA it should be possible to achieve ^{18}N ion intensities approaching 10^{10} atoms/s [ISL91]. This intensity would produce an event rate of one PNC α/hour in the decay of ^{18}O.

Another problem is the reliability of the isotope separator itself. TISOL has demonstrated the ability to run continuously for up to four weeks but at the end of the running period radiation damage to various elements of the separator was evident. As the experiment will require at least 100 days of running, an upgrade of the existing Target/Ion Source is needed. The ability to make remote target changes is definitely necessary.

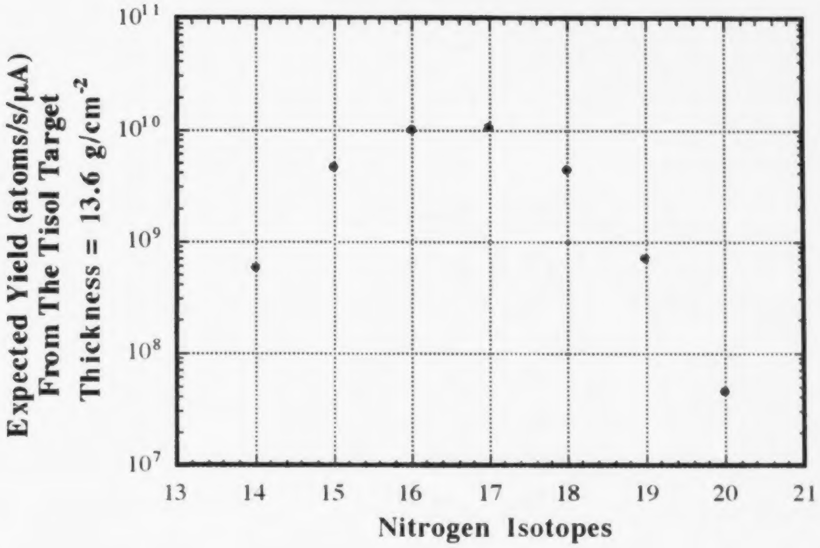

Figure 5.14. The results of a SILT based calculation for the production of heavy Nitrogen isotopes from a Zeolite target. The typical target thickness of the current TISOL target (13.6 g/cm^2) is used.

The required rate of 10^4 events/s raises another complication. This rate exceeds the capacity of a CAMAC/J11-based system. It will therefore be necessary to convert the digital electronics of the existing DAS to either the FASTBUS or other high-speed system. It may also be necessary to rethink the trigger logic to reduce the event rate. Even if such redesigns could reduce the expected data rate somewhat, it is very likely that a CAMAC/J11 system would still be required to operate very close to its design limit, and a newer, high-speed alternative should be investigated.

The required increase in beam intensity is so large that it will likely be accomplished in steps. By taking advantage of this, it would be possible using the existing system, to redo the ^{16}N PNC experiment [Neu74] on the TISOL II facility. This would give an excellent opportunity to examine in detail the process of extracting a small signal from a larger background. It would also allow experience to be gained in the use of a faster, digital electronic system. With the TISOL II upgrade, it should be relatively straightforward to achieve a rate of 10^7 ^{16}N/s beam intensity on the target station. This should result in an α-coincidence event rate of 10 s^{-1}. As the branching ratio to the PNC level is 10^{-4} of the main peak, this generates 10^{-3} PNC α/s or 10^2 per day. This rate is too low to reproduce the results of Neubeck *et al.* [Neu74] without an excessively long running time. Further work on the target to optimize the release of the radioactive nitrogen, and increasing the target thickness will increase the yield of ^{16}N. Combining the target work with an increase in the detection efficiency at the collection station should allow at least another factor of five increase in the yield. It would then take about four weeks of data collection.

In conclusion, the PNC experiment is feasible, but is presently limited by the ability to produce sufficient ^{18}N. The proposed ISAC facility will be required. Detectors have to be understood better to reduce background, and high statistics will be required to allow the backgrounds to be subtracted on a statistical basis.

Chapter 6: Conclusions

The first goal of the thesis work was to develop a flexible $\beta\gamma$ spectroscopy station which would be available for future experiments at TISOL, and to perform an investigation of the $\beta\gamma$ decays of ^{25}Ne, ^{26}Ne and ^{27}Ne as a first test of the system. Linked with this was the implementation of all the associated experimental support services: ion beamline, tape transport system, detector endstation, CAMAC based data acquisition system, and on and off-line analysis software. Since this experiment was one of the first performed at TISOL it also was intended to show the capabilities of TISOL in terms of production of nuclei far from stability. The Ne experiment was intended to confirm the theoretical predictions of Wildenthal *et al.* [Wil83] for the G–T β–decays of heavy Ne isotopes . The final goal of the thesis was to conduct a feasibility study for TRIUMF Experiment 689: the PNC α–decay of ^{18}O. The next sections discuss the results achieved towards these goals.

6.1 TISOL Technical Developments

Major developments have occurred at TISOL since the beginning of the thesis work. They demonstrate the change in emphasis of TISOL from a prototype / engineering study into a maturing facility for the production of radioisotopes capable of a modest physics program. A primary component of this changeover was the construction of the low background experimental area [Dau92]. The original experimental area had a large background from neutron capture reactions which made precision measurements impossible. A new ion beamline was built, extending from just above the dipole magnet to the new experimental area (see Fig. 1.9).

In this new experimental area the decays of the ^{25,26,27}Ne isotopes were investigated and the results obtained were detailed in Chapter 4. This experiment had four beam periods allocated to it: two short test runs and two longer data collection runs. During the test runs extensive development occurred, resulting in the final data acquisition system described in Chapter 3. The first data collection run had been overwhelmed by ^{208}Rn contamination which did not reoccur in the final data collection run due to the combination of a new tape transport system and a good vacuum in the collection station. These two improvements resulted in the very clean spectra observed in Chapter 4. The final run was terminated at about the midpoint of the scheduled beam time by a failure in the tape drive controller electronics.

Although it was not completely successful, the Ne experiment marks a transition from casual studies of production yields with a simple collection foil / detector arrangement to a complete spectroscopy station utilizing a state-of-the-art data acquisition system. At the beginning of this investigation the detector system used by TISOL was unsophisticated, but it was sufficient if all that was required of it was to perform isotope identification and yield measurements. During this thesis work a new detector mounting system was designed, based around a standard 10" box frame. The cover plates could be specifically machined to hold different types of detectors. The Red Giant detector assembly, for example, was mounted in the same box which held the detectors used in the Ne study. Coupling the modular detector mount to a standard TRIUMF data acquisition system now gives TISOL the capability to do complete spectroscopy on the isotopes produced. The moving tape system allows the removal of long-lived contaminants so as to view low intensity beams of short-lived isotopes. The detector station and its associated DAS developed as part of this thesis shall be an enduring legacy to TISOL. The DAS, when utilized to its fullest potential, is useful for studies with many possible decay modes or, in a simpler mode, to study just one decay branch.

The precision of the energy measurements and the low background levels of the data show the utility of the planar HPGe for low-energy γ–rays. In the future, it would be expected that the scheduling problems which prevented the utilization of TRIUMF's modern 40% relative efficiency HPGe detector will not occur, and the detector will be available for TISOL use. This detector will substantially increase both the sensitivity and observed count rate over what was obtained with the coaxial HPGe actually used.

The collection tape transport system worked well. The lack of any background contaminants in any of the spectra caused by long-lived isotopes during the final run demonstrated that the activity was being deposited only on the tape. These observations strongly indicate that the use of a tape collector system and a high vacuum in the collection station are vital for cases where high precision measurements of low production activity is concerned.

Some aspects of the TISOL facility were brought into focus by the attempt to study the isotope ^{27}Ne. This was the first attempt at TISOL to investigate an isotope with no known decay properties. The difficulties encountered in verifying the mass position of the separator were mainly because there were no known γ–decays to indicate when the mass separator was at the correct magnetic field setting and that the beamline was tuned correctly. Very clearly, the optics of the system need to be investigated more rigorously, and calibration points determined for at least the lower mass positions. The facility is still in its preliminary phase. Better understanding of the separator / ion beamline system optics and transmission at a basic level is needed for future investigations into previously-unobserved isotopic regions to be successful.

6.2 The Decay of the Heavy Neon Isotopes ^{25}Ne, ^{26}Ne, ^{27}Ne

This investigation into the decays of ^{25}Ne and ^{26}Ne was the first of its kind at TISOL. For the Ne studies a HPGe coaxial detector, a HPGe planar detector, a ΔE–E plastic scintillator telescope and a ^{3}He neutron detector were in use.

The β ΔE–E telescope gave excellent results for the decay half-life and, within the expected limitations of a plastic scintillator, acceptable results to the observed decay energy. Unfortunately, large systematic errors due to mistakes made during data collection dominate and render the results obtained with this detector imprecise and of limited utility. Any future experiments which utilize this system will have the benefit of what was learned during the data analysis and one will be able to avoid the difficulties encountered.

The DAS worked well and the problems encountered in the hardware timing arrangements were due to inexperience, not to the concept itself. Scheduling conflicts resulted both HPGe detectors being used for the first time in the experiment and in a lack of experienced electronics personnel for set-up and commissioning of the experiment. The lack of experience with these particular HPGe's made determination of the quality of the data being viewed on-line more difficult. As the tape drive controller failed just as the final refinements to the DAS were being completed, there was no time available to correct the errors in electronics, the full impact of which was discovered in the off-line analysis. Additional beam time was unavailable, so the data had to be analysed in spite of its deficiencies.

Table 6.1. A summary of the results obtained for ^{25}Ne(β)^{25}Na compared with previous measurements. The error in the branching ratio is not given because it is believed to be grossly under-estimated.

Property	This Work	[Goo73]
Half-life, $t_{1/2}$ [ms]	604 ± 15	602 ± 8
γ–ray energy [keV]	89.2 ± 0.3	89.5 ± 0.1
γ–ray energy [keV]	981.4 ± 0.8	979.8 ± 0.2
β-endpoint energy [MeV]	6.8 ± 0.4	7.3 ± 0.3
Relative B.R. (980/90)	0.14	0.19 ± 0.02

The experimental results obtained for ^{25}Ne: the half-life, β–endpoint energy, γ-ray energies, and relative branching ratio (see Table 6.1) agree very well with the previous measurement [Goo73]. More beam time would have helped to achieve better statistics for the 980 keV gamma peak and to observe the known high-energy γ–rays. The extremely non-linear efficiency of the coaxial HPGe at energies below 100 keV reduced significantly the role played by the detector and must be understood in greater detail when this type of detector is used in future.

Table 6.2. The results obtained for ^{26}Ne(β)^{26}Na are compared with previous measurements and theoretical predictions. The branching ratio calculation assumes a γ–cascade and the branching ratio quoted for the 151 keV γ–ray is from the 234 keV level.

Property	This Work	Previous Work	[Wil83]
Half-life, $t_{1/2}$ [ms]	199.4 ± 1.1	230 ± 60† 197 ± 1*	162
γ–ray energy [keV]	82.4 ± 0.3	82.5 ± 0.5†	-181
BR [%]	28 ± 1	92.7 ± 0.7†	90
γ–ray energy [keV]	151.7 ± 0.2	—	—
γ–ray intensity [%]	49.3 ± 2.3	—	—
γ–ray energy [keV]	234.1 ± 0.2	233.6 ± 0.2†	—
BR [%]	78 ± 1	7.3 ± 0.7†	—
β-endpoint energy [MeV]	6.9 ± 0.2	7.4	7.0

†Data are from [End90]

*Data are from [Ten92]

The results obtained for the $\beta\gamma$ spectroscopy of ^{26}Ne yielded new information on the decay. The results for ^{26}Ne are summarized and compared to both the existing data [End90] and the theoretical predictions [Wil83] in Table 6.2. In addition to the two previously observed γ–rays at 82 and 234 keV, a γ–ray with an energy of 151 keV was found. Although conclusive evidence for the existence of a γ–cascade could not be obtained, it seems reasonable to assume that the 151 keV γ–ray is in fact from the transition between the 234 and 82 keV energy levels, rather than from a new level at 151 keV. The observation of this gamma ray radically alters the branching ratios for ^{26}Ne decay reported in the literature [End90]. Given the 2nd–forbidden nature of the ^{26}Ne$(g.s.)(\beta)^{26}$Na$(g.s.)$ transition, assigning it a zero branching ratio is appropriate. This experiment cannot conclusively rule out the possibility of higher energy (>0.5 MeV) γ–rays although their branching ratios would have to be <5%, otherwise they would have been detected in the HPGe detectors.

The branching ratio results obtained for ^{26}Ne do not agree well with the theoretical predictions of [Wil83]. This may indicate that the ^{26}Ne wavefunctions used in the calculation are incorrect. This is suspected because of the low half-life predicted, which indicates that their value for $B(GT)$ is too large. [Wil83] achieves excellent agreement with experiment for the case of ^{25}Ne (see Table 2.2), so their calculational principle is sound. There is also reasonable agreement between the prediction and the observed β–endpoint energy although the large systematic errors must also be included.

During the initial search for ^{27}Ne the run was terminated due to failure of the tape drive controller. No evidence could be found for ^{27}Ne, nor its daughter ^{27}Na, nor the granddaughter ^{27}Mg. The ^{27}Ne isotope was to step beyond the region of known nuclei and the failure of the tape controller was particularly disappointing.

For the future, some open questions about ^{26}Ne remain to be answered. Demonstrating the existence of the 234 → 82 keV cascade will require the setting up of a $\gamma\gamma$ coincidence detection system and looking for the tell-tale signature. The possible high energy γ–rays from ^{26}Ne could be easily investigated with a simple detection system. The experiment could begin with ^{25}Ne and collect data until the weak high-energy lines become clear. After collecting sufficient statistics of these high-energy peaks the experiment should switch to ^{26}Ne and count for a time sufficient to accumulate a similar number of events as for ^{25}Ne. This would put very strong limitations on the possible branching ratios and provide an automatic efficiency check and energy calibration for the high energy end of the spectrum. With the TISOL 2 upgrade such an investigation should take only a day or so of running.

Beyond the Ne isotopes, interest lies in investigating other heavier noble gases. TISOL has very competitive production rates for Xe and Ra. Strong yields of Kr isotopes were observed in the runs collected to calibrate the β–telescope. The only noble gas which has not been strongly observed is Ar. The high yields of noble gases and the utilization of either the existing detector station or one derived from it will allow a whole series of decays to be systematically investigated.

6.3 Feasibility Study for the Parity Non-Conserving α–Decay in the ^{18}N$(\beta\alpha)^{14}$C Reaction

The final part of the thesis was devoted to the feasibility of an experiment to observe the PNC α–decay in the ^{18}N$(\beta\alpha)^{14}$C reaction. The major concerns in the study have been discussed in Section 5.4.2.

For the parity violating experiment to be a success, a number of concerns must be addressed. The first and most important is to increase the yield of ^{18}N. The *utmost* priority must be given to increasing the yield from the target. The necessary ion beam intensity will require the ISAC facility. In addition, the target and ion source should be studied to determine the factors critical to the release and ionization of ^{18}N. These studies can and should be carried out with the current TISOL facility.

The use of thinner detectors of increased size will collect the produced α–^{14}C pairs from the decay of the ^{18}N ions more effectively and reduce reduce the effect of the Vavilov tail which produces energy-degraded events. This will also have the effect of reducing the contribution of the β–^{14}C and β–β backgrounds to the PV region. For these reasons their purchase should be considered important to the completion of the experiment.

The magnitude of the β–^{14}C and β–β background has been measured and would seem to be the most significant obstacle to the completion of the experiment. A good knowledge of this background should be gained, so, if necessary, it can be subtracted from the observed data to reveal the PNC peak. The possible contribution to the PV region of a further background from the tails of higher-energy α–peaks should be investigated further by both K–matrix fitting of the existing data and shell model studies into the energy levels of ^{18}O. Every effort must be expended to reduce the background in the region where the PNC α's are expected. The ^{16}O parity violation experiment [Neu74] had a signal to background ratio of ~0.01:1 and were still able to extract the PNC α width. However, the anticipated smaller PNC α-width for the ^{18}N case means that a better signal to background ratio will be necessary — probably at least a factor of 10 better. Further study of the decay ^{18}N(β)^{18}O* to more accurately determine information of interest to the PV experiment should be undertaken. New calculations for the PV alpha width should also be carried out.

The required event rate of α–coincidences which is needed to observe the PNC effect will necessitate the use of a higher speed digital electronic system than the existing CAMAC based electronics. This change, as well as some modifications to the existing mechanical structure of the detector assembly, constitute the last recommendation for the success of the experiment.

The PNC ^{18}N($\beta\alpha$)^{14}C experiment will be challenging to accomplish as are most parity-violation experiments. The construction of the ISAC facility and a series of modifications, well within the current technology, will ensure the successful completion of the experiment.

References

Ade85 Adelberger, E.G., and W.C. Haxton, Ann. Rev. Nuc. Part. Sci. **35** (1985) 504.

Ajz87 Ajzenberg–Selove, F., Nuc. Phys. **A475** (1987) 1.

Azu94 Azuma, R.E., et al., "Constraints on the low energy E1 cross section of $^{12}C(\alpha,\gamma)^{16}O$ from the β–delayed α–spectrum of ^{16}N", Phys. Rev. **C50** (1994) 1194.

Bal84 Balzer, R., R. Henneck, Ch. Jacquemant, J. Lang, F. Nessi-Tedaldi, T. Roser, M. Simonius, W. Haeberli, S. Jaccard, W. Riechart, Ch. Weddingam. Phys. Rev. **C30** (1984)1409.

Bar61 Barton, G., Nuovo Cimento **19** (1961) 512.

Bea86 Beaudoin, G., A. Champagne, H. Jeremie, L. Lassard, "The detection of electrons in the 10 MeV range by plastic scintillators", Nucl. Instr. Meth. **A249** (1986) 379.

Bla91 Blatt, J.M., and V.F. Weisskopf, *Theoretical Nuclear Physics*, New York: Dover (1991).

Bor88 Borge, M.J.G., *et al.*, Nuc. Phys. **A490** (1988) 287.

Bri70 Brink, D.M., *Theory of Nuclear Structure*, Trieste Lectures 1969, International Atomic Energy Agency: Vienna (1970) p. 4.

Bro88 Brown, B.A., and M.Gai, MSU Cycl. Lab. Ann. Rep. (1988), p. 13.

Buc91 Buchmann, L. (spokesperson), TRIUMF Experiment 589 Progress Report, Experimental Evaluations Committee (1991).

Buc92 Buchmann, L., J. Vincent, H. Sprenger, M. Dombsky, J.M. D'Auria, P. McNeely, G. Roy, "The ECR ion source at the TRIUMF isotope separator TISOL", Nucl. Instr. Meth. **B62** (1992) 521.

Buc92b Buchmann, L., *et al.*, TRIUMF Experiment 589: "The $\beta\alpha$ Decay of ^{16}N", E589 Internal Report (1992), unpublished.

Buc93a Buchmann, L., *et al.*, Phys. Rev. Lett. **70** (1993) 2066.

Buc93b Buchmann, L., *et. al.*, Nucl. Instr. Meth. **B79** (1993) 330.

Buc94 Buchmann, L. private communications (1994).

Cab63 Cabbibo, N., Phys. Rev. Lett. **10** (1963) 531.

Cow53 Cowan, C.L. and F. Reines, "Detection of the Free Neutrino", Phys. Rev. **92** (1953) 830.

Dau89 D'Auria, J. M., M. Dombsky, L. Buchmann, J.D. Vincent, J.D. King, "The Proposed ISAC Facility at TRIUMF: A Status Report", Nucl. Instr. Meth. **B40/41** (1989) 418–422.

Dau90 D'Auria, J.M., provided computer program from LAMPF, (1990).

Dau92 D'Auria, J.M., L. Buchmann, M. Dombsky, P. McNeely, G. Roy, H. Sprenger, "Upgrade of the TRIUMF on-line isotope separator, TISOL", Nucl. Instr. Meth. **B70** (1992) 75.

Des72 Desplanques, B., Phys. Lett. **B41** (1972) 461.

Des74 DeShalit, A. and H. Feshback, *Theoretical Nuclear Physics, Vol. 1: Nuclear Structure*, New York: John Wiley & Sons (1974) p. 203.

Des80 Desplanques, B., J.F. Donoghue, and B.R. Holstein, Ann. Rev. **124** (1980) 449.

Dom90 Dombsky, M., Ph.D. Thesis, Simon Fraser University, unpublished.

Dom92 Dombsky, M., L. Buchmann, J. M. D'Auria, P. McNeely, G. Roy, H. Sprenger, J. Vincent, "Targets and ion sources at the TISOL facility", Nucl. Instr. Meth. **B70** (1992) 125.

Dom93 Dombsky, M., private communication (1993).

Duf87 Dufour, J.P., R. Del Moral, F. Hubert, D. Jean, M.S. Pravikov, H. Delagrange, A.C. Mueller, K.H. Schmidt, E. Hanelt, K. Summerer, J. Frehaut, M. Beau, and G. Giraudet, *Rosseau Lake Conference Proceedings*, (1987) p. 349.

Dye74 Dyer, P. and Barnes, C.A., Nucl. Phys. **A233** (1974) 495.

Els84 Elsener, K., et al., Phys. Rev. Lett. **52** (1984) 1476.

End90 Endt, P.M., Nuc. Phys. **A521** (1990) 1.

Eva85 Evans, H.C., et al., Phys. Rev. Lett. **55** (1985) 791.

Fer33 Fermi, E., La Ricerca Scintifica, 2 **No.12** (1933).

Fer34 Fermi, E., "Tentativo d'una teoria dei raggi beta", Nuovo Cimento **11** (1934)1.; Fermi, E., Z. Phys. **88** (1934) 161.

Fer90 Fernow, R. *Introduction to experimental particle physics*, Cambridge: Cambridge University Press (1990).

Fey58 Feynman, R.P. and M. Gell-Mann, Phys. Rev. **109** (1958)193.

Fil89 Filippone, B.W., J. Humblet, and K. Langanke, Phys. Rev. **C40** (1989) 515.

Fra65 Fauenfelder, H. and R.M. Steffen, "Angular Corredlations" in *Alpha-, Beta-, and Gamma- Spectroscopy Volume 2*, ed. K. Siegbahn, Amsterdam: North-Holland (1965) 997.

Fra74 Frauenfelder, H., and E. Henley, *Subatomic Physics*, New Jersey: Prenctice–Hall (1974).

Gie94 Giesen, U., private communications, (1994).

Goo73 Goosman, D.R., D. E. Alburger, J.C. Hardy, "Mass and β Decay of ^{25}Ne, a T = +5/2 Nuclide", Phys. Rev. **C7** (1973) 1133.

Gre87 Greeniaus, L.G., *Triumf Kinematics Handbook*, 2nd ed., (1987) p.VII-104.

Gre91 Green, P.W., *Summary of Nova Commands*, TRI-DNA-91-2 (1991); *The Nova Operation Sequence (OPSEQ)*, TRI-DNA-91-3 (1991).

Gun72 Gunnink, R., and J.B. Niday, University of California Radiation Laboratory Report, UCRL-51061, vol. 1-4 (1972).

Hax87 Haxton, W.C., *Parity Nonconservation in the NN system: Nuclear Structure Issues*, eds. Page, S.A., W.D. Ramsay, W.T.H. van Oers, Proceedings of the Symposium/Workshop on Parity Violation in Hadronic Systems, TRI-87-3, Vancouver: TRIUMF (1987) p.67.

Hel80 Helmer, R.G., and M.A. Lee, Nucl. Inst. Meth. **178** (1980) 499.

Hen74 Henley, E.M., et al., Phys. Rev. **D9** (1974) 755.

Hol88 Holstein, B.R., Can. J. Phys. **66** (1988) 508.

Hug85 Hughes, I.S., *Elementary Particles 2nd ed.*, Cambridge: Cambridge University Press (1985).

ISL91 *The Isospin Laboratory Report*, LAMPF Internal Report LALP 91-51 (1991).

Kra88 Krane, K.S., *Introductory Nuclear Physics*, New York: John Wiley&Sons (1988).

Kre88 Kremer, R.M., *et al.*, Phys. Rev. Lett. **60** (1987) 1475.

Kny84 Knyazkov, V.A., *et al.*, Nucl. Phys. **A417** (1984) 209.

Kub78 Kubodera, K., J. Delurme, and M. Rho, Phys. Rev. Lett. 40 (1978) 755; Guichon, P.A.M., M.Giffon, and C. Samour, Phys. Lett. B74 (1978) 15; Adelberger, E.G., et al., Phys. Rev. **C27** (1983) 2833.

Lac68 Lacaze, R., Nucl. Phys. The (1968) 657.

Lan85 Lang, J., *et al.*, Phys. Rev. Lett. **54** (1985) 170.

Lee56 Lee, T.D., and C.N. Yang, Phys. Rev. **104** (1956) 254.

Leo87 Leo, W.R., Techniques for Nuclear and Particle Physics Experiments, Berlin: Springer-Verlag (1987).

Lud88 Ludgate, G.A., *The VDACS Data Acquistion and Analysis System*, TRIUMF Internal Report (1988).

McN89 McNeely, P., M.Sc. Thesis, University of Alberta (1989), unpublished.

McN89b McNeely, P., G. Roy, J. Soukup, J.M. D'Auria, L. Buchmann, M. McDonald, P.W. Schmor, H. Sprenger, "An ECR Ion Source for Radioactive Beams at TRIUMF", J. d. Physique **50** (1989) C1-807.

McN90 McNeely, P., G. Roy, J. Soukup, J.M. D'Auria, L. Buchmann, M. McDonald, P.W. Schmor, H. Sprenger, J. Vincent, Rev. Sci. Instr. **61** (1990) 273.

Nag79 Nagle, D.E., et al., *Proc. 3rd Int. Symp. on High Energy Physics with Polarized Beams and Polarized Targets*, Argonne 1978. AIP Conf. Proc. **51** (1979) 24.

Neu74 Neubeck, K., H. Schober, and H. Waffler, Phys. Rev. **C10** (1974) 320.

Oln82 Olness, J.W., E.K. Warburton, D.E. Alburger, C.J. Lister, and D.J. Millener, Nucl. Phys. **A373** (1982) 13.

Ort92 Ortec Catalogue, 1991/1992 ed.

Oxo87 Oxorn, K., J.E. Crawford, H. Dautet, J.K.P. Lee, R.B. Moore, L. Nikkinen, L. Buchmann, J.M. D'Auria, R. Kokke, A.J. Otter, H. Sprenger, J. Vincent, "Installation of a Prototype On-Line Isotope Separator at TRIUMF (TISOL)", Nucl. Instr. Meth. **B26** (1987) 143.

Pau34 Pauli, W., Proc. *7th Solvay Conf.*, (*Brussels*, 1933), Paris: Gauthier-Villars, (1934) p. 324.

Phi76 Phillips, G.W., and K.W. Marlow, Nucl. Instr. Meth. **137** (1976) 525.

Pir73 Pirner, H.J., and D.O.Riska, Phys. Lett. **B44** (1973)151.

Pow95 Powell, J., Ph.D. Thesis, University of Toronto, unpublished.

Pre75 Preston, M.A., and R.K. Bhaduri, Structure of the Nucleus, Reading: Addison-Wesley (1975).

Rav87 Ravn, H.L., et al., Nucl. Instr. Meth. **B26** (1987) 183.

Red87 Redder, A., *et al.*, Nucl. Phys. **A462** (1987) 291.

Rei72 Reid, J.M., *The Atomic Nucleus*, London: Penguin Books (1972).

Reu83 Reus, U., and W. Westmeir, *γ–Ray Catalog*, Atomic and Nuclear Data Tables **29** (1983) 204.

Rol88 Rolfs, C. E., and Rodney, W.S., *Cauldrons in the Cosmos*, Chicago: University of Chicago Press (1988).

Roy92 Roy, G., "Parity Violation in Proton–Proton Scattering", in *Symmetry and Spin in the Standard Model, 7th Lake Louise Winter Institute* (*Chateau Lake Louise*, 1992) ed. B.A. Campbell, *et al.*, Singapore: World Scientific (1992) 255.

Roy93 Roy, G., TRIUMF Research Proposal: ^{18}O PNC, Experiment 686, Experimental Evaluation Committee (1993).

Sch72 Schulke, L., Nucl. Phys. **B40** (1972) 386.

Seg77 Segre, E., *Nuclei and Particles 2nd Edition*, W.A. Benjamin, Reading (1977).

Sil85 Silberberg, R., C.H. Tsao, J.R. Letaw, Ap. J. Supp. **58** (1985) 873.

Sno78 Snover, K.A., et al., Phys. Rev. Lett. **41** (1978) 145; Earle, E.D., *et al.*, Nucl. Phys. **A396** (1983) 221.

Ten92 Tengblad, O., M.J.G. Borge, L. Johannsen, B. Jonson, M. Lindroos, T. Nilsson, G. Nyman, A. Poves, H.L. Ravn, J. Retamosa, K. Riisager, P. Sona, K. Wilhemsen, the ISOLDE Collaboration, "Study of Neutron Rich Neon Isotopes", Z. Phys. **A342** (1992)303.

TRI85 *The TRIUMF—ISOL Facility: Proposal for an Intense Radioactive Beams Facility*, submitted to TRIUMF, June 1985.

Wig27 Wigner, E.P., Gottinger Nachrichten (1927) 375.

Wil83 Wildenthal, B.H., M.S. Curtin, and B.A. Brown, "Predicted features of the beta decay of neutron-rich sd-shell nuclei", Phys. Rev. **C28** (1983) 1343.

Wil86 Wildenthal, B.H., *Proc. of Conf. on Weak and Electromagnetic Interactions in Nuclei*, Heidelberg (1986), ed. H.V. Klapdor p. 18.

Woo85 Woosley, S.E., *Nuclear Explosions in Astrophysics*, eds. Buchmann, L., J.M. D'Auria, Proceedings of the Accelerated Radioactive Beams Workshop, Parksville, Canada (September 1985), TRIUMF Internal Report, TRI-85-1 (1985) 4.

Wu57 Wu, C.S., E. Ambler, R.W. Hayward, D.D. Hoppers, and R.P. Hudson, "Experimental Test of Parity Conservation in β-decay", Phys. Rev. **105** (1957) 1413.

Zha89 Zhao, Z., M. Gai, B.J. Lund, S.L. Rugari, D. Mikolas, B.A. Brown, J.A. Nolan, M. Samuel, Phys. Rev. **C39** (1989) 1985.

Zha93 Zhao, Z., et al., Phys. Rev. Lett. **70** (1193) 726.

Zie85 Ziegler, J.F., and J. Biersack, Code TRIM, *The Transport of Ions in Matter*, Pegamon Press, New York, 1985.

Appendix One

Abbreviations and Acronyms

Chapter I

CERN	European Center for Nuclear Research
ECRIS	Electron Cyclotron Resonance Ion Source
ISL	Isospin Laboratory
ISOL	Isotope Separation On Line
ISOLDE	Isotope Separator at CERN
LAMPF	Los Alamos Meson Production Facility
LLN	Louvain La Neuve Accelerator Facility
RNB	Radioactive Nuclear Beams
SILT	computer code to predict production cross-sections
TIS	Target / Ion Source
TISAC	Triumf Isotope Separation and Acceleration Facility
TISOL	Test Isotope Separation On Line or Triumf Isotope Separatio On Line
TOFI	Time of Flight Instrument
TRIUMF	Tri University Meson Facility
A	total number of nucleons
N_t	target thickness in atoms/cm^2
ρ_p	primary production beams particle current
σ_i	cross-section for the production of isotope i
y_i	yield of isotope i
Z	the number of protons in the nucleus

Chapter II

B.R.	branching ratio
G–T	Gamow–Teller
S.M.	Shell Model
$B(N,Z)$	binding energy of the nucleus
c	speed of light in vacuum, 2.9979×10^{10} cm/s
Δ	$M(Z,N) - A - Zm_e$
E_{max}	maximum possible kinetic energy allowed to the electron durin beta decay
E_{rec}	nuclear recoil energy
e	charge on the electron, 1.6022×10^{-19} C
$F(Z', T_e)$	Fermi function
g	beta decay coupling constant
g_A	axial vector coupling constant in beta decay
g_V	vector coupling constant in beta decay
$h=h/2\pi$	Planck constant, 6.5822×10^{-22} MeV-s
H_{if}	matrix element between two nuclear states
j, J	total angular momentum
k	momentum, p/h
l, L	orbital angular momentum
$\lambda_E(l,m)$	transition probability for electric multipole radiation of order l
$\lambda_M(l,m)$	transition probability for electric multipole radiation of order l
M	nucleon mass
$M(Z,N)$	mass of the atomic nucleus
M_Z	mass of the atomic nucleus
m_e	mass of the electron
N	number of neutrons in nucleus
P_n	probability of neutron emission
$\Delta\pi$	change in parity of a state
R	nuclear radius
ρ_N	nuclear density
Q	maximum energy difference between two nuclear states
s_i	Pauli spinors
$t_{1/2}$	half-life
T	isospin
T_e	electron kinetic energy

τ_i	isospin analogue to s_i
V_i	potential
w	transition probability between two nuclear states
ω	angular frequency
$Y_{lm}(\theta,\phi)$	spherical harmonic function

Chapter III

ADC	Analog to Digital Converter
AMP	amplifier
CAMAC	Computer Automated Measurement and Control
CFD	Constant Fraction Discriminator
DAS	Data Acquisition System
G&D	Gate and Delay Generator
Ge(Li)	Lithium Drifted Germanium (Detector)
HPGe	Hyper Pure Germanium (Detector)
ISIS	Ion Source and Injection System
LFIFO	Linear (or analog) Fan In Fan Out
LoFIFO	Logical (or digital) Fan In Fan Out
NIM	Nuclear Instrument Modual
NOVA	New TRIUMF data acquisition system
PMT	Photo Multiplier Tube
PSD	Pulse Shape Discrimination
PV	Parity Violating
SSB	Silicon Surface Barrier (Detector)
TDC	Time to Digital Converter
TFA	Timing Filter Amplifier
TWOTRAN	computer language specifically used to control CAMAC systems
VDACS	VAX Data Acquisition System
α	fine structure constant, ~1/137
$I(x)$	photon intensity
μ	absorption coefficient
r_e	classical electron radius, $2.81794\text{x}10^{-13}$ cm
σ_c	Compton cross section
Φ_{photo}	photoelectric cross section
τ_{pair}	pair production cross section

Chapter IV

DOF	degrees of freedom
MINUIT	CERN library least squares minimization program
a	slope of the efficiency fit for the HPGe detectors
b	intercept of the efficiency fit for the HPGe detectors
χ^2	chi-squared value
χ^2/DOF	chi-squared/degrees of freedom
E_f	used in Kurie plots, $(T_e^2+2T_e m_e c^2)^{1/2}(T_e+m_e c^2)$
F_f	used in Kurie plots, the Fermi function $F(Z',T_e)$
$E_{ff}(E)$	efficiency of HPGe at energy E
$N_{adj}(E)$	N_{obs} adjusted for efficiency and transmission
$N_{obs}(E)$	number of observed counts at energy E
$T(E)$	transmission through detector assembly at energy E
t_{coll}	total ion beam collection time
t_o	time for deflection power supply to ramp-down
t_{stop}	time ion beam deflected
t_{obs}	time of an event
t_1	time of an event occuring during the collection phase corrected for to
t_2	time of an event occuring during the decay phase
Q_β	maximum transition energy during a beta decay

Chapter V

c.m.	center of mass
CP	Charge Parity symmetry (conservation)
OBEP	one boson exchange potentials
PC	parity conserving
PNC	parity non-conserving
PV	parity-violating or parity-violation
PVI	parity violating interaction
$S(E)$	astrophysical S factor
Γ	width of a state
Γ_α	width of state for gamma emission
M_α	Mass of alpha particle
N_α	number of alpha particles in nucleus
$T(\alpha)$	transmission coefficient determined by solving the Schrodinge

	equation for decay process
v_α	velocity of an alpha particle in a nucleus
ω_o	alpha particle collision frequency with the nuclear barrier

Appendix Two

Calculation of the Mass Attenuation Coefficient

To properly analyse any of the gamma ray data collected in this experiment it is necessary to know how much of the gamma flux was lost due to passage through the material between the detectors and the collection point. The effect of material on photons is covered in Section 3.2.1.1. For photons the important parameter is the mass attenuation coefficient, μ:

$$\mu = \frac{\rho N_a}{A}\left(\Phi_{photo} + Z\sigma_c + \tau_{pair}\right) \tag{A2.1}$$

The cross sections themselves can be found in Section 3.2.1.1 For the region of interest it is a fair assumption that the Compton cross section, σ_c, dominates (see fig. 3–6). The Ortec catalog contains a listing of μ for aluminum at various energies. To determine μ two approaches were followed. The first was to fit the aluminum data for μ given in the catalogue to a simple formula over the region where the data were approximately linear. This was then used to calculate μ for aluminum in the experiment. The second approach was to use formula (A2.1) under the assumption that only σ_c contributes to the value of μ. By comparing this value of μ to the the value interpolated from the Ortec catalog, an indication of the possible error can be obtained.

An EXCEL worksheet was created to do the calculations and is shown in Table A2.1. Fig. A2.1 shows the fitting of the data points from the catalog. Also shown are the corresponding data points as calculated by the worksheet. The agreement is very good except at low energies. This is not surprising. Examining Fig. 3.6 in Section 3.2.1.1 indicates that the photoelectric cross section has begun to dominate the compton cross section at low energies. This is exactly what is shown in Fig. A2.1 as the values calculated by the truncated eq. A2.1 are too low.

Table A2.1. Shown below is the calculation for μ for Al and plastic scintillator at all relevant energies for the experiment.

Energy [keV]	Gamma [hv/mec^2]	Material	density [gcm^-3]	Atomic Weight	Z	Cross Section [cm^2]	Att. Coef. μ [cm^-1]
81	0.1585	Al	2.7	26.98	13	5.1596E-25	0.4042
276.4	0.5409	Al	2.7	26.98	13	3.6410E-25	0.2853
302.9	0.5928	Al	2.7	26.98	13	3.5219E-25	0.2759
356	0.6967	Al	2.7	26.98	13	3.3142E-25	0.2596
383.9	0.7513	Al	2.7	26.98	13	3.2184E-25	0.2521
1173	2.2955	Al	2.7	26.98	13	1.9505E-25	0.1528
1333	2.6086	Al	2.7	26.98	13	1.8263E-25	0.1431
81	0.1585	CH	1.032	13.02	7	5.1596E-25	0.1724
276.4	0.5409	CH	1.032	13.02	7	3.6410E-25	0.1217
302.9	0.5928	CH	1.032	13.02	7	3.5219E-25	0.1177
356	0.6967	CH	1.032	13.02	7	3.3142E-25	0.1107
383.9	0.7513	CH	1.032	13.02	7	3.2184E-25	0.1075
1173	2.2955	CH	1.032	13.02	7	1.9505E-25	0.0652
1333	2.6086	CH	1.032	13.02	7	1.8263E-25	0.0610
90	0.1761	Al	2.7	26.98	13	5.0458E-25	0.3953
980	1.9178	Al	2.7	26.98	13	2.1330E-25	0.1671
83	0.1624	Al	2.7	26.98	13	5.1337E-25	0.4022
151	0.2955	Al	2.7	26.98	13	4.4275E-25	0.3469
233	0.4560	Al	2.7	26.98	13	3.8646E-25	0.3028
1808	3.5382	Al	2.7	26.98	13	1.5492E-25	0.1214
90	0.1761	CH	1.032	13.02	7	5.0458E-25	0.1686
980	1.9178	CH	1.032	13.02	7	2.1330E-25	0.0713
83	0.1624	CH	1.032	13.02	7	5.1337E-25	0.1715
151	0.2955	CH	1.032	13.02	7	4.4275E-25	0.1479
233	0.4560	CH	1.032	13.02	7	3.8646E-25	0.1291
1808	3.5382	CH	1.032	13.02	7	1.5492E-25	0.0518